SEISMIC FRAGILITY AND RISK MANAGEMENT OF HIGHWAY BRIDGES IN NEW YORK STATE

by

Ying Pan

A dissertation submitted to the Graduate Faculty in Engineering in partial fulfillment of the requirements for the degree of Doctor of Philosophy,

The City University of New York

2007

UMI Number: 3245046

ProQuest Information and Learning Company
300 North Zeeb Road
P.O. Box 1346
Ann Arbor, MI 48106-1346

This manuscript has been read and accepted for the Graduate Faculty in Engineering in satisfaction of the dissertation requirement for the degree of Doctor of Philosophy.

Date	Professor Anil Agrawal Chair of Examining Committee
Date	Professor Michel Ghosn Co-Chair of Examining Committee
Date	Professor Mumtaz Kassir Executive Officer
	Professor Feng-Bao Lin
	Professor Kolluru Subramaniam
	Dr. Sreenivas Alampalli, NYSDOT Supervisory Committee

THE CITY UINVERSITY OF NEW YORK

ABSTRACT

Seismic Fragility and Risk Management of Highway Bridges in New York State

by

Ying Pan

Advisor: Professor Anil Kumar Agrawal

Co-advisor: Professor Michel Ghosn

Although New York State lies in a region of moderate seismic activity, earthquakes pose a significant hazard to the State's highway infrastructure because of the risk of extensive damage to its existing aging bridge network. The object of this dissertation is to develop an improved method for the seismic fragility analysis of typical New York State highway bridge components and systems, and obtain objective measures to assess their seismic risk.

To meet the stated objectives, typical bridge structural types along with their topological layouts and structural details are identified through a statistical analysis of the National Bridge Inventory (NBI) files. An in-depth parametric study is carried out to evaluate the sensitivity of a bridge's seismic response to variations in its structural parameters. Probabilistic models are developed to describe the structural properties of the critical parameters using experimental data collected from the published literature. Statistical samples of typical New York State bridges are matched with earthquake samples of various intensities for the nonlinear seismic demand analysis. Nonlinear and multivariate regression fits of the seismic analysis results serve to develop probabilistic

models of the demand to capacity ratios for different damage limit states. These models are used to construct seismic fragility curves and fragility surfaces to study the probability of damage for individual components and complete bridge systems as a function of peak ground accelerations or as a function of moment magnitudes and epicentral distances. A second-order reliability method provides narrow bounds on the probability of failure accounting for seismic risk from multiple failure modes.

The effectiveness of several retrofit measures, such as the use of elastomeric bearings, lead rubber bearings, viscous dampers and carbon fiber jackets, are compared by studying the changes that these measures would introduce to the original fragility curves and fragility surfaces. The results of the fragility analysis developed in this research for both as-built and retrofitted bridges would help state engineers develop effective strategies for seismic retrofit prioritization, loss estimation, and network seismic vulnerability assessment.

DEDICATION

To

my parents

Chenglin Pan and Jinxiu Liu

ACKNOWLEDGEMENTS

I would like to express my sincere gratitude and appreciation to my advisor, Professor Anil K. Agrawal, and co-advisor, Professor Michel Ghosn, for their expert guidance, continuous encouragement, and support. My sincere gratitude also goes to Professor John Fillos for his kind support during the course of my studies. I will like to convey my special thanks to Dr. Sreenivas Alampalli and Mr. Rajesh Taneja of NYSDOT for their extensive support and valuable comments during the course of this research.

Finally, I would like to thank my husband, Dr. Ping Tan, and my parents, Chenglin Pan and Jinxiu Liu, for their endless love and selfless mental support as always. I wouldn't have accomplished this work without their encouragement.

This research presented in this dissertation has been supported through National Science Foundation grant number CMS 0099895, U.S. Department of Transportation through Region II University Transportation Research Consortium and the Multidisciplinary Center for Earthquake Engineering Research (MCEER) at the University at Buffalo, State University of New York through the Earthquake Engineering Research Centers Program of the National Science Foundation, under award number EEC-9701471.

TABLE OF CONTENTS

LIST OF TABLES

LIST OF FIGURES

CHAPTER 1

INTRODUCTION

1.1 Statement of Problem

From historical perspective, the modern highway bridge was born in the depression years of the 1930's, came of age in the 1950's to 1970's, and entered its golden years during 1980's [Tonias (1994)]. Past earthquakes, such as San Fernando earthquake (1971), Northridge earthquake (1994), Great Hanshin earthquake in Japan (1995), and Chi-Chi earthquake in Taiwan (1999) have demonstrated that highway bridges are vulnerable to moderate and strong earthquakes [Hwang et al. (2001)]. Considering that bridges built before the mid 1980's were designed without specific consideration of seismic effects, the current transportation network may be exposed to significant seismic risk. This risk increases with the increased deterioration of old bridges. To mitigate potential economic losses due to an earthquake, it is very important to accurately evaluate the seismic performance of these existing bridges and develop an economic approach to effectively strengthen critical components. Several retrofit approaches have been tested and applied to bridges in California and other states with significant seismic risk. However, no previous studies have attempted to analyze the improved seismic performance of these retrofit strategies in a consistent manner that takes into consideration the uncertainties associated with estimating the structural properties of the retrofitted components and comparing the seismic response of the original bridge to that of the retrofitted bridge systems.

A commonly used probabilistic method for analyzing the seismic risk of structural systems is known as the fragility analysis. Current approaches for the seismic fragility analysis and for retrofitting highway bridges have been developed in Western United States. Fragility curves have become a universal tool for determining the conditional failure probability or the probability that structural demand (structural response) caused by various levels of ground shaking exceeds structural capacity to resist a given damage state. In this research field, significant work has already been done on the fragility analyses of typical bridges in Western and Mid America. However, the fragility curves for typical highway bridges in Eastern United States have not been previously investigated.

As per the American Association of State Highway Officials (AASHTO) classification, New York State is in a moderate seismic zone. Although earthquakes in New York State are infrequent, they pose a significant hazard because of the risk of extensive damage to the existing aging bridge network. In fact, previous history has confirmed this observation. For example, an earthquake near Massena Center in New York on September 5, 1944 had a magnitude of 6.0 (VIII) [Mitronovas and Nottis (1993)]. A repeat occurrence of a same magnitude earthquake may cause tremendous damage to the existing bridge network in this region. Moreover, existing fragility curves that have been developed for other regions of the country cannot be applied to New York State and Northeastern United States because of differences in ground motion characteristics, typical bridge types and details, and construction practices. The objective of this dissertation is to develop an improved approach for the seismic fragility analysis of highway bridges applicable for New York State and Northeastern United States and

investigate the benefits of different retrofit approaches in reducing seismic fragility of typical New York steel highway bridges.

1.2 Objectives of Research

One of the most significant outcomes of the application of fragility analyses of highway bridges is identification of structural vulnerabilities of bridge structures and the prioritization of the most cost-effective retrofit measures. The objective of the research presented in this dissertation is to improve the current approach to develop seismic fragility curves, develop fragility surfaces as a function of moment magnitude and epicentral distance for individual bridge components and entire bridge systems, and investigate the effectiveness of different seismic retrofit approaches in reducing seismic fragility. Fragility curves and surfaces display the conditional risk of damage to bridge components at various levels of ground shaking.

Based on the level of seismic fragility of bridges, various retrofit strategies, such as the use of elastomeric bearings, lead-rubber bearings, viscous dampers and carbon fiber jackets, can be compared. The effectiveness of retrofit strategies is verified through the modified fragility curves so that advantages of retrofit approaches can be explicitly quantified in terms of percentage reduction in seismic fragility because of these retrofit actions.

Although the development of analytical fragility curves has been addressed by several researchers [Shinozuka et al. (2000b), Hwang et al. (2001), Choi (2002), Choi et al. (2004)], this dissertation proposes several significant new contributions to the analytical fragility procedure, in addition to the development of fragility curves for New York State. These can be summarized as follows:

1. **Parametric Analysis**: Previous studies considered uncertainties in bridge material properties and gap sizes between deck spans. In this dissertation, we carry out a detailed parametric study of the sensitivity of fragility to superstructure weight, concrete compressive strength, reinforcement yield strength, abutment wall-soil stiffness, friction coefficient of expansion bearings and expansion-joint gap size. We observe that uncertainties associated with the friction coefficient of expansion bearings and superstructure weight have significant effects on bridge ductility in addition to the effects of material strength and gap size which are the only two parameters considered by other researchers.
2. **Analysis of Uncertainties**: Previous studies [Karim and Yamazaki (2000), Deodatis et al. (2000), Choi et al. (2004) and Hwang et al. (2000b)] assumed a set of constant values for the structural capacity of structural components and adopted the empirical value suggested in HAZUS for the dispersion of the seismic capacity and demand, which are based on engineering judgment. These HAZUS values are not related to bridge types and damage states. Actually, structural capacity varies with structural properties, and errors on the estimations of the dispersion will largely influence the final fragility results. To overcome these limitations, estimates of the dispersion in the ratios of structural demand to capacity at different limit states are directly calculated in this thesis based on the results of a regression fit of the data obtained from the nonlinear analysis.
3. **Regression Analysis**: Linear regression on bridge response quantities has been used in previous studies on fragility analysis to cover a wide range of cases in the vicinity of the specific values of PGA used as input during the structural analysis.

In this dissertation, we observe that a quadratic regression provides a better fit on the bridge response data as compared to the commonly used liner regression fit. Furthermore, Multivariate regressions of the fragility as a function of earthquake magnitude, epicentral distance and ductility ratio show further improvement in the predictive model and lead to fragility surfaces as a function of earthquake magnitude (M_w) and epicentral distance (R), which provide better characteristics of the earthquake input when compared to the commonly used PGA.

4. **Bridge Fragility**: Fragilities of individual components are combined to develop fragility curves/surfaces for the entire bridge system using multiple failure modes theory. Second–order reliability bounds are shown to provide narrower bounds on fragility than first-order reliability bounds used in previous studies.
5. **Retrofit Measures**: To demonstrate the effectiveness of several retrofit measures such as the use of elastomeric bearings, lead-rubber bearings, viscous dampers, and fiber reinforced polymer (FRP) jackets, fragility curves and surfaces for the bridge with and without retrofit measures have been developed. Comparisons of these fragility results demonstrate the effectiveness of retrofit measures quantitatively.

In brief, the research presented in this dissertation makes significant original contributions to the state of the art in seismic fragility analysis and the evaluation of the seismic performance of highway bridges. Seismic fragility curves and surfaces developed in this dissertation will be necessary resources for state, local and federal agencies as they develop decision making tools and plans for seismic retrofit of bridges.

1.3 Outline of Dissertation

The seismic fragility and the quantitative evaluation of the effectiveness of various retrofit measures are investigated in this dissertation for highway bridges in New York State. The outline of the dissertation is as follows.

Chapter 1 presents a brief introduction of seismic fragility analysis and this risk management of highway bridges and describes the objectives of the research presented in this dissertation.

Chapter 2 presents a brief review of the state-of-the-art on bridge seismic fragility analysis and seismic risk management using various retrofit approaches.

Chapter 3 describes the method used for the generation of earthquake accelerograms for New York State. Because of the scarcity of actual earthquake data, artificial earthquake records must be generated using the method of Probabilistic Seismic Hazard Analysis (PSHA). The potential seismic events defined by magnitude-distance pairs are selected to generate seismic accelerograms of ground motions at varying hazard levels for fragility analysis.

Chapter 4 presents a detailed statistical analysis of typical bridges in New York State and establishes finite element models for seismic analysis of bridges. Uncertainties in the parameters dominating the behavior of bridge components during earthquakes are identified and quantified for establishing bridge samples for fragility analysis.

Chapter 5 presents the probabilistic analysis of seismic demand and the estimation of structural capacity. The capacity estimation is performed for vulnerable components. Seismic demand is analyzed through nonlinear time history analyses. Seismic fragility curves as a function of Peak Ground Acceleration (PGA) and fragility surfaces as a

function of moment magnitude and epicentral distance are constructed for individual components based on quadratic and multivariate regression analysis results. The theory of structural system reliability is applied to obtain bounds on the fragility of complete bridge systems.

Chapter 6 presents methods for the seismic retrofit of bridges using elastomeric bearings, lead-rubber bearings, viscous dampers, and fiber reinforced plastic (FRP) jackets for bridge columns. Various retrofit schemes are designed for typical bridge components. Approaches for developing analytical structural models of retrofitted bridge components are discussed in detail.

Chapter 7 presents the fragility analysis of retrofitted bridges. The enhanced capacities of bridge components or/and the reduced structural demands are analyzed for damage assessment. Retrofit effectiveness is quantified by comparing the fragilities of bridge components with and without repair.

Chapter 8 presents the conclusions of this dissertation and recommended future research needs in the subject area.

CHAPTER 2

STATE-OF-THE-ART REVIEW

2.1 Introduction

Seismic hazards include ground shaking, fault rupture, soil liquefaction, and lateral or vertical ground movements [Imbsen (2001)]. The 1971 San Fernando earthquake caused severe damage to the regional transportation system, especially, highway bridges. This earthquake prompted the California Department of Transportation (CALTRANS) to upgrade their design criteria (1973) and structural detailing. These design criteria, which were adopted into the 1975 AASHTO specifications with the support of FHWA and AASHTO, have been tested during several earthquakes around the world. After the Loma Prieta (1989) and Northridge (1994) earthquakes, CALTRANS expanded its seismic program to study the seismic vulnerability and prioritize the retrofitting of all its bridges [Imbsen (2001)]. Seismic fragility analysis, which could account for uncertainties in various bridge parameters, began to be used as a powerful tool to evaluate seismic vulnerability of typical bridges around the mid 90's [Hwang and Huo (1998), Mander and Basoz (1999)]. Pioneering research on developing empirical fragility curves based on damage data of bridges and statistical analysis of fragility curves were carried out by Shinozuka et al. (2000a, b). Subsequently, nonlinear static and dynamic procedures were proposed for the development of analytical fragility curves by Shinozuka et al. (2000c) and Hwang et al. (2001). Several researchers have investigated the effectiveness of retrofit measures on the seismic fragility of bridges in Central and

Southeastern United States. For example, DesRoches and Fenves (2000), Choi (2002), Neilson and DesRoches (2003), Nielson (2003), Choi et al. (2004) and DesRoches et al. (2004a, b) proposed a series of fragility analysis results on retrofit effectiveness of elastomeric bearings, lead-rubber bearings, and restrainer cables. Shinozuka et al. (2002) also verified the effectiveness of jacketing of columns of concrete bridges through seismic fragility analysis.

For bridges in Eastern United States, abutment bearings and girder seats are often considered to be the most vulnerable elements under earthquake loading. The lack of continuity in the deck for multi-span bridges is another source of concern for bridge engineers. Furthermore, bridge piers generally lack sufficient confinement to ensure a ductile response because design criteria require only nominal transverse reinforcement. Hence, the New York State Department of Transportation (NYSDOT) started a compressive Bridge Safety Assurance program [NYSDOT (1995)] to address the risk of seismic failure. Figure 2-1 shows the flowchart of this program. The NYSDOT seismic vulnerability assessment is a series of screening and classification steps, which result in a vulnerability rating for each bridge. The seismic assessment of a large inventory of bridges is intended to identify those bridges that are seismically deficient and establish an order of priorities for taking corrective actions. Subsequently, a structural integrity evaluation should be carried out before any retrofit and replacement actions are taken on seismically inadequate bridges. The current methods for performing this evaluation generally fall into (a) capacity/demand ratio methods, and (b) pushover analysis methods [Buckle and Friedland (1995)]. In capacity/demand ratio methods, the components with ratios less than unity are identified for corrective action. It is based on member-by-

member analysis and ignores the interaction between components and load redistribution in case of nonlinear behavior. The pushover method is a nonlinear static analytical method. Neither of these two methods considers the uncertainty in the time history of the ground motion or the uncertainties in bridge structural properties. A method to quantify the probability of damage to bridge components under earthquakes of various intensities by accounting for uncertainties in ground motions and bridge structural properties is known as seismic fragility analysis. This method which has not been previously applied to Northeastern bridges would provided a better assessment of seismic risk and would lead to a more efficient method of prioritizing seismic retrofit programs.

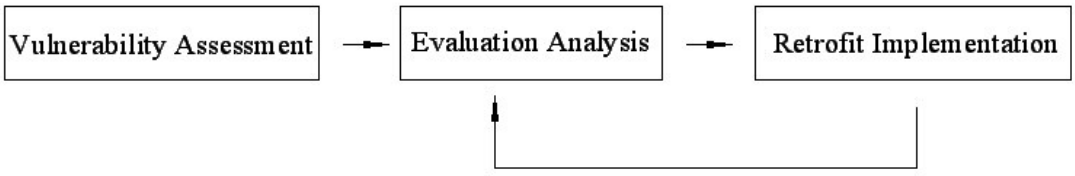

Figure 2-1. Seismic Retrofit Processes.

2.2 Fragility Analysis of Bridges

Seismic vulnerability of highway bridges is usually expressed in the form of fragility curves developed through probabilistic analysis of responses of a random set of bridge samples subject to random samples of ground motion time histories. Seismic fragility is a conditional probability of damage and it gives the likelihood that a structure or structural component will meet or exceed a certain damage level during ground motions of a specific intensity, i.e.,

$$Fragility = P\,[demand > capacity \,|\, \text{Ground motion intensity}\,] \qquad (2\text{-}1)$$

Hence, a fragility curve can be used to predict the level of damage during an earthquake scenario.

Fragility curves can be developed by using empirical methods, expert opinions, or via analytical methods. Empirical fragility curves are developed by utilizing observed damage data during past earthquakes, while analytical curves are developed by numerical simulations of the response of a structural model of a particular type of bridges subject to earthquake ground motions. When sufficient and reliable post-earthquake damage data are available, empirical statistical methods provide the best estimates for fragility curves. A statistical analysis approach has been used to calculate the fragility of bridges subjected to several recent earthquakes, e.g., Loma Prieta (1989), Northridge (1994), and Kobe (1995) [Basoz and Kiremidjian (1998), Shinozuka (2000a), Yamazaki et al. (1999), Karim and Yamazaki (2000)].

Although the empirical fragility method is relatively straightforward, getting adequate damage data for different geological regions is unrealistic. Fragility curves based on expert opinion are very subjective because of discrepancies in the opinions of different experts [ATC-13 (1985)]. High level of uncertainty is inherent in this approach, but the uncertainty level cannot be quantified due to the wide ranges in human judgment in addition to the coarseness of bridge classes.

Hence, analytical fragility curves must be used to assess the performance of highway bridges when actual bridge damage and ground motion data are not available. Analytical fragility curves are developed either through nonlinear static analysis [Shinozuka et al. (2000b)] or nonlinear time history analysis [Hwang et al. (2001), Choi

(2002), Choi et al. (2004)]. Nonlinear static analysis procedures include capacity spectrum method [ATC-40 (1996)], displacement coefficient method [FEMA (1997a, b)] and secant method [COLA (1995)].

The procedure to develop fragility curves using nonlinear time history analysis is shown in Fig. 2-2. A probabilistic seismic demand model is developed for a particular bridge type by simulating response quantities for a random sample of bridges paired with a random sample of ground motions. A detailed dynamic finite element model incorporating nonlinear modeling of bridge components could provide better representation of bridge behavior during an earthquake ground motion input than from equivalent static loading. However, essentially the concept is the same for fragility analysis using nonlinear dynamic or static methods. For fragility analysis, structural capacities are defined for different damage states, and structural demands are related to the ground motion intensity parameters. Hence, probability of failure for a specific damage state, P_f, can be expressed in terms of structural demand, S_d, and structural capacity, S_c, as

$$P_f = P[\frac{S_d}{S_c} \geq 1] \tag{2-2}$$

Since both S_d and S_c are described by lognormal probability distributions, P_f can be further expressed in terms of the standard normal distribution function, such that:

$$P_f = \Phi\left[\frac{-\ln\left(S_c / S_d\right)}{\sqrt{\beta_d^2 + \beta_c^2}}\right] \tag{2-3}$$

where β_c and β_d are lognormal standard deviations of the structural capacity and demand, respectively.

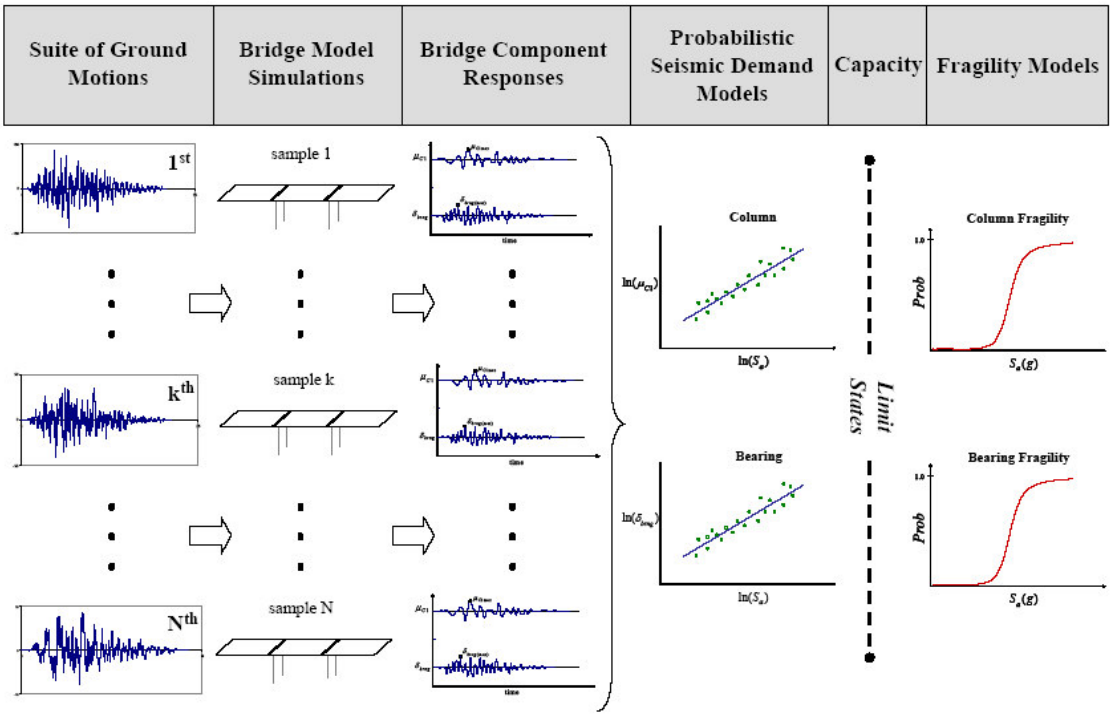

Figure 2-2. Analytical Fragility Curve Generation Using Non-linear Time History Analysis [Nielson, B. (2003)].

Generally, the uncertainty in the expected ground motion time history is one of the sources of uncertainties considered in fragility analysis. Hwang and Huo (1994) carried out studies on uncertainties in random seismic parameters and soil parameters in Mid-America. A suite of one hundred time histories with peak ground accelerations (PGA) ranging from 0.05g to 0.55g were generated by Hwang et al. (2001), and were used for demonstrating the analytical method of fragility analysis for a multi-span continuous concrete bridge in Memphis, Tennessee. Hwang et al. (2001) have also

performed nonlinear time history analysis of three-dimensional bridge model under input ground motion in the transverse direction. Uncertainties in structural material properties and support spring constants were considered to establish random samples of the bridge. Fragility curves for column horizontal displacement responses were developed as a function of the peak ground acceleration and spectral acceleration. The fragility analysis approach, synthetic ground motions and the bridge example presented by Hwang et al. (2001) have been used extensively by other researchers in the subject area [Shinozuka et al. (2000b, c, 2001), Choi et al. (2004)]. Shinozuka et al. (2001) presented empirical and analytical fragility curves developed on the basis of statistical analysis. The maximum likelihood methods were used to estimate two parameters that described a lognormal distribution (median value and standard deviation) in the fragility function. Each event of bridge damage was treated as a realization either from a Bernoulli experiment or from a multi-outcome Bernoulli type experiment.

Simplified procedures based on pushover static analysis method have been proposed as a practical alternative to more complicated nonlinear time history methods for a preliminary fragility analysis by Barron-Corvera (2000), Dutta and Mander (1998), and Shinozuka (2000c). This method uses the intersection of the capacity curve and a reduced response spectrum to estimate the maximum displacement. After considering uncertainties in the capacity spectrum, damage spectrum and damage states, fragility curves are obtained by Monte-Carlo simulation. It has been observed that fragility curves obtained by pushover and nonlinear time history analysis methods are in good agreement only in low ranges of PGAs [Shinozuka et al. (2000c)].

Fragility curves have been used as an effective and powerful tool for retrofit prioritization. Shinozuka et al. (2002) performed nonlinear dynamic analysis for bridges with and without retrofit of concrete bridge columns in Southern California by steel jacketing. The improvement in seismic performance of columns with steel jacketing was quantified by comparing fragility curves of retrofitted bridges to those of the original bridges. DesRoches and Fenves (2000), Choi (2002), Neilson and DesRoches (2003), Nielson (2003), Choi et al. (2004) and DesRoches et al. (2004a, b) have carried out a series of seismic fragility analyses for typical bridges in the Central and Southeastern America with and without retrofit actions. Typical bridge types investigated by Choi (2002) include multi-span simply supported bridges, multi-span continuous bridges, and single-span bridges with concrete or steel I-shape girders. Retrofit strategies include the use of elastomeric bearings, lead-rubber bearings, and restrainer cables. Bridge response quantities were simulated using two-dimensional models with earthquake excitations in the longitudinal direction.

The fragility analysis by Choi (2002) suffers from several limitations. He adopted the displacement ductility criteria following the work of Hwang et al. (2001) to define column capacities during ground motion in the longitudinal direction. Criteria defined by Hwang et al. (2001) are for the behavior of columns in the transverse direction. Since rotation restraints for bridge piers are different in the longitudinal and transverse directions, the correspondence between displacement drifts and moment at pier bottoms will be different in the two directions. Although Choi et al. (2004) performed a sensitivity study to quantify the effects of uncertainty, they only considered material strengths and gap sizes as random variables. Other parameters with significant source of uncertainty,

such as bridge weight and the friction coefficients of bearings, etc., were not considered, although they affect the response quantities significantly. Other common limitations in most previous fragility studies based on nonlinear time history analysis [Hwang et al. (2001), Choi et al. (2004), Choi (2002), Deodatis et al. (2000), Kim and Feng (2003)] include: (i) capacity criteria are defined by a certain set of constant values; (ii) regression analysis is only performed on structural demand; (iii) probabilistic characteristics of both structural capacity and demand have been assumed to follow lognormal distributions with an empirical dispersion value suggested in HAZUS [HAZUS 99-SR-2 (1999)] for $\sqrt{\beta_d^2 + \beta_c^2}$. These values are different in 1997 and 1999 versions of HAZUS, and they are not related to specific bridge types and damage states. In fact, the capacity of bridge components varies with structural parameters, and the correctness of the assumed dispersion value influences the fragility analysis significantly. Hence, fragility curves available in the literature suffer from severe limitations. In this dissertation, the fragility analysis of typical highway bridges in New York State has been carried out by addressing all above the limitations. Hence, this research makes significant contributions to the state-of-the-art by proposing a more comprehensive approach of fragility analysis. It also makes equally significant contributions to the state-of-practice in New York State by developing fragility curves for the region. Fragility curves have also been developed by considering the effects of different retrofit actions. These results can be used in selecting and prioritizing most effective retrofit strategy.

2.3 Seismic Retrofit of Bridges

The process of seismic retrofitting involves the assessment of economic, social and technical issues. There are various corrective actions developed for the most common deficiencies found in highway bridges. The main structural goals of a retrofit are: (1) strengthening, (2) isolation, (3) ductility, (4) displacement allowance, (5) tuning or rearticulating, and (6) energy dissipation [Imbsen (2001)]. These strategies are generally used in combinations, depending on the type and importance of the bridge and the seismic hazard. Most of these retrofit actions are based on experience during past earthquakes on the West Coast, and research sponsored by CALTRANS and FHWA. Primary retrofit strategies are the ones that can improve overall seismic behavior of the bridge and they include column confinement, isolation bearings, and damper/restrainer devices. Secondary corrective actions focus on issues such as strengthening foundation anchorage, adding diagonal-bracing members, replacing original concrete deck, and modifying lightly reinforced concrete cross sections.

Column failure is a significant problem for highway bridges during earthquakes. There are three common modes of failure in bridge columns: (1) Shear failure, (2) Flexural failure and (3) Lap splice failure. Shear failure is a brittle mode of failure and it is caused by inadequate transverse shear reinforcement [Seible and Priestly (1999)]. Shear failure can be catastrophic. Sufficient confinement steel in bridge columns is necessary to assure adequate ductility. Confinement not only provides lateral support to the longitudinal reinforcing steel against buckling, but it also provides increased compressive strength, shear strength, strain capacity and confining stress to the concrete in the column core. Consequently, a properly confined concrete column has higher

ductility, and gets the desired ductile failure mode during earthquakes. Lap splice failure, also a form of brittle failure, of the longitudinal reinforcing steel in the column occurs just above the footing, which is also a critical plastic hinge region. This would not allow the plastic hinge to fully develop prior to the failure of the lap-splice. The capacity of columns to overcome all these failure modes can be improved by the addition of transverse confinement to the columns in the form of either hoops or spirals covered by concrete cover as in Fig. 2-3(a), a steel shell as in Fig. 2-3(b), or a fiber reinforced polymer (FRP) shell as in Fig. 2-3(c) [Haroun et al. (1999)]. Retrofit by applying a steel or FRP shell around the column can either cover the potential plastic hinge region or the entire length of the column. Steel jacketing, shown in Figure 2-3(b), has been recognized as the most widely used and effective technique for retrofitting bridge columns [Chai et al. (1991)]. During the last few years, sheets of fiber-reinforced polymers (FRP), an advanced composite material, have been used extensively and reliably for retrofitting structural members [Bakis et al. (2002)]. The combination of high strength, high stiffness fibers, such as glass and carbon fibers, with low-cost, lightweight, environmentally resistant polymers gives FRP sheets unique properties in terms of strength, lightness, chemical resistance, and ease of application. Mander et al. (1984, 1988) studied the stress-strain behavior of confined concrete and established an analytical model for confined concrete columns under dynamic cyclic axial compression loading. Axial compression tests were carried out on columns confined with spiral and rectilinear hoops to verify his model. This generalized model is good for the confinement by steel reinforcement, where the confining stress is assumed to remain constant. For externally bonded fiber composite shells, more advanced methodologies, which account for

continuously increasing confining stress are required, such as the ones developed by Spoelstra and Monti (1999), or Teng and Lam (2004).

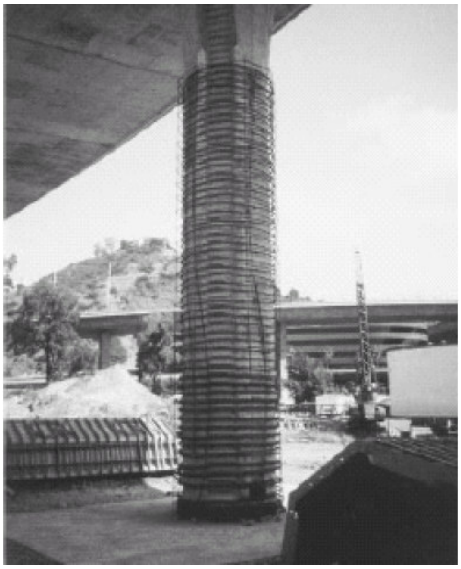

(a) Confinement by Reinforcement and Concrete Shell

(b) Column Steel Jacketing

(c) Column FRP Jacketing

Figure 2-3. Retrofit Strategies for Bridge Columns.

Bearings are sensitive and key elements of highway bridges. Seismic isolation has been recognized as a successful and effective technology for protecting highway bridges from damaging earthquake ground motions. The two basic types of isolation systems that have been employed are elastomeric bearings and sliding bearings [Mayes et al. (1992)]. Elastomeric bearings with low horizontal stiffness elongate the fundamental period of the bridge to avoid resonance with the excitations. The sliding isolation system is based on the concept of sliding friction [Kunde and Jangid (2003)]. An isolation system should be able to support a structure while providing additional horizontal flexibility and energy dissipation. The most widely used isolators for highway bridges are the steel laminated elastomeric bearings shown in Fig. 2-4 with or without lead core, because of their minimal requirement of maintenance and low cost. Laminated elastomeric bearings consist of alternating layers of steel and rubber plates. Bearings are very stiff in the vertical direction because of the steel plates, and they are very flexible in the horizontal direction because of the rubber layers. Lead rubber bearings are similar to the laminated rubber bearing except that a central lead core is used to provide an additional means of energy dissipation and an increased stiffness against normal lateral loads such as wind and vehicular braking forces. The central lead core reduces the lateral displacement of isolators by dissipating energy and adding stiffness. Roeder and Standon (1983, 1987, 1989) have carried out extensive experimental and analytical investigations on the material properties of elastomer, bearing behavior, and the failure modes for elastomeric bearings. It has been observed from the experimental results of Roeder et al. (1987) that a bilinear relationship between shear force and transverse displacement provides the most appropriate model for elastomeric bearings [Kelly (1997)]. Design and construction

requirements for elastomeric bearings, adopted into AASHTO Standard Specifications for highway bridges, are available in a series of NCHRP reports [Stanton and Roeder (1982), Roeder and Stanton (1991), Yura et al. (2001)].

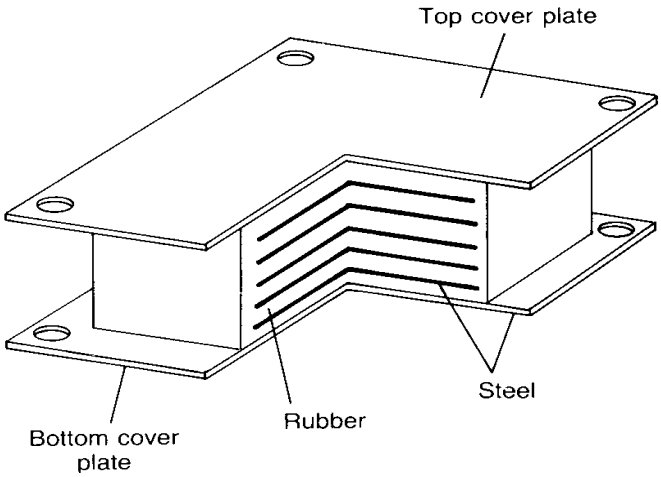

(a) Laminated Elastomeric Bearing

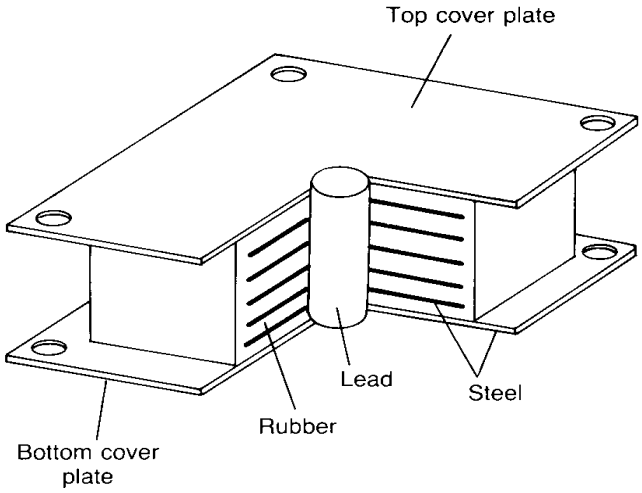

(b) Lead Rubber Bearing

Figure 2-4. Elastomeric Bearings.

Additional devices, such as restrainers and viscous dampers are usually installed in parallel with isolators to restrain their horizontal movement. Restrainers are usually in the form of steel cables, steel tie rods, lock-up devices and stopper bars oriented in the transverse, longitudinal and/or vertical directions to limit excessive relative displacements at expansion joints and to prevent the loss of support. CALTRANS has been installing longitudinal restraining devices at hinges and deck joints since 1971. During the 1989 Loma Prieta and 1994 Northridge earthquakes, it was seen that this type of retrofit is quite effective in protecting bridges. DesRoches et al. (2003) have carried out tests on seismic cable restrainers to model their behavior during earthquakes. Choi (2002) used a bilinear model for restrainer cables, and developed fragility curves for bridges with restrainer cables installed between the decks and abutment or between the decks and piers. Choi (2002) also conducted a similar study on the combination of restrainer cables and elastomeric bearings. Maleki (2004) investigated the nonlinear behavior of restrainers in the form of angles or welded plates, which are placed on each side of the elastomeric bearings. The main shortcoming of restrainer rods and cables is that they do not dissipate any significant amount of seismic energy. Hence, these restrainers either break or cause punch-through action through bridge diaphragm walls at the two ends of the cable/rods during strong earthquakes. Viscous fluid dampers don't suffer from such shortcoming. The damping force of viscous fluid dampers is proportional to the velocity of the isolator's deformation. Feng et al. (2000) proposed using dampers at expansion joints of highway bridges for seismic protection. They have demonstrated that visco-elastic dampers are effective in reducing the relative displacements at expansion joints without causing any increase in ductility demand or

bending moments in columns. There are applications of dampers in Northeastern United States as well. For example, Taylor dampers have been installed on the Triborough Bridge in New York, between the bridge deck and piers to limit the motion of the deck during earthquakes and major windstorms. The original concrete deck of the bridge has been replaced by a lightweight orthotropic steel deck. Using lightweight materials, such as lightweight orthotropic steel or FRP, in bridge decks is an effective seismic retrofit measure, since a smaller structural mass would induce smaller earthquake forces. Besides fluid viscous dampers, other dampers, such as high damping steel connections using shape memory alloys have also been explored for bridge retrofits [Ocel and DesRoches (2002)].

Unlike California, the probability of occurrence of a large earthquake during the life span of a bridge is generally small in New York. Hence, any retrofit measures that are applied have to be cost effective. It has been observed through discussions with NYSDOT engineers that primary bridge retrofit measures currently applied in New York State include: (a) providing superstructure continuity for multi-span simply supported bridges, (b) replacement of steel bearings by isolation bearings, and (c) column confinement by steel or carbon fiber jackets. Because of instability problem with steel rocker bearings, they are being replaced by multi-rotational pot bearings with PTFE sliding surface or steel laminated elastomeric bearings. Expansion joints at piers are also being eliminated by splicing simple spans together to form a continuous girder. This has several benefits, including reduced deterioration of bearings and girders due to leaky joints and increased resistance of the bridge to seismic displacement. In this dissertation,

we will explore the effectiveness of these retrofit measures in terms of the improvements they will make on the fragility of typical New York State steel bridges.

CHAPTER 3

SEISMIC HAZARDS AND SYNTHETIC GROUND MOTIONS

3.1 Historical Earthquakes and Seismic Hazards

Figures 3-1 and 3-2 (USGS a) show seismic maps of the United States and the Eastern United States, respectively. It is observed that earthquake activity in the United States has been predominantly concentrated in California. Fig. 3-3 shows earthquakes in New England and adjoining region. It is observed that more than 400 earthquakes with magnitude greater than 2.0 have occurred in New York State between 1730 and 1986 [Tantala et al. (2000)]. This level of seismic activity places New York State third among most active regions east of the Mississippi River. Only South Carolina and Tennessee are more seismically active than New York State [Isachson et al. (1991)]. Table 3-1 shows recorded earthquakes with magnitude greater than 4.5 in New York State (USGS b). The strongest known earthquake in New York State occurred in the Cornwall-Massena area along the US-Canadian border on September 5, 1944. It had a maximum intensity of VIII on the Modified Mercalli scale (Richter magnitude about 6). Geologists predict that an earthquake of magnitude 5.0 or above on the Richter scale has a 2% probability of occurrence in the New York State region within the next 50 years [Graver and Rubin (1995)].

Seismic risk exposure in New York area has been of increasing concern recently. Most regions of New York State are characterized by moderate levels of seismicity and seismic hazard [Jacob (1993)]. The highest level of seismicity is concentrated in the

northern Adirondacks, New York City Metropolitan area, and Western New York, including Attica and Buffalo. Those locations are shown on state map in Fig. 3-4. It is estimated that billions of dollars of economic damage, and heavy casualty and injury to life can be caused by an earthquake of magnitude $M_w > 5.5$ or 6 in a densely populated area like New York City [Mitronovas and Nottis (1993)].

According to the New York Association of Consulting Engineers, earthquakes with modified Mercalli intensity of VII are likely to occur on average every 100-200 years (i.e., there is a 20 to 40 percent probability of occurrence in 50 years); larger earthquakes with modified Mercalli intensity of VIII-IX may also occur; and earthquakes of even larger magnitude and intensity with very low probability of occurrence can not be excluded [Nordenson (1987)]. Hence, to evaluate the risk to bridge structures under such possible scenarios, ground motions at various hazard levels need to be simulated for the applicable seismic hazard to study the seismic fragility of highway bridges in the New York State region. Seismic guidelines for New York City have been developed through extensive investigations by consulting engineers and the New York City Department of Transportation (NYCDOT). In this dissertation, probabilistic seismic hazard analysis and deaggregation are applied by using the interactive deaggregation programs of the U.S. Geological Survey to simulate ground motion time histories.

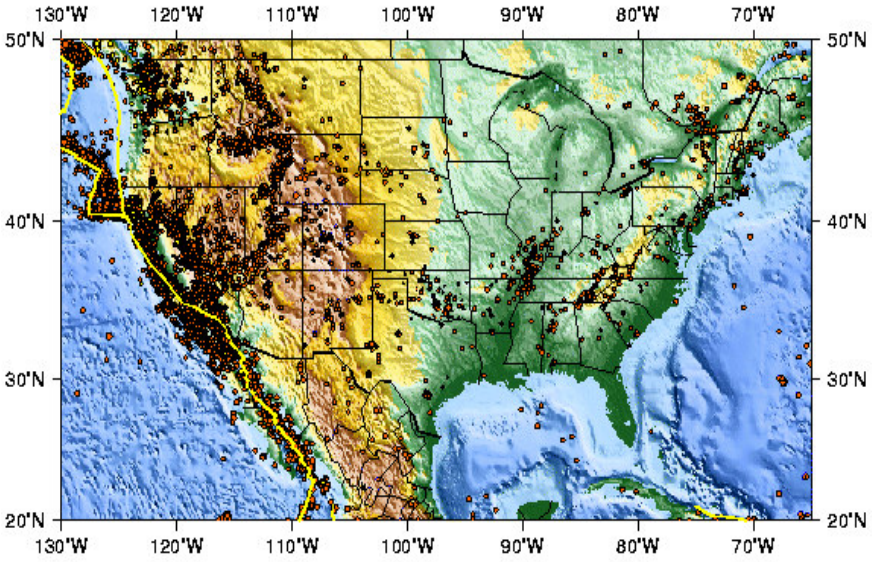

Figure 3-1. Seismicity of the United States.

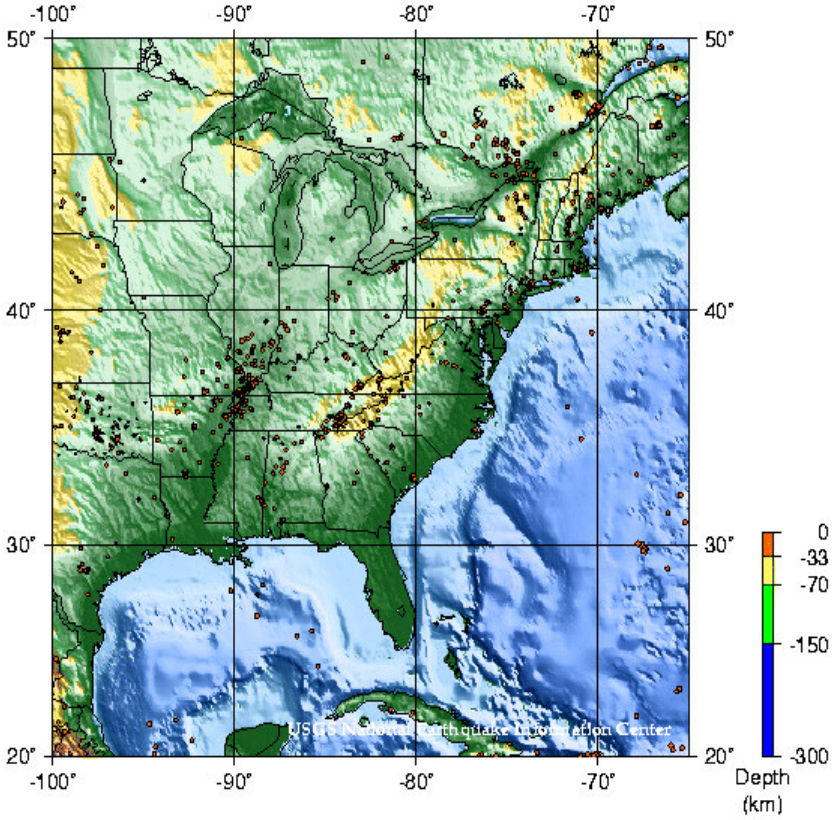

Figure 3-2. Seismicity of the Eastern United States.

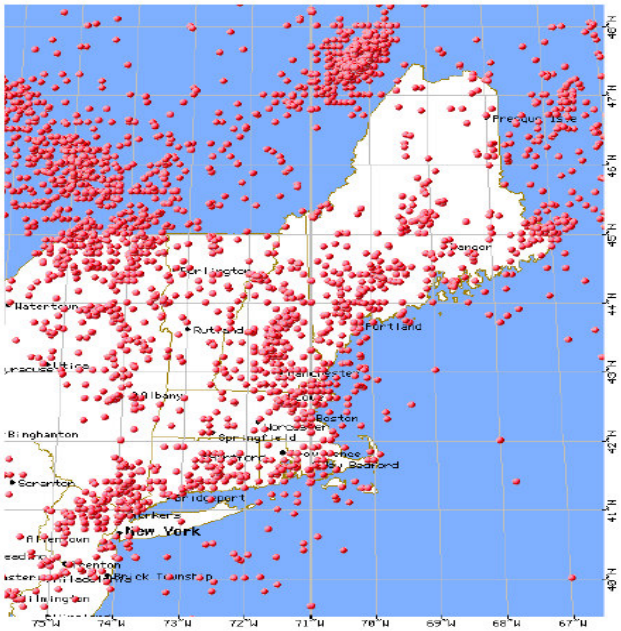

Figure 3-3. Earthquakes in New England and Adjacent Regions (1638-1995).

Figure 3-4. Map of New York State.

Table 3-1. Earthquakes in New York State with Magnitude, $M_w > 4.5$.

Date		Hypocenter		Magnitude (M_w)	Modified Mercalli
		Latitude	Longitude		
1737	12/19	40.8 N	74.0 W	--	VII
1877	11/04	44.5 N	74.0 W	4.9	VII
1884	08/10	40.6 N	74.0 W	5.5	VII
1897	05/28	44.5 N	73.5 W	4.7	VI
1914	02/10	45.0 N	76.9 W	5.2	VII
1929	08/12	42.9 N	78.4 W	5.2	VIII
1931	04/20	43.5 N	73.8 W	4.7	VII
1934	04/15	44.7 N	73.8 W	4.5	VI
1935	11/01	46.9 N	79.1 W	6.2	VII
1944	09/05	45.0 N	74.7 W	6.0	VIII
1966	01/01	42. N	78.2 W	4.6	VI
1983	10/07	43.9 N	74.3 W	5.1	VI

3.2 Existing Artificial Seismic Accelerograms

Seismic retrofit of bridges in New York State may be necessary as a result of the bridge evaluation process mandated by the Federal Highway Administration (FHWA) in 1981. In 1998, rock motions were developed by a panel of experts led by Weidlinger Associates for uniform adoption in the New York City region [Weidlinger Associates (1998)]. To address spatial variability concerns, artificial ground motions were generated at 17 hypothetical piers on a straight line, with 100-m spacing between adjacent piers assumed to have the same foundation conditions [Risk Engineering Inc. (1998)]. By selecting an appropriate subset of these ground motions, users can approximate the

ground motions for any bridge length up to one mile. Return periods of 500 and 2500 years are considered to generate three sets of ground motions for each pier. Ground motions with 10% probability of being exceeded in 50 years can be scaled for design or functional-evaluation. A 2500-year seismic return period represents an extreme event that must be considered for collapse prevention. Figures 3-5 (a)~(c) show a set of three longitudinal acceleration time histories at the same pier. The average response spectrum based on the ground motions of Figures 3-5 (a)~(c) is shown in Fig. 3-5 (d). Fig. 3-6 shows NYC metro region rock acceleration spectra. Comparing Fig. 3-5(d) and Fig. 3-6, it is observed that the response spectra in Fig. 3-5 (d) is compatible with response spectra of an earthquake on rock site in New York City with a return period of 2500 years.

The existing suites of rock motions with return periods of 500 and 2500 years only represent ground motions at two hazard levels. For fragility analysis of highway bridges, ground motions representing various levels of hazard are needed. These ground motions must be simulated on the basis of potential magnitude and epicentral distance data, as described in the next section.

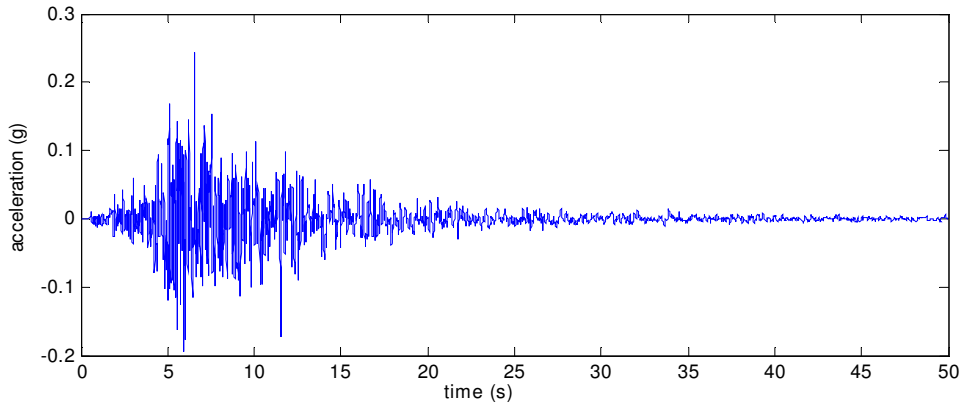

(a) 1st Set Ground Motion in Longitudinal Direction

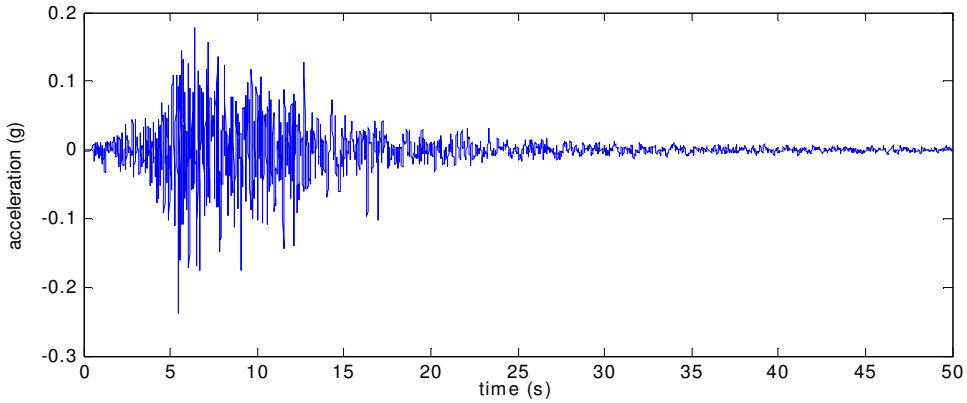

(b) 2nd Set Ground Motion in Longitudinal Direction

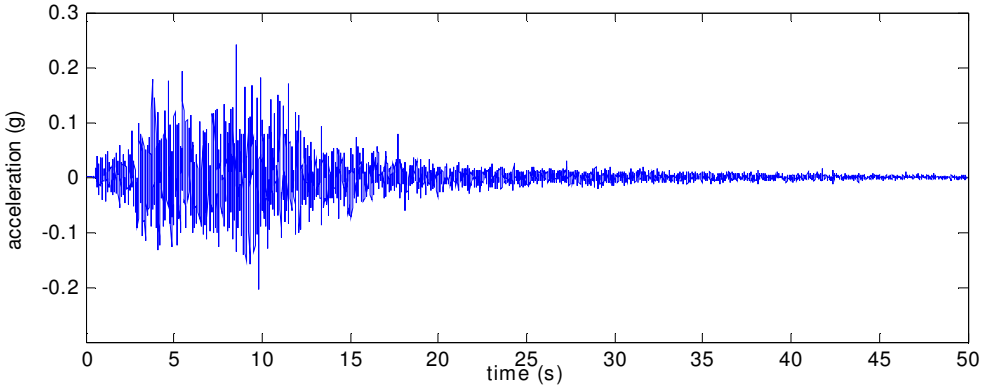

(c) 3rd Set Ground Motion in Longitudinal Direction

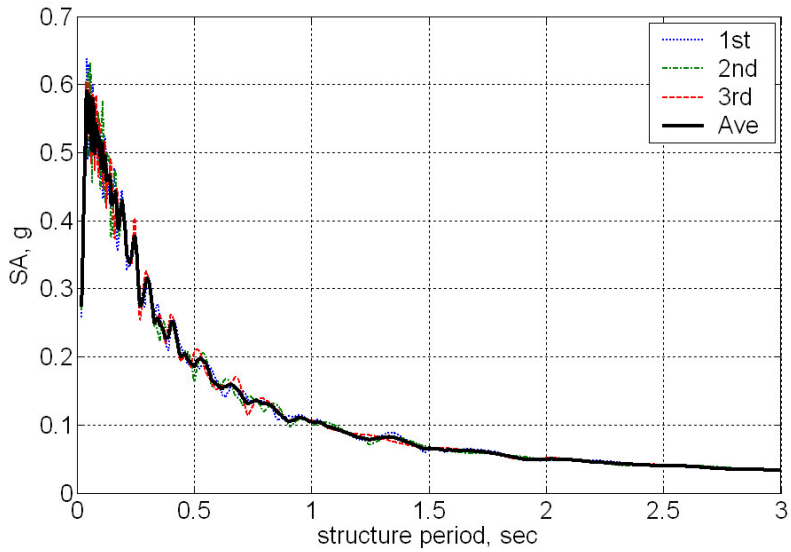

(d) Response Spectra for Ground Motion Sets in Longitudinal Direction

Figure 3-5. Artificial Ground Motions Uniformly Adopted in NYC.

(5% Damping, 2500-year return period)

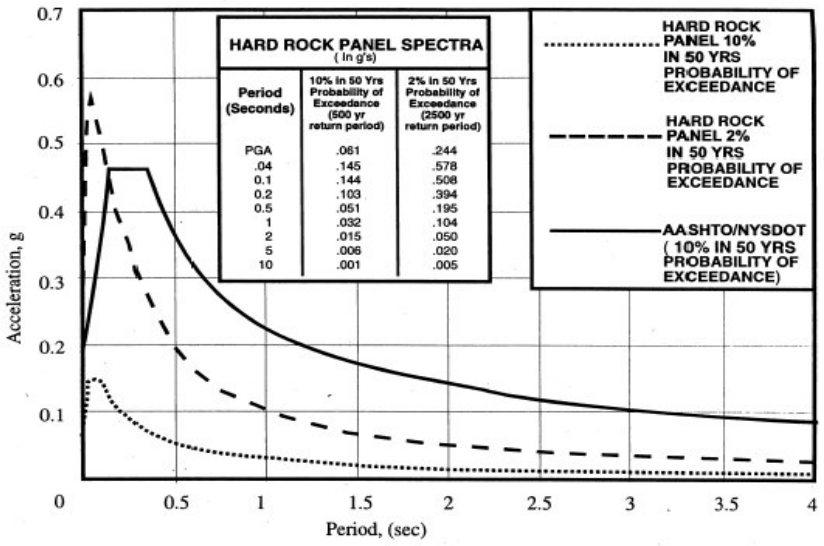

Figure 3-6. NYC Metro Region –Rock Acceleration Response Spectra

(5% Damping –2500 year and 500 year Return Periods)

3.3 Ground Motions Simulation for Fragility Analysis

To perform the fragility analysis of a particular bridge, ground motions with various hazard levels have to be generated to evaluate the probability that the bridge will be subjected to certain damage states within a certain return period. Generated ground motions must be representative of the seismic characteristics of the site, and must represent various hazard levels defined by annual frequency of exceedance of a certain peak ground motion (PGA) or response spectrum acceleration (SA) value.

3.3.1 Probabilistic Seismic Hazard Analysis

Seismic hazard analysis involves quantitative estimation of ground–shaking hazards at a particular site according to certain unique source parameters, rock motions, and soil profiles [Beresnev and Atkinson (2002)]. The method of probabilistic seismic hazard analysis (PSHA) can be applied in New York City region using suspected seismic sources, since actual seismic sources (e.g., faults) are not known. PSHA estimates the mean annual frequency of exceedance at the site by integration of all potential magnitudes and source distances from each elementary source [Kramer (1996)]. Potential elementary seismic sources for each hazard level are binned into magnitude and epicentral distance intervals. The relative exceedance contributions in percent are separated for each bin using a deaggregation procedure. Through the process of deaggregation, the relative contributions to a hazard level in percentage can be expressed as a function of magnitude M_w and epicentral distance, R and deviation ε. Hence, we can identify hazard-dominating scenario events, defined as M_w - R pairs, from deaggregated seismic hazard maps. In order to illustrate the approach, Fig. 3-7 (a) and (b)

show New York City seismic hazard deaggregation maps at two hazard levels, by using the interactive deaggregation programs of U.S. Geological Survey (USGS). The site position (73.83 W, 40.65 N) in New York City and annual frequency of exceedance (1% in 50 years and 2% in 50 years) are defined as input for the program. Probabilistic seismic hazard analysis is conducted to estimate the peak ground acceleration, PGA, at different probability levels. Hazard levels are defined by PGAs and exceedance probabilities. In Fig. 3-7, the vertical axis indicates the relative contribution of each bin (in percentage) with magnitude (M_w) at intervals of 0.2 and epicentral distance (R) at intervals of 25 km. The mean value is calculated from all potential sources by weighing the contributions of each bin. Selecting the mean value will result in better matching of simulated ground motions to targeted values of PGA and SA. The modal value corresponds to the source data contained in the bin with the greatest contribution. Hence, selecting the modal value will always correspond to the greatest contribution for that hazard level.

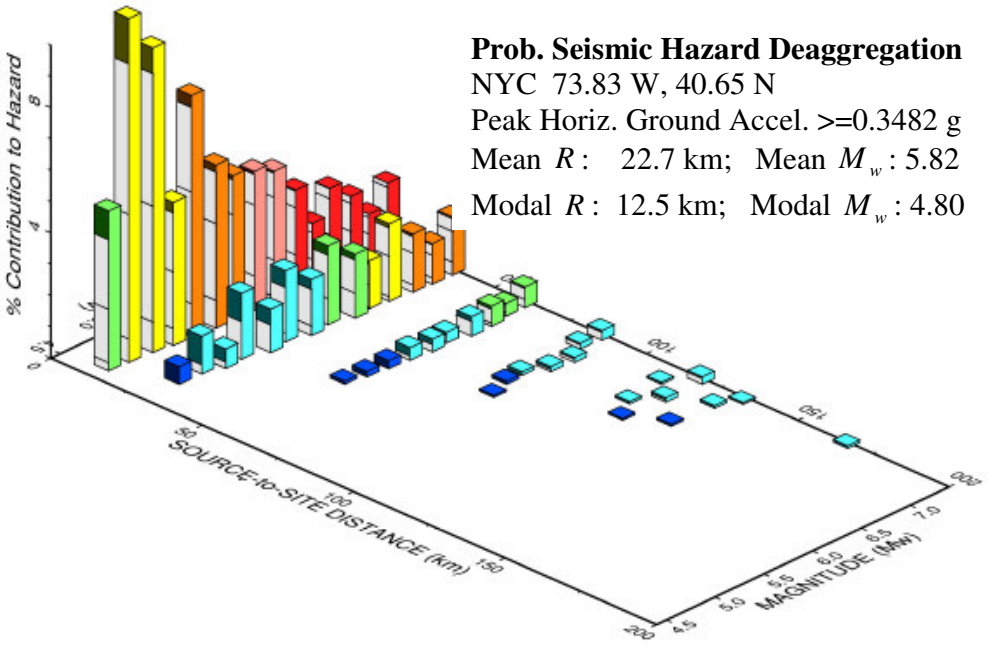

(a) 1% Probability in 50 Years for Exceeding PGA 0.3482g (USGS PSHA)

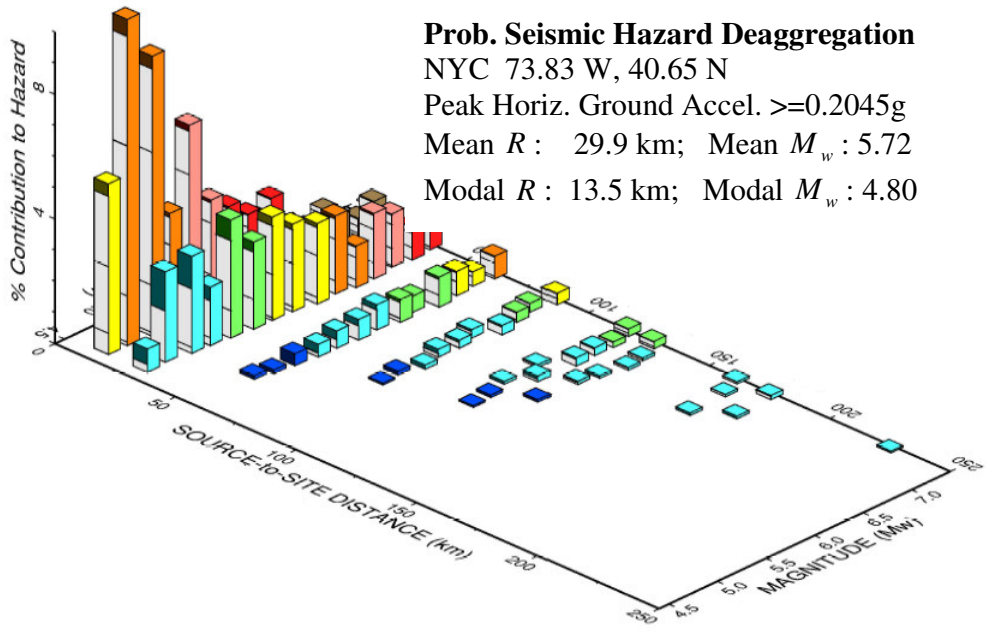

(b) 2% Probability in 50 Years for Exceeding PGA 0.2045g (USGS PSHA)

Figure 3-7. NYC Seismic Hazard Deaggregation Maps.

3.3.2 Stochastic Ground Motion Simulation (SGMS) Code

The Engineering Seismology Laboratory at the State University of New York at Buffalo has developed a Stochastic Ground Motion Simulation (SGMS) code for Eastern North America [Halldorsson and Papageorgiou (2004a, b)]. The SGMS code uses the specific barrier model to describe the earthquake source in a stochastic modeling approach. Fig. 3-8 describes the Specific Barrier Model of the seismic source proposed by Papageorgiou and Aki (1983a, b). The fault plane consists of an aggregate of circular cracks of radius ρ_0 on a fault plane of length *L* and width *W*. The shaded area denotes barriers, and the circles within each crack denote the rupture front at successive time instants. Region-dependent ground motion time histories can be simulated for inter-plate, extensional, and intra-plate tectonic regimes, respectively using this model. Eastern North America (ENA) belongs to intra-plate regime. For this regime, the input distance for SGMS code is the hypocentral distance. To account for the site response, there are only two options for prevalent soil type in ENA sites, which are soil classes A or B-C boundaries, as defined in Table 3-2 [NEHRP (1997)]. Average V_{100} and N_{100} are the shear wave velocity and the blow count for the upper-100 ft site soil profiles. For other specific soil profiles, such as D and E soil types in New York State [Nikolaou, et al. (2001)], we can choose ISOIL=0 for the SGMS program, which gives absolutely no site effects in the generated time history. The site amplification could then be analyzed by using SHAKE91 [Idriss and Sun (1992)], based on the detailed soil information at the site, to obtain ground surface accelerograms. In SHAKE91 program, soil profile is defined for the properties of horizontal soil layers. For each soil layer, soil parameters

required for inputs include layer thickness, unit weight, shear wave velocity or low strain shear modulus, shear modulus reduction curve and damping ratio curve.

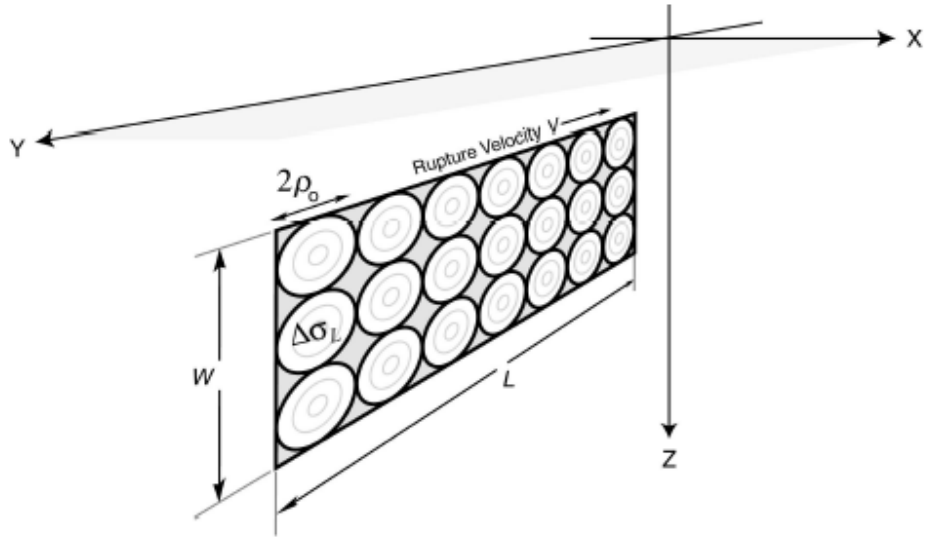

Figure 3-8. Specific Barrier Model of Papageorgiou and Aki (1983 a, b).

Table 3-2. NEHRP Soil Classifications.

Site Class	General Description	Shear-wave Velocity	Blow Count
A	Hard Rocks	V_{100}>1500 m/s	not applicable
B	Rocks	760<V_{100}<1500 m/s	N_{100}> 100
C	Very Dense Soils and Soft Rocks	360<V_{100}<760 m/s	50<N_{100}< 100
D	Stiff Soils	180<V_{100}<360 m/s	15<N_{100}< 50
E	Soft Soils	V_{100}<180 m/s	N_{100}< 15

* NEHRP: National Earthquake Hazard Reduction Program

3.3.3 Ground Motion Generation for Fragility Analysis

As previously described, synthetic ground motions could be simulated using the SGMS program for the New York State region. The most significant input for SGMS

program includes magnitude-hypocentral distance pairs, which could be selected on the basis of deaggregated seismic hazard (DSH) maps from the U.S. Geological Survey interactive program, as illustrated in Fig. 3-7. Deaggregated seismic hazard maps of USGS provide an approach to identify the predominant seismic events. The selection process for seismic events is a trial and error process, since selected magnitude-distance pairs must be compatible with the seismic hazard, which should either represent the most likely earthquakes that may affect the site, or represent the characteristics of various potential hazard levels [Bazzurro and Cornell (1999)]. During the statistical analysis of USGS seismic hazard deaggregation data, both the peak ground accelerations and the spectral accelerations at short and intermediate structural periods are considered as ground motion intensity parameters. Various return periods for earthquakes exceeding certain PGA and SA values are in correspondence with targeted ground motion intensities. As mentioned in section 3.3.1, mean epicentral distance and mean magnitude will result in generated ground motions closer to the targeted values of PGA and SA. However, the mean epicentral distance and mean magnitude may correspond to earthquakes with little contribution to the hazard in some situations. It is the modal distance and magnitude that always correspond to the greatest contribution to a hazard level. However, modal values are dependent on binning details [Harmsen et al. (1999)]. Hence, all potential $M_w - R$ pairs around the statistical modal and mean values are checked when generating earthquakes by this approach.

The number of ground motions required for the fragility analysis also varies depending on the methodology used. Hwang et al. (2000a, b) and Choi (2002) used a suite of ground motions containing 100 accelerograms. Shome et al. (1998) state that the

lognormal assumption for the model allows that suites containing 20 ground motions are sufficient to achieve the required confidence levels. Wen et al. (2003) assert that suites with as few as ten ground motions are adequate to capture the structural response. For the proposed fragility research in this dissertation, 100 ground motions have been simulated and used to achieve the required confidence level.

In summary, Fig. 3-9 presents a flow chart describing the procedure used for ground motion generation for the fragility analysis. The interactive deaggregation program of the U.S. Geological Survey (USGS) is used to perform the PSHA and deaggregation analysis. Predominant events, defined by magnitude-epicentral distance pairs, can then be identified from their level of contribution. Following the recommendation of Harmsen et al. (1999), a set of events is selected by choosing the (M_w, R) pairs, which either have the largest hazard contribution or would produce targeted hazard levels. Uncertainty in the seismic intensities is considered by selecting various (M_w, R) pairs. Then, synthetic ground motions with PGAs larger than 0.1g are simulated through the SGMS program [Halldorsson and Papageorgiou (2004a, b)] by defining the Magnitude (M_w), Epicentral distance *R*, and soil class. Fig. 3-10 shows soil classifications for New York State. It is observed from Fig. 3-10 that soil class B-C boundary is prevalent in New York State region. Hence, in this thesis, soil class B-C boundary is used as input in the SGMS program to consider site amplification effect. A suite of one hundred ground motions at varying hazard levels are generated for the nonlinear dynamic analysis of the bridge. General properties of these records are: (i) Moment magnitude range: 5.5~7.5, (ii) Epicentral distance range: 10~120 km, and (iii) Soil categories: NEHRP B-C boundary (V_{100}=760 m/s).

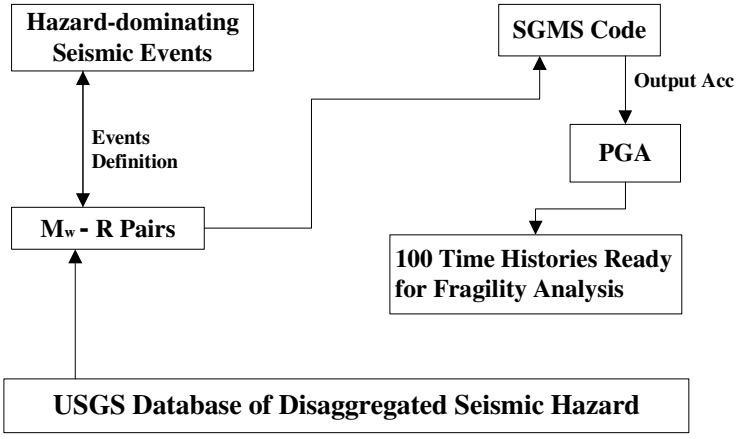

Figure 3-9. Flow Chart for Ground Motion Generation for Fragility Analysis.

Table 3-3 presents the PSHA-derived estimates of potential M_w - R pairs dominant for seismic hazard. Columns 1 to 4 in this table list the record number, epicentral distance, magnitude and hypocentral distance, respectively. In the USGS program for Eastern United States of America, epicentral distances are presented in the seismic hazard deaggregation analysis, whereas the SGMS program requires hypocentral distance as input. For transformation of epicentral distance to hypocentral distance, the earthquake fault depth is assumed to be 10 km, since the recommended depth distribution of earthquakes in the Eastern United States has a median of 10 km with $\pm 2\sigma$ values of 5 and 20 km [Risk Engineering Inc. (1998)]. After identifying the seismic events, i.e. the magnitude-distance pairs as listed in Table 3-3, time history simulations could be performed one by one using the SGMS program. Generated time histories have significant variations in PGAs. Fig. 3-11 shows the distribution of the peak ground accelerations for the selected events. PGAs vary from 0.1g to 1.2g, and cover all the probabilities from weak to strong earthquakes for fragility analysis. The resulting 100

time histories are used to perform the fragility analysis as will be described in the following chapters.

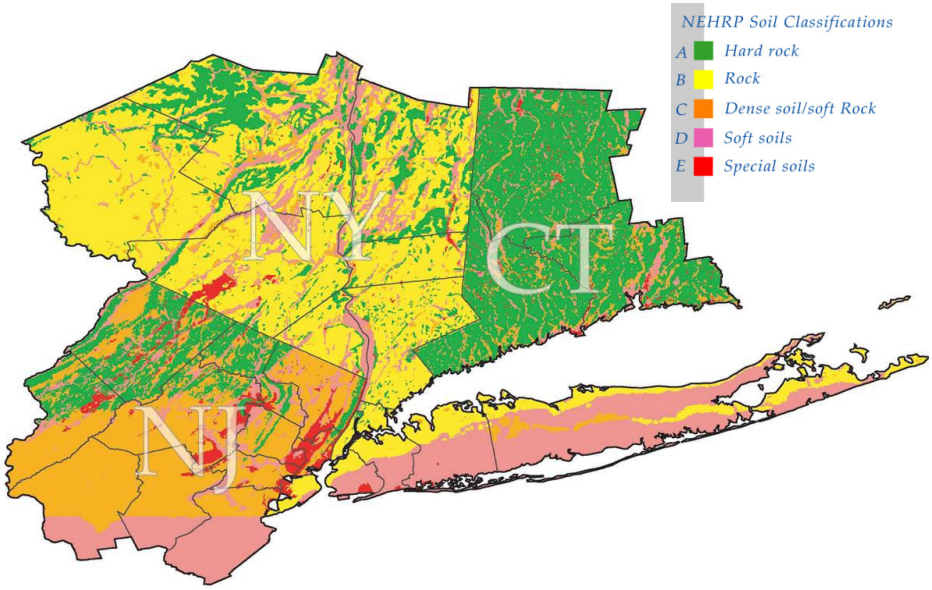

Figure 3-10. Soil Classifications.

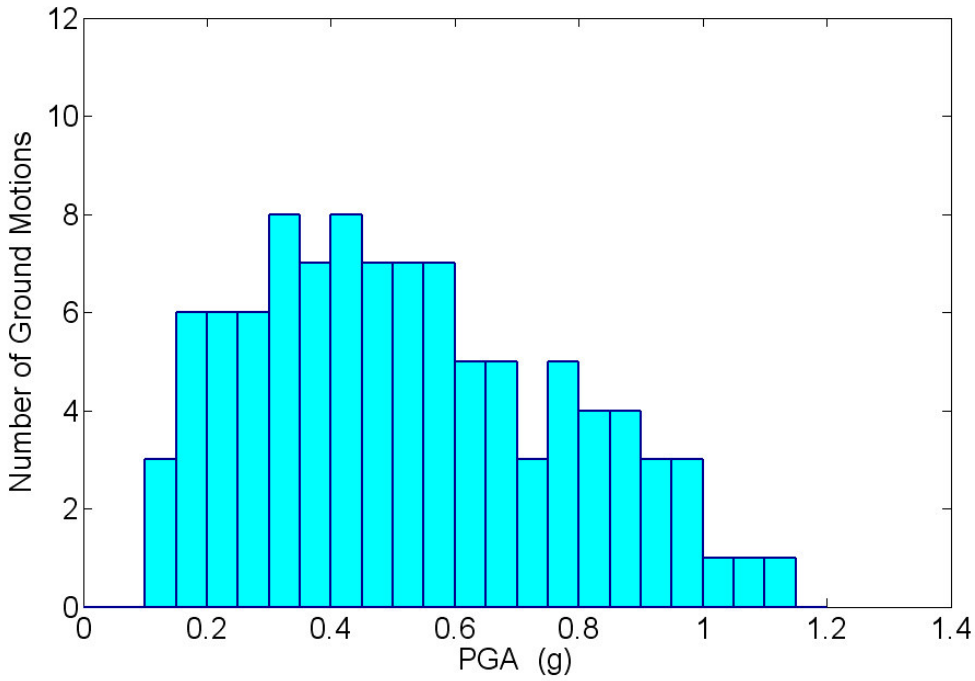

Figure 3-11. PGA Distribution of Simulated Ground Motions.

Table 3-3. Characteristics of Ground Motions for Use in Probabilistic Seismic Analysis.

NO.	EPC	MAG	HOPYC		NO.	EPC	MAG	HOPYC
1	88.6	7.0	89.20		51	61.3	7.0	62.11
2	59.9	7.2	60.70		52	38.5	6.6	39.78
3	36.6	7.2	37.94		53	16.9	6.0	19.64
4	35.4	7.4	36.80		54	36.2	6.8	37.56
5	36.1	7.4	37.50		55	35.8	7.2	37.20
6	15.9	6.6	18.80		56	36.3	7.4	37.70
7	13.0	6.4	16.40		57	14.4	6.4	17.50
8	15.9	7.2	18.80		58	14.4	6.8	17.50
9	13.0	7.2	16.40		59	13.3	6.8	16.60
10	13.4	7.2	16.70		60	14.9	7.2	17.90
11	118.3	7.4	118.7		61	35.1	6.8	36.50
12	60.2	7.2	61.00		62	35.8	7.4	37.20
13	39.0	7.2	40.30		63	16.4	6.4	19.20
14	35.9	7.2	37.30		64	15.6	6.4	18.50
15	15.5	6.4	18.45		65	14.9	6.4	17.90
16	14.8	6.8	17.90		66	13.8	6.4	17.00
17	14.8	6.6	17.90		67	13.2	6.8	16.60
18	13.5	6.8	16.80		68	13.2	7.2	16.60
19	14.6	7.0	17.70		69	14.5	7.4	17.60
20	13.7	7.2	17.00		70	14.9	7.4	17.90
21	85.3	7.4	85.90		71	84.8	7.2	85.40
22	60.3	7.4	61.10		72	61.9	7.4	62.70
23	35.7	7.0	37.10		73	16.4	6.0	19.20
24	35.1	7.0	36.50		74	36.1	7.2	37.50
25	34.8	7.4	36.20		75	35.7	7.2	37.10
26	16.0	6.6	18.90		76	15.4	6.4	18.40
27	15.5	6.6	18.45		77	14.7	6.6	17.80
28	14.9	7.0	17.94		78	15.4	6.8	18.40
29	14.2	7.0	17.40		79	13.8	7.0	17.00
30	15.3	7.2	18.30		80	12.0	7.0	15.60
31	61.4	7.0	62.20		81	62.8	7.0	63.60
32	36.0	6.8	37.40		82	16.0	5.8	18.90
33	35.5	7.0	36.88		83	35.2	6.8	36.60
34	16.5	6.2	19.30		84	34.9	7.4	36.30
35	15.3	6.2	18.30		85	14.8	6.2	17.90
36	16.4	6.2	19.20		86	34.4	7.4	35.80
37	12.9	6.4	16.30		87	16.3	6.6	19.10
38	12.8	6.8	16.24		88	15.0	6.8	18.03
39	12.7	6.8	16.20		89	14.6	7.2	17.70
40	14.1	7.0	17.30		90	12.2	7.0	15.80
41	59.8	6.6	60.60		91	59.8	7.4	60.60
42	86.9	7.4	87.47		92	35.8	6.8	37.20

43	61.8	7.2	62.60		93	15.2	6.4	18.20
44	34.8	6.8	36.21		94	14.7	6.4	17.80
45	15.4	6.2	18.40		95	14.1	6.4	17.30
46	17.8	6.6	20.40		96	17.6	6.6	20.20
47	15.0	6.6	18.00		97	16.1	6.8	19.00
48	14.0	6.8	17.20		98	15.0	7.2	18.00
49	13.0	6.8	16.40		99	12.1	7.0	15.70
50	13.7	6.8	17.00		100	11.9	7.4	15.50

* EPC: Epicentral Distance
MAG: Richter Magnitude
HOPYC: Hypocentral Distance

CHAPTER 4

MODELING OF TYPICAL BRIDGES

4.1 Bridge Inventory and Typical Bridges

4.1.1 Bridge Inventory of New York State

To facilitate the assessment of seismic risk to the transportation infrastructure in a region, it is essential to understand the structural and topological characteristics of the bridge inventory and highway bridge network. Bridge inventory data for bridges in different state and for the entire country can be found in the National Bridge Inventory (NBI) database [FHWA (1988)]. The NBI database was established to catalog biennial inspection data for bridges. This database contains information about the characteristics of a bridge, such as its location, structure type, material type, year built, year retrofitted, condition ranking, etc. However, the database only stores information about the superstructure, and it doesn't contain any information about the substructure or the soil and foundation types.

For the fragility analysis, bridge inventory database of NYSDOT has been used to perform a statistical analysis of typical bridge types. Each bridge in the inventory has been assigned a unique seven-character bridge identification number (BIN). Inventory and inspection data are organized and updated by Record Code. A Record Code is defined as a group of related bridge data. The Bridge Data Management System (BDMS) data are entered in Oracle tables via Record Codes and extracted for user access into Microsoft Access tables. The Bridge Inventory Manual [NYSDOT (2004)] explains the

methods and procedures used for coding the data elements. The statistical analysis of the bridge inventory database is essential to determine typical bridge compositions in New York State by considering bridge material, bearing details, superstructure type, type of pier and foundation. Based on this analysis, a sample bridge representing the most typical types can be selected for detailed modeling and analysis.

4.1.2 Typical Bridges in New York State

The National Bridges Inventory data (2003) reveals that 58.2% of the highway bridges in New York State are multi-beam (slab-girder) types, as shown in Table 4-1. According to the distribution of classification on material type in Table 4-2, 65.6% of the bridges have steel superstructures. Typical bridges studied for seismic risk would be multi-span bridges considering that no detailed seismic analysis is required for single span bridges [AASHTO (1996)]. In general, multiple span bridges are either simply supported (i.e., multi-span simply supported bridges) or continuous with various superstructure types, such as steel girder, prestressed concrete multiple box beam, prestressed concrete girder. Among all multi-span bridges in New York State, 70% are simply supported steel bridges and 27% are multi-span continuous steel bridges. Multi-span simply supported steel bridges and continuous bridges typically have 2 or 3 spans with maximum span lengths in the range of 10 m to 20 m and 30 m to 40 m, respectively.

Based on the above information, two types of bridges considered as typical for the New York State area are: (1) multi-span simply supported (MSSS) steel bridge, (2) multi-span continuous (MSC) steel bridges. The topological layout and structural details of the representative bridges would be designed as per New York State bridge design guidelines on the basis of design drawings of actual bridges.

Through state inventory data, typical bridge components are also investigated. Typically, steel bridge girders are either W-shape (wide-flange) rolled steel beams or steel plate I-girder beams. Rolled beams can be an economical option for steel bridges with span lengths less than 30 m. Steel plate girders are used for longer spans. Main pier types are made of solid concrete pier-walls or multi-column bents. Solid concrete pier-walls are common for bridges over highways. For bridges over rivers or streams, multi-column bents made of two or more columns connected at the top by cap beams are most popular. This type of system forms a concrete rigid frame, since concrete column reinforcement is extended into the cap beam, and is lapped with the cap beam reinforcement to resist the applied moments at the beam/column connections. The abutment is typically composed of a backwall and wingwalls resting on a footing. Depending on the soil profile, the footing could spread directly on the rock or could be supported by cast-in–place concrete piles or steel H-piles. The wing wall could be “U” type or “Splayed” type to help confine the earth behind the abutment. Types of bearings in highway bridges depend on the amount and type of movement as well as the magnitude of the load. Old bearing types in highway bridges are steel bearings and neoprene pads. Steel bearings have been extensively used for slab-on-steel girder bridges, and are being replaced by elastomeric bearings. More detailed information about bridge components would be presented in section 4.2. Curved and/or skew bridges have not been considered in this research, since most highway bridges are not curved except for connectors at highway junctions.

Table 4-1. New York State Highway Bridges Classification
Based on Superstructure Type.

Code	Superstructure Type	Data of 2003	Percentage
1	Slab	1,069	6.2
2	**Stringer /Multi-Beam or Girder**	**10,055**	**58.2**
3	Girder & Floorbeam System	607	3.5
4	Tee Beam	196	1.1
5	Box Beam or Girders (Multiple)	1,307	7.6
6	Box Beam or Girders (Single or Spread)	28	0.2
7	Frame (Except Culverts)	774	4.5
8	Orthotropic	3	0.0
9	Truss-Deck	33	0.2
10	Truss-Thru	626	3.6
11	Arch-Deck	742	4.3
12	Arch-Thru	23	0.1
13	Suspension	19	0.1
14	Stayed Girder	2	0.0
15	Movable-Lift	24	0.1
16	Movable-Bascule	34	0.2
17	Movable-Swing	12	0.1
18	Tunnel	0	0.0
19	Culvert	1,742	10.1
20	Mixed Types	1	0.0
21	Segmental Box Girder	3	0.0
22	Channel Beam	11	0.1

Table 4-2. New York State Highway Bridges Classification
Based on Material Type.

Code	Material Types	Data of 12/2003	Percentage
1	Concrete	2,434	17.7
2	Concrete Continuous	640	
3	**Steel**	**10,211**	**65.6**
4	**Steel Continuous**	**1,189**	
5	Prestressed Concrete	2,067	12.6
6	Prestressed Concrete Continuous	127	
7	Wood	439	2.5
8	Masonry	126	0.7
9	Aluminum Iron	132	0.8
10	Other	17	0.1

4.2 Bridge Characteristics and Modeling

4.2.1 Characteristics of Typical Bridges

Multi-span Continuous (MSC) Bridge

Figure 4-1 shows a hypothetical multi-span continuous bridge that is used in this thesis to explain the seismic response of typical New York State bridges. The continuous steel plate girder bridge with 30 m-36 m-30 m spans has been selected on the basis of typical design details for each component obtained from the review of bridge design drawings provided by New York State Department of Transportation (NYSDOT). The bridge has three spans and two multi-column bents. The superstructure of the bridge consists of a 14.18 m wide, 240 mm thick continuous cast-in-place composite concrete deck with 6 steel plate I-girders equally spaced at 2440 mm. In general, the superstructure is similar to that of the bridge example provided by Barker and Puckett (1997). Each column bent consists of a 900 mm by 1200 mm (3 ft ×4 ft) cap beam and three 5.0 m high, 900 mm (3 ft) diameter circular columns. The nominal concrete strength for columns is $f_c^{'} = 20.7$ MPa (3.0 ksi). The vertical reinforcement in columns consists of 13 #8 Grade 40 (f_y = 40 ksi) bars. Transverse reinforcement consists of #3 spirals at 150 mm (6 inch) spacing. No bars are spliced close to potential plastic hinge regions. Seat-type cantilever abutments with U-shaped wing walls supported on 18 cast-in-place concrete piles support the end bearings of the superstructure. The back wall is 3 m high and as wide as the deck. The wing wall is 3 m in height and 5 m in width. The nominal gap between the deck's ends and the abutments is 76.2 mm (3 inches). The four sets of steel bearings (one set consists of 6 identical bearings transferring the load from the

superstructure to the substructure at each support) consist of low type expansion sliding bearings over the abutments, high type fixed bearings over the first interior bent and high type expansion rocker bearings over the second bent.

Multi-Span Simply Supported (MSSS) Bridge

Fig. 4-2 shows the typical multi-span simply supported steel girder bridge (MSSS) considered in this study. The expansion joints at the column bents divide the composite decks/girders in adjacent spans. The span lengths are 12 m, 20 m, and 12 m, respectively. The nominal gap between the end of the deck and the abutments is 38.1 mm (1.5 inches), and the nominal gap at intermediate expansion joints is 25.4 mm (1 inch). The concrete deck is 10.82 m wide. The spacing between the 5 steel rolled girders is 2.286 m center to center. The substructure is similar to the MSC bridge described above. The height of columns is 5 m. The adjacent columns in the same bent are 4953 mm center-to-center. The cap beam is as wide as the deck width. Each abutment is supported on 16 cast-in-place concrete piles. The back wall of the abutment is 3 m high and 10.82 m wide. The wing wall is 3 m in height and 5 m in width. There are two kinds of steel bearings resting on the cap beams and abutments. In the longitudinal direction, the left end of each bridge superstructure span is supported by high type fixed bearings; and the right end is supported by high type rocker bearings. Other properties of the MSSS bridge are similar to the MSC bridge.

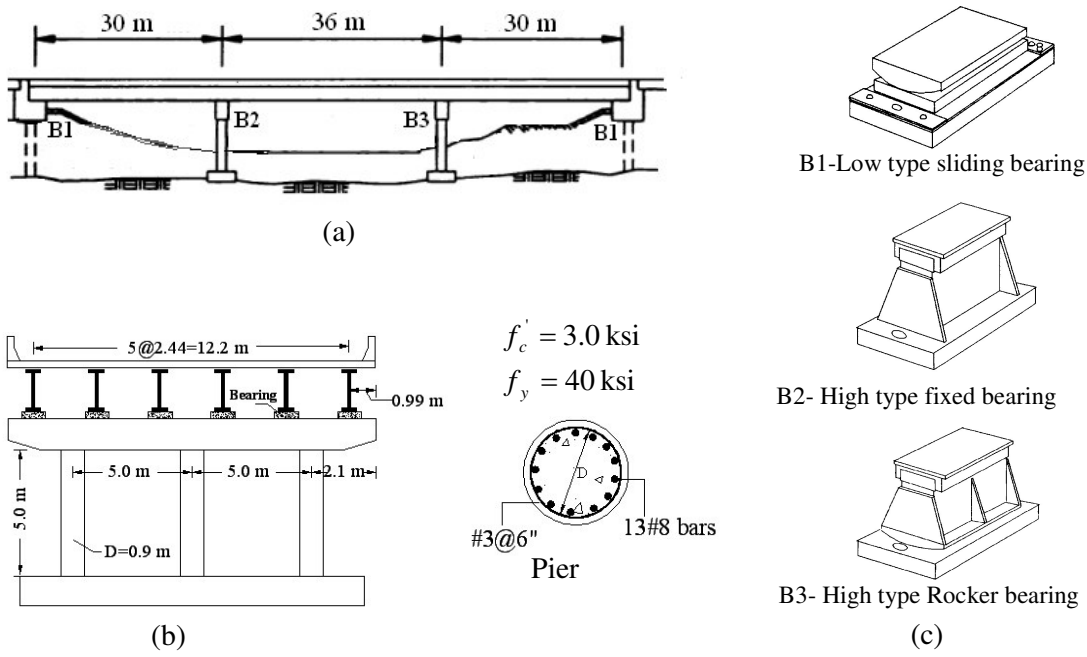

Figure 4-1. Configuration of a Typical Multi-span Continuous Steel Girder Bridge in New York State (a) Elevation; (b) Transverse cross-section; (c) Bearings.

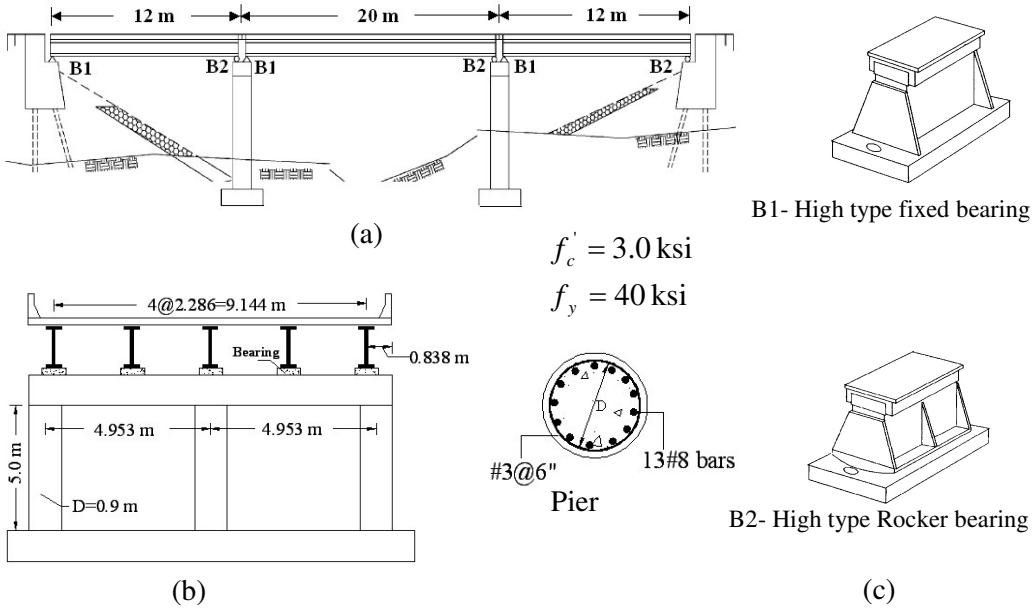

Figure 4-2. Configuration of a Typical Multi-span Simply Supported Steel Girder Bridge in New York State (a) Elevation; (b) Transverse cross-section; (c) Bearings.

4.2.2 Bridge Modeling

Three-dimensional finite element models have been developed for both typical bridges using SAP2000 (9.1.1.V). The advantage of SAP2000 is that various Nonlinear-Link elements are available, and they can be used to model the dampers, gaps, plastic elements, and isolators. In a Nonlinear-Link element, the nonlinear force-deformation relationship could be defined independently for each deformational degree of freedom.

Fig. 4-3 shows the analytical model of the multi-span continuous bridge. Fig. 4-4 shows the analytical model of the multi-span simply supported bridge with details of the expansion joints. In both cases, the deck and steel girders are combined together and modeled as one line of elastic beam elements. All the steel bearings are modeled using multi-linear plastic link elements. The bottom segments of the columns, where plastic hinges are likely to form, are modeled using bilinear plastic elements. The abutments are modeled using beam elements supported on springs. The expansion joints at the abutments are modeled with gap elements. The bases of the column bents are assumed to be fixed for a continuous spread footing on rock. The nodes between girders and bearings, bearings and cap beams, and cap beams and tops of the columns are connected with rigid bars. Due to symmetry, the seismic analysis can be performed independently in the two horizontal directions. The dominance of the longitudinal motion for multi-axis earthquakes is apparent for these two bridge types. This is due to the restraints provided by the bearings at the abutments, and the column boundary conditions which are fixed-free in the longitudinal direction and fixed-fixed in the transverse direction. This observation has also been verified through simplified analytical modeling and detailed simulation results. Hence, the longitudinal motion of the bridge is most critical response

which could cause damage to bridge components. A brief description of nonlinear modeling of column elements, abutment springs, gap elements and bearings is presented in the following paragraphs.

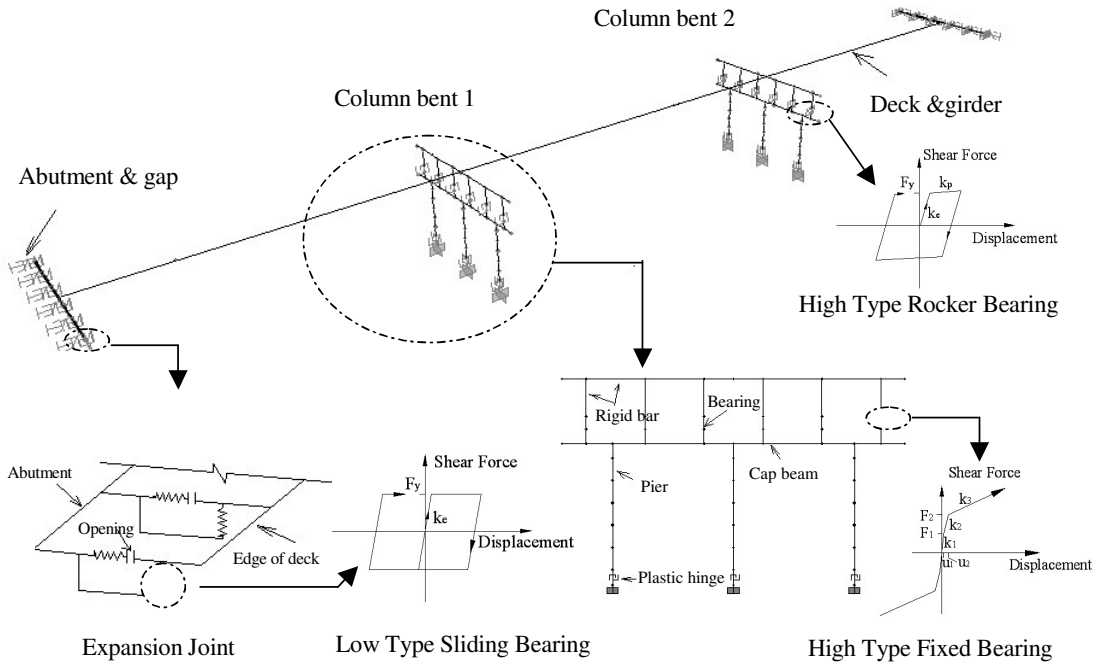

Figure 4-3. Three-dimensional Finite Element Model of the MSC Bridge Using SAP2000.

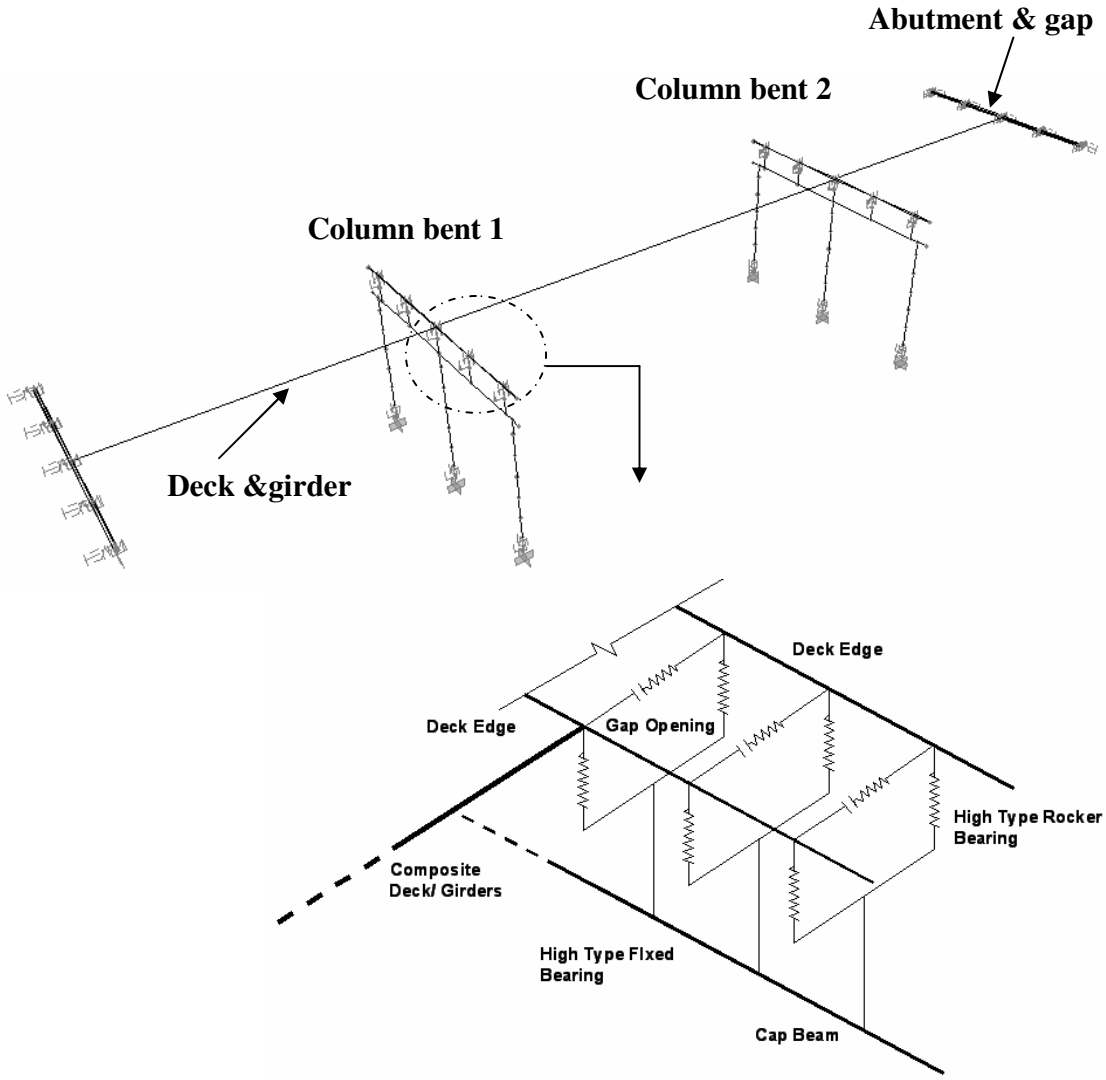

Figure 4-4. Three-dimensional Finite Element Model of the MSSS Bridge Using SAP2000.

Columns

When the bridge is in longitudinal motion, each column acts as a vertical cantilever beam. Plastic hinges can only form at the bottom of the columns for the typical bridges described above, since pinned joints with bearings (both fixed and expansion) can accommodate rotations between the cap beam and the girders. The nominal moment-curvature diagram for each column section is determined using the BIAX program [Wallace and Ibrahim (1996)]. Elastic-perfectly plastic idealization for the moment-curvature relationship can then be assumed, as shown in Fig. 4-5. The equivalent yield curvature ϕ_y is found by extrapolating the line joining the origin and the point corresponding to the first yield point of a reinforcing bar, up to the nominal moment capacity M_n . M_n is the moment corresponding to a compressive strain of $\varepsilon_c = 0.005$ in the extreme concrete fiber. The curvature ϕ_y is computed from Eq. (4-1), where M_y and ϕ_y' are the moment and curvature at first yielding of a vertical reinforcing bar,

$$\phi_y = \frac{M_n}{M_y}\phi_y' \tag{4-1}$$

Assuming a constant curvature over the length of the plastic hinge (L_p), the angle of rotation can be calculated as $\theta = \phi\, L_p$, where L_p is calculated by [Priestley et al. (1992)]

$$L_p = 0.08L + 0.022 f_y d_{bl} \geq 0.044 f_y d_{bl} \quad (f_y \text{ in MPa}) \tag{4-2}$$

In Eq. (4-2), L is the length from the point of contraflexture to the section with maximum moment, and d_{bl} is the diameter of a longitudinal reinforcing bar. The moment-rotation relationship is used as input in SAP2000 to describe the nonlinear behavior of the bilinear

plastic link elements at the base of columns. Each column is assumed to behave in a linear elastic manner outside the plastic hinge length.

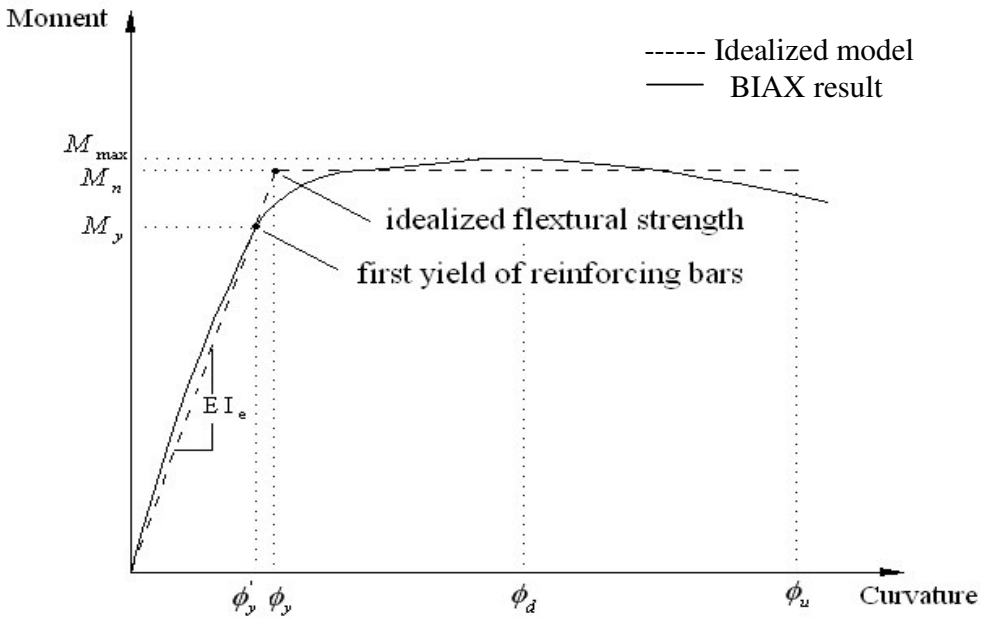

Figure 4-5. Moment-Curvature Diagram of Piers.

Abutments

The seat-type cantilever abutments with U-shaped wing walls of the bridges analyzed in this study are supported on cast-in-place (C.I.P.) concrete driven piles. The back wall is 3 m high and as wide as the deck. The abutments are modeled as beam elements supported on springs with spring stiffness coefficients derived on the basis of empirical relationships. Current CALTRANS practice assumes that contributions to abutment stiffness are due to two sources: (1) abutment wall/soil interaction; and (2) pile/soil interaction. The wall-soil resistance model assumes that pressure on the wall increases as the wall moves toward the backfill and decreases as the wall moves away from the backfill [Clough and Duncan (1991)]. CALTRANS uses a passive abutment

wall-soil stiffness of 115.0 kN/mm/m (200 kips/in/foot) for "average abutment backfill conditions" [CALTRANS (1989)]. The passive earth pressure reaches its maximum value when the soil reaches its ultimate strength of 0.37 MPa (7.7 ksf) after sufficiently large movements of the walls, and it remains constant for further wall movements. The characteristic earth pressure coefficients are assumed to be $K_{\max} = 5.8$; $K_0 = 0.29$; $K_{\min} = 0.17$ for the passive, at-rest and active pressures respectively, as shown in Fig. 4-6. For an ultimate passive soil pressure of 0.37 MPa, the values for the at-rest and minimum active pressure are on the order of 0.02 MPa and 0.01 MPa, which means that at-rest and minimum active pressures are small enough to be negligible. Hence, only the stiffness of the piles under an abutment is considered when an abutment is moving away from the backfill during longitudinal motions. When the abutment wall is pushing against the backfill, both back wall-soil stiffness and pile stiffness contribute to the total stiffness until the soil capacity is exceeded, at which point the pile stiffness alone controls the force-deformation behavior. Pile strength and stiffness are related to the properties of the piles and the interaction of the piles with the surrounding soils. Using the recommendations of CALTRANS [ATC-32 (1996)], the nominal stiffness of 12" driven concrete piles is assumed to be 20 kips/inch/pile (3.5×10^3 kN/m/pile) for a maximum displacement limit of 25.4 mm. The overall abutment stiffness in the longitudinal direction is obtained by the superposition of the effects of the wall and piles. Fig. 4-7 shows the multi-linear plastic model of the abutment of the Multi-span continuous bridge. The model for the abutments of the Multi-span simply supported bridge is similar to Fig. 4-7. The difference is due to the supporting pile numbers under the footings.

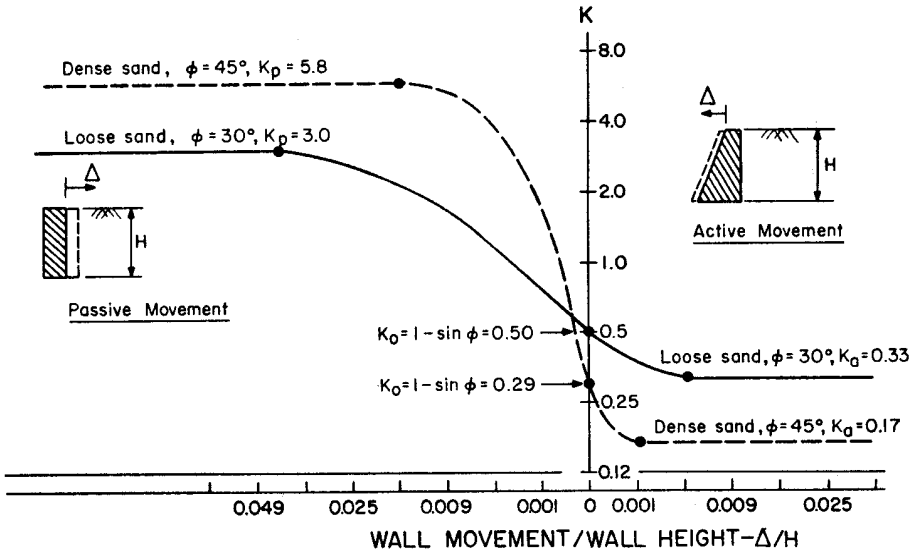

Figure 4-6. Relationship between Wall Movement and Earth Pressure. [Clough and Duncan (1991)]

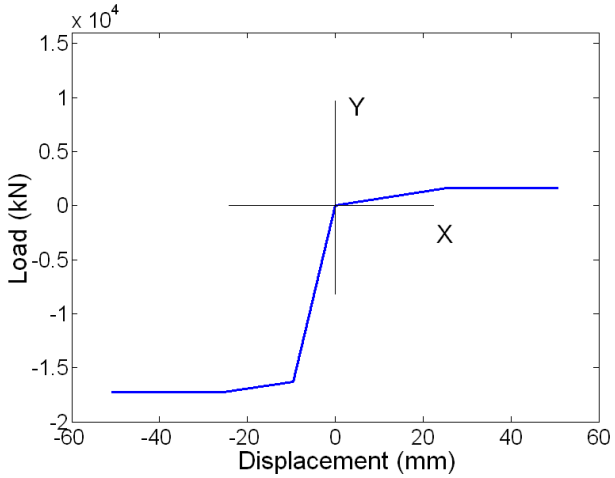

Figure 4-7. Load-Response for Abutment in Longitudinal Direction of the MSC Bridge.

Gap Elements

For the multi-span continuous bridge in this study, the nominal gaps between the deck's ends and the abutments are 76.2 mm (3 inches) each. For the multi-span simply supported bridge, the nominal gaps between the deck ends and the abutments are 38.1 mm (1.5 inches), and the nominal gaps at intermediate expansion joints are 25.4 mm (1 inch).

The gap element of SAP2000 is utilized to account for the possibility of pounding when the longitudinal deformations close an expansion joint. The SAP2000 gap element is set as a "compression-only" connection such that the element does not apply any resistance before the closure of the gap. When the gap closes, pounding occurs either between the abutments and decks or between adjacent decks. An infinite stiffness can be assumed for the gap element after contact is established [Priestley et al. (1996)]. For both the simply supported and multi-span continuous bridges, when the gap between the abutment and the deck closes, the abutment is assumed to be rigidly connected to the bridge deck in the axial direction and begins to contribute in resisting the longitudinal displacements. Similarly for the multi-span simply supported bridge, when the gap between adjacent decks closes, the adjacent decks are assumed to be rigidly connected to each other in the axial direction to ensure compatible movements.

Bearings

Steel bearings are no longer used in new bridges, although most of existing bridges in New York State are supported by steel bearings. There are two types of steel bearings: fixed bearings and expansion bearings. Fixed bearings only allow the rotation of the superstructure relative to the substructure. Expansion bearings allow both rotations

and large relative translational movements [Imbsen (1981), NYSDOT (2002)]. There are three kinds of steel bearings used in the typical bridges analyzed in this dissertation, as shown in Figures 4-1 and 4-2.

(1) Low Type Expansion Sliding Bearing

A low type expansion sliding bearing consists of a pinned joint to accommodate rotations and a sliding element to accommodate longitudinal movements, while restraining transverse movements. Mander et al. (1996) have shown through experiments that low type sliding resistance conforms to Coulomb friction behavior with zero inelastic stiffness. The sliding resistance was found to be proportional to the normal reaction force, with a friction coefficient of about 0.2. Elastic stiffness (before sliding) k_e is found to be as large as 123 kN/mm. The shear stiffness behavior is modeled as shown in Fig. 4-8 (a).

(2) High Type Expansion Rocker Bearing

A high type expansion rocker bearing consists of a pinned joint at the sole plate-rocker interface to accommodate rotations and a rocker to accommodate longitudinal movements. The experimental hysteresis loop is found to be approximately rectangular with the combined friction, resulting from the rocking resistance at the rocker-masonry plate interface and the hinge friction at the plate-rocker interface, being approximately 4% of the normal reaction force. The initial elastic stiffness is k_e =14 kN/mm [Mander et al. (1996)]. The increase in resistance due to accumulated rusty debris on the rocking surface is included in the model by assuming an inelastic stiffness with k_p =0.018 k_e. The behavior is modeled as illustrated in Fig. 4-8(b).

(3) High Type Fixed Bearing

A high type fixed bearing consists of a pinned joint to accommodate rotations while the bearing is rigidly attached to a masonry plate. The limited flexibility during longitudinal loading can be attributed to the shear deformations of the rubber pad as well as the bedding material between the masonry plate and concrete pedestal. The initial stiffness of a high type fixed bearing mounted on a reinforced concrete pedestal is found to be equal to k_1=179 kN/mm. The lateral strength of the bearing is due to the combined action of shear and tension in the anchor bolts. The ultimate lateral strength is reached when the anchor bolts fracture due to prying of the masonry plate from the bedding material. Based on experimental data, Mander et al. (1996) have recommended the use of one bilinear truss and two link elements in parallel to model the bearing behavior in Drain2DX program. The bearing models are incorporated in SAP2000 by a trilinear force-displacement relationship shown in Fig. 4-8(c) with $k_2 = 0.5k_1$, $k_3 = 0.04k_1$, $u_1 = 0.4$ mm, and $u_2 = 0.87$ mm for displacements smaller than 20 mm.

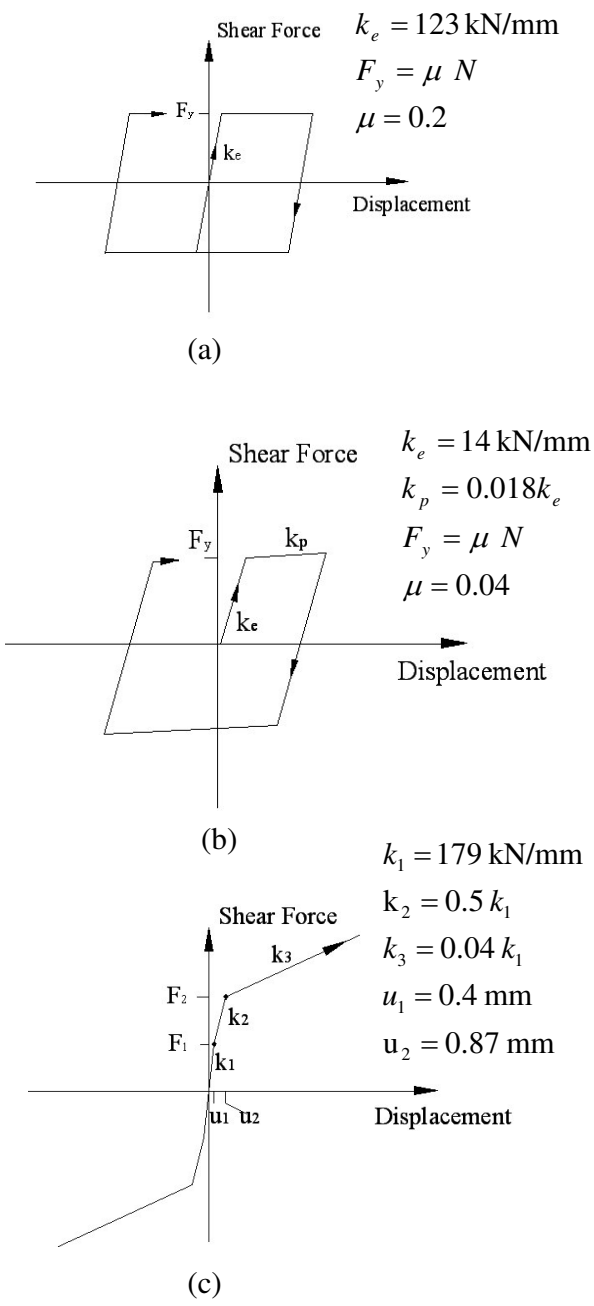

Figure 4-8. Multi-linear Behavior of Bearings in Longitudinal Direction: (a) Low Type Expansion Sliding Bearing; (b) High Type Expansion Rocker Bearing; (c) High Type Fixed Bearing.

4.3 Parametric Analysis

An extensive parametric analysis is carried out to evaluate the sensitivity of the seismic response to variations in superstructure mass, gap size, concrete compressive strength, reinforcing bar yield strength, friction coefficient of expansion bearing and abutment wall-soil stiffness. Actual values of these parameters are difficult to estimate and they may vary significantly with respect to their nominal values. The sensitivity analysis is performed to indicate which parameters should be treated probabilistically to account for their uncertainties. A synthetic accelerogram with 2% probability of exceedance in 50 years (PGA=0.24g) is used for the parametric analysis in this study. This accelerogram is one of those being recommended by the New York City Department of Transportation for bridge seismic design, as mentioned in section 3.2 of Chapter 3. The synthetic earthquake accelerogram is scaled to three values of PGA = 0.24g, 0.70g and 1.0g to observe the sensitivity of the response to parametric variations under different earthquake intensities. The curvature ductility (ϕ / ϕ_y) of the most critical column is used to show the effects of variations in each of the parameters listed above. In this sensitivity analysis, only one of the parameters is varied at a time, while the other five parameters remain constant.

The superstructure mass affects the inertial force as well as the period of the bridge. To study the effect of variations in the actual mass of the bridge, the superstructure mass is varied by a factor of 0.8 to 1.3 times the nominal value. The gap size at expansion joints may influence the seismic response of bridges because of pounding. For example, the gap size between the deck and the abutment controls the maximum observed column drift in the multi-span continuous bridge, since the abutment

would offer a large passive resistance to limit further pier drift after the closure of the gap. Due to temperature variations, gap sizes might lengthen or shorten. In this sensitivity analysis, the change in gaps in the bridge are assumed to be synchronized and can be scaled simultaneously by a factor of 0.5 to 1.5 of their original design values. Concrete strength, $f_c^{'}$, is investigated for a ratio ranging from 1.0 to 1.7 times the nominal value and steel yield strength is varied by a ratio ranging from 1.0 to 1.3. The passive abutment wall-soil stiffness value of 115.0 kN/mm/m (200 kips/in/foot) is varied by a factor of 0.3 to 1 since this assumed stiffness value by CALTRANS may overestimate the actual stiffness [Maroney et al. (1994)]. Further, considering the uncertainty in the degree of corrosion in bearings, the coefficient of friction is taken to be in the range of 0.8 to 1.5 times of the base values $\mu = 0.04$ and $\mu = 0.2$ simultaneously for both the high type rocker and the low type sliding bearings in multi-span continuous bridges. For the high type rocker bearings in multi-span simply supported bridge, the base value of the coefficient of friction is taken as $\mu = 0.12$, and a range of $\mu = 0.04 \sim 0.12$ is considered for the sensitivity investigation. The results of the parametric study are shown in Fig. 4-9 and Fig. 4-10 respectively for the MSC and MSSS bridges.

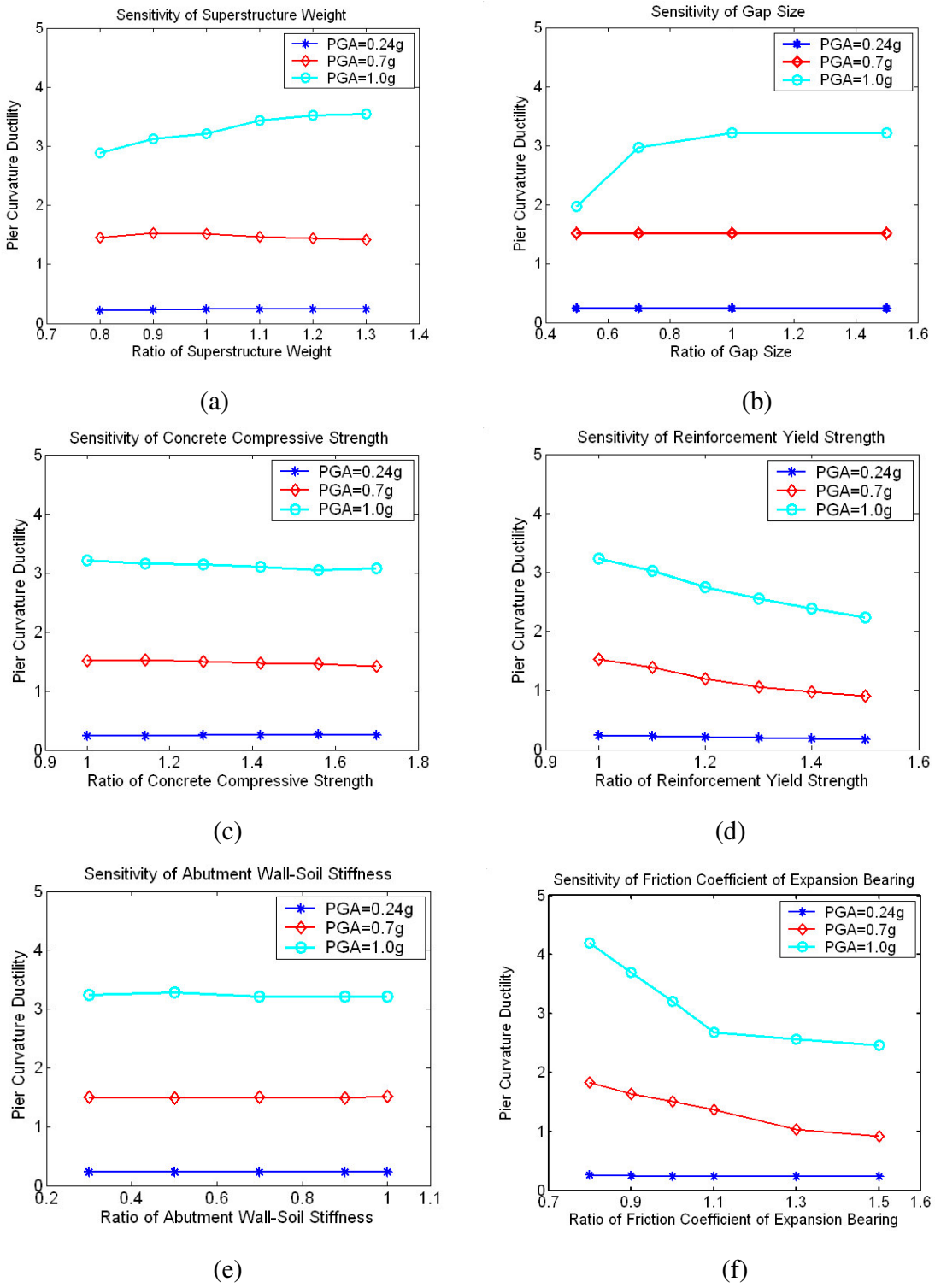

Figure 4-9. Results of Parametric Study of Multi-span Continuous Steel Girder Bridge.

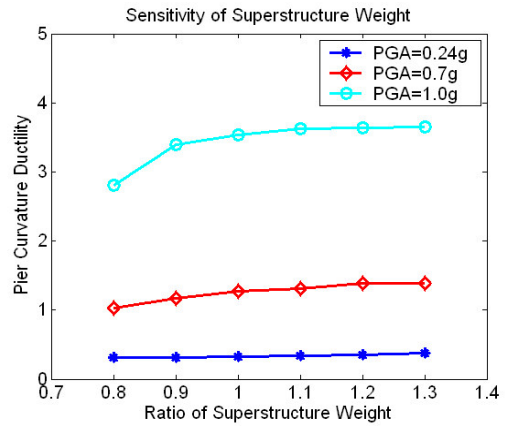

(a)

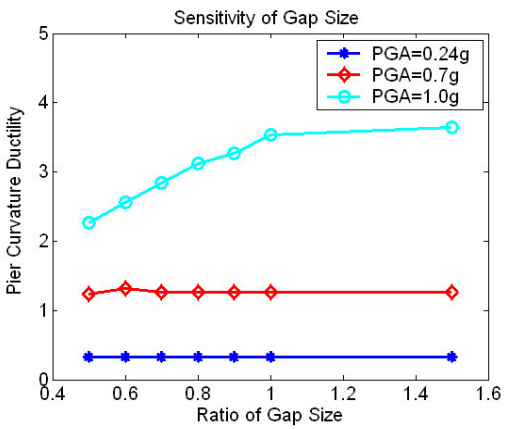

(b)

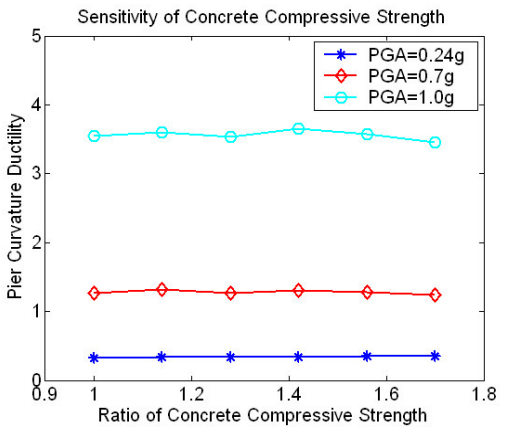

(c)

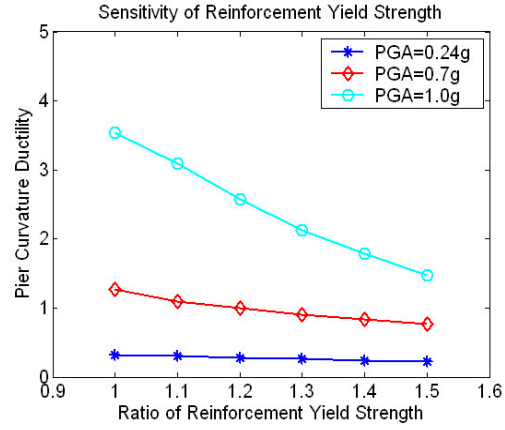

(d)

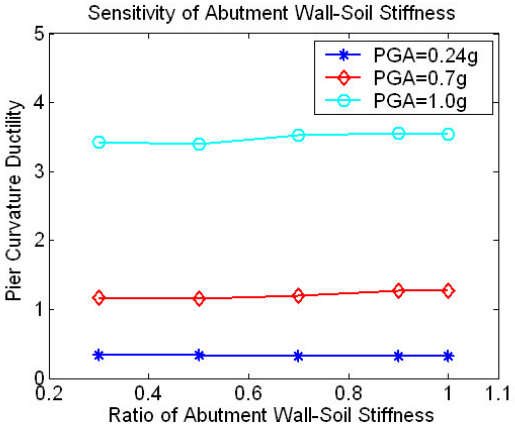

(e)

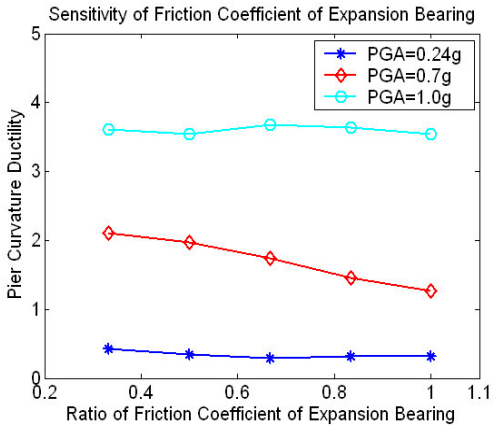

(f)

Figure 4-10. Results of Parametric Study of Multi-span Simply Supported Steel Girder Bridge.

The following observations are made from the results shown in Figs. 4-9 and 4-10:

1. Increasing superstructure mass leads to larger curvature ductility. This occurs even though the increase in inertial forces caused by the larger bridge mass may be offset to some extent by the resulting longer structural period, which induces a smaller acceleration response.
2. The gap size has a significant effect on column ductility during strong earthquakes. In the multi-span continuous bridge, pier ductility decreases sharply when the size of the gap between deck and abutment decreases. A similar situation occurs in the multi-span simply supported bridge, since the smaller gap sizes provide more restraint to the deck movement and generate decreased forces on the piers. However, for earthquakes with PGA less than 0.7 g, the gap size is not critical since the gaps don't usually close.
3. The pier ductility ratio decreases when the concrete compressive strength and the steel yielding stress are increased. The bridge response is significantly less sensitive to the concrete compressive strength as compared to steel yield strength.
4. The abutment wall-soil stiffness is not a sensitive parameter for either multi-span continuous bridges or multi-span simply supported bridges subjected to earthquakes with PGA up to 1.0 g.
5. The friction coefficient of expansion bearing is a significant parameter. In the multi-span continuous bridge, the second column bent may be subject to a larger share of seismic forces in superstructure because of larger friction coefficients of the high type rocker bearing mounted on the cap beam of this bent. For the multi-span simply supported bridge, the overall effect of the variation in expansion bearing

friction coefficient seems more complex because of the participation of the fixed bearing on the same column bent and pounding under strong earthquake.

To compare the sensitivities of the bridge response to the above listed parameters, both the parameter and the curvature ductility are normalized with respect to their respective nominal values. The slopes of the curves in Fig. 4-11 and Fig. 4-12 show the sensitivity of variations in the parameters. It is observed that the most important parameters are the friction coefficient of bearings, reinforcement yield strength, superstructure weight, and concrete compressive strength (in the order of decreasing importance for the MSC bridge).

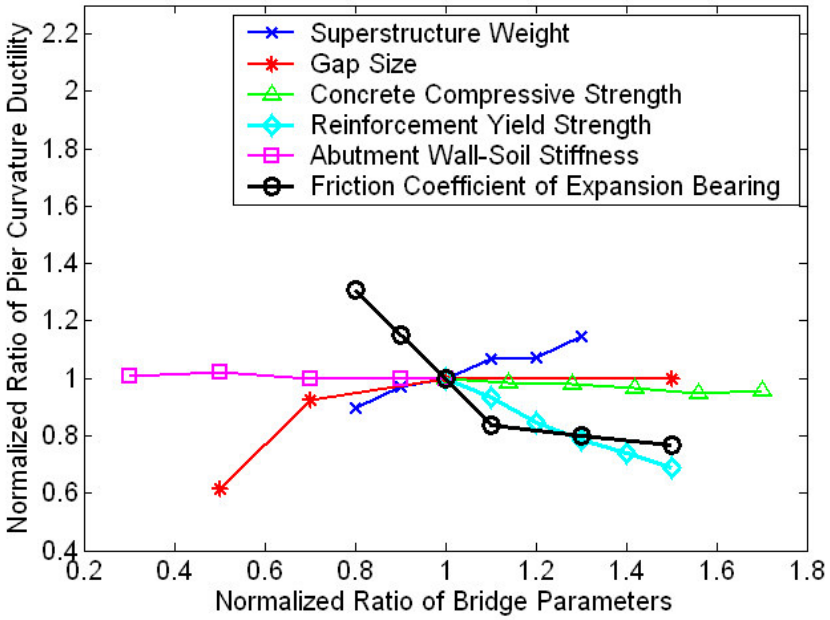

Figure 4-11. Sensitivity Analysis of the MSC Bridge Parameters for PGA=1.0 g.

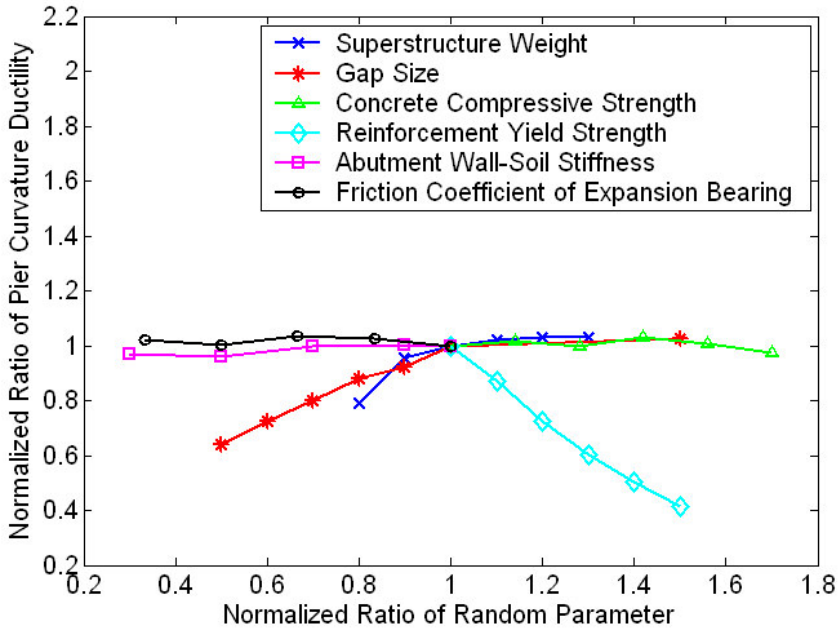

Figure 4-12. Sensitivity Analysis of the MSSS Bridge Parameters for PGA=1.0 g.

Previous studies considered uncertainties only in material properties and the gap size between deck spans. In this study, we observe that uncertainties associated with the friction coefficient of expansion bearings and superstructure weight have significant effects on bridge ductility in addition to the concrete compressive strength, reinforcement yield strength and gap size. Hence, uncertainties associated with these five parameters must be considered in developing the fragility curves as explained in the following sections.

4.4 Uncertainties in Structural Properties

Since the fragility analysis provides a solution to a probability problem, the Latin Hypercube Sampling (LHS) approach is used [Wyss and Jorgensen (1998), Ayyub and Lai (1989)] to account for the uncertainties allocated with estimating the parameters discussed above. LHS is a probabilistic simulation method used to obtain a set of bridge samples to achieve the high levels of accuracy while reducing the sample size. In this approach, probability distributions are assumed for each parameter, and the probability density function of each random variable is divided into a histogram with equal probability intervals so that the corresponding cumulative distributions are graded linearly. As illustrated in Fig. 4-13 (a), the density function diagram of a normally distributed variable is divided into strips having equal areas. The intersecting points (from A to J) on the x axis are the Latin Hypercube Samples for this normally distributed variable, and the cumulative distributions corresponding to these samples increase linearly from 5% to 95%, as shown in Fig. 4-13 (b). The probability density function and cumulative distribution function for the normal distributed variable are expressed by the following two equations,

$$f_x(x) = \frac{1}{\sigma\sqrt{2\pi}} \exp[-\frac{1}{2}\left(\frac{x-\mu}{\sigma}\right)^2] \tag{4-3}$$

$$P(X \le b) = \frac{1}{\sigma\sqrt{2\pi}} \int_{-\infty}^{b} \exp[-\frac{1}{2}\left(\frac{x-\mu}{\sigma}\right)^2] dx = \phi(\frac{\text{b - } \mu}{\sigma}) \tag{4-4}$$

where μ and σ are the mean and standard deviation of the variant.

For variables assumed to follow lognormal distributions, the Latin Hypercube Sampling procedure is the same, while the probability density function and cumulative distribution function are expressed by the following two equations,

$$f_X(x) = \frac{1}{\varsigma\, x\sqrt{2\pi}} \exp[-\frac{1}{2}\left(\frac{\ln x - \lambda}{\varsigma}\right)^2] \tag{4-5}$$

$$P(X \le b) = \int_{0+}^{b} \frac{1}{\varsigma\, x\sqrt{2\pi}} \exp[-\frac{1}{2}\left(\frac{\ln x - \lambda}{\varsigma}\right)^2] dx = \phi(\frac{\text{lnb - } \lambda}{\varsigma}) \tag{4-6}$$

where $\lambda = \ln\mu - \frac{1}{2}\varsigma^2$ and $\varsigma^2 = \ln(1 + \frac{\sigma^2}{\mu^2})$, if $\text{COV} \le 0.30$, $\varsigma \approx \text{COV}$; λ and ς are the mean and standard deviation of $\ln x$, and μ and σ are the mean and standard deviation of x.

Uncertainties in different bridge parameters are discussed in the following paragraphs.

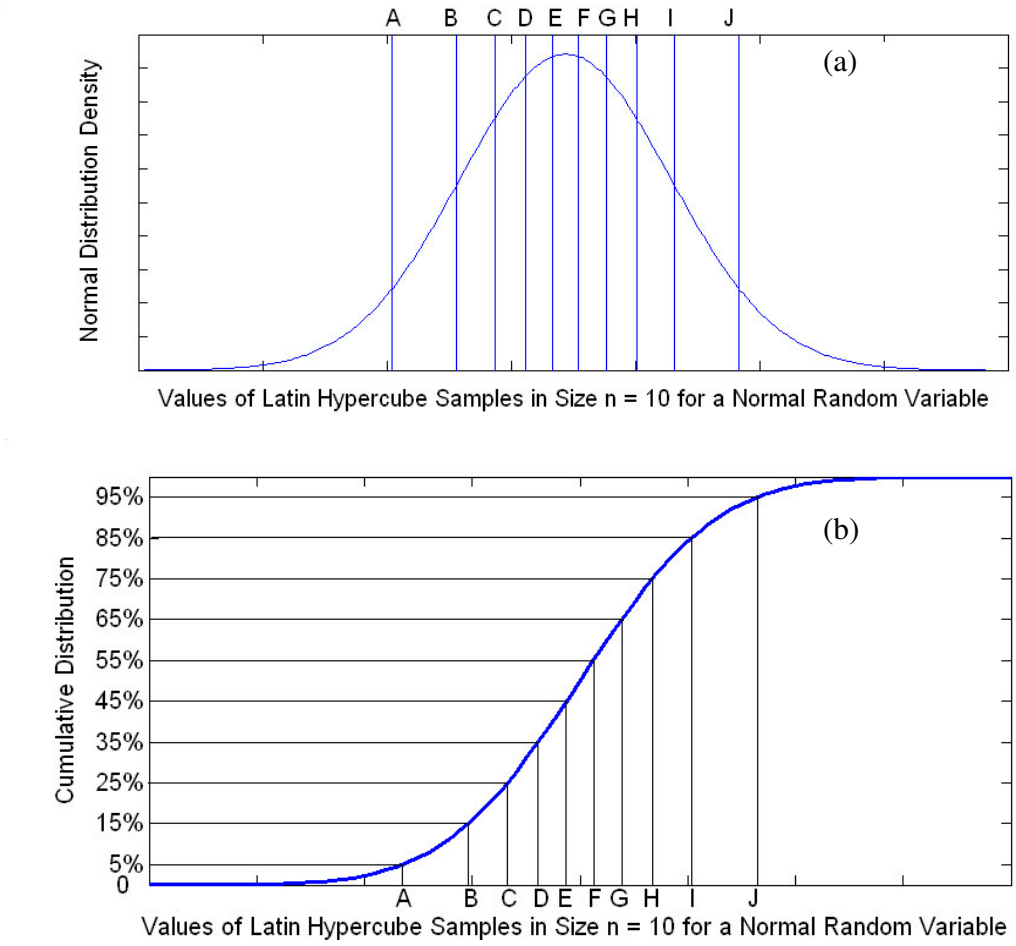

Figure 4-13. Generation of Bridge Parameter Samples by the Latin Hypercube Sampling Approach.

Bridge Superstructure Weight: Typical bridges in New York State have a monolithic deck of 240 mm total concrete thickness, including an integral wearing surface. Estimation of the actual weight of the structure is associated with large degrees of uncertainty due to variations in material densities, member sizes, and overlay thickness. Following the work of Nowak (1993), we assume that the superstructure weight is normally distributed with a bias λ = 1.05, and a coefficient of variation (COV) = 0.10. For the multi-span continuous bridge in Fig. 4-1, the total nominal distributed weight for

the superstructure (slab, girders and wearing surface) is equal to 110.20 N/mm. Hence, the total superstructure weight of this bridge in LHS samples varies from 96.7 N/mm to 134.7 N/mm. For the multi-span simply supported bridge in Fig. 4-2, the total nominal distributed weight for the superstructure is equal to 80.1 N/mm, with the values of LSH samples varying from 70.3 N/mm to 97.94 N/mm.

Yielding Strength of Reinforcing Steel: Since the column diameter is a deterministic parameter, uncertainties associated with column capacity and stiffness are mainly due to uncertainties in the material strength. According to Priestley et al. (1996), yielding strength of Grade 40 reinforcing steel, which was used widely for bridges built before 1980s in New York State, may vary from 276 MPa up to 406 MPa. In this paper, the yield strength of Grade 40 reinforcement is considered as a lognormal random variable in Eq. 4-5, with a mean value of 336 MPa and COV of 0.117. Hence, the yield strength of reinforcing steel varies from 275.6 MPa to 405.1 MPa for cumulative probability distributions between 5% and 95%.

Concrete Compressive Strength: Concrete compressive strength of 20.7 MPa (3.0 ksi) is the standard design strength for bridges built in New York State during the 1970's and 1980's. According to MacGregor (1992), 3.0 ksi concrete can be assumed to have a strength that follows a normal probability distribution with mean value 27.2 MPa and a standard deviation of 4.24 MPa (COV =0.16). It is noted that these strengths represent the 28-day strength. As the concrete ages, the strength increases with time. This factor has not been considered in the analysis.

Gap Size: Considerable variations in temperature conditions will cause large deviations in a gap's size from its nominal value. The average annual mean temperature in New

York State ranges from 40°F in the Adirondacks to 55°F in the New York City area. Actual temperatures vary from -5°F to 90°F. Hence, the temperature variation ΔT, that is the difference between temperature during a seismic event and the one during construction, can be modeled as a random variable in the range of -95°F to +95°F. For the purpose of estimating the gap size when a seismic event occurs, the temperature variations ΔT are considered to follow a normal distribution, with mean $\mu = 0$ and standard deviation $\sigma = 58$ to obtain ΔT samples in the temperature ranging from -95.4°F to 95.4°F corresponding to 5% to 95% cumulative probability.

The change in gap size because of temperature variations is $\alpha \times \Delta T \times L$. Coefficients of thermal expansion α for steel and concrete are in the range of (6.1~6.7) $\times 10^{-6}/^{o}F$ and (4.1 ~7.3) $\times 10^{-6}/^{o}F$, respectively. For a composite deck, the coefficient of thermal expansion α of the composite superstructure can be calculated as

$$\alpha = \frac{\alpha_c \Delta TL + FL/(E_c A_c)}{\Delta TL} \tag{4-7}$$

where F is the force transmitted between the concrete deck and steel beams to ensure compatibility of the displacements, and is determined by

$$\alpha_c \Delta TL + \frac{FL}{E_c A_c} = \alpha_s \Delta TL - \frac{FL}{E_s A_s} \tag{4-8}$$

By taking the mean values of coefficients α for steel and concrete respectively, the coefficient of thermal expansion α of the composite superstructure is calculated to be $6.0 \times 10^{-6}/^{o}F$. For the multi-span continuous bridge, the gap between the deck end and each abutment is assumed to be 76.2 mm (3 inches) for as-built conditions, L=66 m for the right span and L=30 m for the left span, as shown in Fig. 4-14. In the multi-span simply supported bridge, the nominal gaps between the deck's ends and the abutments

are 38.1 mm (1.5 inches), and the nominal gaps at intermediate expansion joints are 25.4 mm (1 inch) for as-built conditions. The span lengths are $L = 12\,\text{m}$ for the first multi-column bent and $L = 20\,\text{m}$ for the second span, as shown in Fig. 4-15. The values for the samples of gap sizes are calculated by subtracting $\alpha \Delta T L$ from the nominal values of each gap. The uncertainties of gap size due to temperature changes are thus considered.

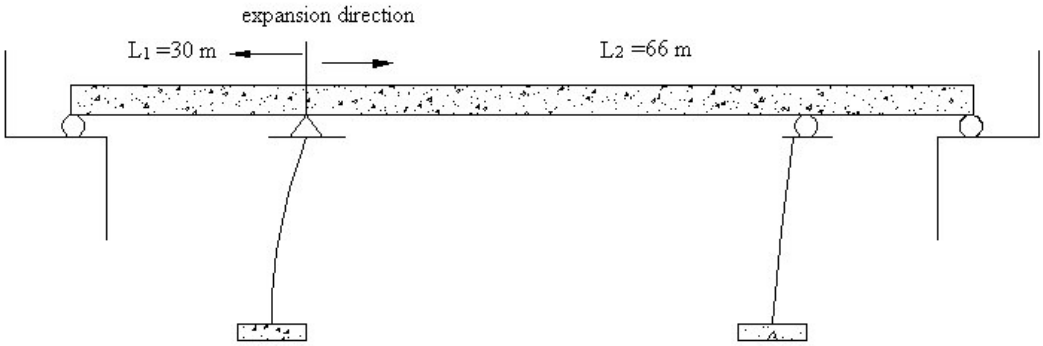

Figure 4-14. Length for Free Expansion due to Temperature Changes for the Multi-span Continuous Bridge.

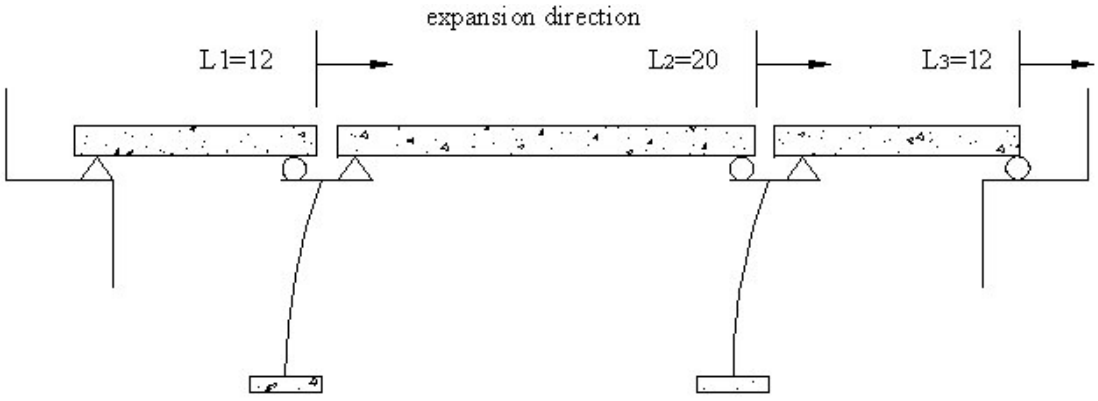

Figure 4-15. Length for Free Expansion due to Temperature Changes for the Multi-span Simply Supported Bridge.

Friction Coefficient of Expansion Bearings: The degree of corrosion in bearings changes the friction coefficient of low type sliding bearings and high type rocker bearings. The experiments by Mander et al. (1996) have shown that badly corroded expansion bearings in simply supported bridges, due to leakage at the deck joints, could have friction coefficients as large as three times those of clean worn expansion bearings in continuous bridges. They have suggested that $\mu = 0.04$ and $\mu = 0.2$ should be used for a clean well-worn rocker bearing and a clean sliding surface of a low type sliding bearing, and $\mu = 0.12$ be used for a partially seized and badly corroded surface. Considering the uncertainty of the degree of corrosion, the coefficient of friction is assumed to follow a uniform distribution in the range of 0.16 to 0.3 for the low type sliding bearings, and in the range of 0.032 to 0.06 for the high type rocker bearings in the multi-span continuous bridge. For the multi-span simply supported bridge, considering the possibility of severe leakage at expansion joints, the coefficient of friction of high type rocker bearings in the bridge is assumed to follow a uniform distribution in the range of 0.04 to 0.12.

Given the probabilistic descriptors of the random variables, ten samples for each of the critical parameters are obtained and are subsequently combined to create ten samples of MSC bridge models and ten samples of MSSS bridge models using Latin Hypercube pairing approach.

4.5 Bridge Model Sampling for Fragility Analysis

Histograms simulating the frequency distributions of each of the random variables mentioned above are assembled for the purpose of creating a set of nominally identical

but statistically different bridge samples for fragility analysis. To limit the bridge sample size, each of the random variables must be paired to form a total of ten bridge samples. Instead of pairing the variables randomly, the Latin Hypercube Sampling (LHS) restricted pairing concept is used so that the correlation matrix is as close as possible to the actual correlation matrix. Since the five random variables are assumed to be uncorrelated, the following sets of ten representative bridge samples for the MSC and the MSSS bridges have been obtained by LHS concept using a trial and error approach to make the correlation matrices close to an identity matrix, where the diagonal terms are equal to 1.0 while all the off-diagonal terms are very close to zero.

$$\begin{array}{ll} f_y: & (1\ \ 2\ \ 3\ \ 4\ \ 5\ \ 6\ \ 7\ \ 8\ \ 9\ \ 10) \\ f_c^{'}: & (2\ \ 7\ \ 10\ \ 8\ \ 1\ \ 4\ \ 9\ \ 3\ \ 5\ \ 6) \\ W: & (9\ \ 4\ \ 3\ \ 5\ \ 7\ \ 2\ \ 10\ \ 1\ \ 6\ \ 8) \\ \Delta T: & (9\ \ 2\ \ 10\ \ 1\ \ 4\ \ 5\ \ 3\ \ 6\ \ 8\ \ 7) \\ \mu_b: & (5\ \ 1\ \ 7\ \ 9\ \ 8\ \ 6\ \ 4\ \ 3\ \ 10\ \ 2) \end{array} \tag{4-9}$$

Each of the columns in the matrix of Eq. (4-9) represents one bridge sample. For example, the first sample will be associated with 1st, 2nd, 9th, 9th and 5th bin of the histograms for f_y, $f_c^{'}$, W, ΔT, and μ_b, respectively. The two-dimensional chart in Fig. 4-16 illustrates the pairing between two input variables. Every row or column has only one pair of variables. Hence, pairs fall into non-overlapping intervals of equal probability. This procedure is repeated, for the other variables.

f_y \ f_c	1	2	3	4	5	6	7	8	9	10
1		●								
2							●			
3										●
4								●		
5	●									
6				●						
7									●	
8			●							
9					●					
10						●				

Figure 4-16. Two-Dimensional Representation of Pairing Latin Hypercube Samples for a Set with Sample Size N=10 Utilizing f_c and f_y.

CHAPTER 5

FRAGILITY ANALYSIS OF TYPICAL BRIDGES

5.1 Methodology

Fragility is defined as the conditional probability that a structure or a structural component would meet or exceed a certain damage level for a given ground motion intensity. Mathematically, fragility is defined as

$$P_f = P[\frac{S_d}{S_c} \geq 1] \tag{5-1}$$

where P_f is the failure probability for a specific damage state, and S_d is the structural demand and S_c is the structural capacity. In Eq. (5-1), structural demand, S_d, depends on earthquake ground motion intensity.

The flow chart in Fig. 5-1 shows the systematic procedure proposed for fragility analysis of highway bridges in this research. For each bridge type to be analyzed, 10 bridge samples are generated using the Latin Hypercube Sampling approach described in Chapter 4. Each of these bridge samples is matched with 10 earthquake samples generated as described in Chapter 3. Hence, there are 100 earthquake-bridge samples for each bridge type considered to be investigated using a series of nonlinear time history analyses. Based on the analyzed seismic response data and estimated capacities, a probabilistic analysis for seismic demand and capacity is carried out to develop the fragility curves/surfaces as a function of earthquake characteristic parameters for each damage state considered.

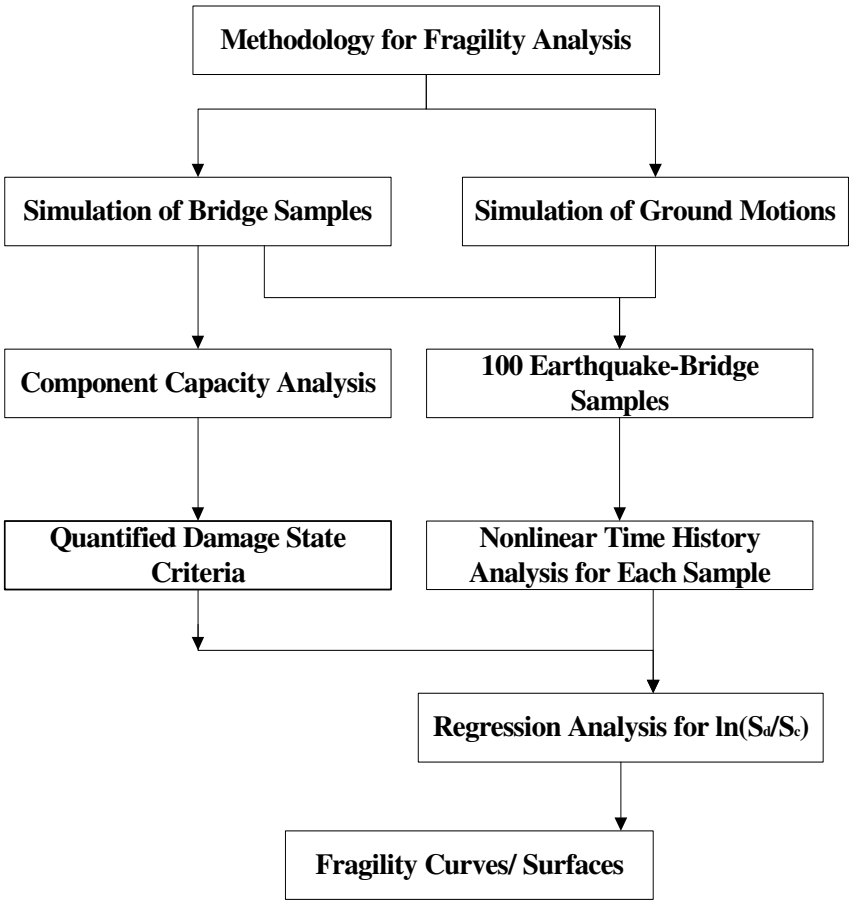

Figure 5-1. Steps for Development of Analytical Fragility Curves/ Surfaces.

5.2 Capacity Estimation of Bridge Components

Past experiences have shown that the vulnerabilities of bridges during earthquakes are mainly due to damage to critical components, such as columns and bearings. For example, large relative movements at the expansion joints may result in the loss of support, and excessive ductility demands on bridge piers may result in column failure in shear or flexure. Hence, estimating the capacity of bridge components is essential for

defining damage state of structural components and the entire structure on the basis of the analytical models described in Chapter 4.

5.2.1 Deformation Capacity of Steel Bearings

There are three kinds of bearings used in the typical multi-span continuous bridge considered in this research. These bearings are: high type fixed bearings, high type rocker bearings, and low type sliding bearings. In the typical multi-span simply supported bridge being considered, high type fixed bearings and high type rocker bearings are used.

Potential damage to high type fixed steel bearings can be associated with bond failure of high strength anchor bolts and rocking of the bearing on the bedding material, which would start when the displacement exceeds 20 mm [Mander et al. (1996)]. Beyond this displacement, concrete cover of the reinforced concrete pedestal starts to crack and spall beneath the masonry plate. Subsequently, nuts would be loosened, and anchor bolts would be raised and bent slightly. The ultimate failure mode of high type fixed bearings would be due to wide rocking of the bearing back and forth, and even overturning of the bearing after fracture of the anchor bolts. Based on Mander's experimental results shown in Fig. 5-2, strength and stiffness degradation in high type fixed steel bearings were observed at a deformation of approximately 20.0 mm. Based on a series of experimental tests of bearings [Mander et al. (1996), Randall et al. (1999)], a displacement limit of 40 mm is assumed to correspond to extensive concrete cracking/spalling of the reinforced concrete pedestals of high type fixed bearings. At this limit, complete bond failure causes wide back and forth rocking of the bearing [Choi et al. (2004)].

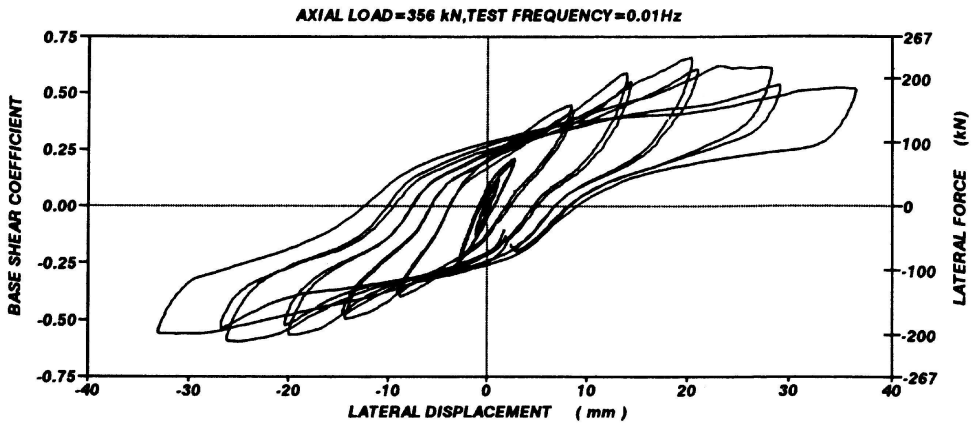

Figure 5-2. Hysteresis Loop for the High Type Fixed Bearing Mounted on Concrete Pedestal-Longitudinal Direction.

For the multi-span continuous bridge in this study, fixed bearings are mounted on the multi-column bent. The deformation of a fixed bearing represents the relative displacement between the deck and the pier. This flexibility at the top of cantilever piers accommodates the longitudinal deck movement. The displacement threshold of 20 mm for initiating the bond fracture of the anchor bolts is significantly above the values observed from 100 cases of dynamic analysis simulations performed for the multi-span continuous bridge. Hence, failure of the bridge because of failure of fixed bearings is unlikely for the fragility analysis of the multi-span continuous steel bridge. However, the scenario is different for multi-span simply supported bridges. It is observed that the largest fixed bearing deformation occurred in the fixed bearing located at the left abutment. In 100 time history analysis cases, we found that the deformation could be as large as 20.7 mm for the earthquake with PGA around 1.0g. Hence, seismic fragility of high type fixed bearings will be considered exclusively for the multi-span simply supported bridges.

Instability of expansion bearings may lead to unseating of the bridge deck because of excessive deformation of the bearing. High type rocker bearings may overturn about the edge of bottom of the rocker (by rolling off the rocker on the masonry plate), when the deformation exceeds half the width of the rocker. Instability of low type sliding expansion bearings occurs when translation of the sliding plate over the bronze plate is larger than half the width of the masonry plate. The deformation capacity of expansion bearing should be modified according to the dimensions of the bearings as illustrated in Fig. 5-3.

Figure 5-3. Typical High Type Rocker Bearings

Fig. 5-4 (a) shows a detailed drawing of high type rocker bearings used on top of the second column bent of the multi-span continuous bridge in this study. The radius and width of the rocker are 330 mm (13 inches) and 305 mm (12 inches), respectively. Hence, the displacement limit is 153 mm for high type rocker bearings in the multi-span continuous steel bridge. Fig. 5-4 (b) shows a detailed drawing of low type sliding bearings of the type used over the abutments of the multi-span continuous bridge with phosphor bronze plate of width 203 mm. Hence, the displacement limit is 102 mm for low type sliding bearings in the multi-span continuous steel bridge.

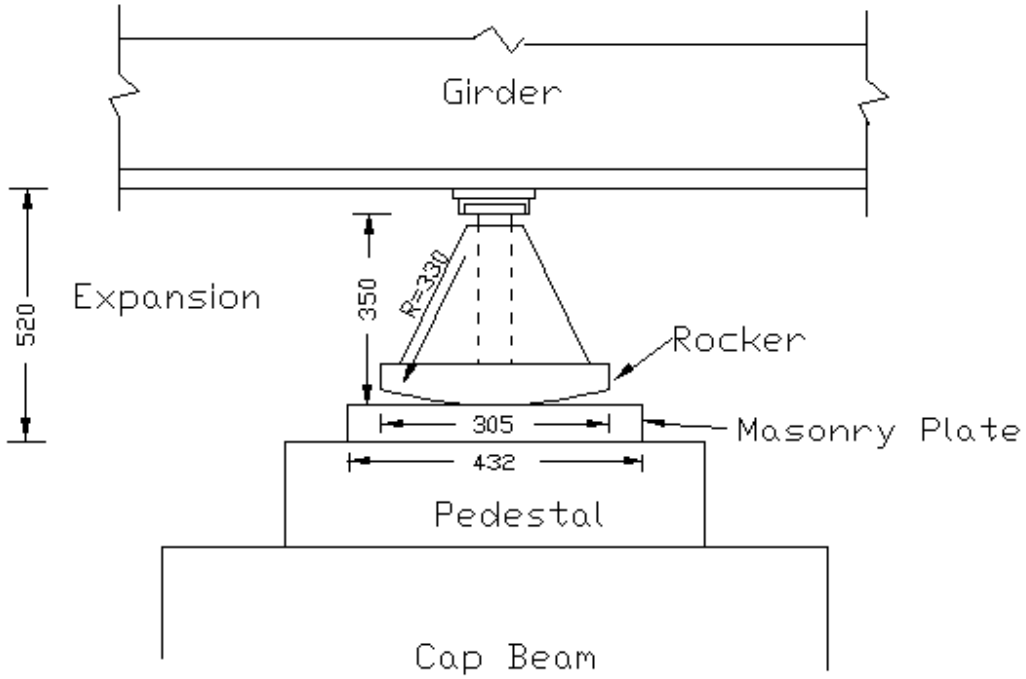

(a) Unit: mm

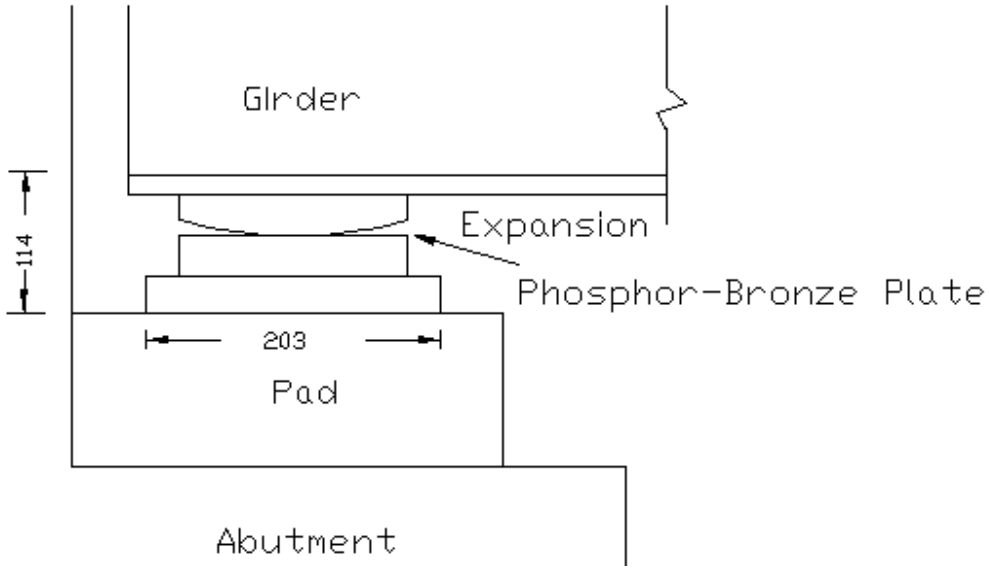

Unit: mm

(b)

Figure 5-4. Expansion Bearings in Multi-Span Continuous Steel Bridge; (a) High Type Expansion Bearing; (b) Low Type Sliding Bearing

Fig. 5-5 shows one of the intermediate expansion joints on the cap beam of the column bent used for the multi-span simply supported bridge. The high type rocker bearing in Fig. 5-5 has a narrower rocker width than the one in Fig. 5-4 (a) because of space limitation and the need to accommodate the adjacent high type fixed bearings. The rocker bearing in Fig. 5-5 has a rocker radius of 229 mm (9 inches), and a rocker width of 203 mm (8 inches). Hence, the rocker bearing would fail from the support when the bearing deformation exceeds 102 mm.

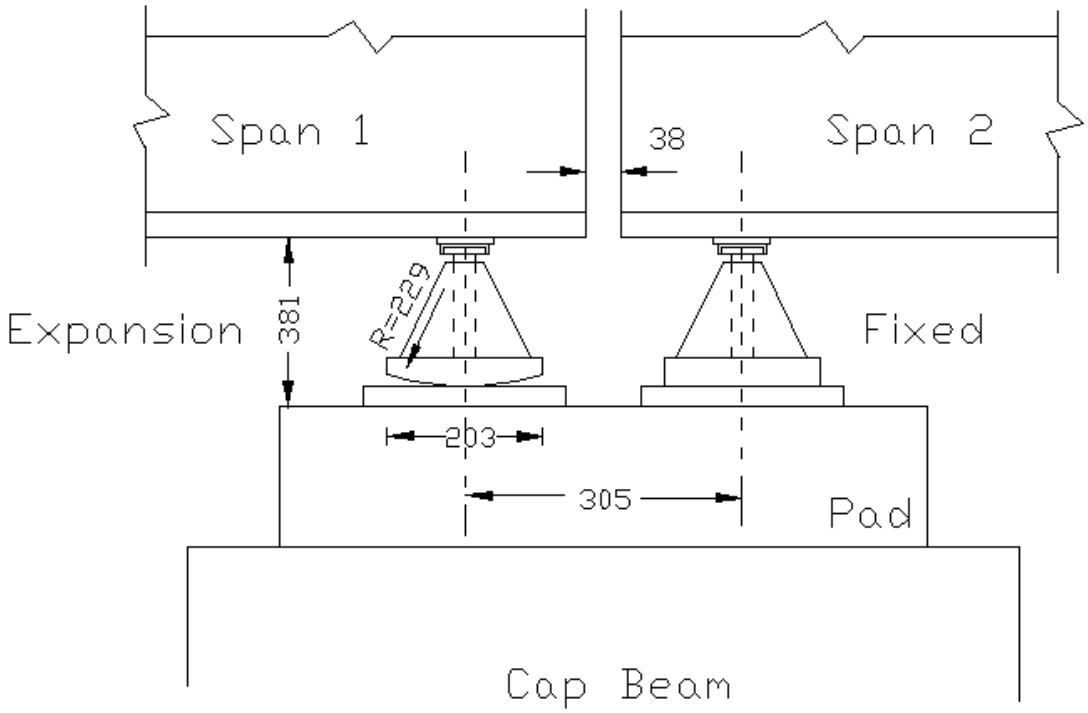

Unit: mm

Figure 5-5. Bearings at an Expansion Joint of Multi-Span Simply Supported Bridge.

5.2.2 Shear and Flexural Capacities of Bridge Piers

Shear Capacities

Figure 5-6 shows the criteria for assessing column shear failure [Buckle and Friedland (1995)]. The shear strength of bridge piers degrades with increasing in flexural ductility. In Fig. 5-6, V_{di} is the initial shear strength and V_{dd} is the ductile shear strength. The shear strength of columns is contributed by the concrete, transverse reinforcement, and axial compressive force [Priestley et al. (1996)] and can be expressed as,

$$V_n = V_c + V_s + V_p \tag{5-2}$$

where

$$V_c = k\sqrt{f_c'}A_e \qquad \text{(in psi units)} \tag{5-3}$$

$$V_s = \frac{\pi}{2}\frac{A_h f_{yh} D' \cot\theta}{s} \qquad \text{for circular columns} \tag{5-4}$$

$$V_p = P\tan\alpha \tag{5-5}$$

In Eq. (5-3), the effective shear area $A_e = 0.8A_{gross}$, and k varies according to the column displacement ductility μ_Δ. For non-ductile regions and for plastic hinges with $\mu_\Delta \le 2$, $k = 3.5$; for plastic hinges with $\mu_\Delta \ge 4$, $k = 1.2$; and a linear interpolation is assumed between $\mu_\Delta = 2$ and $\mu_\Delta = 4$. In Eq. (5-4), D' is the core dimension from center to center of peripheral hoops. The angle of cracking θ may be taken as 30^o as recommended by Priestley et al. (1996). The parameter α in Eq. (5-5) is the angle formed between the column axis and the strut from the point of load application to the center of the flexural compression zone at the pier bottom for cantilever columns in this study. $\tan\alpha$ may be taken as 0.2 for simplicity [Buckle and Friedland (1995)].

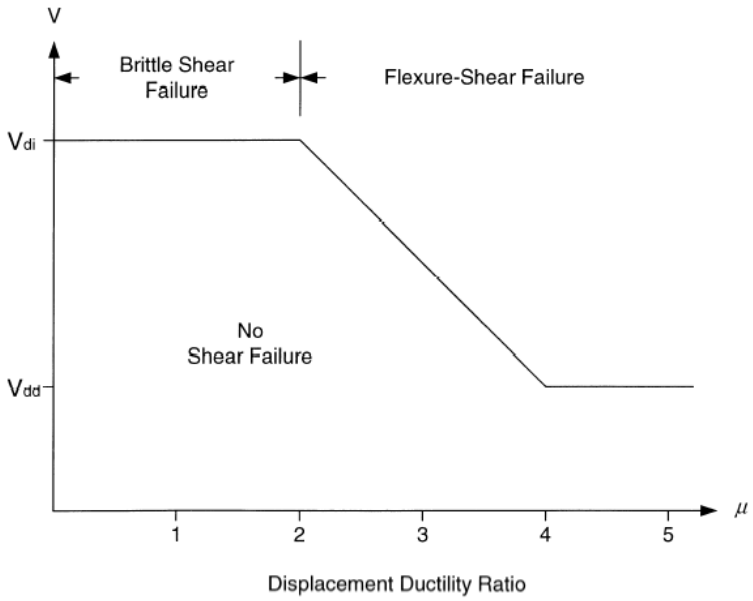

Figure 5-6. Relationship between Lateral Displacement Ductility Ratio and Column Shear Strength.

The shear strengths of 10 bridge samples of the multi-span continuous (MSC) and multi-span simply supported (MSSS) steel bridges are calculated according to Eq. (5-2) and are shown in Figs. 5-7 and 5-8, respectively. Since the piers in the MSSS steel bridge have lower axial forces, their shear capacities are smaller than those of the MSC steel bridges. However, it has been observed from extensive numerical simulation that the maximum shear forces in columns of these two types of bridges are always significantly below their shear capacities under ground motions in the longitudinal direction. Hence, the piers of the two types of bridges are unlikely to undergo shear failure. Rather, the piers will fail because of excessive flexural ductility demand exceeding the ultimate ductility capacity that is provided.

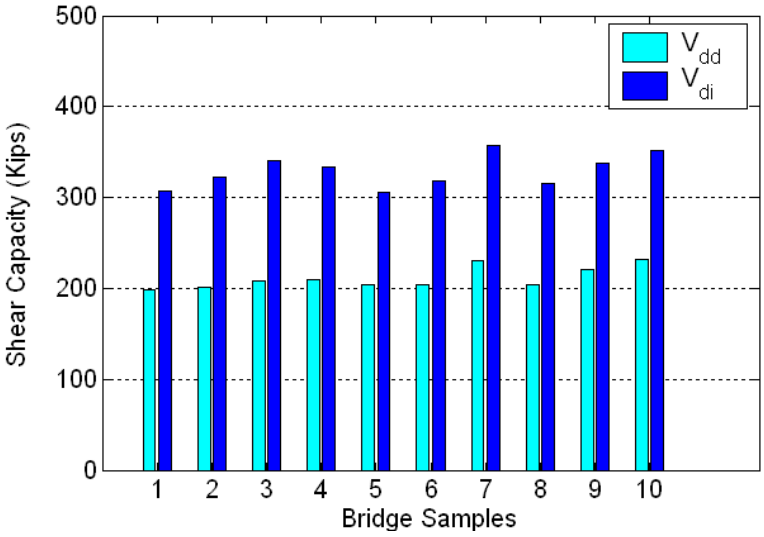

Figure 5-7. Pier Shear Capacities for MSC Bridge Samples

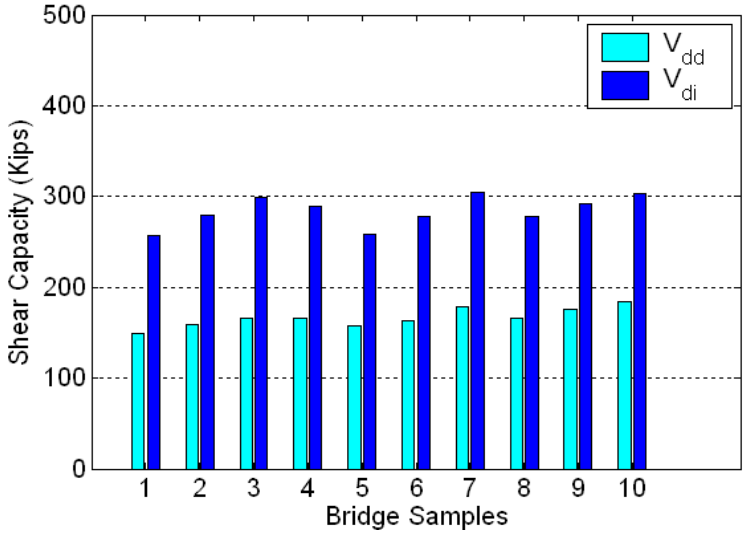

Figure 5-8. Pier Shear Capacities for MSSS Bridge Samples

Flexural Capacities

Typical inelastic behavior of concrete bridge piers is modeled as shown in Fig. 5-9 where the moment-curvature relationship is idealized as elastic-perfectly plastic with critical points associated with the curvatures $\phi_y^{'}$, ϕ_y, ϕ_d, ϕ_u. These critical points are related to the extent of damage in a pier during earthquake ground motions. The parameter $\phi_y^{'}$ indicates the initiation of yielding. The moment that induces the first yielding in the column longitudinal reinforcement is $M_y = EI_e\phi_y^{'}$. The bifurcation point at ϕ_y is associated with the formation of a plastic hinge in the pier. For this case, the idealized moment capacity, M_n, corresponds to the moment when the longitudinal compressive strain of the extreme concrete fiber reaches $\varepsilon_c = 0.005$ [Priestley and Park (1987) and Watson and Park (1994)]. Hence, ϕ_y can be calculated as $\phi_y = M_n / EI_e = M_n\phi_y^{'} / M_y$. Degradation in strength of piers occurs at ϕ_d, when the maximum moment $M_{\max}$ is reached. Crushing of concrete occurs at ultimate curvature ϕ_u when the strain in the concrete is equal to ε_{cu}, where ε_{cu} accounts for the confining effect of transverse reinforcement, and can be calculated on the basis of energy balance [Mander et al. (1988)],

$$\varepsilon_{cu} = 0.004 + \frac{1.4\rho_s f_{yh}\varepsilon_{su}}{f_{cc}^{'}} \tag{5-6}$$

In Eq. (5-6), $\rho_s = 4A_h / D^{'}s$ is the volumetric ratio of confining steel, ε_{su} = strain corresponding to the maximum tensile stress in the transverse steel and is commonly taken as 0.15 for grade 40 reinforcement, and 0.12 for grade 60 reinforcement. The

parameter $f_{cc}^{'}$ in Eq. (5-6) is the compressive strength of the confined concrete,

$$f_{cc}^{'} = f_{c}^{'}(2.254\sqrt{1+\frac{7.94f_{l}^{'}}{f_{c}^{'}}} - 2\frac{f_{l}^{'}}{f_{c}^{'}} - 1.254) \tag{5-7}$$

where $f_{l}^{'} = K_e f_{yh}\rho_s / 2$ is the effective lateral confining stress with $K_e = 0.95$ being confinement effectiveness coefficient for circular sections. Welded hoops or interlocking spirals are required for the confinement to be effective. For the case when concrete in a bridge pier is poorly confined, ε_{cu} should be taken as 0.005. In this study, concrete in bridge piers is considered to be well confined for the transverse reinforcement in the plastic hinge zone.

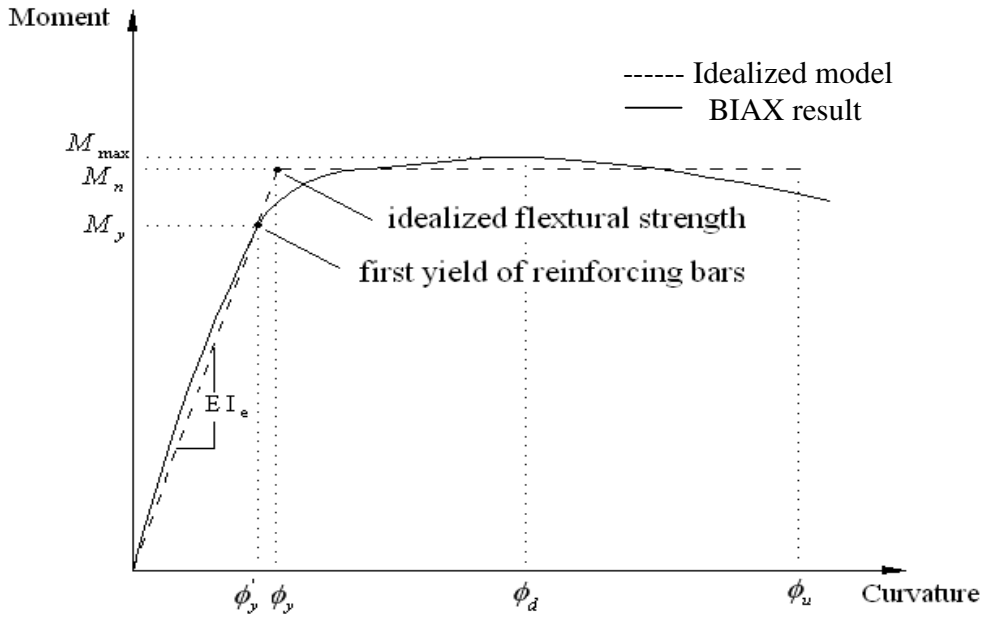

Figure 5-9. Moment-Curvature Diagram of Bridge Piers

Moment curvature analysis of bridge piers has been carried out by using a computer program BIAX [Wallace (1992), Wallace and Ibrahim (1996)]. The capabilities of BIAX program include the calculation of section properties, interaction diagrams, or moment-curvature relations for bridge piers. A bilinear material model for steel reinforcement and a modified Kent-Park model for stress-strain relations of confined and unconfined concrete [Kent and Park (1971), Park et al. (1982)] are used in BIAX. In order to verify the validity of the moment-curvature relationship obtained from BIAX program, the xSECTION program [CALTRANTS (1999)] is also used, which is based on the more advanced Park model considering complex strain hardening for reinforcing steel, and the Mander models for confined and unconfined concrete [Mander et al. (1988). Fig. 5-10 shows comparisons between moment-curvature relationships obtained by BIAX and xSECTION programs along with their corresponding idealized elastic-perfectly plastic models. It is observed that the moment-curvature diagrams using BIAX and xSECTION almost coincide with each other. The plots in Fig. 5-10 have been obtained for a reinforced concrete column of 36-inch diameter, with 13 #8 rebars, #3 spirals at 6 inch pitch and axial load P = 341 kip. The initial compressive strength of unconfined concrete ($f_c^{'}$) is 5 ksi. The concrete stress at failure when the strain is ε_{cu} for unconfined concrete, $f_{cu}^{'}$ = 2.5 ksi. This value will be modified for confined concrete by Mander's model in xSECTION program. The initial strain corresponding to the peak of the unconfined concrete curve ($\varepsilon_0 = 0.002$) and the spalling strain of unconfined concrete (ε_p =0.005) are specified for both BIAX and xSECTION programs. The grade 40 steel has the following material parameters: yield strain $\varepsilon_y = 0.0138$, hardening strain

$\varepsilon_h = 0.0195$, ultimate strain $\varepsilon_{su} = 0.12$, yield strength $f_y = 40$ ksi, and an ultimate strength $f_{su} = 60$ ksi. In Fig. 5-10, the idealized bilinear model 1 is based on the analytical results from the BIAX Program. Effective elastic stiffness is determined by the ratio of moment and curvature at first yield of a longitudinal reinforcing bar, i.e., $EI_e = M_y / \phi_y'$. The idealized moment capacity M_n for this case corresponds to $\varepsilon_c = 0.005$. The idealized bilinear model 2 is generated by xSECTION program, where the initial slope of the moment-curvature curve is generated by passing a line through the origin and the point of first yielding of rebars. However, the horizontal line portion of the model is determined by balancing positive and negative areas of the actual curve by the area under the idealized curve. The values corresponding to the characteristic points ϕ_y', ϕ_y, ϕ_d, ϕ_u for the two idealized models are presented in Table 5-1. It is observed from Table 5-1 that values corresponding to characteristics points and moment capacities from the two programs are comparable. Since the xSECTION program needs many more material property information than the BIAX program, it is determined that BIAX provides an efficient way for the huge number of calculations needed for the fragility analysis, and will be used in this study to establish the moment-curvature models for piers in each bridge sample.

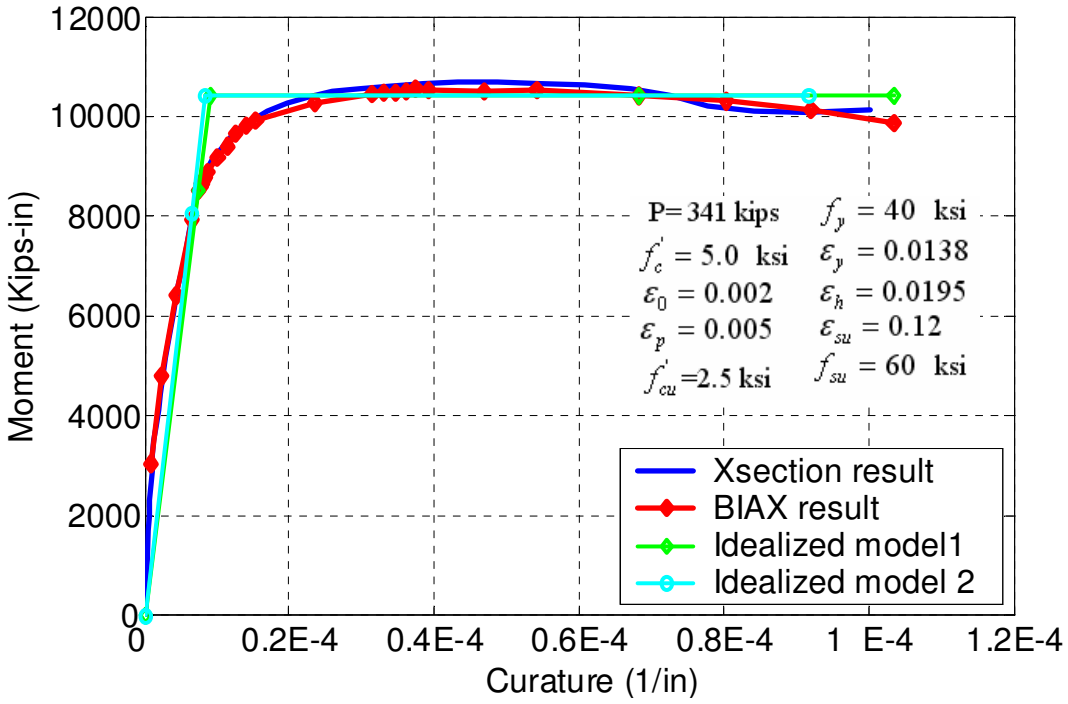

Figure 5-10. Pier Moment-Curvature Plot by BIAX and xSECTION Programs

Table 5-1. Characteristic Points and Moment Capacities using BIAX and xSECTION Programs.

	M_y (kip.in)	M_n (kip.in)	M_{max} (kip.in)	$\phi_y^{'}$ 10^-4/in	ϕ_y 10^-4/in	ϕ_d 10^-3/in	ϕ_u 10^-02/in
BIAX	8536	10410	10550	0.75	0.91	0.37	0.1034
xSECTION	8052	10428	10692	0.65	0.85	0.43	0.1002

Figs. 5-11 and Fig. 5-12 show values of $\phi_y^{'}$, ϕ_y, ϕ_d, ϕ_u obtained for columns of ten bridge samples for multi-span continuous and multi-span simply supported steel bridges, respectively. The capacity difference among samples for the same bridge type is due to variations in material strength and bridge superstructure weight. Curvature capacities $\phi_y^{'}$ and ϕ_y for piers of the multi-span continuous steel bridge are slightly larger than those for piers of the multi-span simply supported steel bridge. However, the curvature capacities ϕ_d and ϕ_u for piers of the MSC steel bridge are much smaller than those for piers of the MSSS steel bridge. This is because of the much lower axial force in the piers of multi-span simply supported bridge compared to those of the multi-span continuous bridge samples.

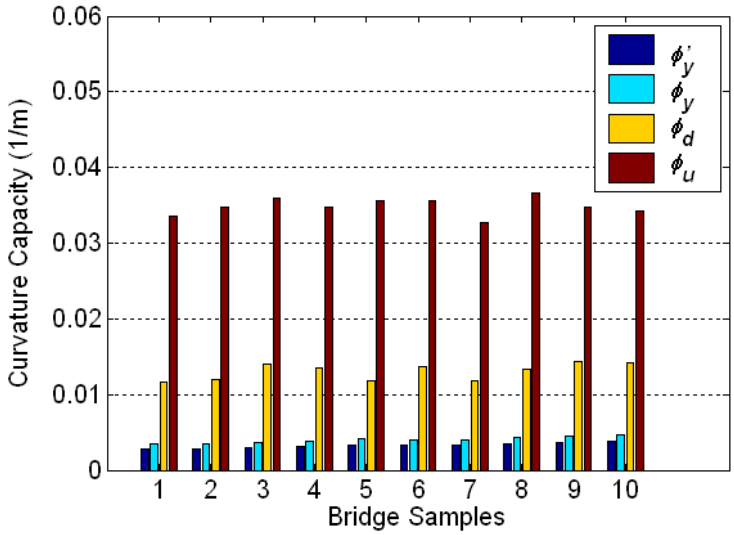

Figure 5-11. Pier Curvature Capacities for MSC Bridge Samples.

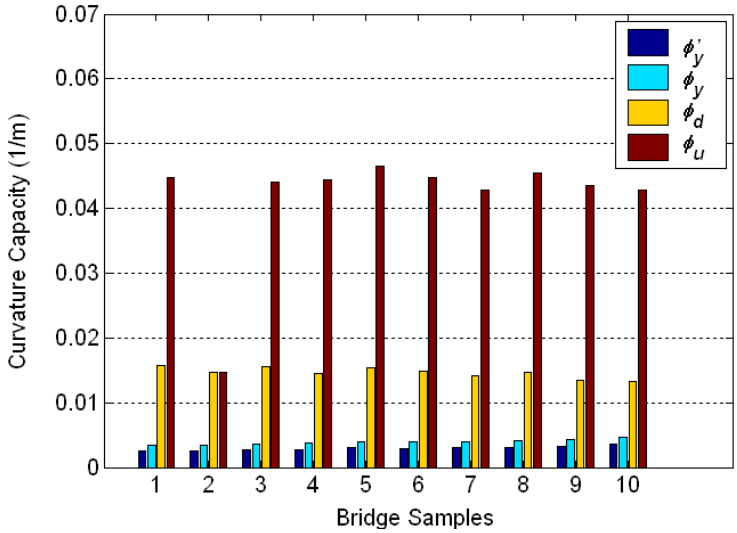

Figure 5-12. Pier Curvature Capacities for MSSS Bridge Samples.

To understand the effect of the pier axial force on the moment curvature relationships, Fig. 5-13 compares the moment-curvature curves of a pier under axial forces, $P = 395$ kips and $P = 149$ kips in the two types of bridges. It is observed that the

pier with the lower axial force will yield and form a plastic hinge at smaller curvatures and will undergo strength degradation and ultimate collapse at a much higher curvature.

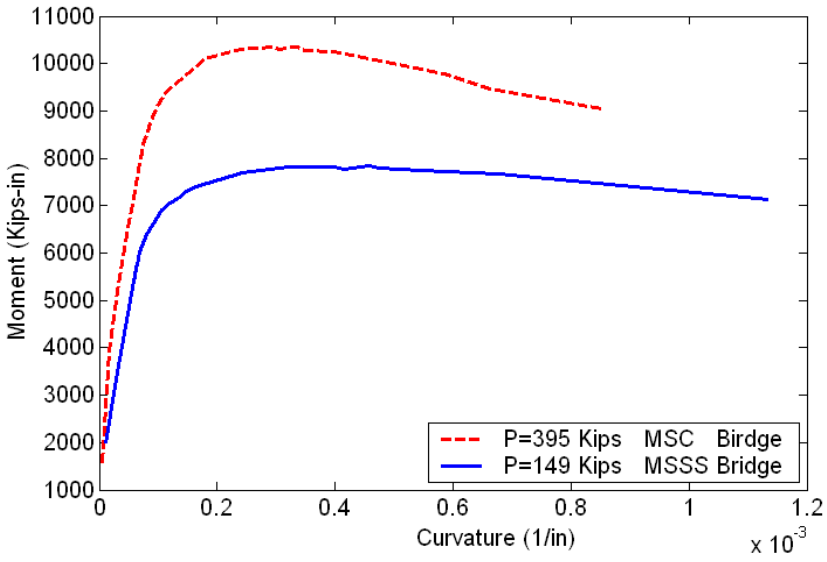

Figure 5-13. Moment-Curvature Relationships for a Pier with Different Compressive Loads

5.2.3 Deformation Capacity of Abutments

Excessive deformation at one or both abutments is another common type of damage to highway bridges. Past performance of bridge abutments has indicated that an abutment displacement of more than 61 mm (2.4 inches) may cause problems, whereas movements less than this amount are repairable and may cause little distress to a bridge structure [FHWA (1987)]. Likewise, HAZUS99-SR2 (1999) states that moderate movement of the abutment should be less than 51mm (2 inches). For seat type abutments in the multi-span continuous bridge considered in this study, the two expansion joints at the abutments permit large longitudinal movements of the bridge, thereby reducing the

deformation of the abutments as well as the degree of soil mobilization. For the multi-span simply supported bridge in this study, the fixed bearings supported by one of the abutments may induce relatively large abutment deformations. The maximum active displacement of abutments is observed to be 20.1 mm (0.8 inch) for 100 cases of nonlinear time history analyses. The maximum passive displacement is less than 2.7 mm for these 100 cases. The passive earth pressure induced by this level of maximum passive displacement is significantly smaller than the ultimate strength of 7.7 ksf. Hence, the probability of seismic damage to bridge abutments is quite low and can be ignored for typical bridges in New York State.

5.3 Damage Limit States for Steel Bridges

Based on the foregoing discussions and the preliminary analysis of the response of bridge components, the following damage limit states are considered to establish fragility curves for critical bridge components.

Multi-span Continuous Steel Bridge

- Four different levels of pier damage corresponding to four curvature thresholds ϕ_y', ϕ_y, ϕ_d, and ϕ_u.
- Instability in high type rocker bearings when the displacement exceeds half of the rocker width, i.e., 153 mm.
- Instability in low type sliding bearings when the displacement exceeds half of the masonry plate width (i.e., 102 mm).
- Either instability of an expansion bearing or collapse of a column would lead to the failure of the entire bridge system.

Multi-span Simply Supported Steel Bridge

- Four different levels of pier damage corresponding to four curvature thresholds $\phi_y^{'}$, ϕ_y, ϕ_d, and ϕ_u.
- Instability in high type rocker bearings when the displacement exceeds half of the rocker width, i.e., 102 mm.
- Extensive damage in high type fixed bearings when the displacement exceeds 20 mm. Bond failure of the anchor bolts and degradation of bearing stiffness and strength is initiated at this displacement level.
- Ultimate damage is assumed for high type fixed bearings when the bearing displacement exceeds 40 mm. Extensive concrete cracking and spalling at the pedestals would occur at this displacement level. Consequently, high type fixed bearing starts rocking widely on the pedestal.
- Either wide rocking of a fixed bearing, or instability of an expansion bearings, or concrete crushing of a column would lead to the ultimate failure of the entire bridge system.

5.4 Probabilistic Analysis of Seismic Demand and Capacity

As discussed previously, seismic fragility is defined as,

$$P_f = P[\frac{S_d}{S_c} \geq 1] \tag{5-1}$$

In Eq. (5-1), the random nature of structural demand S_d and structural capacity S_c are described by the lognormal probability distribution [Hwang et al. (2001), Choi et

al. (2004), Shinozuka et al. (2000b)]. Hence, fragility P_f in Eq. (5-1) can be expressed as a standard normal distribution function, i.e.,

$$P_f = \Phi\left[\frac{-\ln\left(\mu_c / \mu_d\right)}{\sqrt{\beta_d^2 + \beta_c^2}}\right] \tag{5-8}$$

where P_f is the fragility for a specific damage-state, μ_c and μ_d are the mean values, β_c and β_d are the lognormal standard deviations of structural capacity and demand, respectively. In previous studies, the structural capacity μ_c against a given damage type is assumed to be constant and structural demand μ_d is determined by regression analysis on the structure's response data [Karim and Yamazaki (2000), Deodatis et al. (2000), Choi et al. (2004) and Hwang et al. (2001)]. Furthermore, for the composite logarithmic standard deviation, $\sqrt{\beta_d^2 + \beta_c^2}$ known as the dispersion, an empirical value suggested in HAZUS [HAZUS 99-SR-2 (1999)] is used. The proposed empirical values in the 1997 and 1999 versions of HAZUS are different and are not related to bridge types and damage states. In fact, the capacity of bridge components varies with structural parameters, and the correctness of the assumed dispersion will largely influence the accuracy of the fragility results. To overcome this limitation, we propose to estimate the dispersion directly from regression of seismic response quantities of bridge components and the estimated capacity of each bridge sample.

The uncertainty in bridge property parameters in section 4.4 may not only affect the structural demand S_d, but also the structural capacity, S_c. For example, variation in bridge superstructure weight will affect the normal force on piers and bearings, and will

induce different force-displacement relationships for the piers and expansion bearings. In addition, the ductility capacity of piers is also affected by uncertainties in material strengths.

In this study, uncertainties in bridge property parameters are incorporated in the fragility analysis through a set of earthquake-bridge samples. After performing the nonlinear time history of each earthquake-bridge sample, maximum response quantities of individual components are divided by the corresponding capacities for each earthquake-bridge sample to obtain S_d / S_c ratios. These S_d / S_c ratios are plotted on a log-log scale as a function of the peak ground acceleration (PGA) of the corresponding earthquake ground motions. Regression analysis between S_d / S_c ratios and PGA is carried out to establish a relationship between $\ln(S_d / S_c)$ and the seismic intensity, i.e., PGA, for different components at various damage states. It is assumed that $\ln(S_d / S_c)$ follows a normal distribution around the regression curve, as shown in Fig. 5-14. This is consistent with the lognormal distribution assumption for S_d and S_c in the previous studies. If S_d and S_c follow lognormal distributions, then $\ln S_c$ and $\ln S_d$ follow normal distributions and the function $\ln(S_c / S_d)$ also follows a normal distribution. The fragility for a specific damage-state can be determined by:

$$P_f = P[\frac{S_d}{S_c} \geq 1] = 1 - \phi(\frac{\ln(1) - \lambda}{\varsigma}) = \phi(\frac{\lambda}{\varsigma}) \tag{5-9}$$

where λ and ς are the mean and standard deviation of $\ln(S_d / S_c)$ obtained from the regression analysis. The parameter λ in Eq. (5-9) is expressed as a function of the earthquake intensity parameter, e.g., PGA. The standard deviation ς is a value obtained

from the response and capacity data. Hence, the effects of uncertainties in capacity and demand can be evaluated simultaneously through the statistical characteristics of the regression parameters.

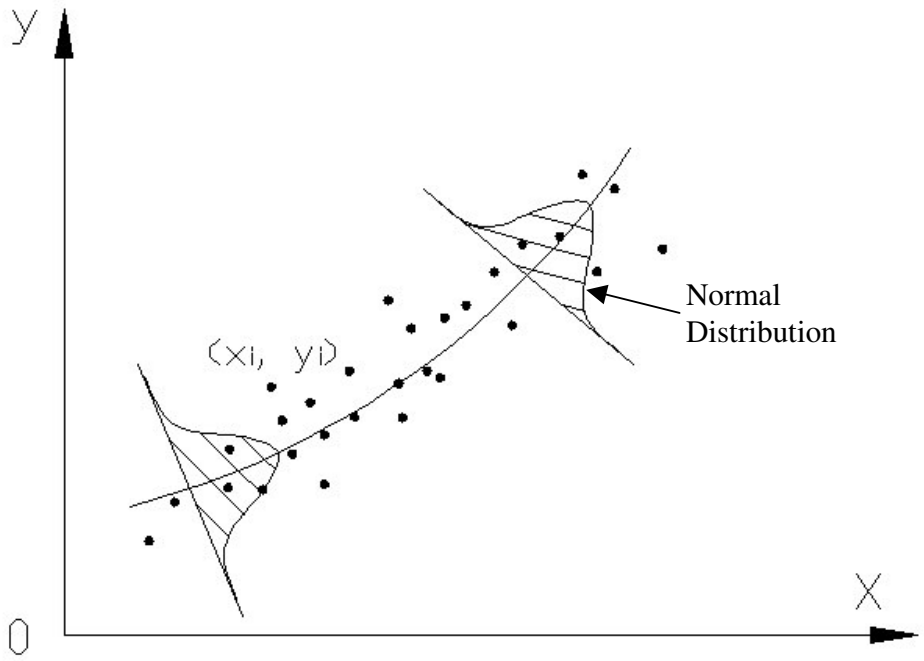

Figure 5-14. Spread of Data around the Best-fit Regression Curve.

5.5 Fragility Curves for Bridge Components

Nonlinear time history analyses of 10 bridge samples are carried out for the multi-span continuous and multi-span simply supported steel bridges using 100 simulated earthquake ground motions. Each bridge sample is subjected to 10 different ground motions selected to cover a wide range of PGAs. Hence, a total of 100 analysis cases are performed for each of the two types of bridges. For each of the 100 analysis cases, maximum response quantities of bridge components and estimated capacities of bridge

samples at various damage states are collected. Both linear and quadratic regressions are then performed between the logarithm of demand to capacity ratio, and ln(PGA). Using linear regression equations, the parameter λ, which is the mean of $\ln(S_d/S_c)$, is expressed as a function of PGA,

$$\lambda = a\ln(PGA) + b \tag{5-10}$$

Similarly, λ can be obtained by quadratic regression as,

$$\lambda = \mathrm{a}(\ln(\mathrm{PGA}))^2 + \mathrm{b}\ln(\mathrm{PGA}) + \mathrm{c} \tag{5-11}$$

In Eqs. (5-10) and (5-11), a, b and c are the regression coefficients. The standard deviation for the regression curves is obtained as,

$$\varsigma = \sqrt{S_r/(n-2)} \tag{5-12}$$

The coefficient of determination r^2 gives an indication of the "fit" strength of the regression equation and is expressed as,

$$r^2 = 1 - \frac{S_r}{S_t} \tag{5-13}$$

where S_t is the sum of the squares of the residuals with respect to the average, and S_r is the sum of squares of the residuals with respect to the regression line. For example, $S_t = \sum_{i=1}^{n}(y_i - \bar{y})^2$, $\bar{y} = \frac{1}{n}\sum_{i=1}^{n} y_i$; and $S_r = \sum_{i=1}^{n}(y_i - \lambda_i)^2$ for the scattered points (x_i, y_i) of Fig. 5-14. Once parameters λ and ς have been obtained through regression analysis, fragility curves can be developed as a function of PGA by Eq. (5-9) which is repeated here

$$P_f = \phi(\frac{\lambda}{\varsigma}) \tag{5-9}$$

Fragility Curves for Multi-span Continuous (MSC) Steel Bridge

Fig. 5-15 (a) to (d) present plots of linear and quadratic regressions of column curvature ductilities as a function of PGAs for the piers in the first multi-column bent of the MSC steel bridge for four levels of damage to bridge columns corresponding to exceeding the critical curvatures $\phi_y^{'}$, ϕ_y, ϕ_d, and ϕ_u. Fig. 5-15 (e) and (f) are the regression plots for expansion bearing displacement as a function of PGAs at the instant of instability in the bearings.

Fig. 5-16 shows fragility curves for piers and bearings in the multi-span continuous bridge. It is observed from Fig. 5-16 (a) that the median PGAs (corresponding to 50% probability of capacity exceedance) for the damage states of first yielding of longitudinal reinforcement ($\phi_y^{'}$), formation of the plastic hinge (ϕ_y), beginning of strength degradation (ϕ_d) and concrete crushing (ϕ_u) in bridge piers are 0.60g, 0.66g, 1.07g and 1.48g, respectively. The median PGA for bearing instability is around 1.24g for both the high type rocker and low type sliding bearings. The fragility curves for the two types of bearings in Fig. 5-16 (b) almost overlap, although their regression equations and standard deviations in Fig. 5-15 (e) and (f) are different.

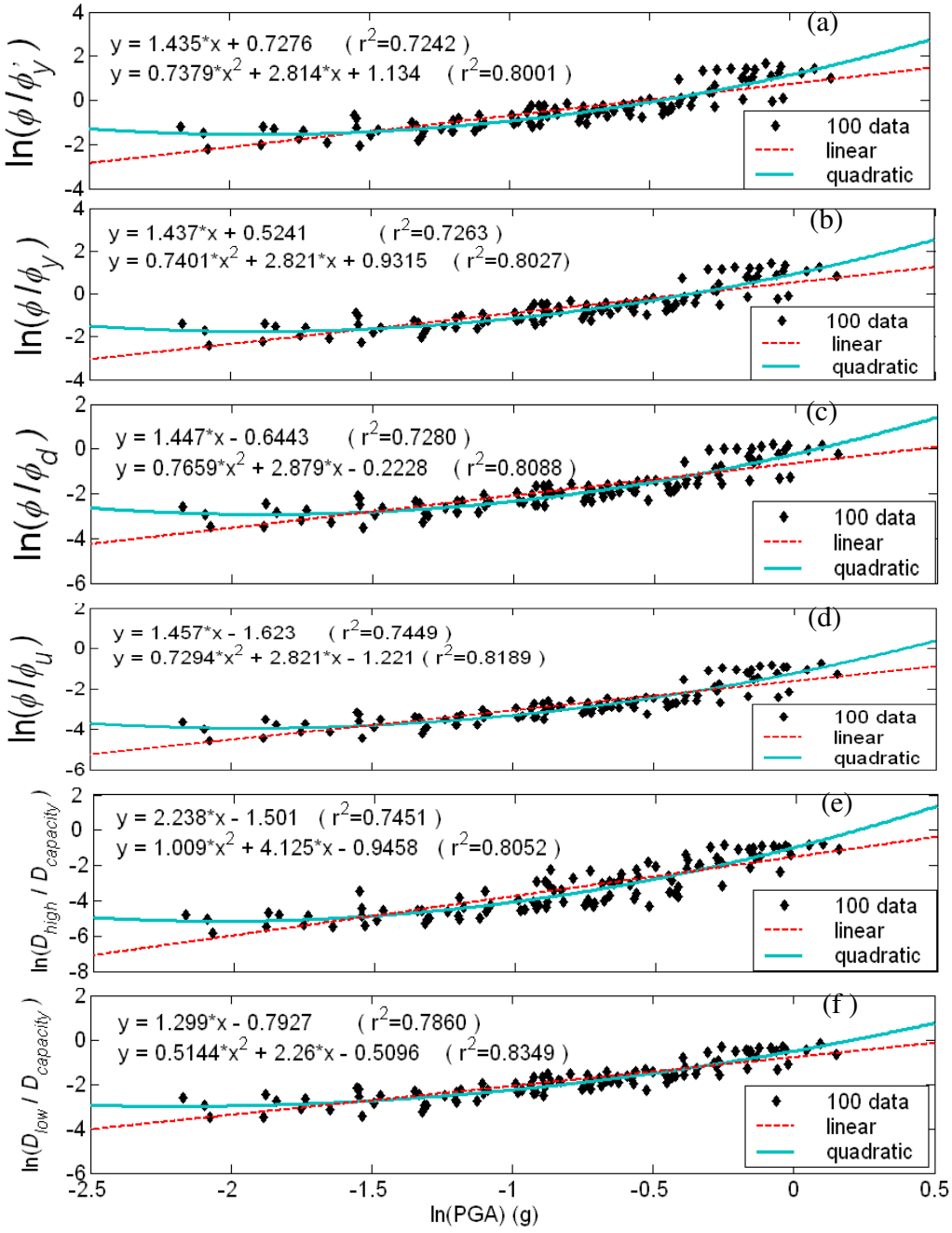

Figure 5-15. Linear and Quadratic Regression Analyses of Component Ductility in MSC Bridge (a) Pier Curvature $\phi_y^{'}$; (b) Pier Curvature ϕ_y; (c) Pier Curvature ϕ_d; (d) Pier Curvature ϕ_u; (e) High Type Rocker Bearing Displacement Limit 153 mm; (f) Low Type Sliding Bearing Displacement Limit 102 mm.

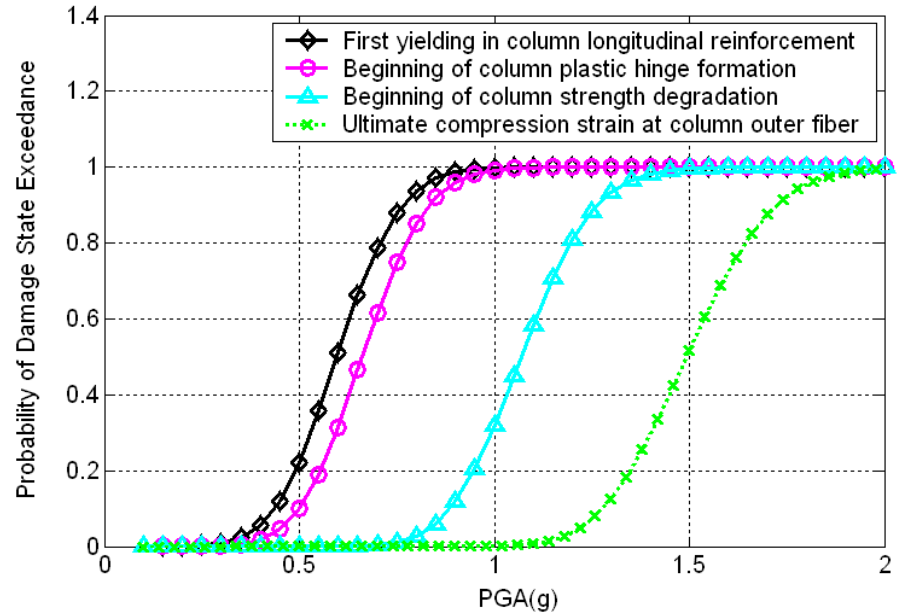

(a) Piers in Multi-Span Continuous Bridge

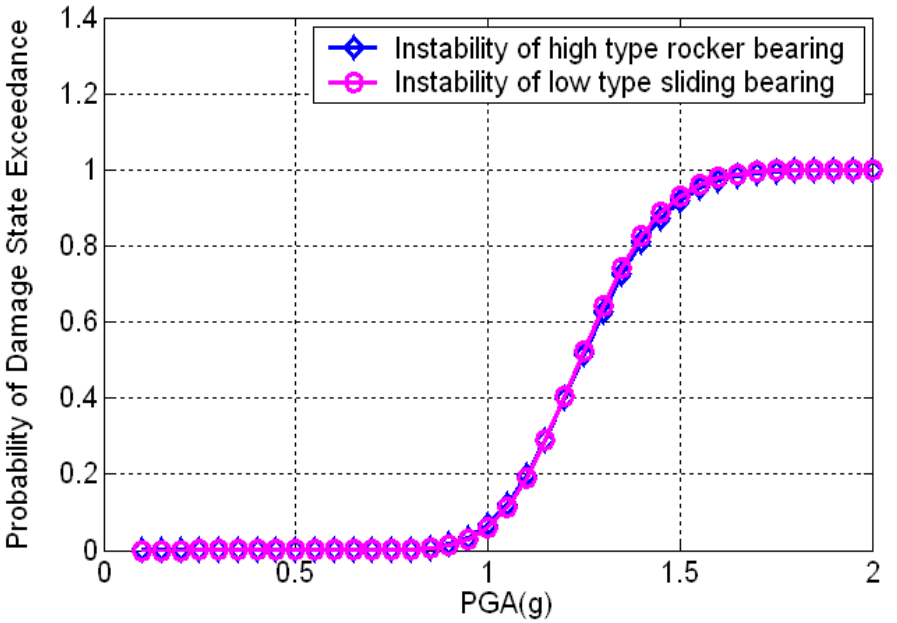

(b) Expansion Bearings in Multi-Span Continuous Bridge

Figure 5-16. Fragility Curves for Individual Components versus PGA for Multi-Span Continuous Bridge.

Fragility Curves for Multi-Span Simply Supported (MSSS) Steel Bridge

It has been observed from the results of nonlinear time history analysis for the MSSS bridge samples that piers in the first multi-column bent have slightly larger curvature than piers in the second column bent for most of the 100 cases of analyzed. Hence, piers in the first multi-column bent have higher risk of damage. Figs. 5-17 (a) to (d) show regression analysis results for the ratio of demand to capacity of column curvature as a function of PGAs for piers in the first multi-column bent. For high type fixed bearings, the largest deformation occurs in the fixed bearings located at the left abutment. Displacement capacities of the fixed bearing are 20 mm and 40 mm for the initiation of bond fracture and wide rocking of bearings with extensive cracking/spalling in the concrete pedestal, respectively. Figs. 5-18 (a) and (b) show regression plots for these two damage states of the bearings. Likewise, there are three sets of high type rocker bearings supported by the first column bent, the second column bent and the right abutment in the multi-span simply supported bridge. Figs. 5-19 (a), (b) and (c) show regression plots for the damage ratio of these bearings as a function of PGA when bearing instability is induced.

From the regression plots of Figs. 5-15, and 5-17 to 5-19 for the two types of bridges, it is observed that the quadratic regression results in a better fit to bridge response quantities than the conventionally used linear regression as manifested by the larger values of the coefficient of determination r^2 for quadratic regressions case. Hence, the quadratic regression approach presented in this research will yield more reliable fragility curves than the linear regression approach.

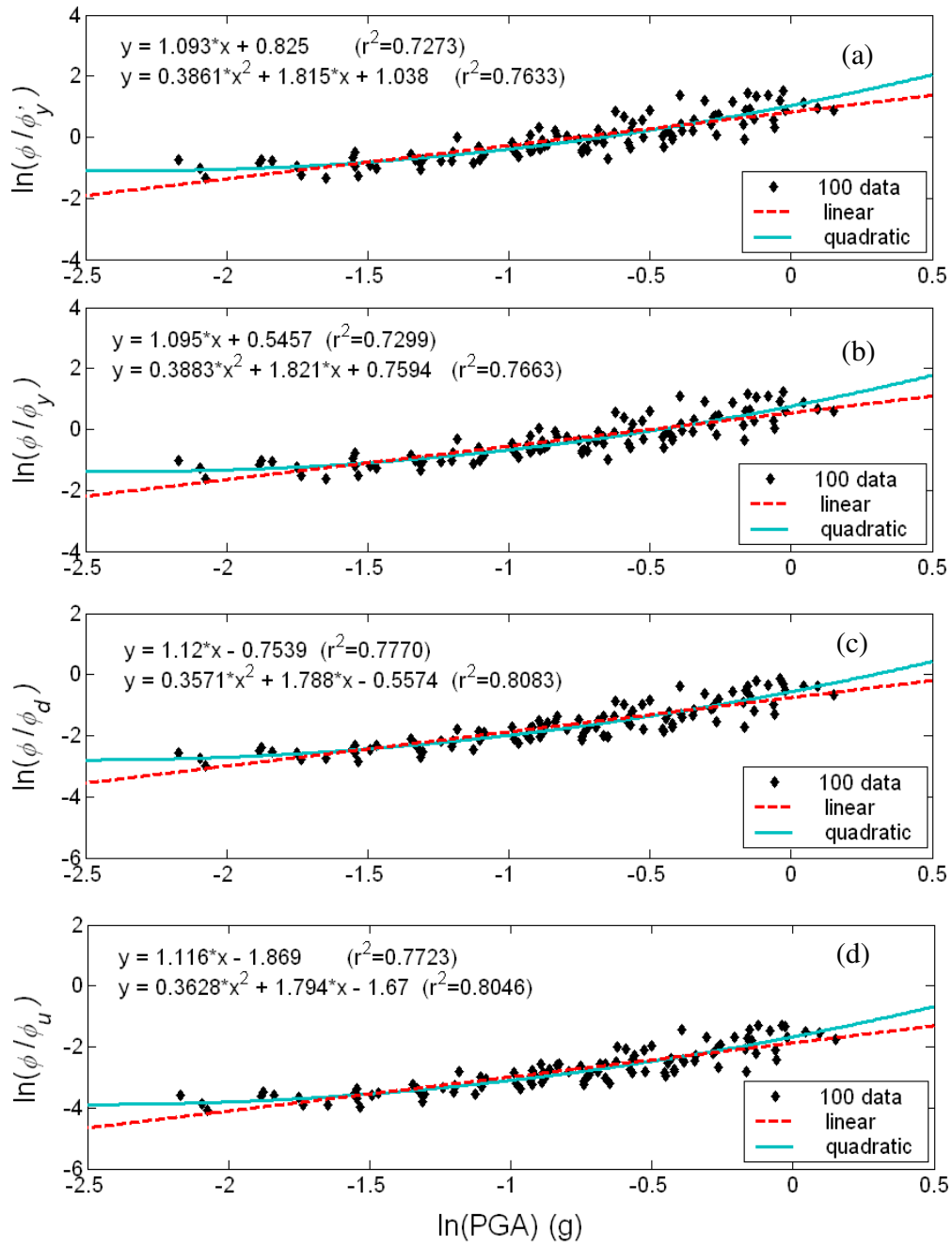

Figure 5-17. Linear and Quadratic Regression Analyses of Pier Curvature Ductility in MSSS Bridge (a) Pier Curvature $\phi_y^{'}$; (b) Pier Curvature ϕ_y; (c) Pier Curvature ϕ_d; (d) Pier Curvature ϕ_u.

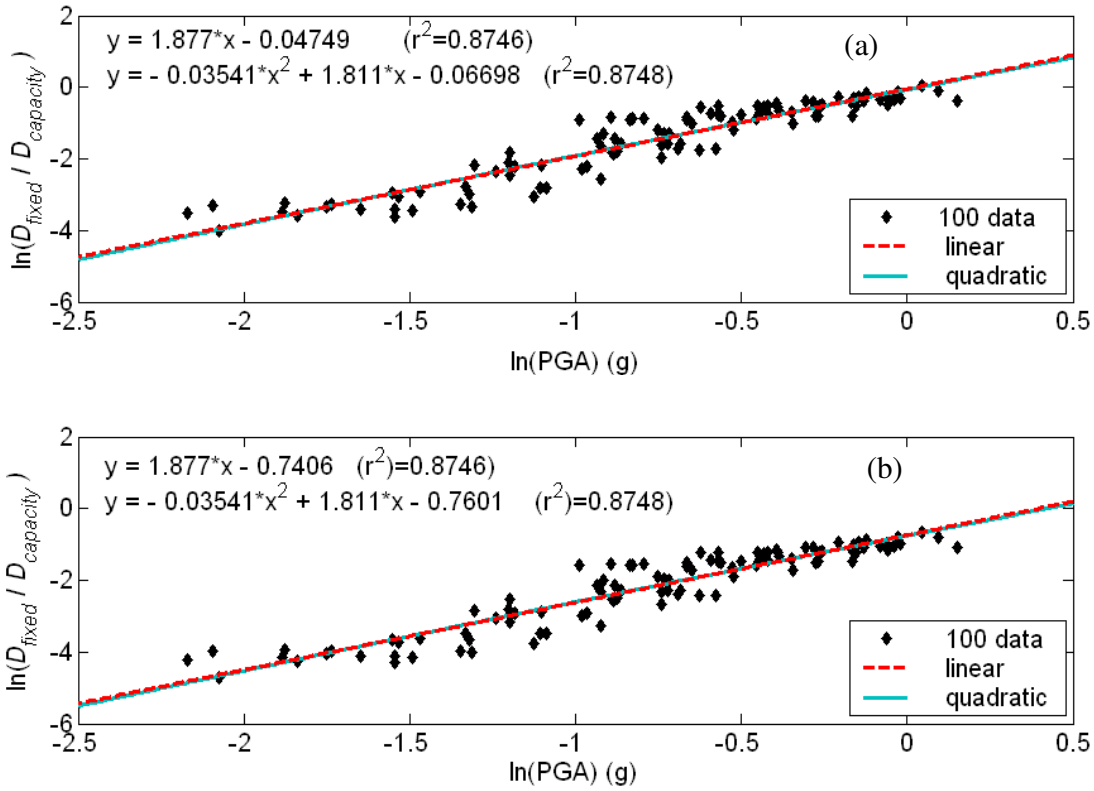

Figure 5-18. Linear and Quadratic Regression Analyses of High Type Fixed Bearing Displacement Ductility in MSSS Bridge; (a) Displacement Limit 20 mm; (b) Displacement Limit 40 mm.

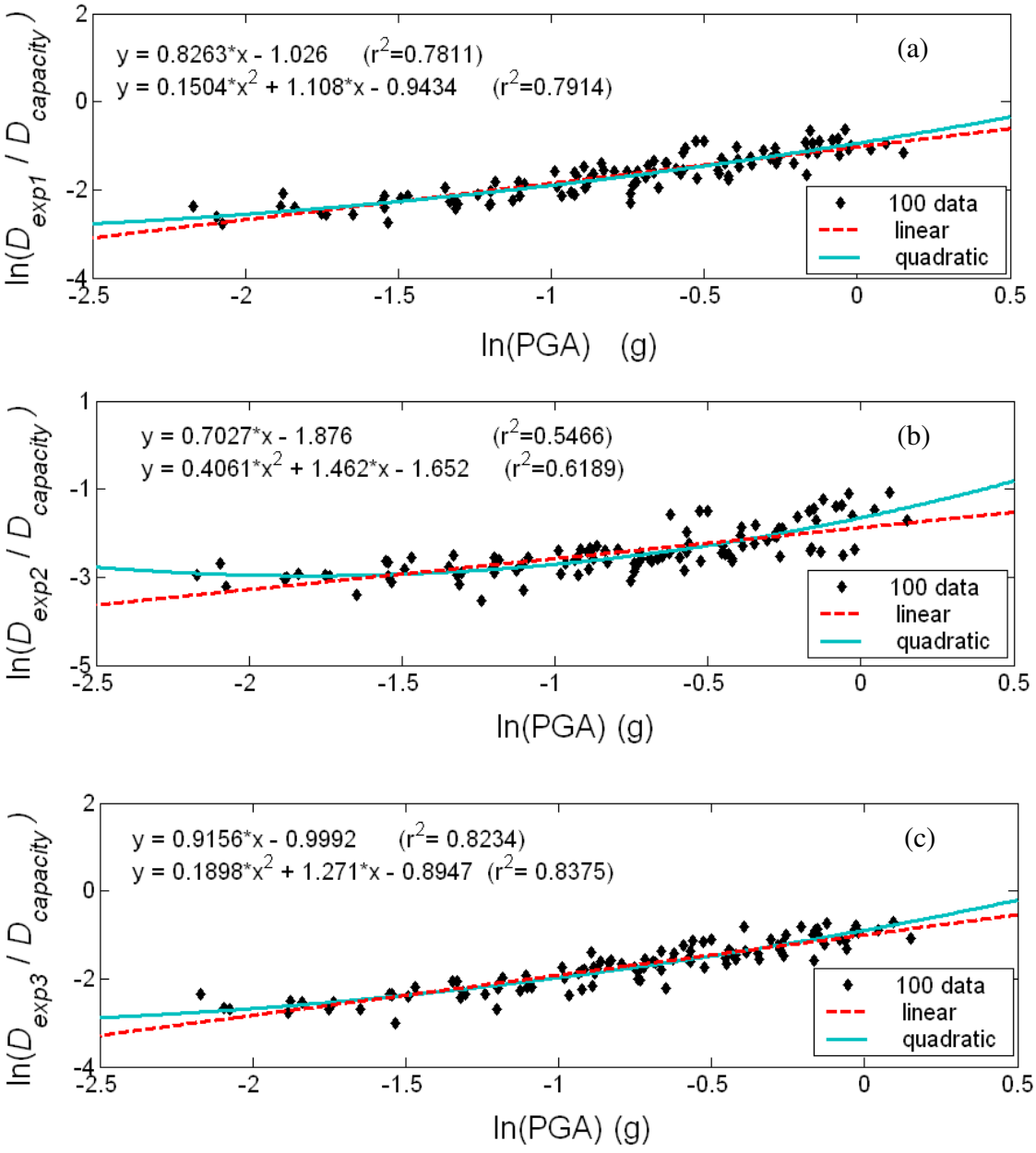

Figure 5-19. Linear and Quadratic Regression Analyses of High Type Rocker Bearing Displacement Ductility in MSSS Bridge with Displacement Limit 102 mm; (a) Expansion Bearings on 1st Column Bent; (b) Expansion Bearings on 2nd Column Bent; (c) Expansion Bearings on Right Abutment.

Fig. 5-20 shows fragility curves for the piers and bearings of the multi-span simply supported bridge. It is observed from Fig. 5-20 (a) that the median PGAs (with 50% fragility) are 0.51g, 0.63g, 1.34g for the first three damage levels to bridge columns, expressed in terms of the ductilities $\phi_y^{'}$, ϕ_y and ϕ_d, respectively. The probability of ultimate collapse of a bridge column expressed in terms of reaching the ductility ϕ_u is approximately 20% at 2.0g PGA. Hence, columns of multi-span simply supported bridges in New York State are unlikely to suffer complete collapse during a likely earthquake in this region. Thus, multi-span simply supported bridges are found to be even safer than multi-span continuous bridges in terms of strength degradation and crushing of concrete in piers.

Fig. 5-20 (b) shows fragility curves for high type fixed bearings, which are mounted on the left abutment in the multi-span simply supported bridge. Two damage states are evaluated for this bridge: (i) Beginning of bond failure of anchor bolts, resulting in stiffness and strength degradation of high type fixed bearings, and (ii) wide rocking of bearings with extensive cracking/spalling of concrete pedestals. PGAs for 50% probability of exceeding these two damage states (i.e., median PGAs) are 1.04g and 1.52g, respectively. Fig. 5-20 (c) shows fragility curves of high type rocker bearings supported by the first column bent, the second column bent and the right abutment for damage state corresponding to instability of these bearings. It is observed that expansion bearings mounted on the right abutment have the largest risk of failure among these three sets of bearings. However, the risk of instability of expansion bearings is very low for this type of bridge, even under a very strong earthquake. The time history analysis results reveal that the shear deformations of high rocker expansion bearings in MSSS bridge are

much lower than those in MSC bridges. This is due to smaller spans that exert smaller forces on the bearings.

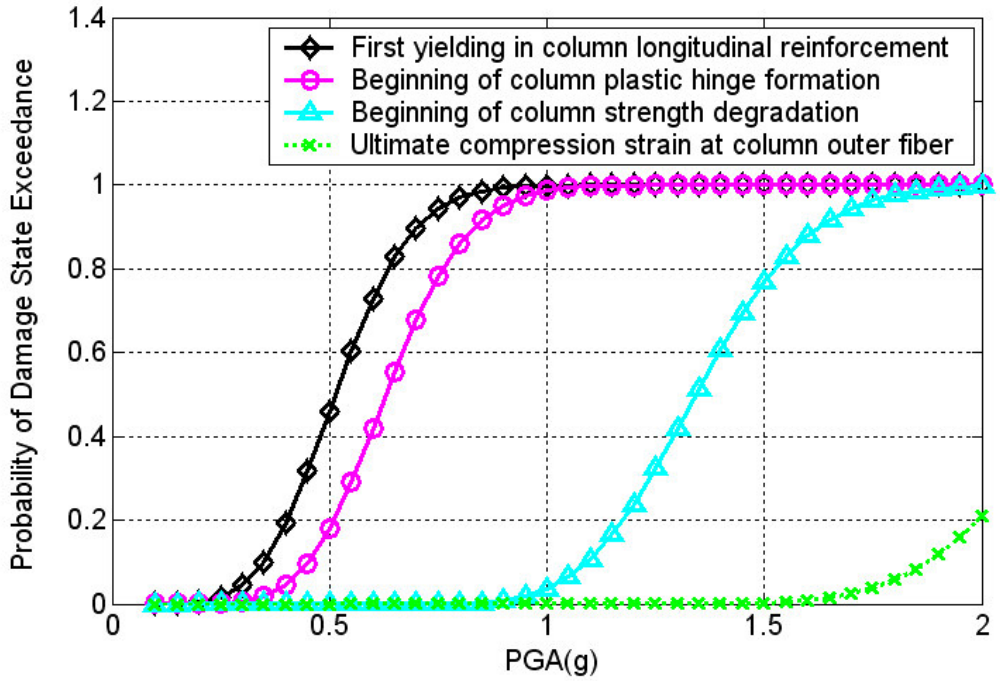

(a) Piers in MSSS Bridge

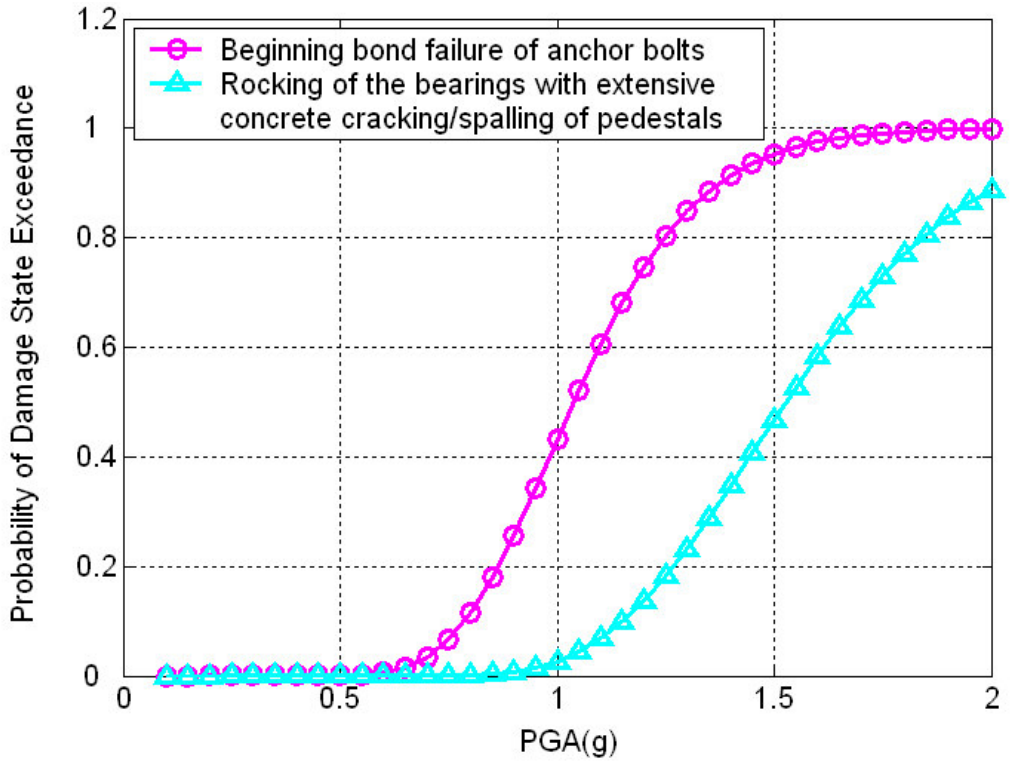

(b) Fixed Bearings in MSSS Bridge

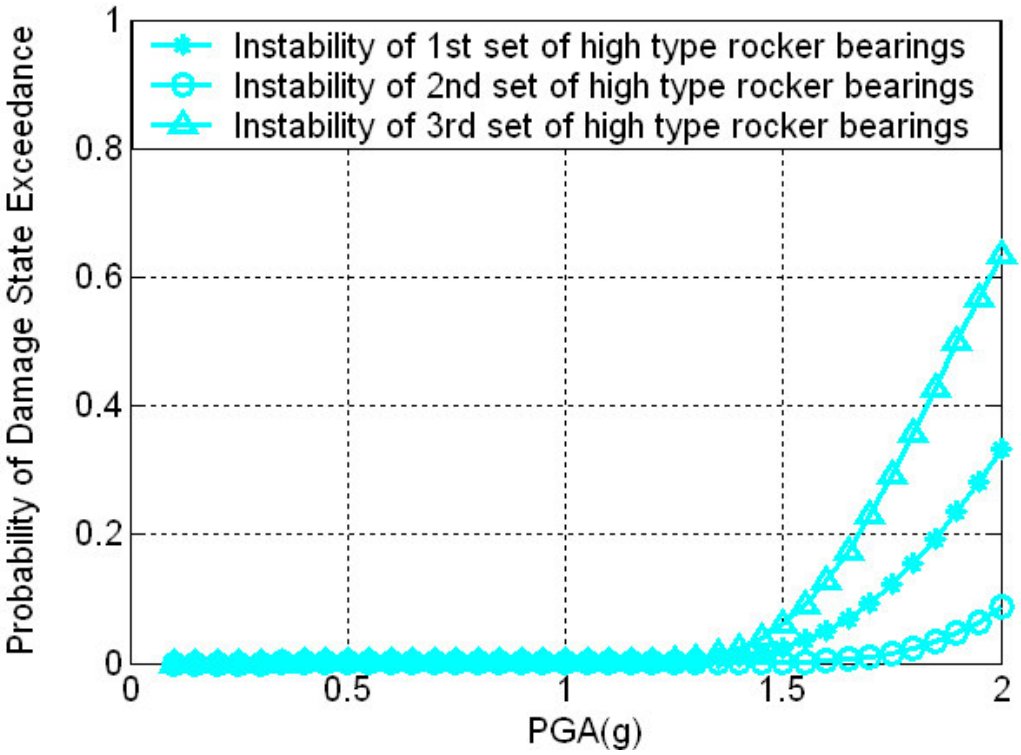

(c) High Type Rocker Bearings in MSSS Bridge

Figure 5-20. Fragility Curves of the Components in MSSS Bridge

5.6 Fragility Surfaces of Bridge Components

In general, data on earthquake moment magnitude and epicentral distance are more readily available and more representative characteristics than PGA. Hence, the relationship between seismic fragility of highway bridges and the (M_w, R) pairs for an earthquake at a site would be more meaningful. Since 100 pairs of (M_w, R) are selected from the USGS database to simulate 100 earthquake time histories, multivariate regression analyses could be used to develop relationships between $\ln(S_d/S_c)$ and ($\ln M_w$, $\ln R$) pairs in the form,

$$\lambda = a + b\ln(M_w) + c\ln(R) \tag{5-14}$$

where λ is the mean values of $\ln(S_d/S_c)$ which is assumed to be normally distributed around the inclined regression plane. Coefficients *a*, *b* and *c* in Eq. (5-14) are determined by the least-square method. The standard deviation for the regression plane is obtained from

$$\varsigma = \sqrt{S_r/(n-3)} \tag{5-15}$$

Fragility surfaces for each specific damage-state can be computed using Eq. (5-9) with the calculated λ and ς values for potential seismic events within the practical range of $M_w \le 7.5$ and $R \ge 10$ for New York State. It has been observed that the coefficient of determination r^2 has larger values for the multivariate regression in M_w and R than those for linear and quadratic regressions for PGA's. This implies that the multivariate regression $\ln(S_d/S_c)$ as function of M_w and R has better fit to scattered data for

$\ln(S_d/S_c)$. Hence, fragility surfaces are likely to give better estimates of fragilities than fragility curves as functions of PGA.

Fragility Surfaces for Multi-span Continuous (MSC) Steel Bridge

Fig. 5-21 (a) to (d) show multivariate regression results of column curvature ductility as functions of $\ln M_w$ and $\ln R$ for the multi-span continuous bridge. Fig. 5-21 (e) and (f) show multivariate regression planes for displacement of the expansion bearings at the damage state of instability. The inclined regression plane is a function of both R and M_w. By comparing Fig. 5-21 with Fig. 5-15, it is observed that the coefficients of determination (r^2) for multivariate regressions are larger than those for linear and quadratic regressions.

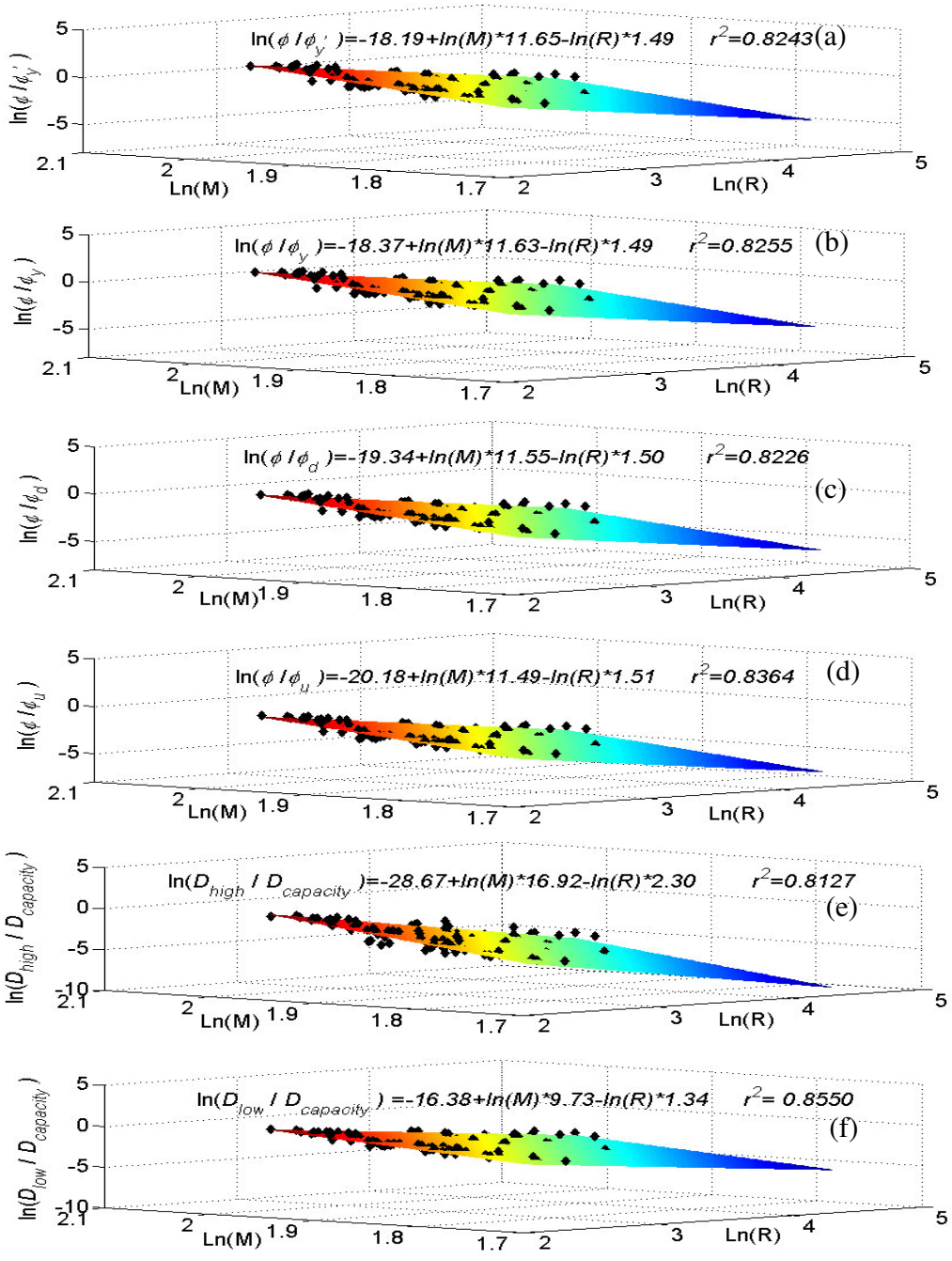

Figure 5-21. Multivariate Regression Analysis of Component Ductility for MSC Bridge as a function of M_w and R in km; (a) Pier Curvature $\phi_y^{'}$; (b) Pier Curvature ϕ_y; (c) Pier Curvature ϕ_d; (d) Pier Curvature ϕ_u; (e) High Type Rocker Bearing Displacement Limit 153 mm; (f) Low Type Sliding Bearing Displacement Limit 102 mm.

Figs. 5-22 (a) to (d) show fragility surfaces of bridge piers. As expected, the fragility increases with a decrease in R and an increase in M_w. Within a practical range of $M_w \leq 7.5$ and $R \geq 10$ for this region, the maximum fragility for exceeding curvatures $\phi_y^{'}$ and ϕ_y can reach 100%, while the maximum fragilities for exceeding curvatures ϕ_d and ϕ_u are 88% and only 9% for the among most probable earthquakes in the New York State. The range of M_w and R that would lead to a certain failure probability can be determined more clearly by plotting fragility surfaces and fragility contours. For example, it is observed that Fig. 5-23 has contour curves for 10%, 50% and 90% probabilities of exceeding the curvature ϕ_y. The hatched area in Fig. 5-23 gives the range of earthquake magnitudes and epicentral distances that may cause the formation of plastic hinges in piers with more than 50% probability of exceeding the curvature ϕ_y. Alternatively, given an earthquake with known magnitude, the fragility can be determined by cutting a section through the fragility surface to obtain a fragility curve for different distances to the epicenter. For example, curves in Fig. 5-24 (a) are obtained by cutting sections in fragility surface of Fig. 5-22 (b) at M_w = 7.4, 7.0, 6.6, and 6.2. Fig. 5-24 (a) shows that the probability of forming a plastic hinge in a pier decreases sharply with increasing epicentral distance, and bridges farther than 50 km from epicenter are quite safe. This distance is relatively shorter than that observed for sites in the Western United States. This happens because the high frequency contents in earthquakes in Northeastern United States die off with distance more rapidly than low frequency contents observed in earthquake records from Western United States. Contour plots can also be used to determine damage probabilities for different earthquake magnitudes at a

particular site as shown in Fig. 5-24 (b). The complete system damage could either be due to bearing instability or/and column collapse. Fig. 5-25 (a) and (b) show fragility surfaces for bearings for damage states corresponding to instability in high type rockers and low type sliding bearings, respectively. It is observed that the maximum probabilities of collapse due to these two types of bearings are 58% and 68%, respectively. Hence, from the fragility surface analysis, it is observed that low type sliding bearings can cause higher risk of instability as compared to high type rocker bearings. In fact, the instability of the high type rocker bearings will have more severe consequences, since relatively tall bearings could tip over and cause the superstructure to drop a considerable distance to fall off of the bridge seat [NYSDOT (2002)].

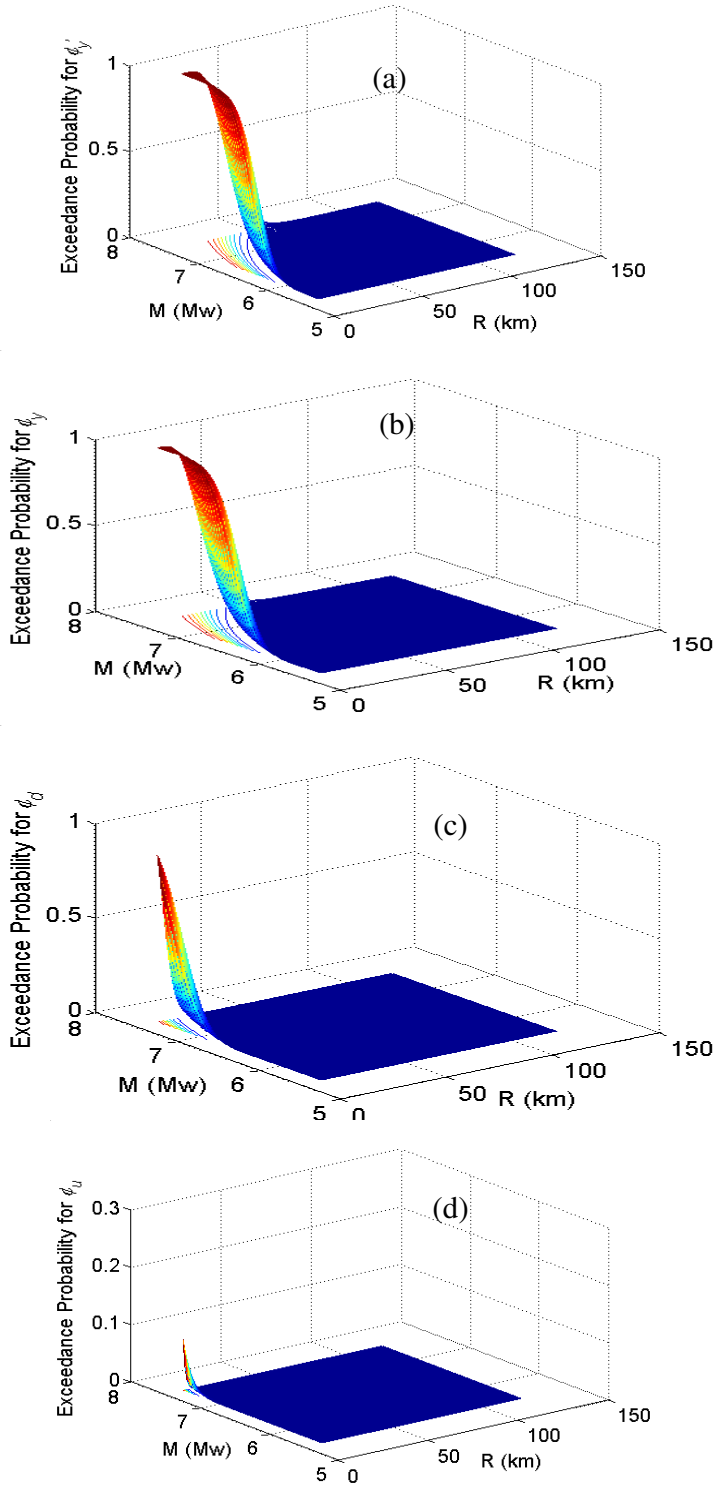

Figure 5-22. Fragility Surfaces of Bridge Piers in MSC Bridge at Different Damage States; (a) Pier Curvature $\phi_y^{'}$; (b) Pier Curvature ϕ_y; (c) Pier Curvature ϕ_d; (d) Pier Curvature ϕ_u.

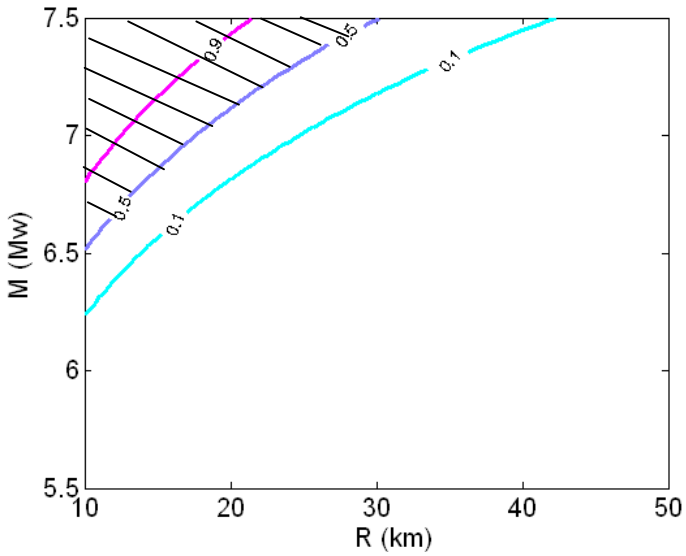

Figure 5-23. Contour Map of Bridge Piers in MSC Bridge for Probability of Exceeding ϕ_y

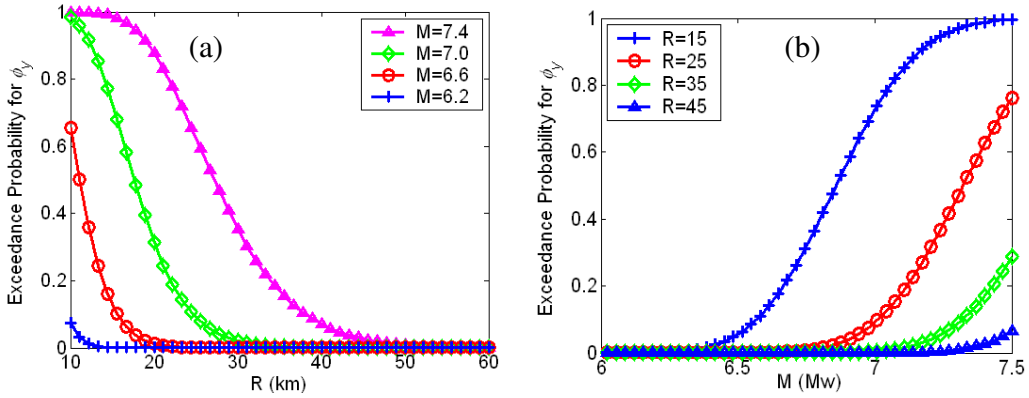

Figure 5-24. Cut Sections in Fragility Surface for Probability of Exceeding ϕ_y of Piers in MSC Bridge.

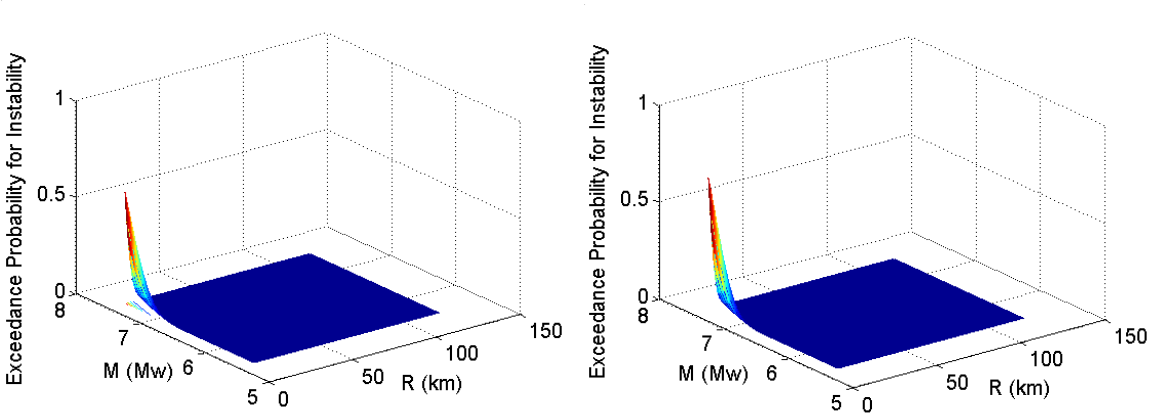

(a) High Type Rocker Bearing (b) Low Type Sliding Bearing

Figure 5-25. Fragility Surfaces for Instability of Expansion Bearings in MSC Bridge.

Fragility Surfaces for Multi-span Simply Supported (MSSS) Steel Bridge

Figs. 5-26 (a) to (d) show multivariate regression curves for the ratios of curvature demand to capacity of the bridge piers in the first multi-column bent. Figs. 5-27 (a) to (d) show fragility surfaces for the pier of multi-span simply supported bridge. It is observed that the maximum fragility for exceeding curvatures $\phi_y^{'}$ and ϕ_y can reach 100%, while the maximum fragilities for exceeding curvatures ϕ_d is only 46%, which is much lower than the 88% value observed for the piers in the multi-span continuous bridge for the same damage state. There is very small or negligible risk of ultimate failure of piers of typical multi-span simply supported bridges subject to probable earthquakes in New York State because of the shorter span lengths of bridges. The observation from the fragility surface for ultimate collapse in Fig. 5-26(d) is consistent with the results of the PGA fragility curve in Fig. 5-20 (a).

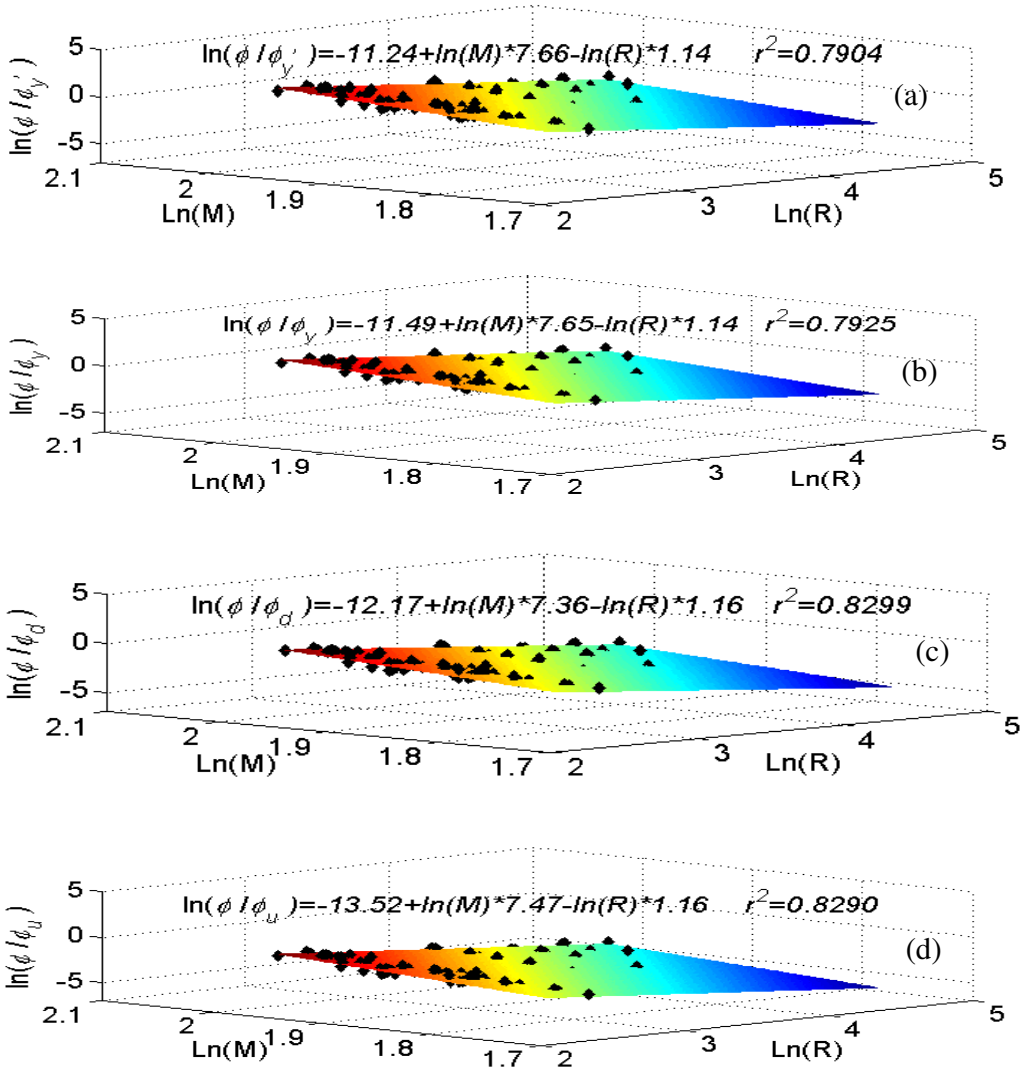

Figure 5-26. Multivariate Regression Analyses of Pier Curvature Ductility in MSSS Bridge; (a) Pier Curvature $\phi_y^{'}$; (b) Pier Curvature ϕ_y; (d) Pier Curvature ϕ_d; (e) Pier Curvature ϕ_u.

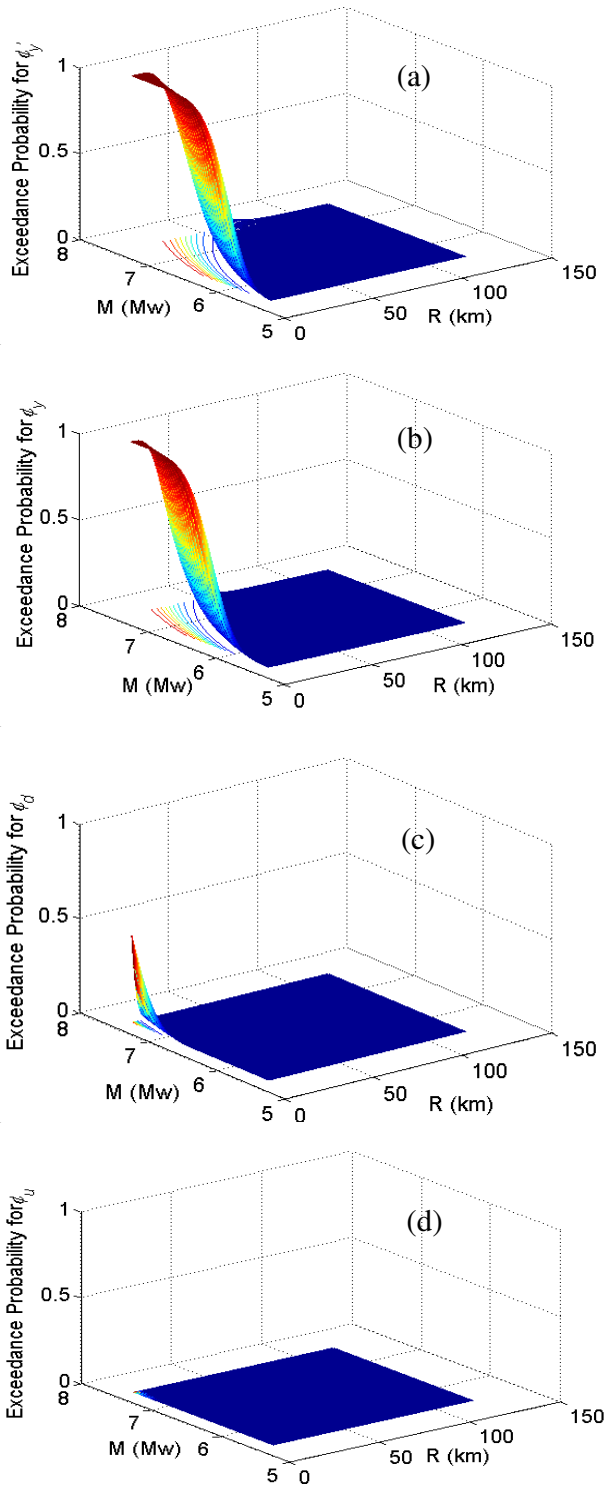

Figure 5-27. Fragility Surfaces of Bridge Piers in MSSS Bridge at Different Damage States; (a) Pier Curvature $\phi_y^{'}$; (b) Pier Curvature ϕ_y ; (c) Pier Curvature ϕ_d ; (d) Pier Curvature ϕ_u .

Figures 5-28 (a) to (b) present regression results for the deformation of the high type fixed bearing for the two damage states discussed earlier. Figures 5-29 (a) and (b) show fragility surfaces corresponding to the same two damage states. It is observed that the maximum probability of exceedance is 98% and 72% for these two damage states. These values are higher than those obtained for the high type fixed bearings shown in Fig. 5-20. Fig. 5-30 (a), (b) and (c) show regression analysis results for the high type expansion bearings at the first column bent, the second column bent and the right abutment at the start of instability. From the fragility surfaces for these three sets of bearings, it is observed that the fragility of expansion bearings is quite low. Although the third set of bearings (on the right abutment) has the largest deformation, the maximum probability of instability is still lower than 2%, as shown in Fig. 5-31.

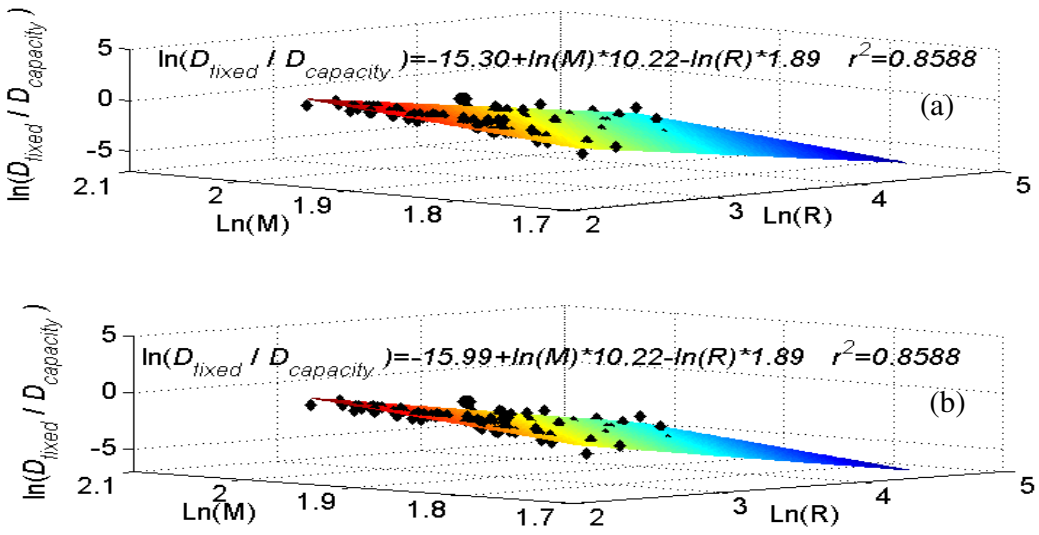

Figure 5-28. Multivariate Regression Analyses of High Type Fixed Bearing Displacement Ductility in MSSS Bridge (R in km); (a) Displacement Limit 20 mm; (b) Displacement Limit 40 mm.

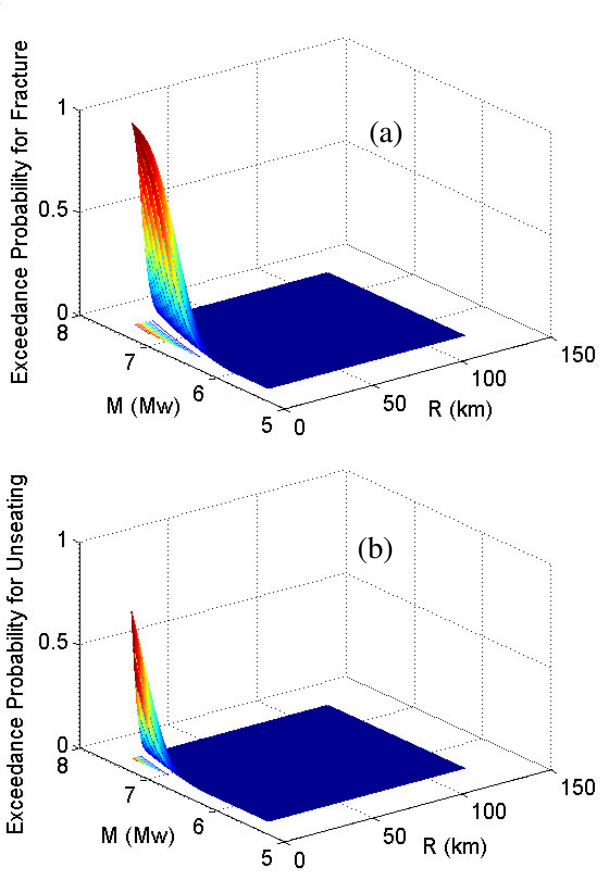

Figure 5-29. Fragility Surfaces of High Type Fixed Bearings in MSSS Bridge at Different Damage States; (a) Bond Fracture of Anchor Bolt; (b) Rocking of Bearings with Extensive Concrete Cracking/Spalling of Pedestals.

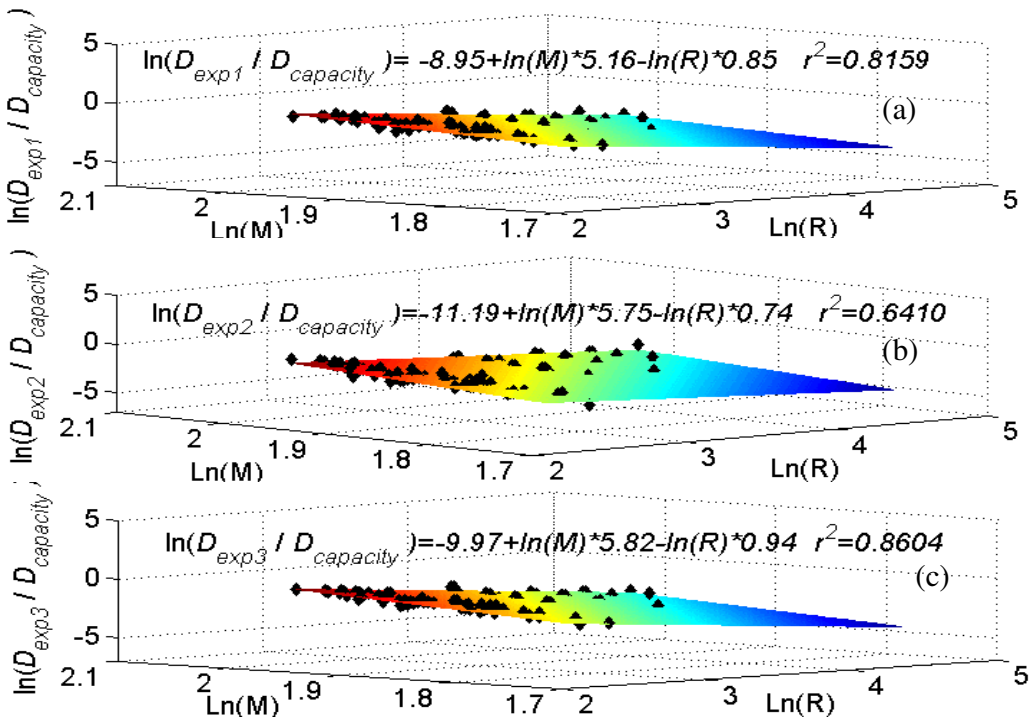

Figure 5-30. Multivariate Regression Analyses of High Type Rocker Bearing Displacement Ductility in MSSS Bridge with Displacement Limit 102 mm (R in km); (a) Expansion Bearings Mounted on 1st Column Bent; (b) Expansion Bearings Mounted on 2nd Column Bent; (c) Expansion Bearings Mounted on Right Abutment.

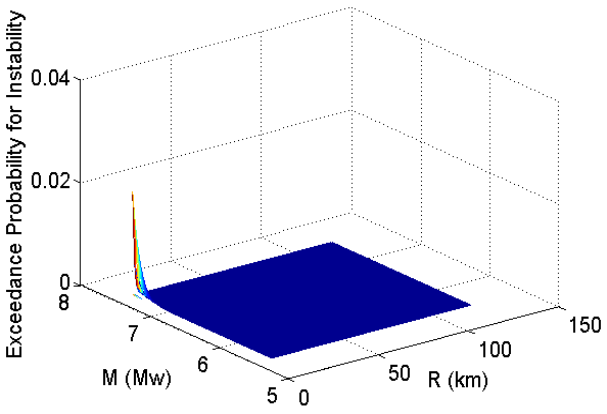

Figure 5-31. Fragility Surfaces for Instability of High Type Rocker Bearings in MSSS Bridge

5.7 Fragility of Bridge Systems

Since the collapse of a pier and/or the loss of bearing supports will lead to the collapse of the bridge structural system, their fragility curves/surfaces should be combined to obtain the seismic fragility for the collapse of the bridge.

First-order Reliability Bounds

The first-order upper and lower bound estimates of the probability of failure ignore the possible correlation between these failure modes and can be expressed as, [Cornell (1967), Kottegoda and Rosso (1997)]:

$$\max_{i=1}^{m} \left[P(F_i)\right] \leq P_{sys} \leq 1 - \prod_{i=1}^{m} \left[1 - P(F_i)\right] \tag{5-16}$$

where $P(F_i)$ is the probability of failure in mode i. For independent failure modes, the system failure probability can be represented by the product of the mode survival

probabilities. In the case where all failure modes are fully dependent, the weakest failure mode will always be the most likely to fail.

For the multi-span continuous bridge, the first three damage levels of columns (rebar yielding, plastic hinge forming, and strength degrading) are predominant among all the components and could control the safety of the whole bridge. However, the ultimate damage states of high type rocker bearings (rocking off masonry plate) and low type sliding bearings (sliding off masonry plate) have higher fragility than the piers in concrete crushing. The fragility of the three modes should be combined, since either failure model will make the bridge fail. The combined fragility curve for the ultimate damage state of bridge is shown in Fig. 5-32 with the upper and lower bounds producing a median PGA being between 1.15g and 1.24g.

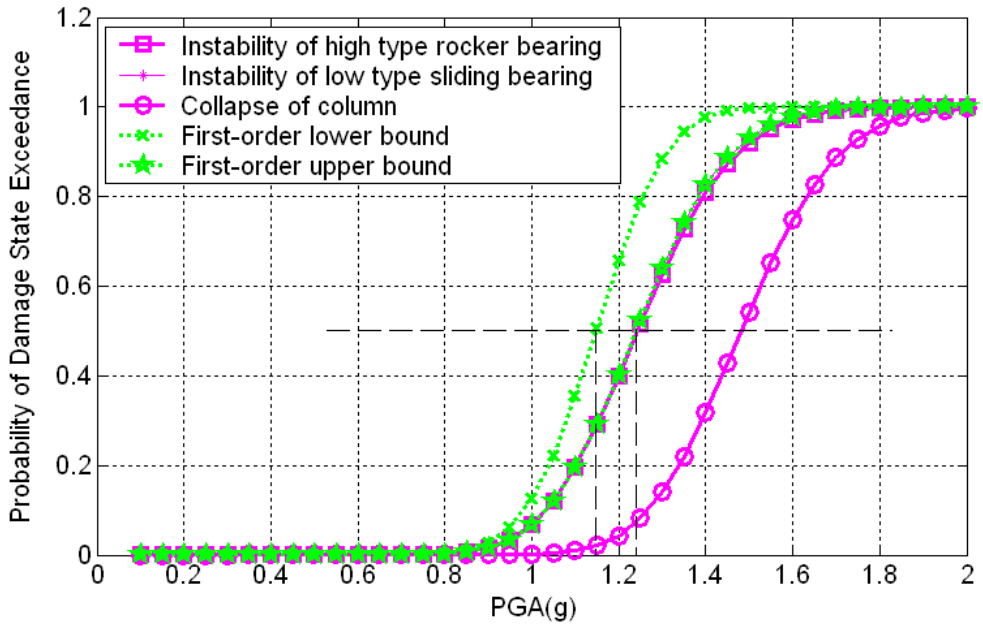

Figure 5-32. Fragility Curve Bounds for MSC Bridge at Ultimate Damage State by First-order Reliability Method .

For the multi-span simply supported bridges, multiple extensive damage states (piers strength degrading and fixed bearing bond fracture) should be combined to find the fragility of the whole bridge.

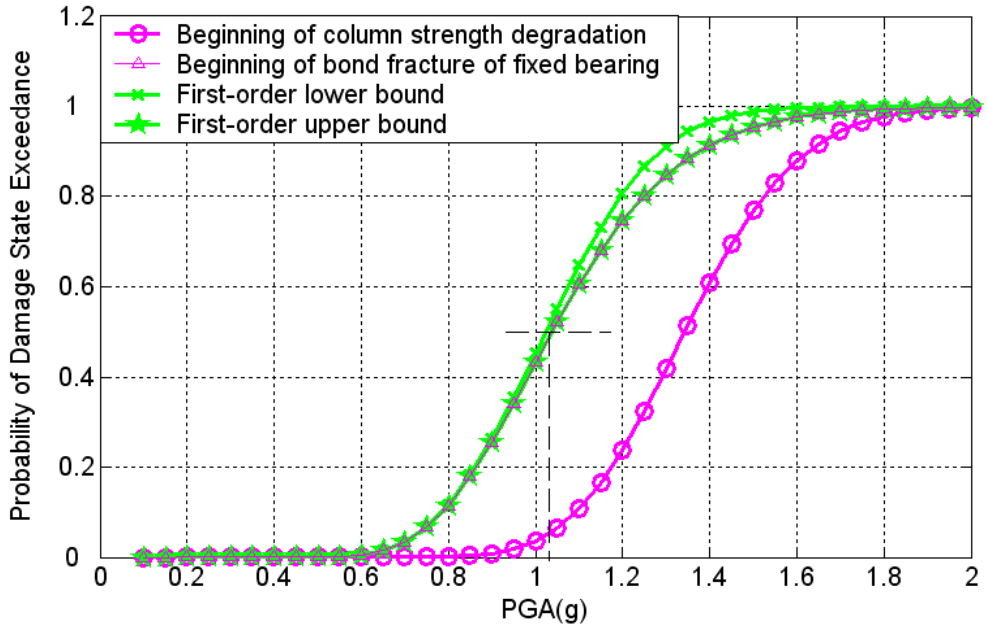

Figure 5-33. Fragility Curves for MSSS Bridge at Extensive Damage State by First-order Reliability Method.

As shown in Fig. 5-33, the bounds on the median PGAs corresponding to extensive damage state are from 1.02g to 1.04g for the MSSS Steel bridge. The bounds are close since the risk of extensive damage of the fixed bearing is far more dominant than extensive damage in the piers. Further, the ultimate damage state of piers (concrete crushing), high type fixed bearings (wide rocking of the bearing due to extensive concrete cracking/spalling on pedestals), and high type rocker bearings (rocking off the rocker from the masonry plate) should be considered as the ultimate multiple failure modes of the multi-span simply supported bridges, as shown in Fig. 5-34. The bounds for median

PGAs are close, i.e., from 1.50g to 1.52g, for the multi-span simply supported bridge to reach ultimate failure with 50% probability. At this probability of exceedance, the risk to the high type fixed bearing practically controls this collapse limit state for the whole bridge system.

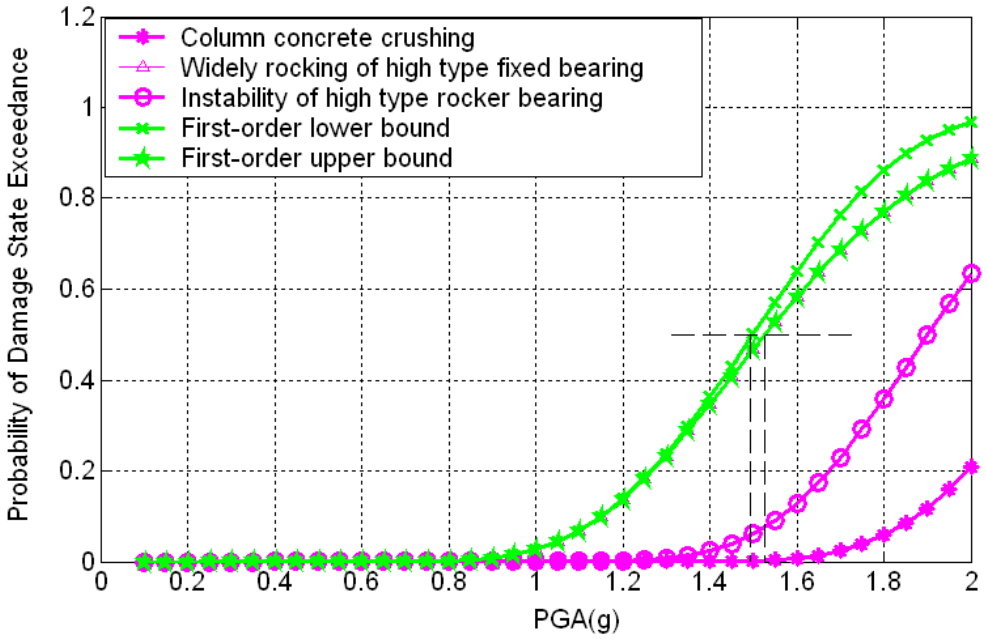

Figure 5-34. Fragility Curves for MSSS Bridge at Ultimate Damage State by First-order Reliability Method.

Second-order Reliability Bounds

As an alternative method to the first-order bounds, considering that the different multiple failure modes may be correlated, a narrower gap between the lower and upper bounds can be obtained using the second order bounds [Melchers (1999)]. For example, the lower bound for the combination of three limit states becomes:

$$p^{-} = p(F_1) + [p(F_2) - p(F_2 \cap F_1)]^{+} + [p(F_3) - p(F_3 \cap F_1) - p(F_3 \cap F_2)]^{+} \quad (5\text{-}17)$$

In Eq. (5-17), $[\quad]^{+} \equiv \max(\quad, 0)$, where F_i denotes the event "failure of the structure due to failure in the *i* th mode", and $(F_i \cap F_j)$ is the event that failure occurs in both the *i* the and *j* th modes. Simultaneously, the second-order upper bound is expressed as

$$p^{+} = p(F_1) + p(F_2) + p(F_3) - [p(F_2 \cap F_1)]^{+} - [p(F_3 \cap F_1), p(F_3 \cap F_2)]^{+} \quad (5\text{-}18)$$

where the joint probability between F_i and F_j is defined as

$$p(F_i \cap F_j) = p(\frac{S_{di}}{S_{ci}} \geq 1, \ and \ \frac{S_{dj}}{S_{cj}} \geq 1) = p(\ln(\frac{S_{di}}{S_{ci}}) \geq 0, \text{ and } \ln(\frac{S_{dj}}{S_{cj}}) \geq 0) \quad (5\text{-}19)$$

The joint probability in Eq. (5-19) is obtained by double integration of the joint bivariate normal density function between two variates x_i and x_j [Ang and Tang (1975)]

$$f_{Xi,Xj}(x_i, x_j) = \frac{1}{2\pi\sigma_{x_i}\sigma_{x_j}\sqrt{1-\rho^2}} \exp\left[\frac{-1}{2(1-\rho^2)}\left\{\left(\frac{x_i - \mu_{x_i}}{\sigma_{x_i}}\right)^2 - 2\rho\left(\frac{x_i - \mu_{x_i}}{\sigma_{x_i}}\right)\left(\frac{x_j - \mu_{x_j}}{\sigma_{x_j}}\right) + \left(\frac{x_j - \mu_{x_j}}{\sigma_{xj}}\right)^2\right\}\right]$$

with correlation coefficients being defined as

$$\rho = \frac{COV(X_i, X_j)}{\sigma_i \sigma_j} = \frac{E[(X_i - \mu_i)(X_j - \mu_j)]}{\sigma_i \sigma_j} \quad (5\text{-}20)$$

In Eq. (5-20), $X_i = \ln(S_{di}/S_{ci})$, and $X_j = \ln(S_{dj}/S_{cj})$, μ_i and μ_j are the mean values expressed by the regression equations of X_i and X_j as a function of PGA. In Eq. (5-20), σ_i and σ_j are the standard deviations of X_i and X_j.

For example, the second-order reliability method could be applied for the multi-span continuous bridge at the ultimate damage state. The analysis results show that the joint probability between instability of the bearings and column collapse is much less than the joint probability between failures in two kinds of bearings. This observation

implies that the second-order bounds in Eq. (5-17) and Eq. (5-18) are quite close and a single estimate for the second order fragility can be approximately obtained as,

$$p \approx p(F_1) + p(F_2) + p(F_3) - [p(F_2 \cap F_1)]^+ \tag{5-21}$$

where F_1 and F_2 are two kinds of expansion bearing failure events, and F_3 is the column collapse failure event. Fig. 5-35 shows the second order bound with system failure occurring at a median PGA of 1.19g falling between the First-order bounds.

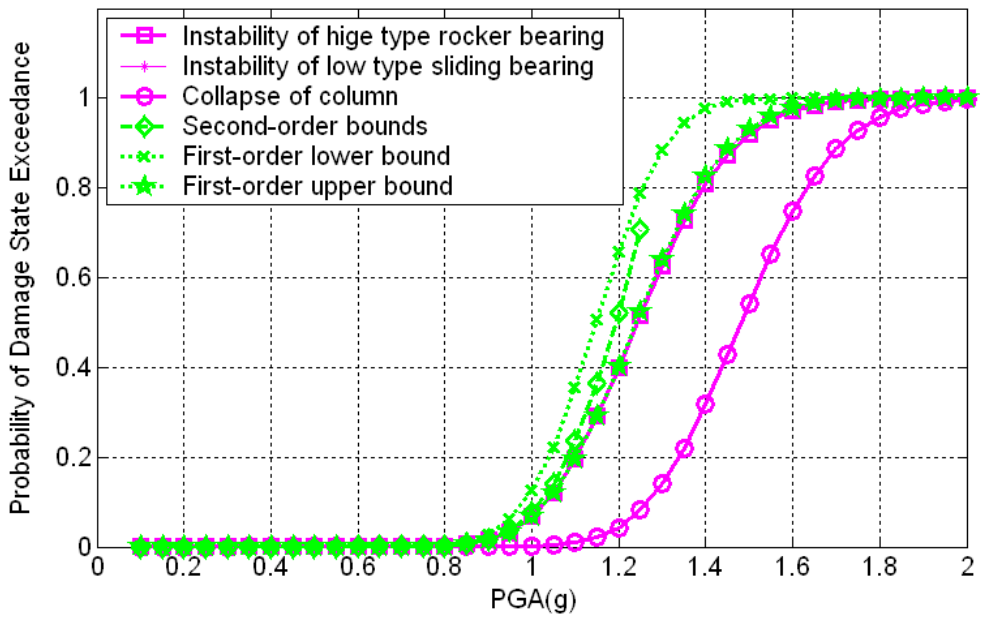

Figure 5-35. Fragility Curves for MSC Bridge at Ultimate Damage State by Second-order Reliability Method.

Similarly, the combined fragility surface for the MSC system collapse can also be obtained using the second-order bounds, as shown in Fig. 5-36, with the maximum probability being 87%.

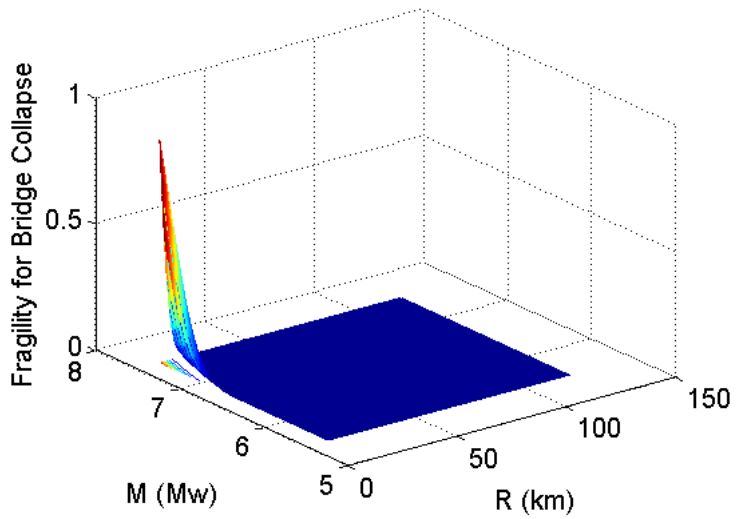

Figure 5-36. Fragility Surface for MSC Bridge Collapse by Second-order Reliability Method.

In Summary, fragility curves for the multi-span continuous bridge are shown in Fig. 5-37, by defining the bridge slight damage as initiation of longitudinal rebar yielding in piers, the bridge moderate damage as the formation of plastic hinge in piers, the bridge extensive damage as the pier strength degradation, and the bridge ultimate damage as the pier collapse and/or bearing instability. For the multi-span continuous bridge, median PGAs (corresponding to 50% probability of capacity exceedance) are 0.60g, 0.66g, 1.07g and 1.19g for the slight damage, moderate damage, extensive damage, and ultimate damage limit state. The fragility curves for the multi-span supported simply bridge are shown in Fig. 5-38, by defining the bridge slight damage as initiation of longitudinal rebar yielding in piers, the bridge moderate damage as the formation of plastic hinge in piers, the bridge extensive damage as the pier or fixed bearing strength degradation, and the bridge ultimate damage as the pier collapse, expansion bearing instability and/or the

wide rocking of fixed bearings due to concrete crushing of pedestals. The corresponding median PGAs for the multi-span simply supported bridge are 0.51g, 0.63g, 1.02g, and 1.50g for these four damage states. Hence, compared with MSSS bridges, MSC bridges are generally more susceptible to a severe seismic event. Retrofitting should focus more on preventing the extensive and ultimate damages of MSC bridges that are most affected by the performance of bridge piers and high type rocker bearings. Although, the multi-span simply supported bridges are found to be safer than multi-span continuous bridges in terms of strength degradation and crushing of concrete in piers, the most critical component for MSSS bridge is the high type fixed bearings. The bond failure and wide rocking of the high type fixed bearings will lead to the change of connection condition between superstructure and substructure, and thus cause severe damage to bridge structures.

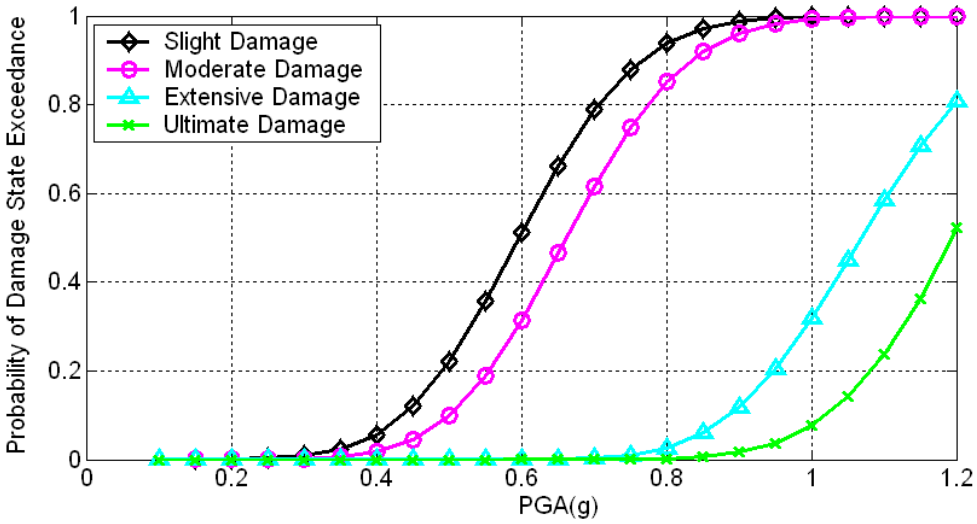

Figure 5-37. Fragility Curves for MSC Bridge System.

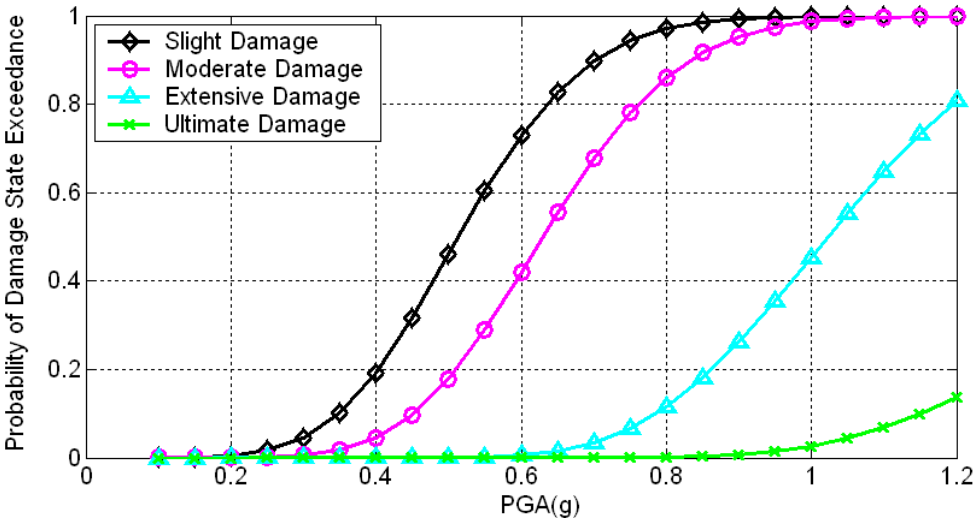

Figure 5-38. Fragility Curves for MSSS Bridge System

5.8 Modeling Uncertainties

The fragility analysis performed in the previous sections of this Chapter accounted for the uncertainty in estimating the critical parameters including the earthquake characteristics, weight of the superstructure, gap size, friction coefficient of expansion bearings as well as the material properties for concrete and steel reinforcement. However, another main source of uncertainty is known as modeling uncertainty, which represents our limited ability to properly model the behavior and capacity of a structure even when the material and geometric properties are perfectly known. Such modeling uncertainties are also known as epistemic uncertainties, which are distinguished from the aleatory uncertainties that are associated with the material and structural properties. Modeling uncertainties are very difficult to estimate, as they require extensive sets of data, which are not readily available in the case of the models used in this study. Specifically, modeling uncertainties should be included to consider the differences in the actual behavior of the bridge columns as compared to the assumed moment-curvature models used in the previous sections. Similarly, and perhaps more importantly, the models used to represent the behavior of the bearings were taken from the design specifications provided by the vendors and their associates. These specifications normally make approximate and conservative assumptions on the behavior that are adequate for design purposes but not necessarily valid for actual safety assessment and reliability evaluations. Although in most situations, the application of the approximate models lead to conservative evaluations, if the models are associated with high levels of uncertainties, it is possible to run into cases where the conservative bias is not sufficient to compensate for the effect of the modeling uncertainties.

To illustrate the potential errors that the omission of the modeling uncertainties may produce, a simple example is used in this section to study the change in the fragility of the MSC bridge before and after considering modeling uncertainties in the ultimate curvature ductility capacity. Based on previous experimental work, researchers have found that the actual ductility capacity of bridge columns may vary with a COV of 35% from the mean estimated value. To account for modeling uncertainties in the reliability analysis, it is common to introduce a modeling variable herein designated as, λ, which gives the ratio of the actual capacity (which is a random variable) to the mean capacity. For this example, the mean of λ for ductility capacity is taken as 1.0 and its COV=35%. This λ is treated as a random variable with a normal distribution and it is included in the LHS sampling and pairing. The time history analysis is repeated as explained before with the original five random variables to obtain the seismic demand for the MSC bridge. The ductility demand is then compared to the ductility capacity for each bridge sample. The regression analysis is executed to establish the relationship between $\ln(S_d/S_c)$ and the logarithm of the earthquake PGA. The regression results show that the curve obtained after including the modeling variable, λ, is similar to that previously calculated without considering λ, as shown in Fig. 5-39. However, the dispersion coefficient changes from $\varsigma = 0.398$ to $\varsigma = 0.561$ which has a large effect on the probability of failure. For example, as shown in Fig. 5-40, for earthquakes having a PGA =1.2g, the fragility for column collapse will change from 4.3% if the modeling uncertainties are ignored to 11.5% when λ is included. Although this may not be very significant for this bridge type in the New York site, such differences may be magnified for other locations and bridges which may have been under-designed or that may have deteriorated over time. It is noted

that in this example the mean value of λ is taken as 1.0. It is possible that the models used may have in-built safety factors which may compensate for the increase in fragility. However, this cannot be ascertained without a rigorous analysis of all the uncertainties associated with all the structural and material models used to calculate the seismic demand as well as the seismic capacities. Such an analysis of modeling uncertainties is outside the scope of this thesis and relegated to future research.

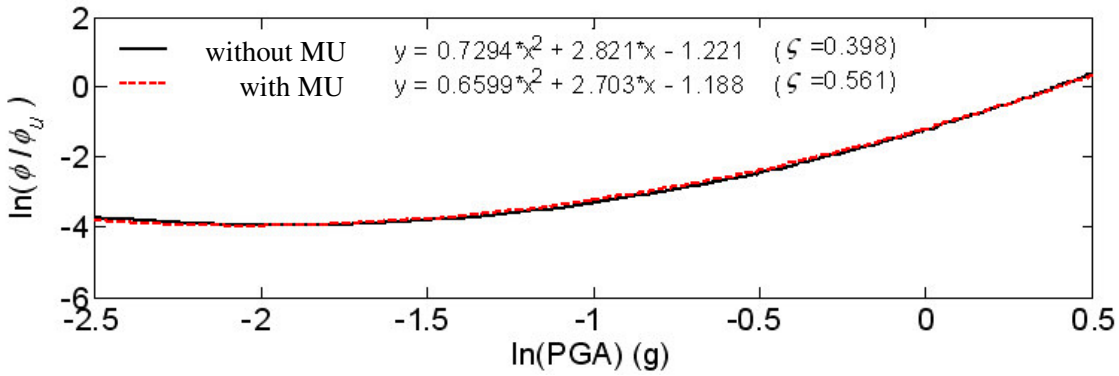

Figure 5-39. Comparison of Regression Curves for MSC Bridge with and without Modeling Uncertainties (MU).

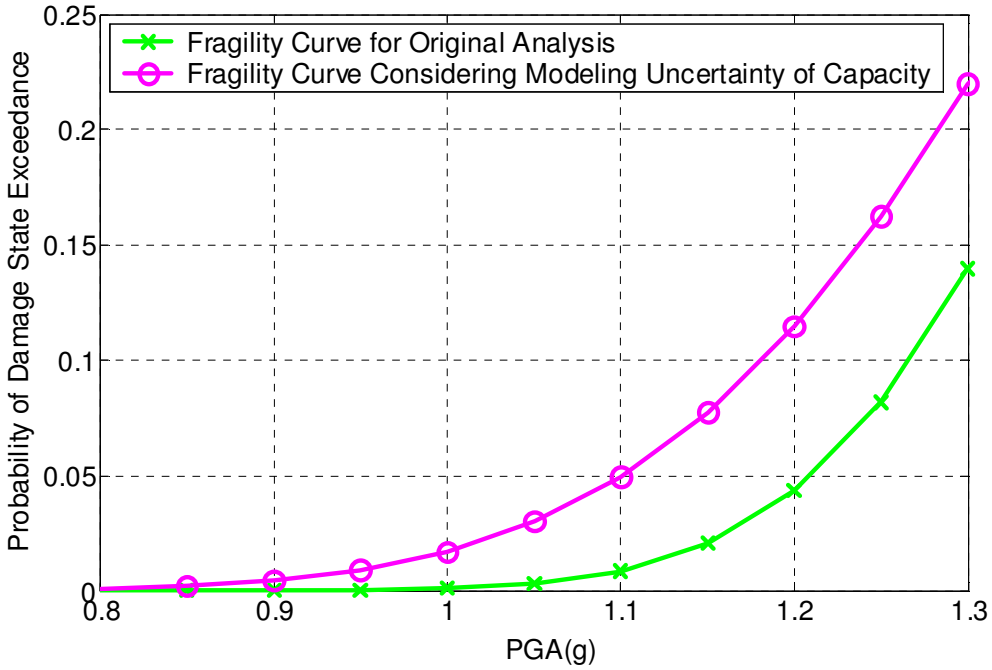

Figure 5-40. Comparison of Fragility with and without Modeling Uncertainty in Column Ductility Capacity.

CHAPTER 6

SEISMIC RETROFIT OF BRIDGES

6.1 Retrofit Measures Overview and Modeling

Bridge rehabilitation involves structural or functional upgrades to existing bridge components. Rehabilitation work can be classified as either minor or major. Minor rehabilitation addresses non-structural repairs. Major rehabilitation involves structural repair, and primary member replacement or strengthening [Maine DOT (2003)]. In general, the primary goal of seismic retrofitting of existing bridge components is to minimize the risk of collapse and/or severe structural damage of all or parts of a bridge to prevent the loss of the use of a vital transportation route passing over or under a bridge. Functionally, seismic retrofit is carried out by removing seismic deficiencies through an appropriate rehabilitation scheme, usually a major one.

The choice of a retrofit scheme should have clear economic implications. Acceptable and unacceptable types of damage should be quantified, since a compromise between cost and safety is always required. For example, flexural yielding is an acceptable damage for piers because it is visible and repairable. Unacceptable damage usually includes loss of girder support, column collapse, and connection failure [FHWA (1987)]. Hence, column capacity in terms of curvature ductility at the plastic hinge section needs to be large enough to avoid column collapse. A bearing failure may precipitate the loss of girder. Connections, like the fixed connection at a fixed steel bearing, are important in maintaining the overall integrity of the bridge. All of these

unacceptable types of damage should be paid extra attention in planning of appropriate retrofit strategies.

In this chapter, various optimal retrofit strategies are designed for typical bridge components in New York State to address structural vulnerabilities identified through the fragility analysis of Chapter 5. Retrofit schemes considered include the installation of elastomeric bearings or lead-rubber bearings, the installation of energy-dissipating devices, such as dampers, jacketing of bridge piers using fiber reinforced plastic (FRP), and introducing continuity in beams of multi-span bridges originally designed as simple spans.

6.1.1 Elastomeric Bearings

Elastomeric bearings have been used in the United States for the last four decades because of minimal maintenance requirements and low cost. Elastomeric bearings consist of thin steel laminated plates between elastomeric layers. Hence, they are flexible under shear stress, and stiff against volumetric changes under uniaxial compression. Stiff steel layers in the laminated elastomeric bearings also restrain lateral expansion of elastomer, which causes a large increase in compressive stiffness and improves the stability of bearings under horizontal load. Hence, a steel reinforced elastomeric bearing is able to support relatively large compressive loads while accommodating large translations and rotations. A bearing must be designed with reasonable elastomer layer thickness, number of layers and bearing shape factor so as to control the stress in the steel reinforcement and the strain in the elastomer. Fatigue, stability, delamination, yield and rupture of the steel reinforcement, stiffness of the elastomer, and geometric constraints must all be considered during the design. Detailed guidelines for elastomeric bearings, developed by

Standon and Roeder (1982), are available in AASHTO LRFD Specifications (1998). Simplified design methods for elastomeric bearings using spreadsheets have been developed by Standon and Roeder (1996).

Elastomeric bearings show a substantially linear response, governed essentially by the properties of rubber, bearing shape and size [Priestley et al. (1996), Roeder et al. (1987)]. The horizontal stiffness of elastomeric bearings is determined by,

$$K_h = \frac{GA}{h} \tag{6-1}$$

where G is the shear modulus of rubber, h is the total rubber height and A is the gross rubber area. Vertical stiffness of rubber is obtained as

$$K_z = \frac{6GS^2Ak}{(6GS^2 + k)h} \tag{6-2}$$

where k is the bulk modulus of rubber, taken as 2000 MPa (290 ksi) [Priestley et al. (1996)]. The shape factor, S, is a function of bearing plan dimensions ($L \times W$) and single rubber layer thickness h_{ri},

$$S = \frac{A}{2h_{ri}(L + W)} \tag{6-3}$$

Based on experiments, Roeder and Stanton (1991) have observed that the bearing compressive stiffness is approximately proportional to S^2, and shear deformation under horizontal force is essentially independent of the shape factor.

For the finite element models used in this study, elastomeric bearings are modeled using the link element with six independent springs, one for each degree of freedom [SAP2000 (2004)]. As a horizontally flexible and vertically stiff shear element, the

stiffness of two horizontal springs is determined by Eq. (6-1); the stiffness of the vertical spring by Eq. (6-2); and both torsional and rotational stiffness are taken as zero.

It is observed from Eqs. (6-1) and (6-2) that both horizontal and vertical stiffness of elastomeric bearings depend on the shear modulus, G. Uncertainty exists in the estimation of the shear modulus, G, of elastomer in bearings. Bearing manufacturers evaluate the elastomeric materials on the basis of Shore A Durometer hardness, although the shear modulus is the preferred means of specifying the elastomer. Based on the NYSDOT Standard Sheets of elastomeric bearings, all elastomers shall be 50-durometer hardness on the Shore A scale. For this specified hardness, the elastomer at 73^{o} F must have a shear modulus between 95 to 130 psi according to AASHTO LRFD Specifications (1998). This range is consistent with variations in shear modulus of elastomers found in practice.

Temperature dependent variations in elastomeric properties may be another significant source of uncertainty in the properties of elastomeric bearings. The extent depends upon the elastomer compound, temperature and the duration of exposure. Low temperature tests have shown that two types of low temperature stiffening, i.e. crystallization and instantaneous thermal stiffening, occur in elastomers. Crystallization is dependent on time and temperature and it occurs after the elastomer has been exposed to low temperatures on the order of 14^{o} F (-10^{o} C) for a period of days or weeks. Instantaneous thermal stiffening occurs very quickly (in a few hours) and normally results in a dramatic increase in stiffness at temperatures around -40^{o} F (-40^{o} C) because of glassification of rubber material [Roeder et al. (1989)]. New York State belongs to the low temperature zone C [AASHTO (1998)]. As mentioned in Chapter 4,

the temperature varies from -5^{o} F to 90^{o} F during a year in this region. Based on data collected by Rejcha (1964), it has been observed that there is no evident change in the shear modulus of 50-durometer hardness elastomer in the temperature range of -5^{o} F to 90^{o} F. Hence, the only uncertainty in shear modulus considered is due to the range of 95 to 130 psi specified in AASHTO LRFD (1998). This range will be considered for generating bridge samples with different elastomeric bearing properties.

6.1.2 Lead-Rubber Bearings

Lead-rubber bearings were first developed in New Zealand in 1975 [Skinner et al. (1993)] and have been used widely for seismic protection of bridges around the world. A lead-rubber bearing is a conventional elastomeric bearing modified by inserting a cylindrical lead plug in its center. The lead plug contributes high damping through energy-dissipating effects during strong earthquake and provides required rigidity under service loads. Using lead-rubber bearings between the superstructure and the substructure can result in a significant reduction in forces as compared to the non-isolated bridges, and can successfully overcome the shortcomings of elastomeric bearings because of decreased bearing deformation [Robinson (1982), Clark et al. (1993), Mori et al. (1999), Ghobarah and Ali (1988)]. Fig. 6-1 shows the shear force-displacement hysteretic loops of the same elastomeric bearing without and with a lead plug [Skinner et al. (1993)] in dashed and solid lines, respectively. The hysteresis loop of the elastomeric bearing is mainly elastic with shear stiffness of rubber and a small amount of hysteresis. The enclosed area in the figure is a measure of the energy dissipated during one cycle of motion. It is observed from Fig. 6-1 that the lead-rubber bearing has more energy-dissipating capability than the elastomeric bearing.

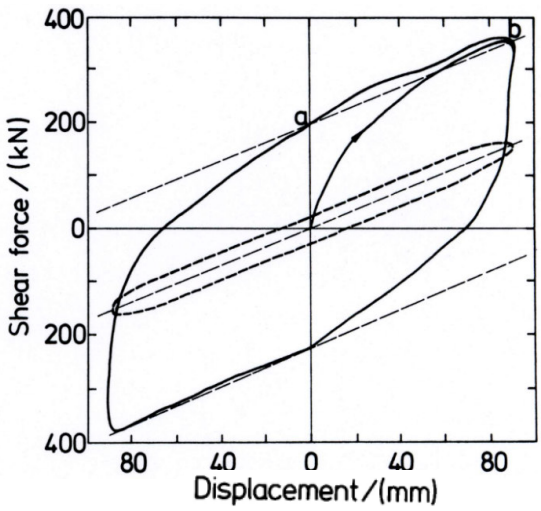

Figure 6-1. Dynamic Force-displacement Hysteresis Loop of Elastomeric Bearings and Lead-rubber Bearings.

Lead has a low yield shear strength ($\tau_y = 10.5$ MPa) and high initial shear modulus (130 MPa). It has been verified through experimental studies that lead possesses elastic-perfectly plastic behavior after yielding. Hence, the hysteretic behavior of lead-rubber bearings can be modeled by a bilinear curve as shown in Fig. 6-2. The curve is characterized by a yielding force, and pre- and post-yield stiffnesses. The total yield force of the bearing is contributed by lead core plasticity and rubber elasticity, i.e.,

$$F_y = F_{lead} + F_{rubber} \tag{6-4}$$

where $F_{lead} = \tau_y A_{lead}$, τ_y is the yield shear stress of the lead material, and A_{lead} is the section area of lead core; F_{rubber} is the shear force resisted by rubber, $F_{rubber} = K_{rubber} D_y$, i.e. the product of shear stiffness of rubber and the yield displacement of lead core. Here, the shear stiffness of rubber, K_{rubber}, is obtained as $K_{rubber} = G_{rubber}(A_{gross} - A_{lead})/h_{rubber}$ and the displacement D_y when the lead core yields, $D_y = F_{lead}/(G_{lead} A_{lead}/h_{lead})$. After

yielding, only the steel laminated elastomer will contribute to the post-yield stiffness of lead-rubber bearings. Hence, the shear force for a given displacement on the post-yield portion would be the sum of the elastic force of elastomeric bearing and the plastic force required to deform the lead core.

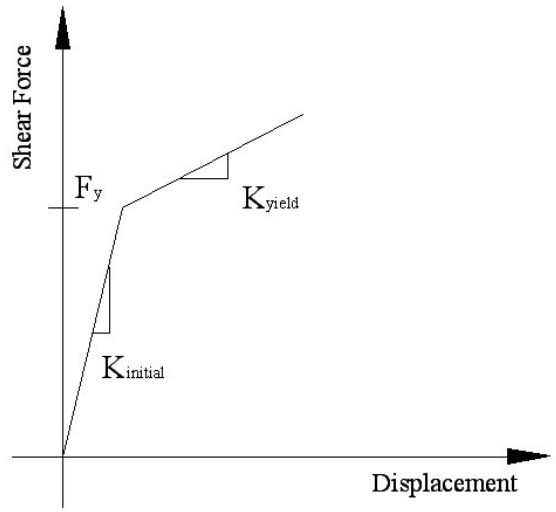

Figure 6-2. Bilinear Model of Lead-rubber Bearing.

The design of lead-rubber bearings is carried out by adding an additional design step to determine the size of the lead plug to the detailed design procedure of elastomeric bearings. In this additional step, two parameters related to the rubber core are considered, namely pre-yield to post-yield stiffness ratio, $K_{initial} / K_{yield}$, and the yield force F_y. A stiffness ratio with a value up to 10 is often used in design practice [Robinson (1982), Priestley et al. (1996), Skinner et al. (1993)]. A lead plug with a diameter equal to one-fourth of the diameter of a circular bearing can approximately accomplish a pre-yield to post-yield stiffness ratio of $K_{initial} / K_{yield} = 10$. A yield force on the order of 5% of the compressive axial force is recommended for moderate earthquakes having similar

severity of the El Centro earthquake (PGA=0.319g). For example, a lead core about 100 mm in diameter is required to produce a plastic damping force of around 100 kN for a typical 2 MN rubber bearing [Skinner et al. (1993)]. For a more severe design ground motions, the value of yield force F_y should be larger.

6.1.3 Viscous Dampers

Viscous dampers reduce displacement demand on structures by dissipating a portion of the seismic energy. Various theoretical and experimental studies on the implementation of viscous dampers have demonstrated their potential in improving the response of structures [Tsopelas (1994), Delis et al. (1996), Aiken and Kelly (1995)]. A typical viscous fluid damper, as illustrated in Fig. 6-3 [Constantinou et al. (1993a), Constantinou and Symans (1993b)], depends on the flow of high-viscosity silicone fluid to achieve energy dissipation. The general form for the force in a nonlinear viscous damper can be expressed as [Soong and Dargush (1997)],

$$f_D(t) = c_\alpha \left|\dot{u}(t)\right|^\alpha \operatorname{sgn}(\dot{u}(t)) \tag{6-5}$$

where $\dot{u}(t)$ is the relative velocity across the damper and c_α is the experimentally determined viscous damping coefficient. Here, α is a constant controlling damper nonlinearity with a practical range between 0.2 and 2, and sgn(·) gives the sign of the term in parenthesis. When $\alpha = 1$, $f_D(t) = c_1\dot{u}(t)$ represents a linear viscous damper. Nonlinear viscous dampers, for which $0 \leq \alpha < 1$, are generally less dependent on velocity as compared to linear dampers, and they limit the peak damper forces at large structural velocities while providing sufficient supplemental damping.

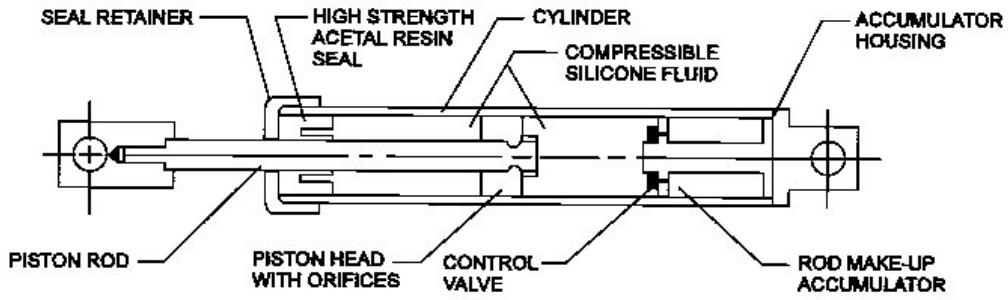

Figure 6-3. Viscous Liquid Damper.

In this study, linear viscous dampers will be utilized as one of the seismic retrofit strategies that will be considered for the two types of bridges analyzed in this study. Fig. 6-4 shows the general force-displacement hysteresis loop and force-velocity relationship for linear viscous dampers. Linear viscous dampers are modeled by damper-link elements available in SAP2000. These elements are characterized by a dashpot in series with a spring. For a desired pure damping behavior, the effect of the spring can be made negligible by making the spring stiffness sufficiently large. The viscous damping coefficients of the dampers should be designed to produce similar superstructure displacement as that obtained under pre-set modal-damping ratios. Different levels of critical damping ratios could be considered for the viscous damping coefficient design. In the bridge finite element model, the specified equivalent modal-damping ratio works in combination with the structural components' inelastic force-displacement hysteresis together to represent the whole energy dissipating mechanism. Bearing deformations and superstructure displacements would reduce with an increase in the damping coefficients of the viscous dampers installed on the bridge.

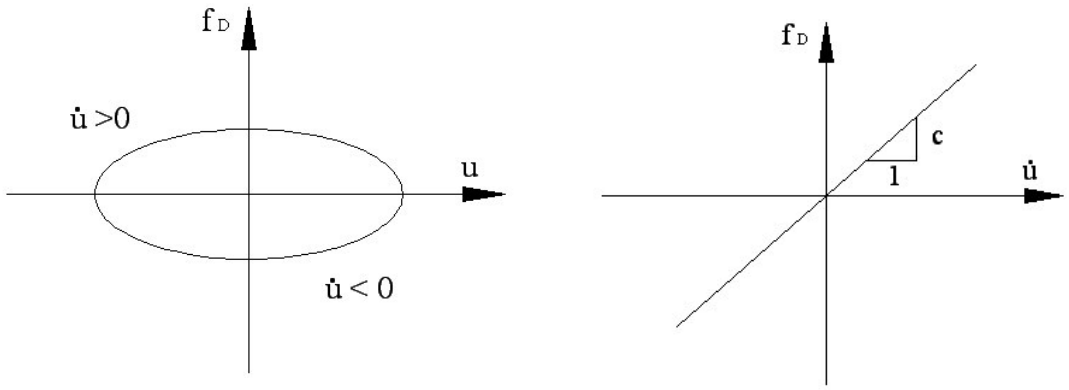

(a) Force-displacement Hysteresis Loop (b) Force-velocity Relationship

Figure 6-4. Linear Viscous Damper.

6.1.4 Fiber Reinforced Polymer (FRP) Jackets

The advantages of using fiber reinforced polymer (FRP) composites in bridge retrofit have been demonstrated successfully through its widespread applications for rehabilitation of bridge deck systems, bond repairs, internal reinforcement and seismic column strengthening. The California Transportation Department (CALTRANS) has been carrying out the retrofit of concrete bridge piers using FRP composite materials for several years [Haroun et al. (1999)]. Other states are beginning to adopt this FRP technology in their bridge retrofit programs. The combination of high strength, high stiffness fibers, such as fiberglass, kevlar, aramid and carbon fiber, with low-cost, non-corrosive resin matrix (epoxy, polyester or vinyl ester) results in unique properties in terms of strength, lightness, chemical resistance, and ease of application [Bakis et al. (2002)].

To upgrade the pier flexural ductility capacity of the typical bridges in this study, the focus would be on confinement of the potential plastic hinge region of the circular columns using FRP. For such a case, fibers would be aligned in the circumferential direction to provide extra axial and shear strength to the concrete, since FRP is principally loaded in hoop tension while concrete is loaded in triaxial compression. In earlier studies, the stress-strain model of Mander et al. (1988) for steel confined concrete was directly used in the analysis of FRP-confined concrete columns [Saadatmanesh et al. (1994), Seible et al. (1995), Purba and Mufti (1999)]. However, this model is not suitable since a constant confining pressure is assumed in the Mander's model, which is the case for steel-confined concrete when the steel is in plastic flow. FRP composites remain linear elastic until final rupture, and the lateral confining pressure in FRP-confined concrete increases continuously with the applied load.

Recently, many theoretical and experimental studies have been carried out to develop stress-strain models and ultimate failure criteria for FRP confined concrete [Teng and Lam (2004), Xiao and Wu (2000), Spoelstra and Monti (1999), Seible et al. (1995), Pessiki et al. (2001)]. The stress-strain response of FRP-confined concrete is characterized by a monotonically ascending bilinear response with a sharp softening point at a stress level near the strength of unconfined concrete $f_c^{'}$ ($\varepsilon_{co} = 0.002$), as shown in Fig. 6-5 for the sufficiently FRP confined concrete [Bakis et al. (2002), Spoelstra and Monti (1999)]. This is different from steel-hoop confined concrete, whose behavior includes a post-yield descending branch.

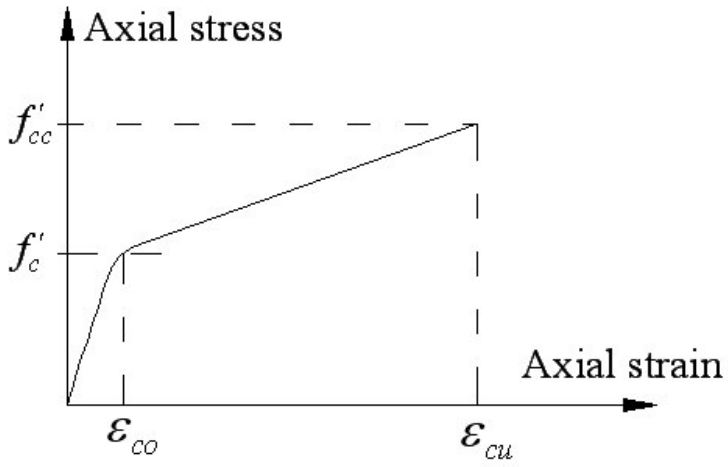

Figure 6-5. Axial Stress-strain Response of FRP-confined Concrete.

Monotonically ascending stress-strain curves have been observed in the majority of existing experiments on FRP-confined concrete since the confining pressure provided by the jacket increases with an increment of axial stress in the concrete [Xiao et al. (1991), Teng and Lam (2004), Harmon and Slattery (1992), Demers and Neale (1994), Howie and Karbhari (1994), Nanni and Braford (1995)].

Various axial stress-strain models for FRP confined concrete exist either in closed-form expressions based on interpretation of experimental results or in the form of curves derived by using incremental numerical iteration. For the pier moment-curvature analysis in this study, the closed-form expressions will be used. Theseexpressions use either strictly bilinear models [Nanni and Norries (1995), Karbhari and Gao (1997), Xiao and Wu (2000), Gergely et al. (1998)], or smoothly transited bilinear models with a parabolic first portion for the stress-strain curves of FRP confined concrete, such as Lam and Teng's model [Lam and Teng (2003), Teng and Lam (2004)].

In particular, the model proposed by Lam and Teng (2003), shown in Fig. 6-6, is the most appropriate for realistic modeling of effect of FRP on concrete confinement, since it has been calibrated using a large experimental database and has been established on the basis of extensive reviews of existing models, interpretation of existing test data and observation from the open literature. The stress–strain curve consists of a parabolic first portion and a straight-line second portion, which are expressed by the following two equations,

$$\sigma_c = E_c\varepsilon_c - \frac{(E_c - E_2)^2}{4f_c^{'}}\varepsilon_c^2 \qquad \text{for} \qquad 0 \le \varepsilon_c \le \varepsilon_t \qquad \text{(6-6 a)}$$

$$\sigma_c = f_c^{'} + E_2\varepsilon_c \qquad \text{for} \qquad \varepsilon_t \le \varepsilon_c \le \varepsilon_{cu} \qquad \text{(6-6 b)}$$

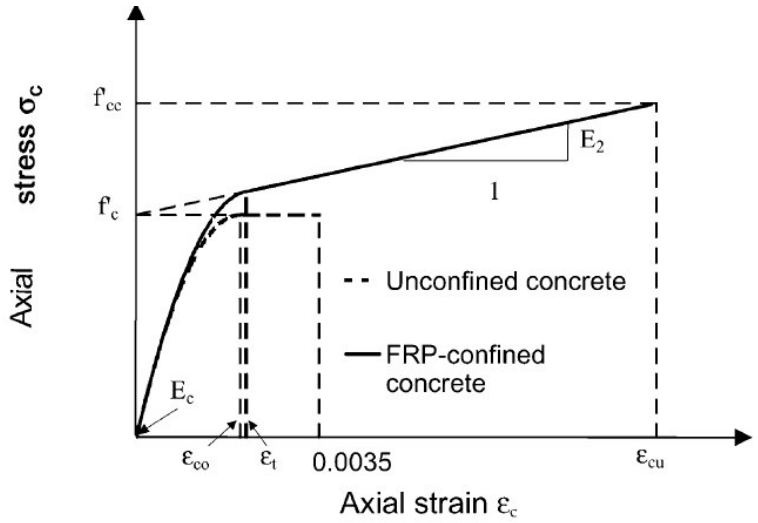

Figure 6-6. Lam and Teng's Stress-Strain Model for FRP-confined Concrete.

These two portions meet with a smooth transition at ε_t, which is given by

$$\varepsilon_t = \frac{2f_c^{'}}{(E_c - E_2)} \tag{6-7}$$

where E_2 is determined by the ultimate condition of FRP confined concrete as $(f_{cc}^{'} - f_c^{'})/\varepsilon_{cu}$.

The most commonly observed failure mode for FRP-confined concrete is the tensile failure of the jacket. Hence, $f_{cc}^{'}$ and ε_{cu} at the ultimate state correspond to FRP hoop rupture when the hoop stress reaches tensile strength of FRP. An experimentally derived expression for the ultimate compressive strain of confined concrete is expressed as [Lam and Teng (2003)]

$$\varepsilon_{cu} = \varepsilon_{co}\left[1.75 + 12\left(\frac{f_{lu}^{'}}{f_c^{'}}\right)\left(\frac{\varepsilon_{ju}}{\varepsilon_{co}}\right)^{0.45}\right] \tag{6-8}$$

where $f_{lu}^{'} = 0.5\rho_j f_{ju}$ is the maximum effective lateral confining pressure at rupture of the fiber; the volumetric ratio ρ_j of a confinement jacket, having thickness t_j and diameter d_j, is calculated as $\rho_j = 4t_j / d_j$; and $f_{ju} = E_j\varepsilon_{ju}$ is the maximum tensile stress of the jacket with elastic modulus E_j and actual hoop rupture stain ε_{ju}. In Eq. (6-8), ε_{co} is taken as 0.002. Actual values of f_{ju} and ε_{ju} are generally not the same as the material ultimate tensile strength and strain provided by manufacturers. In fact, extensive experimental results have shown that the actual hoop rupture strain ε_{ju} of FRP-confined concrete column is considerably smaller than the material tensile test results of flat coupons [Shahawy et al. (2000), Xiao and Wu (2000), Pessiki et al. (2001), Lam and Teng (2004), Moran and Pantelides (2002), Spoelstra and Monti (1999), Jin et al. (2003)].

The difference between the results of axial coupon tests and the rupture of confining FRP may be attributed to several factors, such as the tri-axial stresses in the concrete, cracking discontinuities in the concrete, overlapping zone in FRP. Based on tests of 52 carbon fiber-reinforced polymer (CFRP) wrapped specimens, the average ratio of the hoop-rupture strain to the flat coupon ultimate tensile strain is found to be 58.6% [Lam and Teng (2003)]. Additionally, the peak compressive stress of the confined concrete $f_{cc}^{'}$ is expressed as,

$$f_{cc}^{'} = f_{c}^{'}\left(1 + 3.3\frac{f_{lu}^{'}}{f_{c}^{'}}\right) \tag{6-9}$$

The use of Eq. (6-9) is recommended only when the actual confinement ratio $f_{lu}^{'} / f_{c}^{'} \geq 0.07$. Otherwise, the concrete should be considered to be insufficiently confined.

With the above stress-strain relations for confined concrete and steel, theoretical moment-curvature analysis for FRP retrofitted columns can be calculated by using equilibrium and strain compatibility conditions. For instance, ultimate curvature and moment capacity can be determined using the following steps.

Considering Fig. 6-7, the neutral axis depth can be found through equilibrium Eq. (6-10).

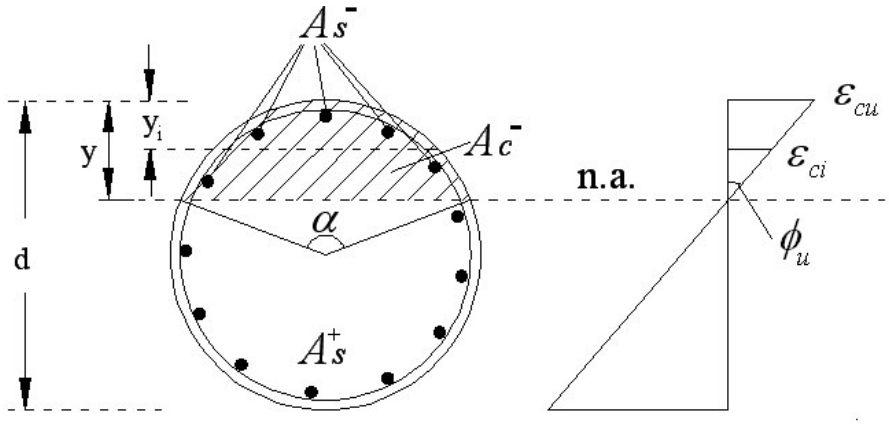

Figure 6-7. Circular Cross Section of FRP Confined Concrete Column.

$$F_c + F_s^- - F_s^+ = P \tag{6-10}$$

where F_c, F_s^-, and F_s^+ are the compressive force of concrete, compressive force of rebars, and tension force of rebars at the fiber failure, respectively; and P is the external axial load transferred by superstructure. For a neutral axis position *y* and section diameter *d*, α in Fig. 6-7 is equal to $2\arccos(1-2y/d)$. For the total longitudinal rebar area A_s, the area of steel under compression can be determined as $A_s^- = A_s\alpha/(2\pi)$, and the area of steel under tension is $A_s^+ = A_s - A_s^-$. The stresses for steel bars in compression and tension are taken as steel yield stress f_{sy}. Although some rebars close to the neutral axis might be elastic, their contributions approximately cancel out in the equilibrium, and does not affect the accuracy of results,

$$F_s^- = f_{sy}A_s \arccos(1-2y/d)/\pi \tag{6-11}$$

$$F_s^+ = f_{sy}A_s(1-\arccos(1-2y/d)/\pi) \tag{6-12}$$

The compressed concrete area A_c^- is $A_c^- = d^2(\alpha - \sin\alpha)/8$. The concrete compressive stress at location y_i could be obtained according to the confined concrete axial stress-strain model in Fig. 6-6 and the strain at this location, which is equal to $(1 - y_i / y)\varepsilon_{cu}$ on the assumption of plane section. Hence, the compressive force in the concrete, F_c, can be obtained by integration of corresponding stress on the strip area of Δy_i as

$$A_\Delta = d \sin[\arccos(1 - 2y_i / d)] \cdot \Delta y_i \tag{6-13}$$

Using the neutral axis position *y*, the curvature can be calculated as $\phi_u = \varepsilon_{cu} / y$. The ultimate moment capacity M_u is the sum of the couples generated by the forces F_c, F_s^-, and F_s^+ at this section. The entire moment-curvature curve can be established by iterating this procedure for various values of compressive strain in extreme concrete fiber of a section.

Experimental and analytical studies have demonstrated that fiber-reinforced polymer jackets with fibers oriented in the circumferential direction significantly increase the ductility capacity of bridge piers under cyclic lateral load [Teng and Lam (2004), Yeh and Mo (2005)]. On the other hand, the ultimate flexural strength is increased only by 10% or less [Monti et al. (2001), Haroun et al. (1999), Feng and Bahng (1999), Seible et al. (1997), Seible (1999), Sheikh and Bayrak (2001)]. The contribution of FRP jackets to flexural strength is minimal especially when the axial load is small [Alkhrdaji and Nanni (2000)]. The yield curvature and elastic stiffness are not significantly altered by the presence of FRP jacket, since confinement is activated only after the behavior of concrete becomes non-linear [Bakis et al. (2002), Priestley et al. (1996), Gergely et al. (1998)]. Hence, the retrofit of bridge piers through FRP wrapping will only causes significant

increase in their flexural ductility capacity. The optimal thickness of FRP jackets to meet certain curvature demand can be designed knowing the fiber material properties.

6.2 Seismic Retrofit Design for MSC Steel Bridge

The retrofit strategies to be considered for the typical multi-span continuous steel bridge in this study include: (1) replacing steel fixed bearings and expansion bearings by steel laminated elastomeric bearings (EB) with sole plate; (2) replacing steel fixed bearing and expansion bearings by lead-rubber bearings (LRB); (3) using viscous dampers in combination with elastomeric bearings; and (4) jacketing of bridge piers by carbon fiber reinforced polymer (CFRP). Both elastomeric and lead-rubber bearings have much larger deformation capacities than steel bearings, and they can effectively isolate the superstructure from the destructive effects of ground motions. The combination of lead-rubber bearings and viscous dampers can provide added benefit of energy dissipation. Jacketing of bridge piers by CFRP increases the ultimate ductility capacity of piers significantly. These retrofit strategies have been used widely around the world in seismic retrofit/upgrade of bridge components. The main objective of this study is to carry out an in-depth and comparative study on the capability of these retrofit measures to reduce the seismic fragility of bridge components.

6.2.1 Replacement of Steel Bearings by Elastomeric Bearings

According to the detailed design specifications of NYSDOT (1999) for steel girder bridges, elastomeric bearings with sole plate (Type E.B.) are used to replace steel fixed bearings and expansion bearings. The installation requires that a steel sole plate of 40 mm minimum thickness be vulcanized to the top of the bearing, and is welded or

fastened to the bottom flange of steel girders. A 25 mm thick steel masonry plate is bolted to the substructure. An elastomeric bearing is installed between the top sole plate and the bottom masonry plate. Elastomeric layers of 50 Durometer hardness and 12 mm thickness per layer are specified by NYSDOT in order to decrease the horizontal force and the danger of slippage. The internal steel load plate thickness is 3 mm by as per NYSDOT standards.

To simulate a retrofit scenario for the MSC steel bridge analyzed in this thesis, the dimensions of the replacement elastomeric bearings and the number of layers are designed as per the design spreadsheet developed by Roeder and Stanton (1996) following Method A of the AASHTO LRFD Specifications (1998). NYSDOT standards for elastomeric bearings are also considered in the bearing design. The bearings installed on abutments and piers will be subject to different levels of axial loads. Hence, these two sets of bearings, referred to as EB1 and EB2 in Fig. 6-8, will have different designs. Plan and elevation drawings of EB1 and EB2 types of bearings are presented in Figs. 6-9 and 6-10, respectively.

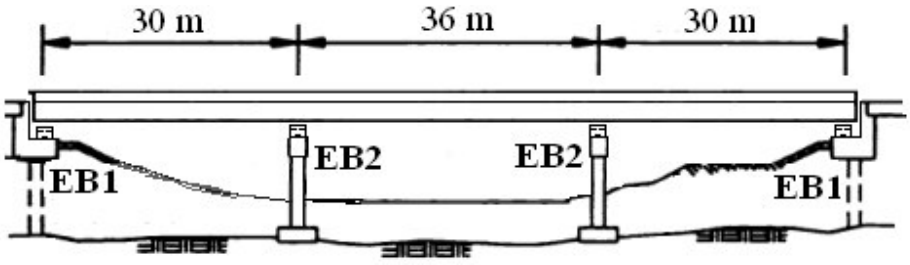

Figure 6-8. Retrofit Scheme for Elastomeric Bearings in MSC Bridges.

Six EB1 type bearings per line are installed in the transverse direction under the bottom flanges (as wide as 400 mm) of the steel plate I-girders equally spaced at 2440

mm on the abutments at the two ends of the bridge, as shown in Fig. 6-8. Likewise, a total of twelve EB2 type bearings are installed under the girders over the multi-column bents. The pads of EB1 type bearing are 250 mm long (in the bridge longitudinal direction), 450 mm wide and 87 mm high consisting of five 3 mm steel laminates vulcanized to six 12 mm layers of rubber. The top sole plate is 280 mm long, 480 mm wide and 40 mm thick. The bottom steel masonry plate is 330 mm long, 650 mm wide and 25 mm thick to leave enough spaces for two 24 mm diameter anchor studs. The shape factor for EB1 type bearing using Eq. (6-3) is 6.7. The EB2 bearing is of a bigger size, with pads of dimension 350 mm long, 450 mm wide and 102 mm high. Each EB2 bearing consists of six steel laminates vulcanized to seven layers of rubber. The shape factor of bearing EB2 is 8.2.

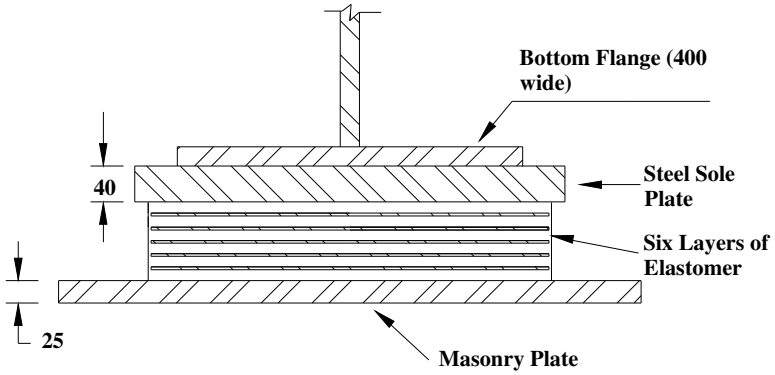

(a) Elevation

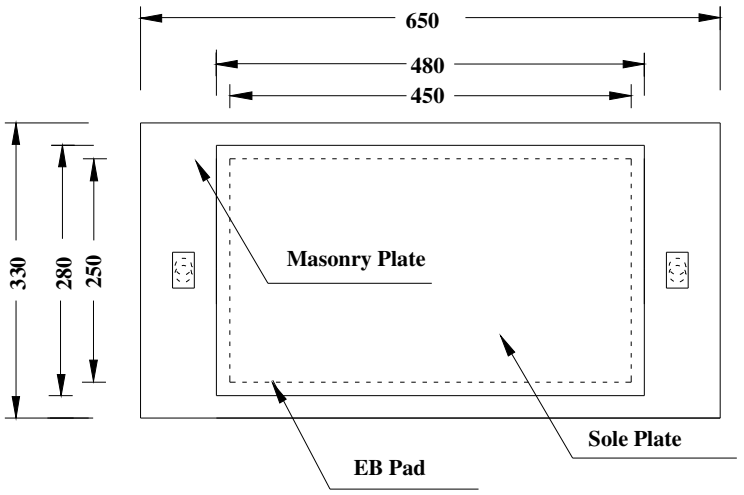

Unit: mm

(b) Plan

Figure 6-9. Elastomeric Bearings of the Type EB1.

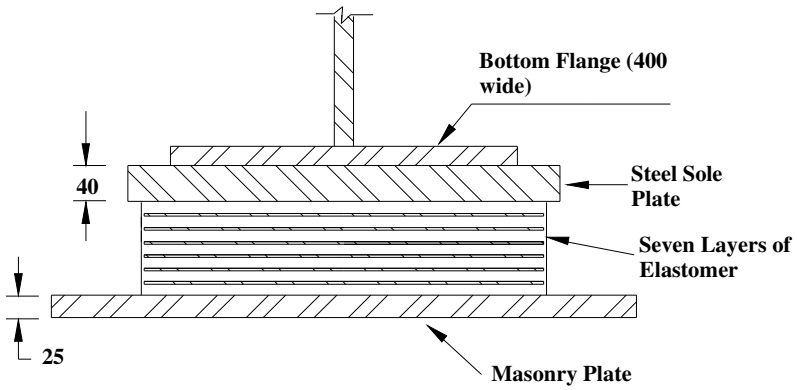

(a) Elevation

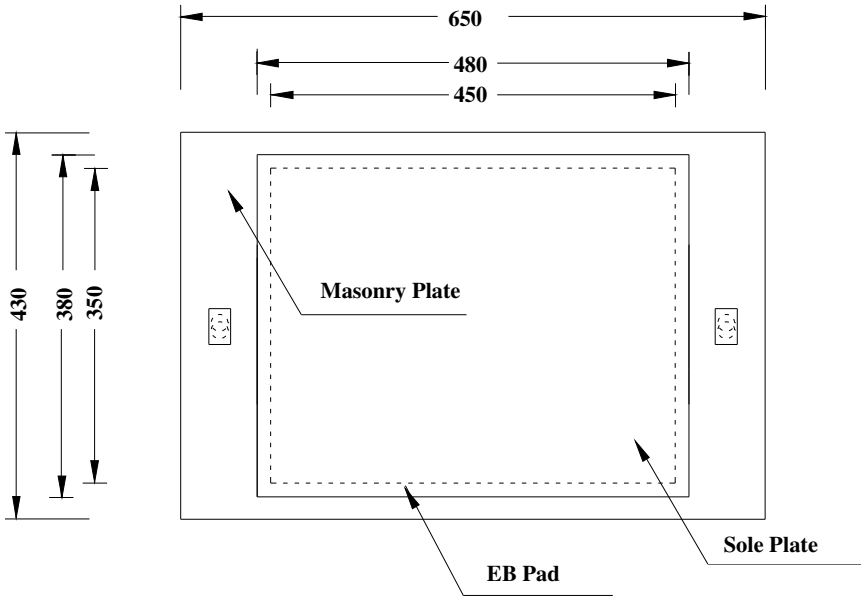

Unit: mm

(b) Plan

Figure 6-10. Elastomeric Bearings of the Type EB2.

Considering uncertainties in shear modulus of elastomers in the range of 95 to 130 psi as discussed in section 6.1.1. Fig. 6-11 shows the ranges for the shear force versus displacement curves for the two types of bearings.

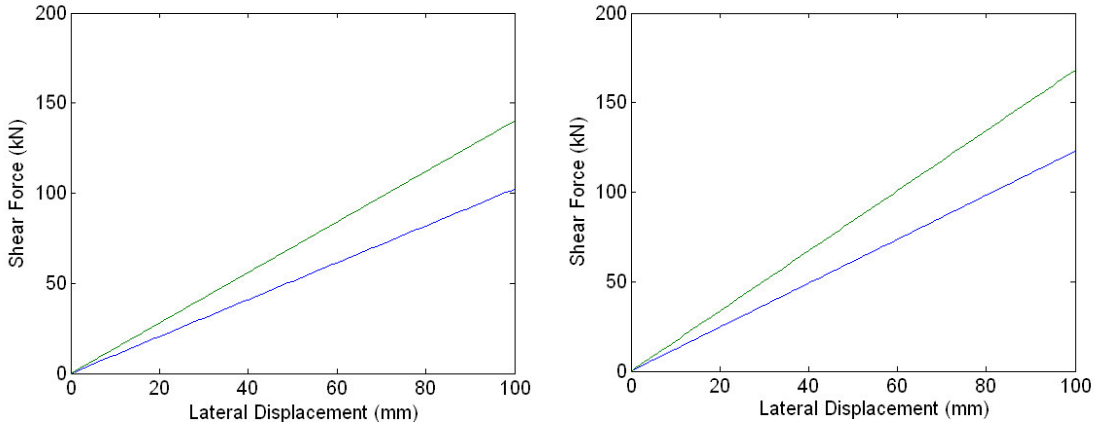

(a) Bearing EB1 (b) Bearing EB2

Figure 6-11. Shear Force-displacement Models of Elastomeric Bearing

A parametric analysis has been carried out to evaluate the variations in seismic response of bridge components because of variations in the shear modulus of the elastomers by modeling elastomeric bearings as three-dimensional link elements. Figs. 6-12 (a) to (e) show variations in various response quantities as a function of the shear modulus of bearings. It is observed from Fig. 6-12 that the pier curvature ductility (ϕ / ϕ_y) generally increases with increased shear modulus. On the other hand, the superstructure displacement decreases with increased shear modulus. The pier ductility of the bridge retrofitted with elastomeric bearings has been efficiently controlled for moderate and strong earthquakes, as compared to the ductility of as-built bridge in Chapter 4. Pier bases of the bridge retrofitted with elastomeric bearings don't develop any plastic hinge (i.e.,

$\phi / \phi_y < 1$) for earthquakes with PGA less than 0.7g, although the steel reinforcement yields during an earthquake with PGA around 0.7g. For earthquakes with PGA = 1.0g, pier curvature ductility of the retrofitted bridge decreases from 4 to less than 2. The piers in the two multi-column bents have similar seismic response, since the same type of bearings (EB2) on the two bents distributes the seismic forces uniformly. Bearing EB1 has larger displacement than bearing EB2, since the cantilever piers accommodate a part of superstructure displacement. Overall, pier curvature ductility varies from -9% to 4% and deck displacement could vary from 15% to -10% because of the ±15% (95 to 130 psi) variations in shear modulus of elastomer. Hence, bearing displacements are more sensitive than pier curvature ductility to variations in shear modulus of elastomer.

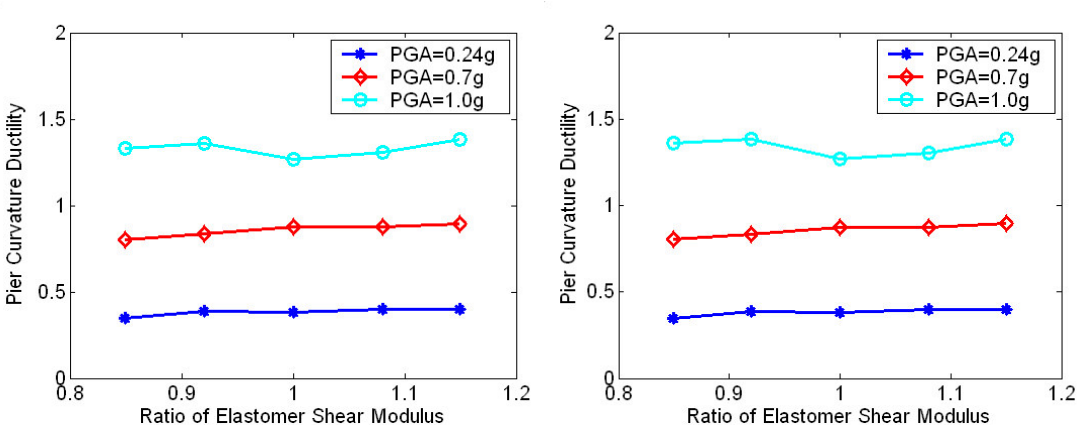

(a) Piers in the 1st column-bent

(b) Piers in the 2nd column-bent

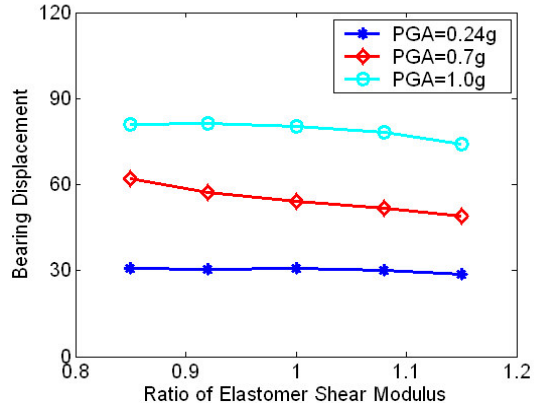

(c) Bearing EB1

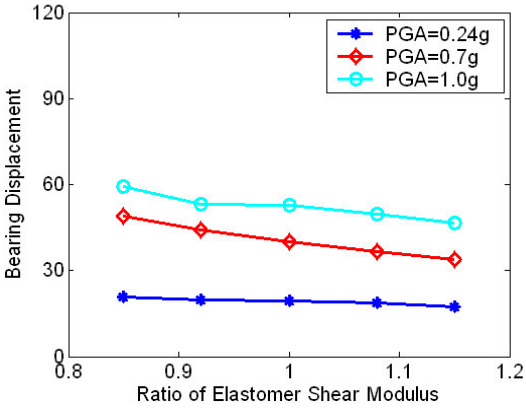

(d) Bearing EB2

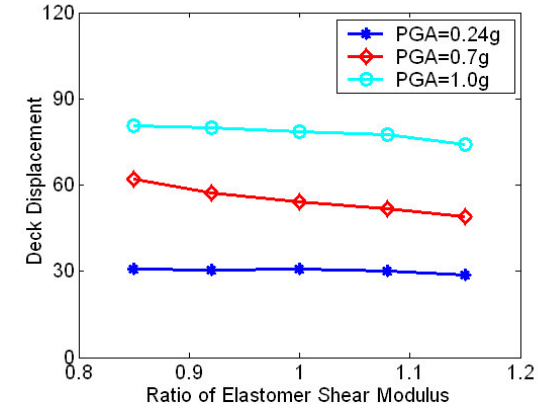

(e) Deck

Figure 6-12. Results of Parametric Study of Elastomer Shear Modulus for MSC Steel Bridge on the response of (a) and (b) Pier Curvature Ductility; (c) and (d) Elastomeric Bearing Displacement; (e) Deck displacement.

6.2.2 Replacement of Steel Bearings by Lead-Rubber Bearings

Two types of lead-rubber bearings, termed as LRB1 and LRB2, are used to replace fixed steel bearings and expansion bearings as a retrofit scenario for the multi-span continuous steel bridge, as shown in Fig. 6-13. For the design of lead-rubber bearings, the plan area and the total height of the rubber layers determine the bearing flexibility, and the diameter of the lead core determines the desired level of energy dissipation or equivalent hysteretic damping.

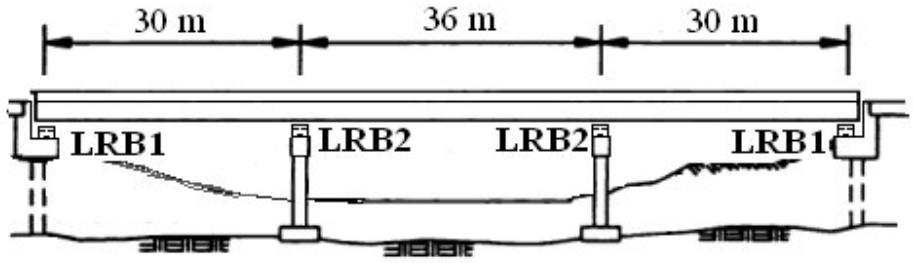

Figure 6-13. Retrofit Scheme for Lead-rubber Bearings in MSC Bridges.

Bearings LRB1 and LRB2 have the same dimensions as the elastomeric bearings EB1 and EB2 described in section 6.2.1. The LRB1 Bearing contains a lead core with a diameter of 38 mm. At the median value of shear modulus of the elastomer, the pre-yield and post-yield stiffness of LRB1 are $K_{initial} = 2.9$ kN/mm and $K_{yield} = 1.2$ kN/mm, respectively. The yield force of the bearing is 20.3 kN corresponding to a displacement of 7 mm. The stiffness ratio of the bearing is $K_{initial} / K_{yield} = 2.4$, and the yield force F_y is 10% of the nominal value of the compressive axial force in the bearing. The LRB2 bearing has a lead core with a diameter of 60 mm. At the median value of shear modulus of elastomer, pre-yield and post-yield stiffness of the bearing are $K_{initial} = 5.0$ kN/mm and

$K_{yield} = 1.4$ kN/mm, respectively. The yield force of LRB2 is 41.46 kN, and its yield displacement is 8.2 mm. Hence, the stiffness ratio of the bearing is $K_{initial} / K_{yield} = 3.5$ and the yield force, F_y, is 6% of the nominal compressive axial force of the bearing. For modeling in SAP2000, each LRB is idealized as an isolator link element with bilinear shear force-displacement relationship, infinite compressive stiffness and zero torsional and rotational stiffness. The sensitivity of the shear force vs. lateral displacement relationship to variations in shear modulus of elastomers is shown in Fig. 6-14 for LRB1 and LRB2 bearings. The shear modulus in Fig. 6-14 varies between $G_{\min} = 95$ psi, $G_{\max} = 130$ psi for a median value of 112.5 psi. It is observed that the elastic stiffness of the bearings is not affected significantly by variations in the shear modulus of bearings.

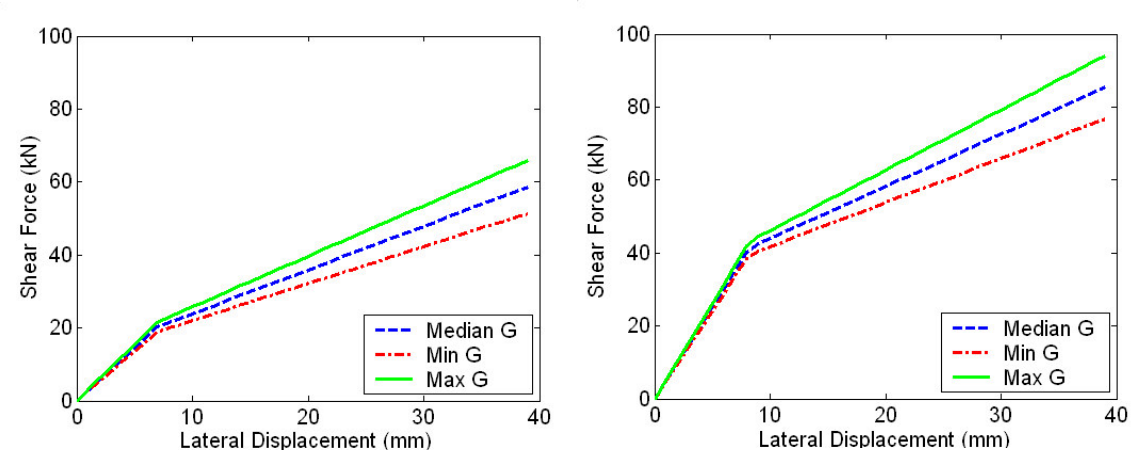

(a) Bearing LRB1 (b) Bearing LRB2

Figure 6-14. Shear Force-displacement Models of Lead-rubber Bearing.

Nonlinear time history analysis has been carried out using the same synthetic base accelerogram used in Chapter 4 with PGAs scaled to 0.24g, 0.70g and 1.0g and a shear modulus of elastomer, G = 112.5 psi. The results show that bearing and deck

displacements of the bridge with LRB are reduced significantly compared to those of the un-retrofitted bridges without any significant increase in pier curvature ductility. Hence, it is concluded that the selected size for the lead cores is reasonable. The effect of the lead-rubber bearings on the response is similar to the effect of the elastomeric bearing, although the fundamental period of the bridge with LRB is 0.9 sec as compared to 1.3 sec for the bridge with elastomeric bearings. As a result, LRB induces larger earthquake forces and pier ductility, as shown in Fig. 6-15 (a). However, the hysteretic energy dissipation caused by the lead core results in a significant reduction of bridge deck and bearing displacements in the bridge with LRB, as shown in Fig. 6-15 (b).

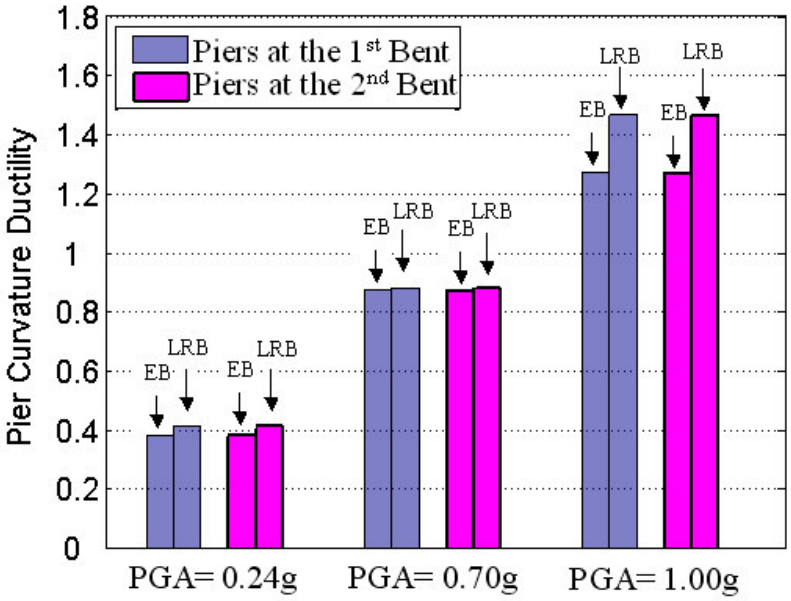

(a) Pier Curvature Ductility of Retrofitted MSC Bridge

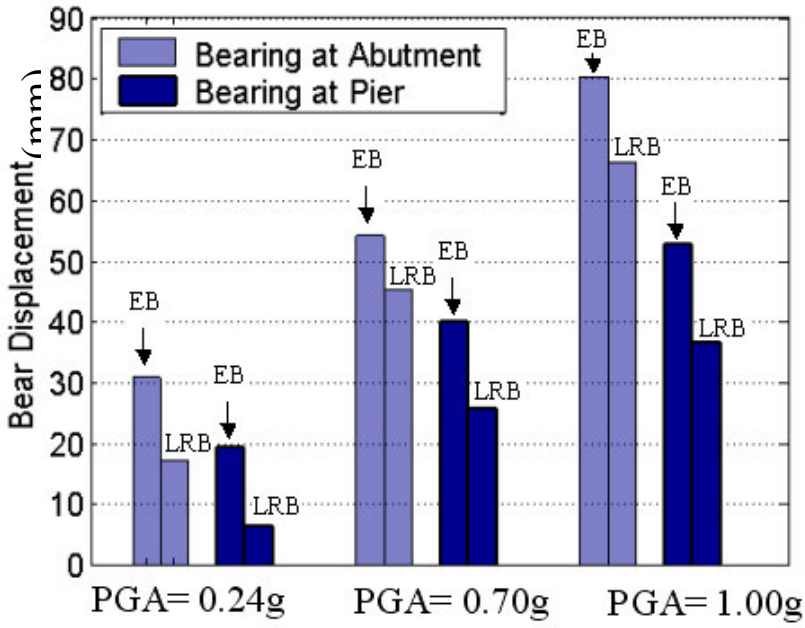

(b) Bearing Displacement of Retrofitted MSC Bridge

Figure 6-15. Comparison of Retrofit Effect due to Elastomeric Bearings and Lead-Rubber Bearings in MSC Bridge.

6.2.3 Elastomeric Bearings with Supplementary Viscous Dampers

Although elastomeric bearings can effectively reduce the seismic forces in bridge piers, the deck displacement may become excessive during strong earthquakes. The deck displacement can be reduced by installing a supplementary damping device in parallel with elastomeric bearings without significantly compromising the isolation effects of the elastomeric bearings. This retrofit option consists of elastomeric bearings in parallel with viscous dampers between the deck and abutment at the two ends of the bridge, and only elastomeric bearings between the piers bents and superstructure, as shown in Fig. 6-16. Lee and Kawashima (2004) investigated the seismic response of bridges by installing a damper between the deck and piers (internal damper). However, this arrangement was found to increase pier ductility because of the additional forces introduced by the dampers on the piers. Hence, the proposed scheme which consists of installing dampers between the deck and abutments only is more appropriate in reducing seismic fragility of the bridge, with damper forces only applied to the abutments.

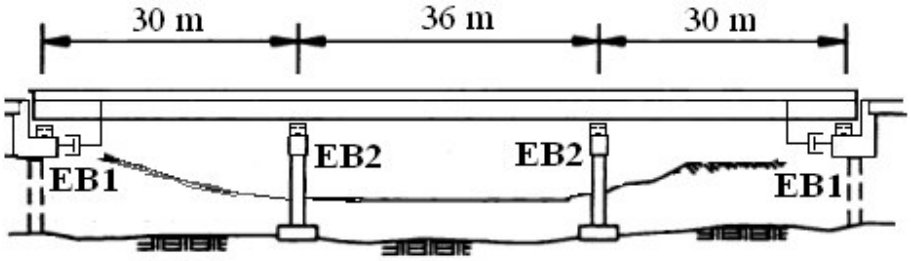

Figure 6-16. Retrofit Scheme for Elastomeric Bearings and Viscous Dampers in MSC Bridge.

In this retrofit scenario for the MSC bridge, the dampers installed at the two ends of the bridge are assumed to have identical damping characteristics. Artificial accelerograms with 2500-year return period [Risk Engineering Inc. (1998)] and with

PGAs normalized to 0.24g, 0.70g and 1.0g have been used as basis earthquakes for damper design. For the bridge with` elastomeric bearings only, a 5% modal damping is assumed for all the modes. In order to determine the appropriate design values for viscous damping coefficients, time-history analyses have been carried out for the bridge with only elastomeric bearings and assuming Rayleigh damping coefficients so that the damping ratio in the fundamental mode of the bridge is increased to 10%, 15%, 20% and 25%. Then, the analysis of the bridge with dampers is carried out by varying the dampers' properties so that the deck displacement matches those of obtained for the different damping levels (i.e., 10%, 15%, 20% and 25%). Fig. 6-17 shows the deck displacement for different damper coefficients for the three levels of PGA considered. It is observed that damper coefficients c= 0.25, 0.50, 0.75 and 1 kip-sec/in produce similar displacements as those of the bridge with only bearing retrofit and preset damping levels of 10%, 15%, 20% and 25%, respectively.

Fig. 6-18 shows pier curvature ductilities for the bridge with and without dampers for the three PGA levels. It is observed that dampers cause significant decrease in pier curvature ductilities for seismic input with 0.24g PGA. The effect of dampers is diminished for higher PGAs since other energy dissipating mechanisms, such as the nonlinear behavior of the piers and bearings, have already contributed to dissipating the input seismic energy.

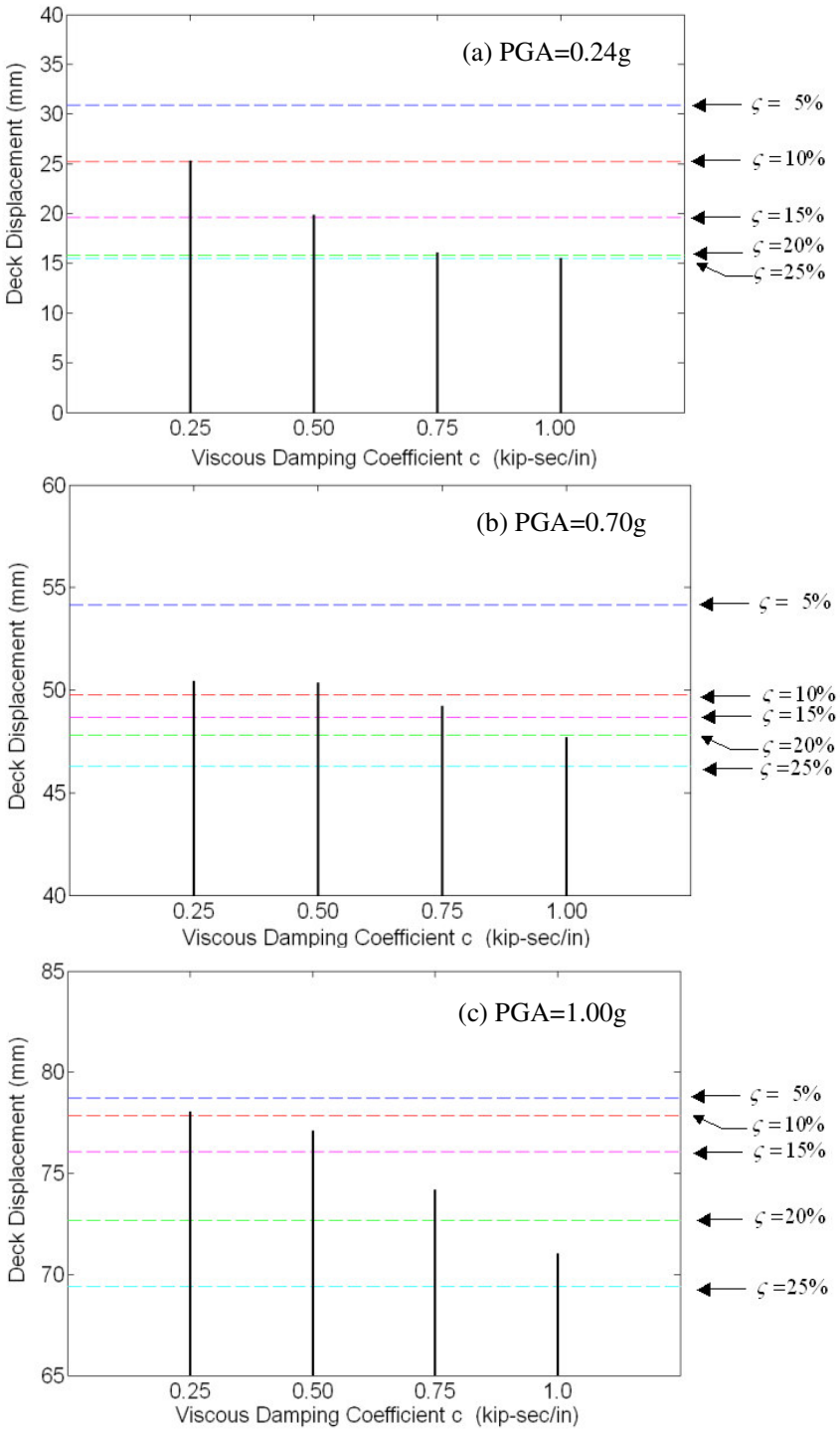

Figure 6-17. Damping Coefficients of Viscous Dampers for the Equivalent Critical Damping.

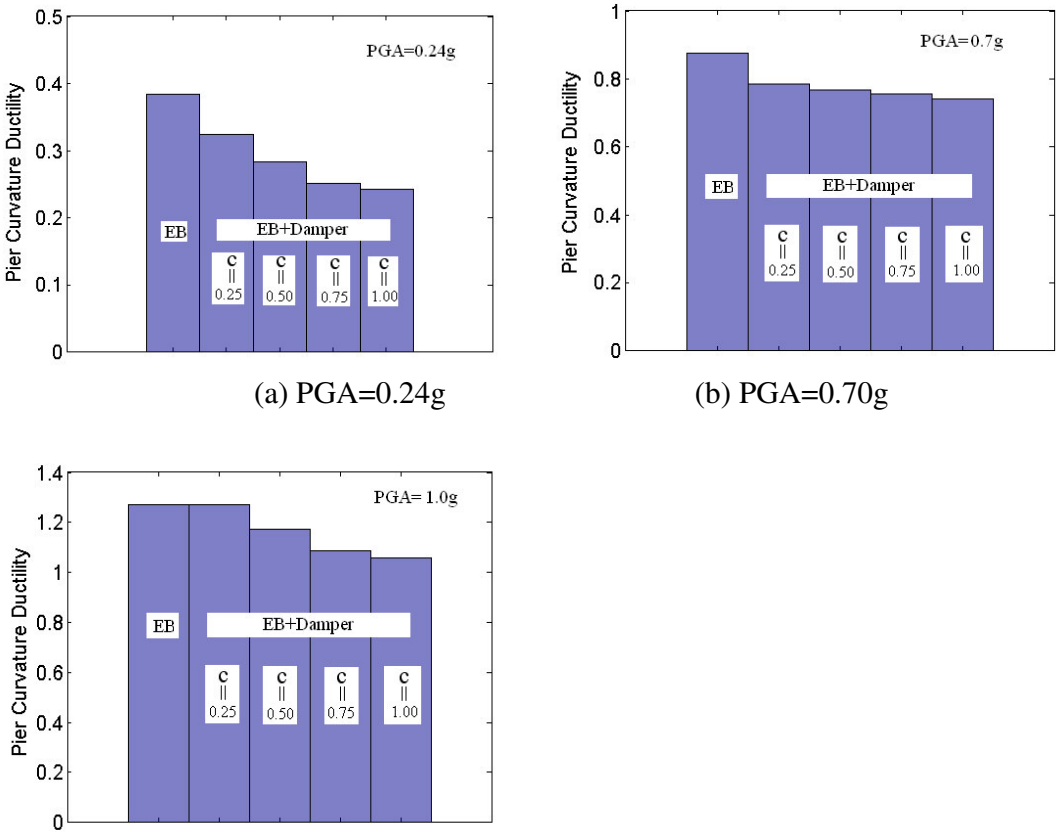

(a) PGA=0.24g (b) PGA=0.70g

(c) PGA=1.0g

Figure 6-18. Pier Curvature Ductility for (1) EB: retrofitted by elastomeric bearing alone; (2) EB+Damper: elastomeric bearing with external viscous damper for c=0.25, 0.50, 0.75 and 1.00 kip-sec/in.

6.2.4 Pier Confinement by Carbon Fiber Jackets

Proper confinement of concrete columns can substantially increase the compressive strength and ultimate compressive strain in the piers. The gain in ultimate compressive strain significantly enhances the ductility and energy absorption capacity in

the plastic hinge region of concrete columns and eliminates the risk of column collapse. In addition, the axial load capacity of the columns is also increased.

For the MSC bridge in this study, improved column confinement is achieved by wrapping the reinforced concrete piers by carbon fiber reinforced polymer (CFRP) jackets with fibers oriented in the hoop direction. The jacket design starts by defining an upgrading index, *I*, as the ratio of target to available curvature ductility at the pier base section. Then, the optimal thickness of CFRP jackets in terms of the desired upgrading index *I*, and the CFRP mechanical characteristics, i.e., the ultimate strength f_{ju} and fiber hoop rupture stain ε_{ju} can be calculated by [Monti et al. (2001)]

$$\rho_j = 4t_j / d_j = 0.8I^2 \frac{f_{cc}^{'ava}}{f_{ju}} \cdot \frac{\varepsilon_{cu}^{ava^2}}{\sqrt{\varepsilon_{ju}^3}} \tag{6-14}$$

where $f_{cc}^{'ava}$ and ε_{cu}^{ava} are initially available peak concrete compressive stress and ultimate strain when only the steel-hoop confinement is present, as computed by Eqs. (5-7) and (5-6). The validity of Eq. (6-14) for determining optimal CFRP thickness has been verified through comparisons with experimental data of concrete columns wrapped by CRPF. This design equation is best suited for cases having [Monti et al. (2001)]

$$TAR = \varepsilon_{cu}^{tar} \sqrt{f_{cc}^{'tar} / f_c^{'}} = (2.5 f_{lu}^{'} / f_c^{'} \times \varepsilon_{ju}^{3/2})^{1/2} > 0.01 \tag{6-15}$$

where ε_{cu}^{tar} and $f_{cc}^{'tar}$ are the target concrete ultimate strain and the target confined concrete compressive strength to be attained through FRP confinement; $f_{lu}^{'}$ is the maximum effective lateral confining pressure at rupture of the fiber; and ε_{ju} is the actual hoop rupture stain. Additionally, the value of $f_{lu}^{'} / f_c^{'}$ should fall between 0.07 and 0.3 for the concrete to be sufficiently confined to meet the design criteria set by Spoelstra and

Monti (1999), Lam and Teng (2003). However, the confinement ratio should not exceed 0.3, since any further increase in pressure results in lower confinement effectiveness expressed by $(f_{cc}^{'} - f_{c}^{'})/f_{lu}^{'}$, where $f_{cc}^{'}$ is peak compressive stress of the confined concrete.

The carbon fiber sheet adopted in this study has a thickness of 0.165 mm per ply. The CFRP's ultimate tensile strain is 0.0152 from flat coupon tensile tests and the tensile modulus is 250 GPa (36.26 Msi) (MBrace Composite Strengthening System supplied by Master Builders, Inc, CF 130 product). The above material properties are typically used in practical applications as described in the open literature [Lam and Teng (2004), Theriault et al. (2004), Parvin and Wang (2001)]. These properties are close to the properties of another popularly used carbon fiber product, FTS-C1-20, manufactured by Tonen Corporation of Tokyo (ply thickness 0.11mm, tensile modulus 230 GPa, ultimate elongation 0.015) [Purba and Mufti (1999), MacRae et al. (1999), Tonen (1995)]. The hoop rupture strain ε_{ju} in this study is taken to be 58.6% of the ultimate tensile strain in flat coupon tests that is specified to be 0.0152. Thus, $\varepsilon_{ju} = 0.0089$. The maximum tensile strength of the jacket at the fiber rupture is $f_{ju} = 2226.8$ MPa. Given the median strengths of concrete and reinforcing steel in section 4.4, $f_{c}^{'} = 27.2$ MPa and $f_{y} = 336.47$ MPa, the peak compressive stress of concrete and its ultimate strain $f_{cc}^{'ava}$ and ε_{cu}^{ava} are obtained as 29.7 MPa and 0.009 from Eqs. (5-7) and (5-6), respectively, considering the confinement from the steel-hoop only. The ultimate curvature ϕ_u is obtained as 0.0344 (1/m) for the ultimate compressive strain of $\varepsilon_{cu} = 0.009$ by using the BIAX program. The available ultimate curvature ductility capacity $\phi_u / \phi_y^{'}$ is obtained as

10.3 for the steel-hoop confined concrete. For designing the FRP jacketing, the upgrading index I is set as 2 to mitigate the risk of strength degradation and concrete crushing in the piers. Then, following Eq. (6-14), 6 layers of carbon fiber jackets, with a total thickness of $t_j = 0.93$ mm, are used for the additional FRP confinement of the piers. As a result, the CFRP confinement volumetric ratio is $\rho_j = 0.43\%$ for the circular column with 3 ft (900 mm) diameter. The maximum lateral confining pressure for this case would be provided as $f_{lu}^{'} = 4.8$ MPa (700 psi). The confinement ratio is $f_{lu}^{'} / f_c^{'} = 0.18$, i.e., the columns are sufficiently confined since $0.07 < f_{lu}^{'} / f_c^{'} < 0.3$. The value of *TAR* is 0.0193, which is larger than 0.01 using Eq. (6-15). The application of CFRP jacketing would increase the compressive strength of concrete, $f_{cc}^{'}$, to 43.1 MPa as per Eq. (6-9), which is 1.6 times the unconfined strength. Simultaneously, the ultimate compressive strain ε_{cu} increases to 0.0118. Hence, the strain enhancement ratio is $\varepsilon_{cu} / \varepsilon_{co} = 5.9$. These enhancement ratios of 5.9 for strain and 1.6 for strength are quite reasonable, and they fall within the range observed from 52 CFRP-wrapped cylinder test data used to generate the stress-strain model of Lam and Teng (2003).

Fig. 6-19 shows the schematic diagram of the retrofit design of concrete columns by CFRP jacketing. The primary CFRP confinement region l_j at the base of column is the plastic hinge length. However, a secondary confinement region adjacent to the plastic hinge region with half jacket thickness is added to follow the recommended construction practice [Seible et al. (1997), Priestly et al. (1996)].

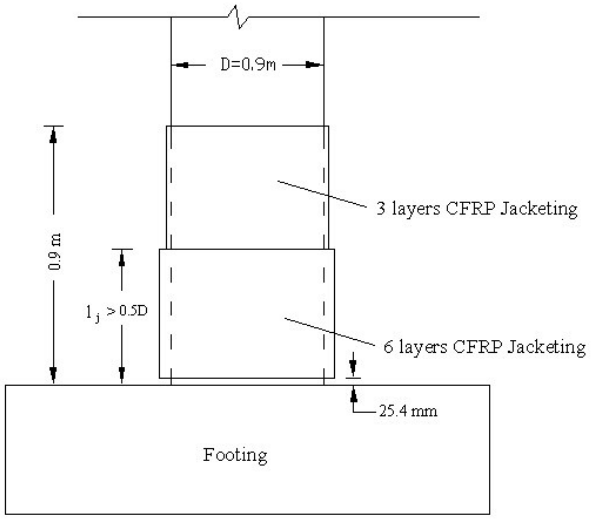

Figure 6-19. Retrofit Scheme for CFRP Pier Jacketing in MSC Bridge.

6.3 Seismic Retrofit Design for MSSS Steel Bridge

The retrofit measures to be evaluated for the typical multi-span simply supported steel bridge considered in this study include (1) replacing the fixed steel bearings and expansion bearings by elastomeric bearings with sole plate; (2) splicing simple spans together to form a continuous span simultaneously with the use of elastomeric bearing replacements.

6.3.1 Replacement of Steel Bearings by Elastomeric Bearings

The design of the elastomeric bearings in the MSSS bridge follows a similar approach to that used for the MSC bridge in Section 6.2.1. Bearings located under the 12 and 20 m spans, as shown in Fig. 6-20, are respectively under nominal vertical axial loads of 98 and 160 kN due to the superstructure dead load. The steel W30×108 rolled girders have bottom flanges which are 267 mm wide. An elastomeric bearing has been designed

and is mounted on the abutments and piers of the bridge. At each support, five bearings labeled as EB3 are arranged in the transverse direction under the girders with equal spacing of 2286 mm, as illustrated in Figure 6-20.

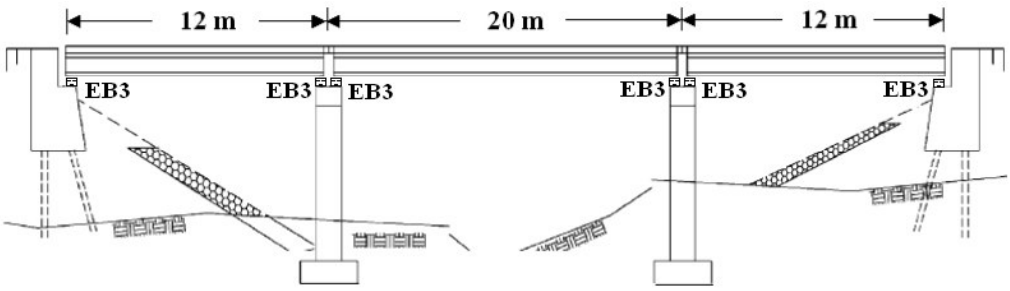

Figure 6-20. Retrofit Scheme for Elastomeric Bearings in MSSS Bridge.

Figure 6-21 shows the details of the designed bearing, EB3. The pad of the bearing is 250 mm long, 250 mm wide and 72 mm high, and consists of four 3 mm steel laminates vulcanized to five 12 mm layers of 50 Durometer hardness rubber. The top sole plate is 280 mm long, 300 mm wide and 40 mm thick, and is 30 mm wider than the flange. The bottom steel masonry plate is 330 mm long, 470 mm wide and 25 mm thick. The shape factor of the bearing is 5.21 as per Eq. (6-3).

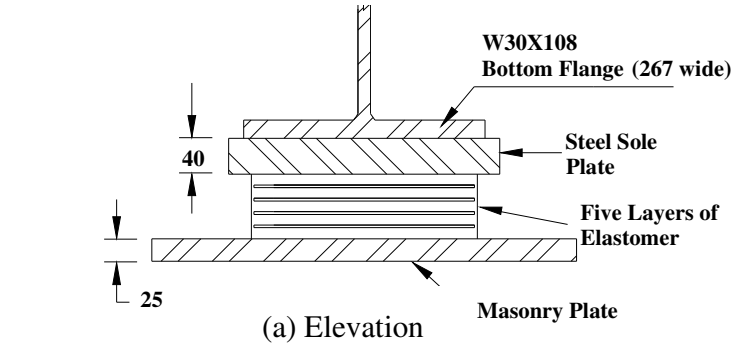

(a) Elevation

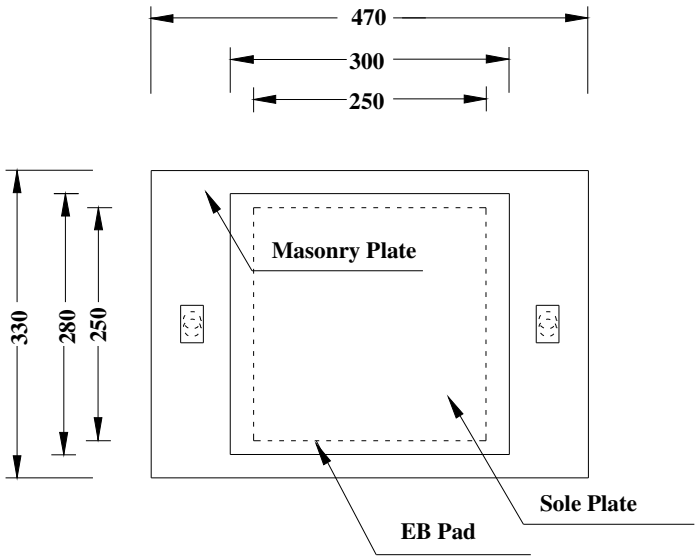

(b) Plan

Figure 6-21. Elastomeric Bearings of the Type EB3.

A parametric analysis is carried out to evaluate the seismic response of the MSSS bridge with EB3 elastomeric bearings by varying the shear modulus of the elastomer from 95 to 130 psi. The shear force-displacement relationship of the bearing EB3 is shown in Fig. 6-22, which shows that the shear stiffness of the EB3 bearing is much lower than those of the EB1 and EB2 bearings previously used for the retrofit of the MSC bridge.

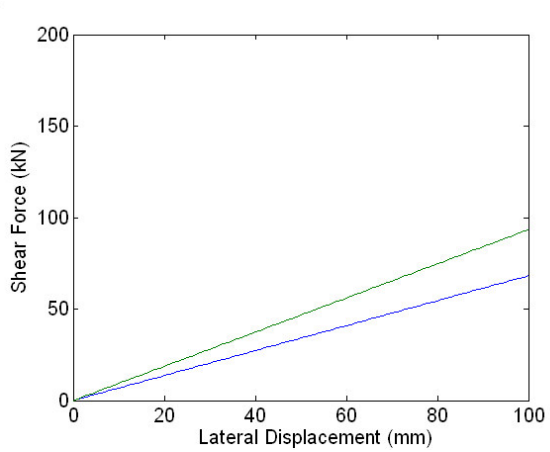

Figure 6-22. Shear Force-displacement Models of Elastomeric Bearing EB3.

Fig. 6-23 shows plots of pier curvature ductility and deck displacements as functions of the shear modulus of the elastomers for different levels of PGAs. It is observed that the pier curvature ductility (ϕ/ϕ_y) generally increases and the deck displacement decreases with an increase in shear modulus. The sensitivity of the response quantities to variations in shear modulus is more complex than that for MSC bridge due to the internal expansion joints between the spans. Under different earthquake levels, the three decks may have different tendency because of pounding between the decks and the interaction of the decks with the pier bents. The curvature ductilities of the piers are reduced by almost half due to bearing replacement. The MSSS bridge retrofitted with elastomeric bearings has lower curvature ductility than that of the MSC bridge with elastomeric bearings. Plastic hinges don't form during earthquakes with PGA less than 0.7g, and the maximum bearing displacement which is less than 60 mm for all the cases considered occurs on the bearings on top of the pier bents. The maximum abutment displacement is on the order of 15 mm. These displacement values are considered

acceptable because they are lower than the displacements observed under LRB retrofit for the MSC bridge. Therefore, energy-dissipating devices, such as lead-rubber bearings and viscous dampers, are not required.

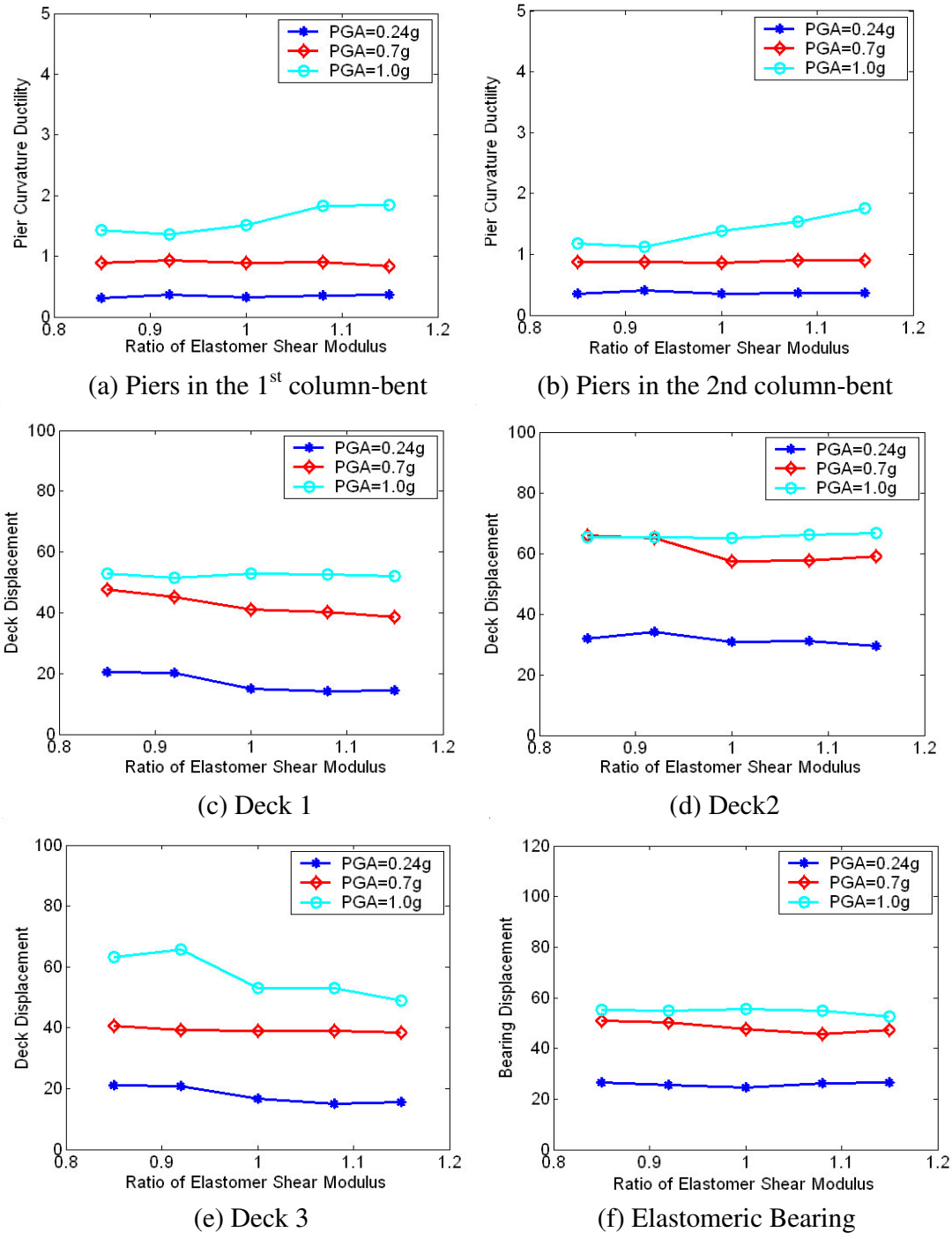

(a) Piers in the 1st column-bent

(b) Piers in the 2nd column-bent

(c) Deck 1

(d) Deck2

(e) Deck 3

(f) Elastomeric Bearing

Figure 6-23. Results of Parametric Study of Elastomer Shear Modulus for MSSS Steel Girder Bridge on (a) and (b) Pier Curvature Ductility; (c) ~ (e) Deck Displacement; (f) Displacement of Elastomeric Bearing.

6.3.2 Retrofit by Combination of Span Continuity and Elastomeric Bearings

Another common retrofit strategy used during the rehabilitation of MSSS bridges in New York State consists of eliminating the expansion joint at the piers by splicing simple spans together to form a continuous girder, as shown in Fig. 6-24. Normally, bearing replacement is also done as part of this retrofit. The seismic performance of the retrofitted bridge still needs to be investigated, although this strategy has several non-seismic benefits including (i) reducing the possibility of deterioration of the girder and substructure from leaky joints, and (ii) slightly improving the load carrying capacity of the superstructure [NYSDOT (2002)].

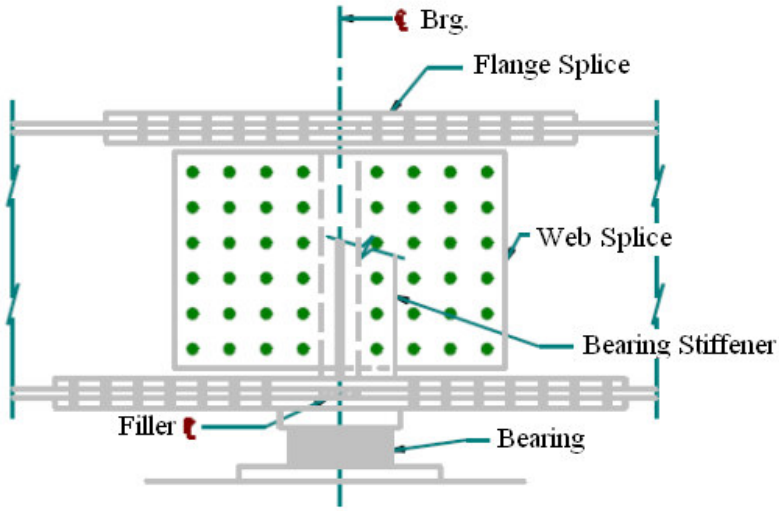

Figure 6-24. Details of Continuous Retrofit for MSSS Bridge.

Fig. 6-25 shows the elevation view of the MSSS bridge considered in this study retrofitted by the combination of continuity and elastomeric bearings. The number of bearings on the pier bents has been reduced from 10 to 5, hence both live and dead loads on each individual bearing are increased. The design of the elastomeric bearing has been carried out for bearings mounted on the pier bents and they are designated as EB4 in Fig.

6-25. Bearing EB4 has the same plan dimension as bearing EB1 in Fig. 6-9, except that only 5 elastomer layers are needed. The pad is 250 mm long (in longitudinal direction), 450 mm wide and 72 mm high. The shape factor of bearing EB4 is 6.7. For the bearings mounted on the abutments, bearings EB3 have the same design details as described in Fig. 6-21. For each bearing line, five bearings are arranged in the transverse direction with equal spacing of 2286 mm underneath the girders.

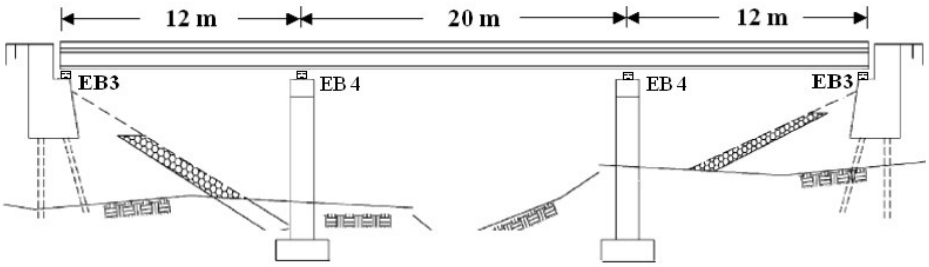

Figure 6-25. Retrofit Scheme for Elastomeric Bearing in Spliced MSSS Bridge.

In order to investigate the effectiveness of the splices used to make the bridge continuous, a comparative study has been carried out between strategy A: elastomeric bearings alone and strategy B: retrofitted by deck-girder splicing and bearing replacement. The results of the time history analyses under the base earthquake with different PGA values are shown in Fig. 6-26. The results in Fig. 6-26 are obtained using the median elastomer shear modulus of the bearings which is 112.5 ksi. It is observed that although the pier ductility demand for strategy B is higher than that for strategy A, the maximum deck and bearing displacements for strategy B are smaller. Making the bridge continuous increases it resistance to seismic displacements and eliminates pounding between the decks. In case of strategy A, although direct damage to the decks due to collision is limited, the collision transfers a large inertial force from one deck to the other resulting in

damage to the bearings or the columns. Hence, strategy B is more beneficial than strategy A.

The analysis performed in this chapter investigated the effects of different retrofit scenarios using a deterministic analysis of the bridge response. The next chapter will compare the fragility of MSC and MSSS bridges retrofitted using different strategies to that of the original non-retrofitted bridges.

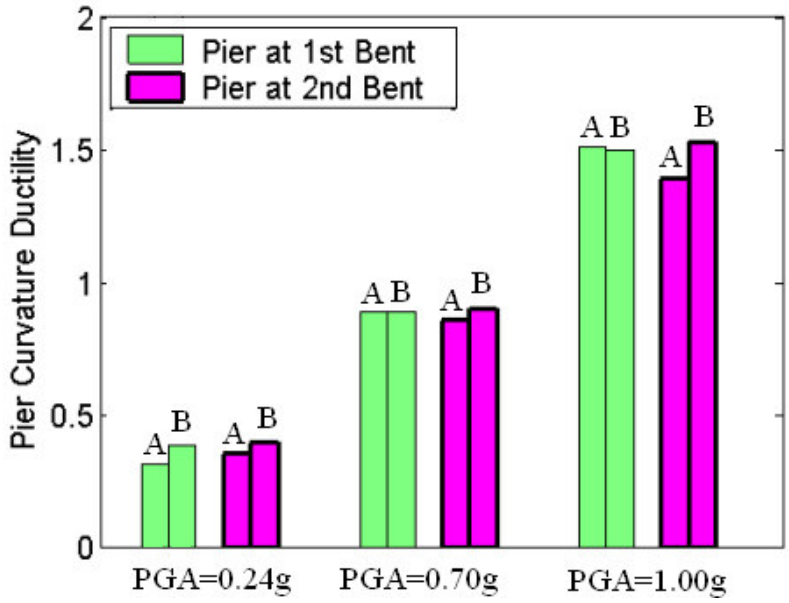

(a) Pier Curvature Ductility

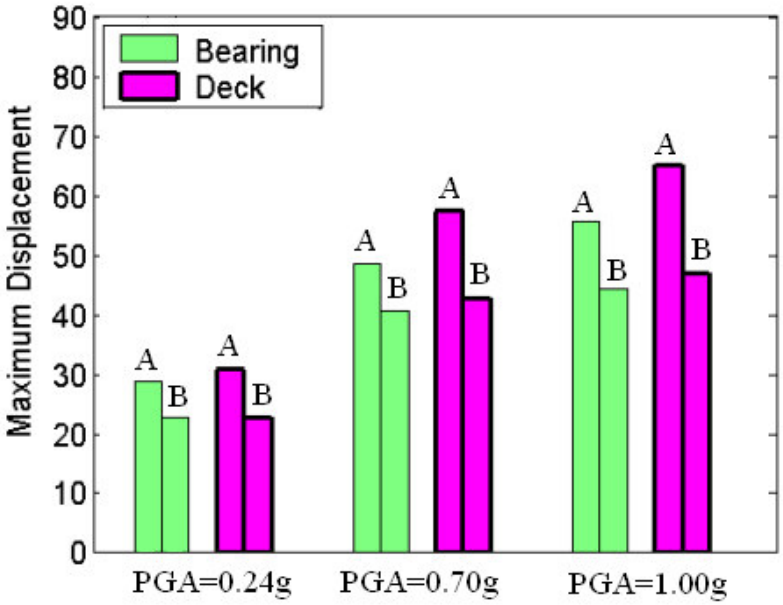

(b) Maximum Displacement of Bearing and Deck

Figure 6-26. Comparison of the Effect of Two Retrofit Strategies for MSSS Bridge

A: Replacement of Steel Bearing by Elastomeric Bearing

B: Retrofit by Combination of Span Continuity and Elastomeric Bearing.

CHAPTER 7

FRAGILITY ANALYSIS OF RETROFITTED BRIDGES

The fragility analysis of both multi-span continuous and multi-span simply supported bridges with the various retrofit strategies discussed in previous chapter has been carried out to investigate the effectiveness of the different retrofit options. Fragility curves are established for each retrofit scheme, and retrofit effectiveness is evaluated by comparing the fragility curves of the retrofitted bridges with those of the original bridges. The procedure of fragility analysis follows the same steps developed in Chapter 5. The regression equations used to calculate the fragility are provided in Appendix I and II for the MSC and MSSS bridges respectively.

7.1 Fragility Analysis of Retrofitted MSC Steel Bridge

7.1.1 Replacement of Steel Bearings by Elastomeric Bearings

Steel bearings in the multi-span continuous bridge have been replaced by elastomeric bearings as shown in Fig. 6-8. The actual value of the shear modulus G for the 50-durometer hardness elastomer varies in the range of 95 psi to 130 psi [AASHTO (1998)]. Ten samples of the bridge retrofitted with elastomeric bearings are generated by the Latin Hypercube Sampling approach assuming a normal distribution for the shear modulus with a mean value of 112.5 psi and COV of 0.095. The values of the shear modulus samples vary from 94.9 psi to 130.1 psi for a cumulative probability distribution between 5% and 95%. The other statistical bridge parameters are considered as described

in Chapter 5. The pairing sequence in Eq. (4-9) is applied to form a total of ten bridge samples.

Because of retrofitting by elastomeric bearings, the fundamental periods of the ten MSC bridge samples change from a range of 0.3~0.6 seconds in as-built condition to a range of 1.2~1.5 seconds. These fundamental periods are calculated by using the elastic stiffness of the elastomeric bearings. Hence, the elastomeric bearings isolate bridge columns from undesirable lateral forces acting on the superstructure, thereby reducing spectral accelerations drastically. Decreasing curvature demand on bridge piers because of reduced lateral loads leads to lower pier fragility of retrofitted bridges. Fig. 7-1 shows fragility curves for piers of the retrofitted bridge for different damage states by solid curves. For comparison, fragility curves for the as-built bridge are shown by dashed lines. Fig. 7-1 shows that elastomeric bearings reduce the seismic fragility of bridges significantly. For example, the probability of inducing yielding in the column's longitudinal reinforcements during an earthquake with PGA=0.8g is reduced from 90% for the as-built bridge to 60% for the retrofitted bridge. The probability of beginning of column strength degradation at PGA=1.2g is reduced from 80% for as-built bridge to a value close to 1% for the retrofitted bridge.

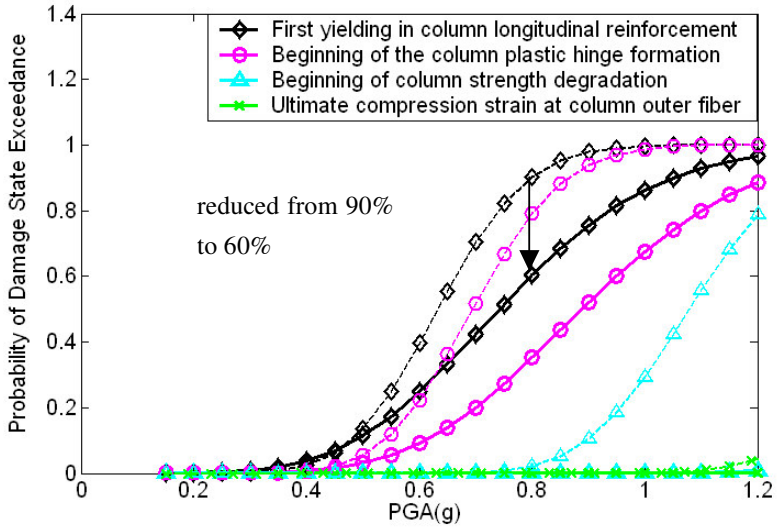

Figure 7-1. Fragility Curves of Piers for MSC Bridges Retrofitted by Elastomeric Bearings.

However, elastomeric bearings increase displacement demands at bearing supports, as compared to the as-built condition. For the fragility analysis of bearings for superstructure displacement, the capacity of the elastomeric bearings for fragility analysis must be reevaluated. The allowable seismic displacement for the rectangular elastomeric bearing is given by,

$$\Delta_b = B(1 - A'/A) \tag{7-1}$$

where A' is overlapping of top and bottom area of a bearing at the maximum displacement, and B is the side dimension of the bearing in the ground motion direction, as shown in Fig. 7-2. The seismic overlap factor A'/A is taken as 0.6 in this study [Skinner et al. (1993)]. Hence, the allowable value of Δ_b is $0.4B$. The longitudinal side dimension, B, is 250 mm for bearings EB1 and 350 mm for EB2. It has been observed from nonlinear seismic analysis of the retrofitted bridge that the bearing EB1 has a larger

displacement demand than the bearing EB2. Hence, bearing EB1 mounted on abutments has higher risk of failure than bearing EB2 mounted on pier bents. Fig. 7-3 shows fragility curves for elastomeric bearings in the retrofitted bridge and steel expansion bearings in as-built bridge. It is observed that the fragility of elastomeric bearings increases significantly as compared to steel bearings. However, the probability of failure of the bearings is still low for probable earthquakes in New York State. For example, the probability of failure of elastomeric bearings during a 1.0 PGA earthquake is 25% as compared to 9% for the as-built case. This slight increase in bearing fragility is at the benefit of reducing seismic fragility of the bridge piers significantly.

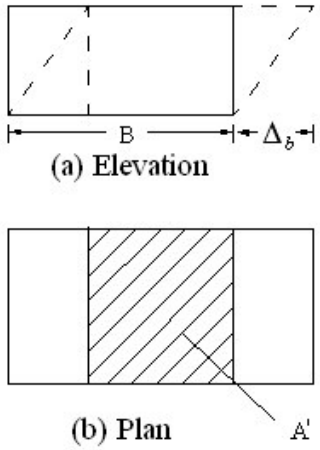

Figure 7-2. Sketch of Deformed Elastomeric Bearing

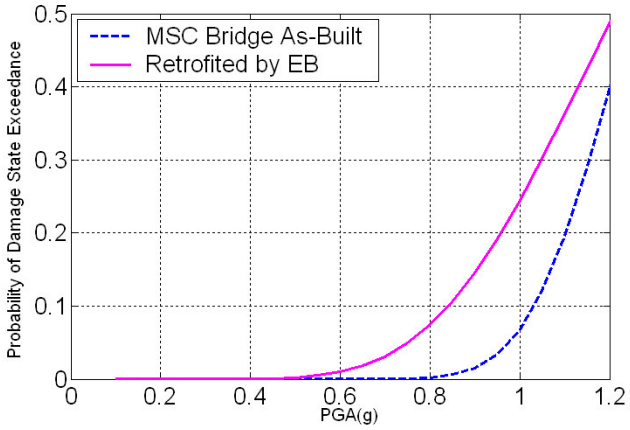

Figure 7-3. Fragility Curves of Bearings in as-Built MSC Bridge and Bridge Retrofitted by Elastomeric Bearings.

7.1.2 Replacement of Steel Bearings by Lead-Rubber Bearings

The fragility analysis is performed for MSC bridges retrofitted by the lead-rubber bearings LRB1 and LRB2 described in Chapter 6. Since the dimensions of these bearings are the same as those of the elastomeric bearings EB1 and EB2, their displacement capacities are the same as those of EB1 and EB2, respectively, and are defined by Eq. (7-1). However, the energy dissipation capability of the lead-core in LRBs is useful in reducing both the bearing displacement and the pier curvature ductility simultaneously. Fig. 7-4 presents fragility curves for pier curvature ductility for the bridge retrofitted by lead-rubber bearings for different damage states. For comparison, the corresponding fragility curves for the as-built bridge and the bridge with elastomeric bearings are also shown. It is observed that the fragility curves for the elastomeric and lead-rubber bearings are quite close to each other. Slightly higher pier ductility for lead-rubber bearings is caused by the reduced isolation effect because of the higher effective shear stiffness of the lead-core. For PGA less than 0.57g, LRB has a higher fragility than the as-built

bridge (i.e., negative retrofit effect), since the bridge isolated with LRB exhibits a behavior similar to a bridge with a fixed-connection during small bearing displacements due to very high initial stiffness of the bearing before lead core yields [Skinner, et al. (1993)]. In this situation, LRB may impart seismic inertial forces even larger than those observed in the as-built case, and transfer undesired lateral forces to the substructure. Hence, the application of lead-rubber bearing in MSC bridges is recommended only for strong design-level earthquakes, i.e., with PGA at least larger than 0.6g in the New York State region.

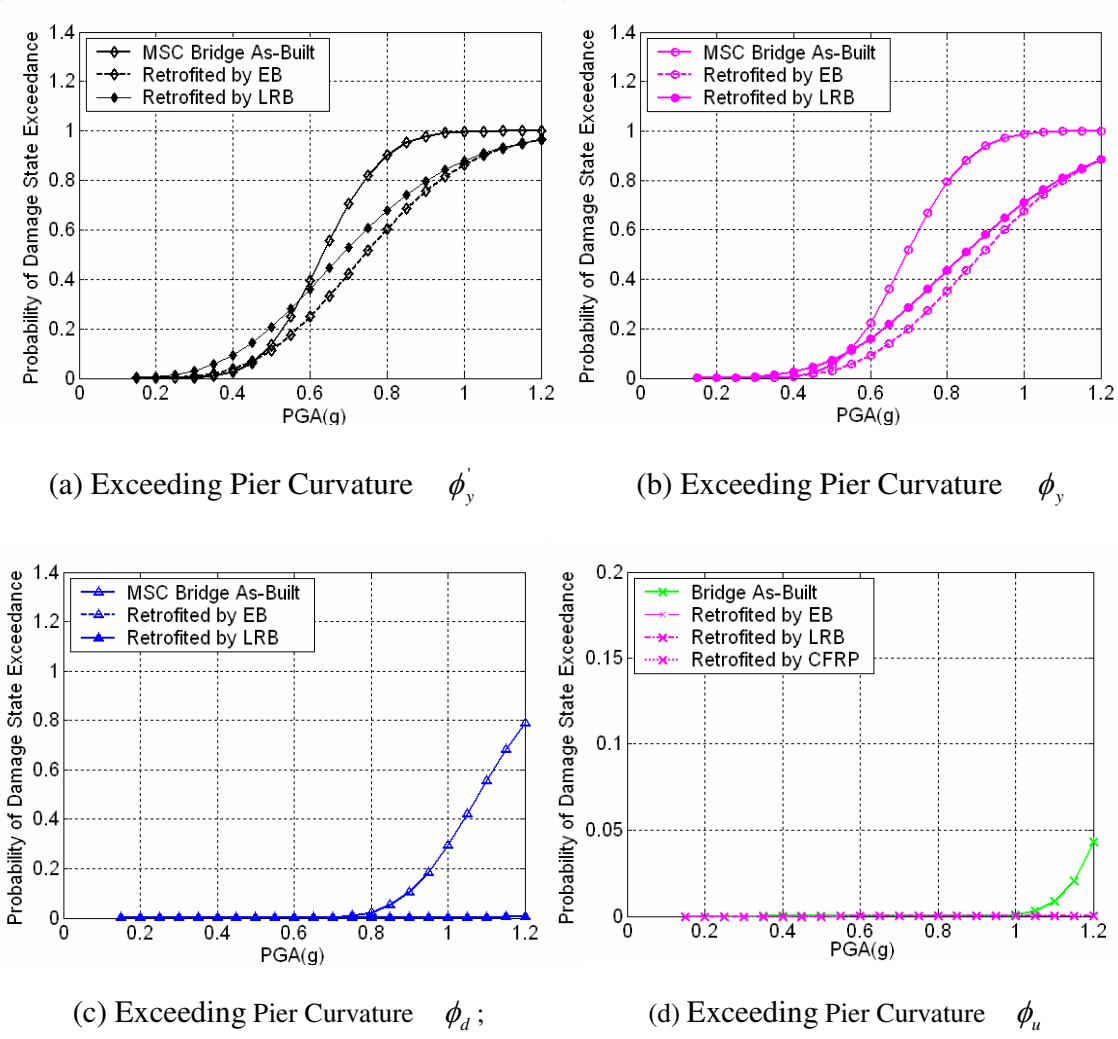

(a) Exceeding Pier Curvature $\phi_y^{'}$

(b) Exceeding Pier Curvature ϕ_y

(c) Exceeding Pier Curvature ϕ_d;

(d) Exceeding Pier Curvature ϕ_u

Figure 7-4. Fragility Curves of Piers versus PGA for MSC Bridges at the Damage States: (a) First yielding in column longitudinal reinforcement; (b) Beginning of column plastic hinge formation; (c) Beginning of column strength degradation; (d) Ultimate compression strain at column outer fiber.

Fig. 7-5 shows pier curvature fragility surfaces for bridges retrofitted by lead-rubber bearings. Unacceptable types of damage due to strength degradation and column collapse have almost been eliminated by retrofitting the bridge with LRB.

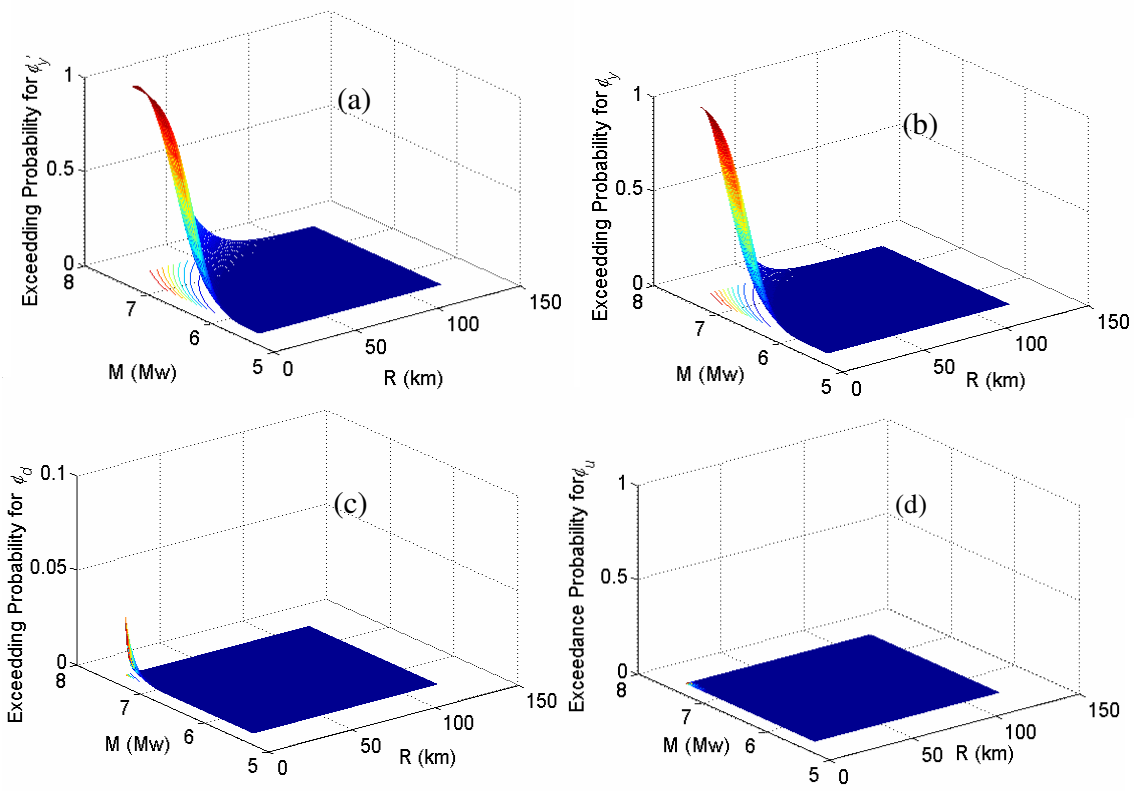

Figure 7-5. Fragility Surfaces of Piers for MSC Bridges Retrofitted by Lead-Rubber Bearings at Different Damage States: (a) ϕ_y'; (b) ϕ_y; (c) ϕ_d; (d) ϕ_u.

The retrofit effect of lead-rubber bearings and elastomeric bearings can be compared using cut sections or contour maps of fragility surfaces. In Fig. 7-6, contour curves for the 50% probability of exceeding the yield curvature ϕ_y have been plotted for three cases. The contour curves in the upper left corner of the plot show a range of earthquake magnitudes and epicentral distances to cause plastic hinges at pier bottoms with more

than 50% probability. This range of M_w and R has been significantly narrowed by bearing replacement. It is again observed that elastomeric bearings perform better than LRB, since EB has narrower area between the upper left hand corner of the plot and the solid contour curve.

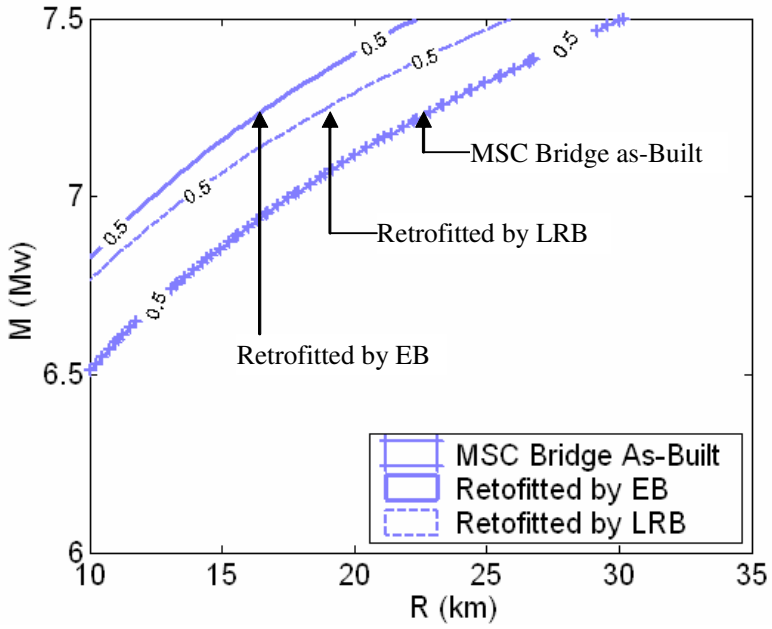

Figure 7-6. Fragility Contour for Pier Curvature Ductility in MSC Bridges for Damage State ϕ_y.

The main advantage of lead-rubber bearings over elastomeric bearings is in terms of lower superstructure displacement. A reasonable design of lead-rubber bearings can assure a desirable level of performance in terms of reducing both the pier curvature ductility and the superstructure displacement. Fig. 7-7 compares the fragility curves obtained by using elastomeric and lead-rubber bearings. It is observed that LRBs reduce the probability of collapse of a bridge because of bearing failure significantly.

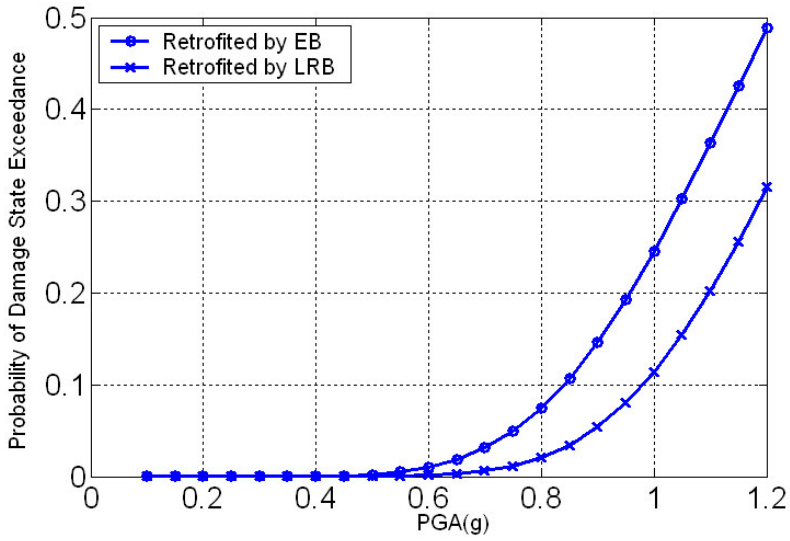

Figure 7-7. Fragility Curves of Bearings in MSC Bridges Retrofitted by Elastomeric and Lead-Rubber Bearings.

7.1.3 Elastomeric Bearings with Supplementary Viscous Dampers

It was seen in Chapter 6 that viscous dampers in parallel with elastomeric bearings can effectively reduce pier curvature ductility as well as bearing displacement. The fragility analysis is executed for the MSC bridge retrofitted by this combination designed for damping coefficients of 0.25, 0.50, 0.75 and 1 kip-sec/in. Fig. 7-8 (a) and 7-7 (b) show fragility curves for bridge pier curvature ductility for first two damage states, i.e., yielding in column longitudinal reinforcement and beginning of the column plastic hinge formation. These plots also show fragility curves for the bridge without viscous dampers, i.e., bridge retrofitted by elastomeric bearings only. Damage states for strength degradation and ultimate collapse have been effectively eliminated by the isolation effect of the elastomeric bearings. It is observed that viscous dampers with large damping

coefficients contribute to further reduction in the probability of damage in the first two pier curvature damage states significantly. Fig. 7-9 shows the fragility curves for bearing displacement damage states. It is observed that the probability of limit state exceedance at PGA=1.2g are 41%, 36%, 32% and 28% for the multi-span continuous bridges retrofitted by combinations of elastomeric bearings and viscous dampers with coefficients 0.25, 0.50, 0.75 and 1 kip-sec/in, respectively. The probability of exceedance for the bridge without viscous dampers (i.e., with elastomeric bearings) is 49% at 1.2g PGA. Hence, the combination of elastomeric bearings and properly designed viscous dampers can reduce both pier curvature ductility and bearing displacement effectively.

Fig. 7-10 shows fragility contours of the bridge retrofitted by a combination of elastomeric bearings and viscous dampers. The contour lines in Fig. 7-10 give M_w and R values for 50% probability of column plastic hinge formation. It is observed that multi-span continuous bridges located at $R = 10$ km from the epicenter have more than 50% probability of developing plastic hinges and inelastic deformation in piers during earthquakes of $M_w \geq 6.5$. In the same sense, an earthquake with M_w=7.5 will cause more than 50% probability damage for bridges situated at $R \leq 30$ km. This probability decreases drastically after the bridge has been retrofitted by elastomeric bearings in combination with viscous dampers. For example, for bridges retrofitted by elastomeric bearings in parallel with viscous dampers with coefficient c = 1 kip-sec/in, 50% probability of developing plastic hinges for bridges located at 10 km from the epicenter will occur only for earthquakes with $M_w \geq 7.1$. Similarly, an earthquake with M_w=7.5 will only cause more than 50% probability damage for bridge situated at $R \leq 16$ km. This

again demonstrates that viscous dampers can be used effectively to retrofit bridges to increase the seismic resistance of bridges.

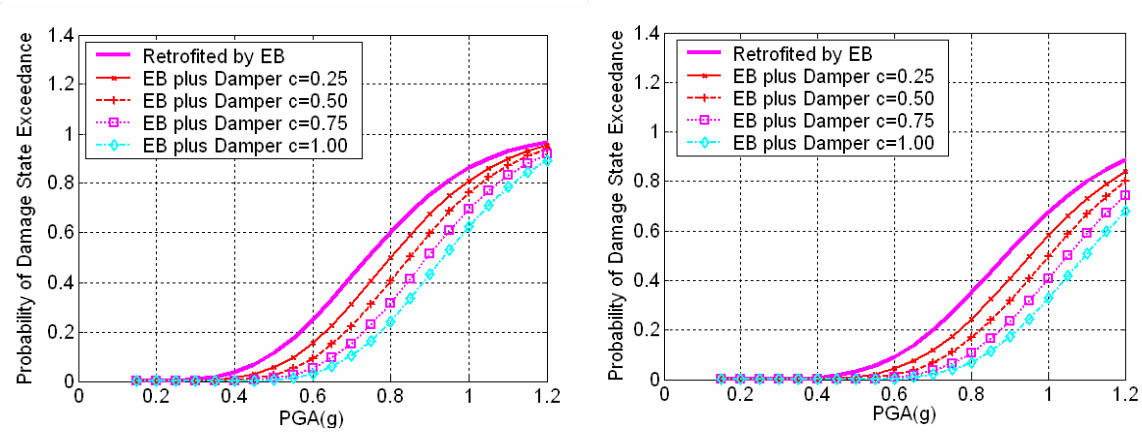

(a) Exceeding Pier Curvature $\phi_y^{'}$ (b) Exceeding Pier Curvature ϕ_y

Figure 7-8. Fragility Curves of Piers versus PGA for MSC Bridges Retrofitted by Elastomeric Bearings in Combination with Viscous Dampers with Damping Coefficients c = 0.25, 0.50, 0.75, and 1.00 kip-sec/in.

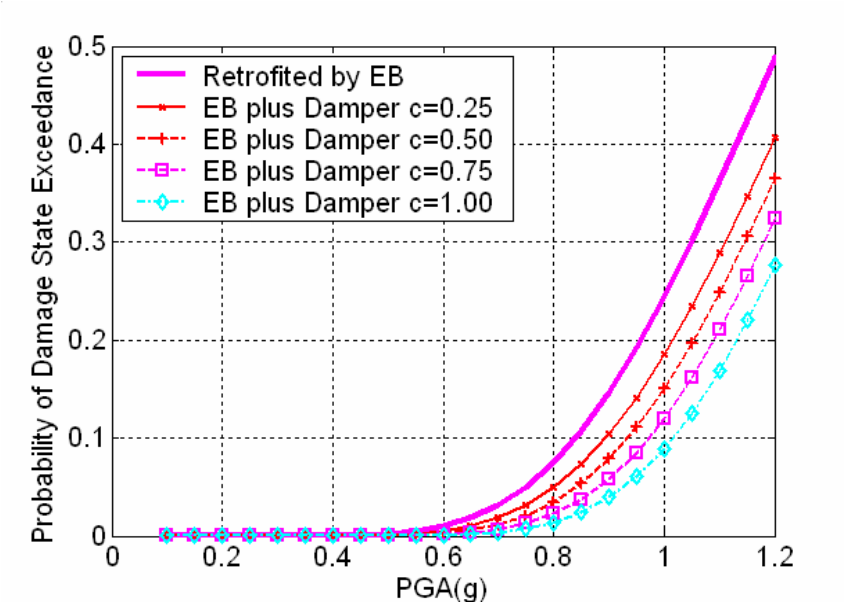

Figure 7-9. Fragility Curves for Elastomeric Bearings in Combination with Viscous Dampers in Retrofitted MSC Bridges.

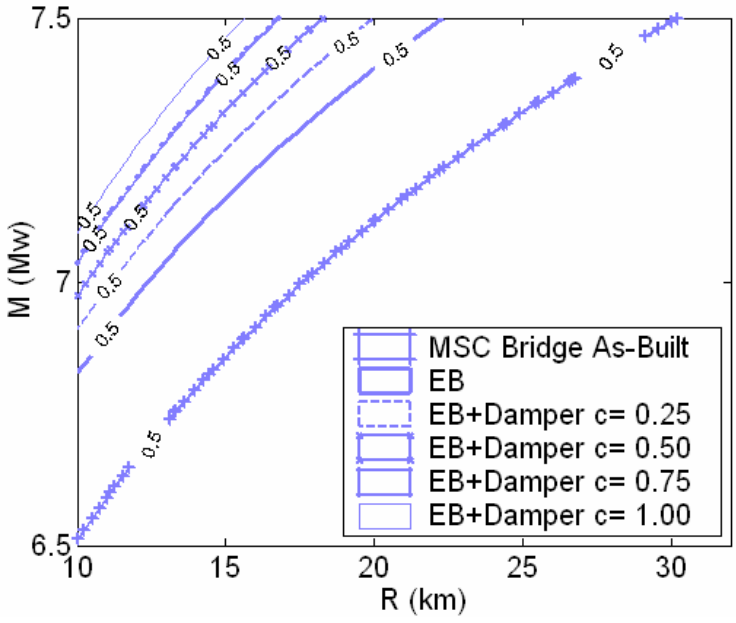

Figure 7-10. Fragility Contours of Bridge Piers in MSC Bridges for Probability of Exceeding ϕ_y.

7.1.4 Pier Confinement by Carbon Fiber Jackets

Six layers of carbon fiber reinforced plastic (CFRP) jackets with a total thickness of 0.93 mm have been designed for piers of multi-span continuous bridges. This design of CFRP is based on median strengths of concrete and steel with a target to double the pier curvature capacity through CFRP wrapping. Ten bridge samples with different concrete compressive strength $f_c^{'}$ and modulus of elasticity E_c due to uncertainty in confined concrete strength need to be statistically generated using the LHS method. Hence, actual capacity upgrading ratios because of FRP jacketing should be investigated for each bridge sample. For this purpose, a computer program to establish axial stress and strain relationships of CFRP confined concrete using Lam and Teng's Model [Lam and Teng (2003), Teng and Lam (2004)] was developed. Fig. 7-11 shows the stress-strain relationship for the 10 bridge samples with piers retrofitted by CFRP. The depth of neutral axis of the confined concrete section at the ultimate load is found for each bridge sample by considering the uncertainty in pier normal force and yield strength, f_y, of reinforcing bars. For example, Fig. 7-12 shows stress and strain distributions for bridge sample No.6 of Fig. 7-11 at the ultimate state when the longitudinal concrete compressive strain reaches 0.0124, and the lateral strain of concrete reaches the ultimate strain of the CFRP and fiber hoop fractures. After the state of first hoop fracture, there is a sudden drop in compressive load capacity. This state is considered as the ultimate condition. The neutral axis depth y is found as 167 mm for this sample, which is less than 1/4 of the cross section depth. Table 1 shows the neutral axis, the ultimate concrete compressive strain, and the ultimate curvature capacity $\phi_u = \varepsilon_{cu} / y$ for each of the ten bridge samples. It is observed from Table 1 that CFRP jackets effectively increase the compressive

strength and ultimate strain of concrete. Actual ratios of curvature capacity of bridge with and without CFRP for the10 bridge samples are scattered from 1.92 to 2.23 around the target ratio of 2, as shown in Fig. 7-13. The small scatters around the target value of 2 demonstrate that the design equation in Eq. (6-14) can be used to predict capacity of bridge piers with CFRP jackets reliably.

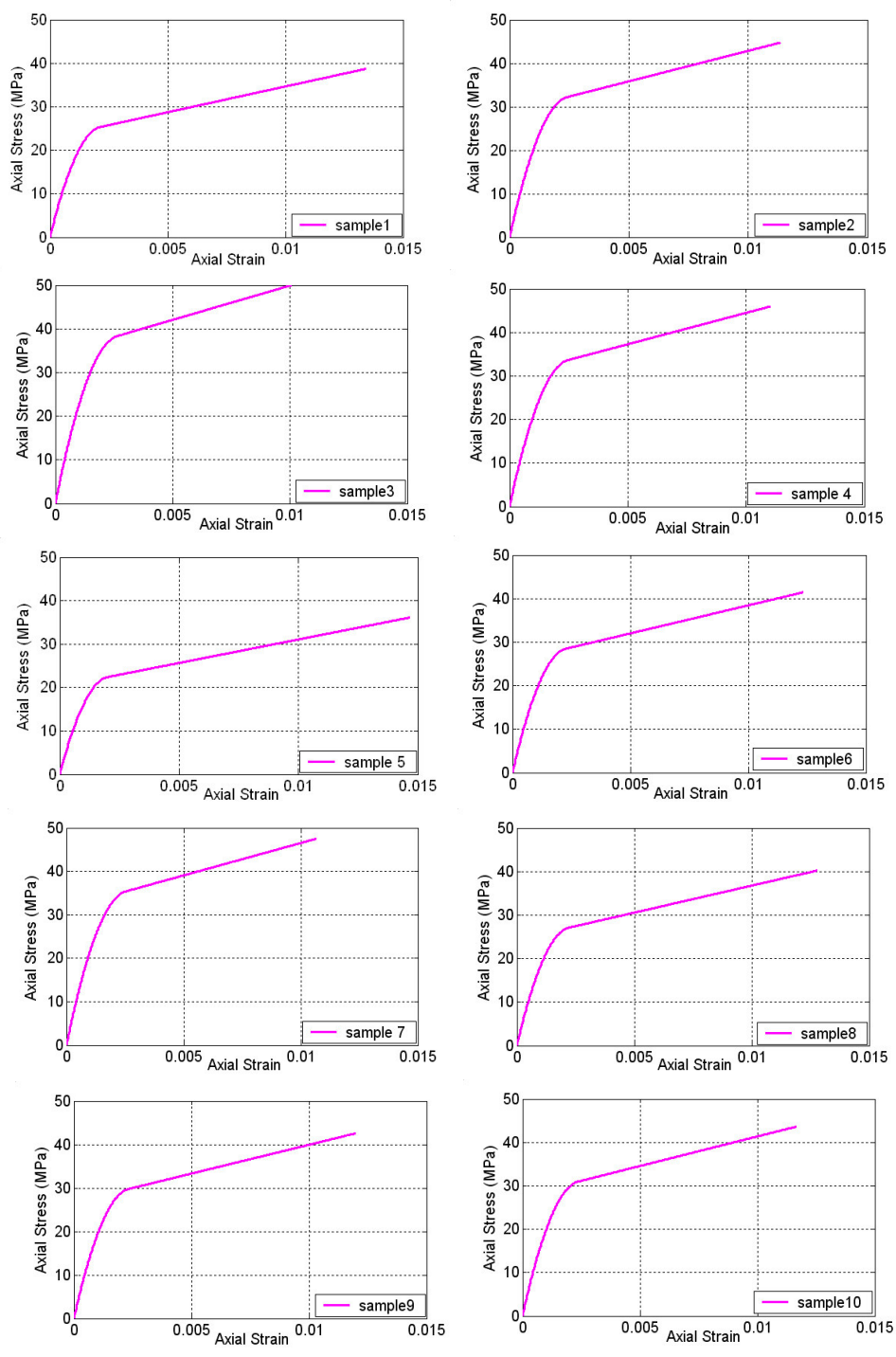

Figure 7-11. Axial Stress-Strain Relationships of piers of MSC Bridge Samples wrapped by CFRP.

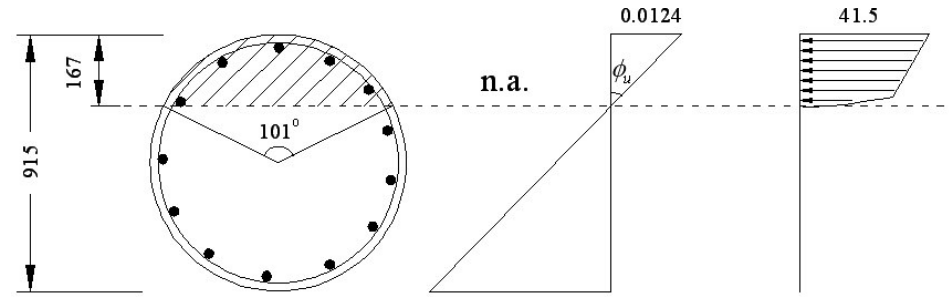

(a) Ultimate Condition

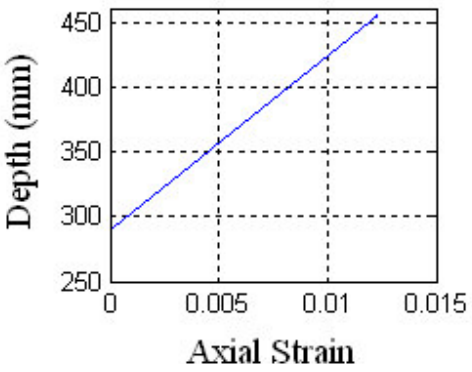

(b) Compressive Strain Distribution

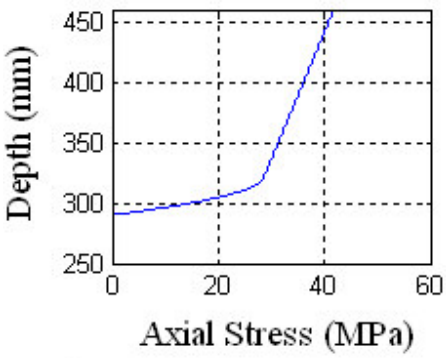

(c) Compressive Stress Distribution

Figure 7-12. Stress and Strain Distributions of CFRP-Confined Cross Section of Piers in a MSC Bridge Sample (Unit: mm, MPa).

Table 7-1. Ultimate Curvature Capacity for Piers in MSC Bridge Samples Retrofitted by CFRP Jackets.

Samples	Neutral Axis (in)	Angle α	Ultimate Strain ε_{cu}	Curvature Capacity (1/in)	Ductility $\phi_{cu} / \phi_y^{'}$	Enhanced Ratio
1	7.08	105.3	0.0134	0.0018990	26.2	2.23
2	6.21	98.1	0.0114	0.0018304	25.2	2.07
3	5.79	94.5	0.0101	0.0017516	23.3	1.92
4	6.26	98.5	0.0110	0.0017646	22.3	2.00
5	7.52	108.8	0.0147	0.0019563	22.9	2.17
6	6.57	101.2	0.0124	0.0018811	22.7	2.08
7	6.60	101.4	0.0107	0.0016171	18.8	1.94
8	6.67	102.0	0.0128	0.0019202	21.9	2.06
9	6.87	103.6	0.0120	0.0017455	18.8	1.97
10	6.99	104.6	0.0117	0.0016691	16.9	1.92

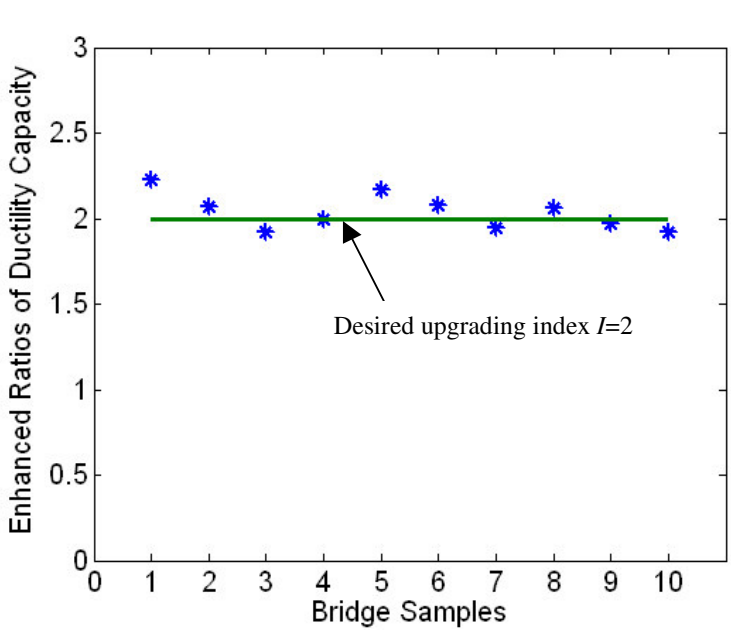

Figure 7-13. Enhanced Ratios of Pier Curvature Ductility Capacity for CFRP Confinement Designed with Upgrading Index *I*=2.

In the above discussions, transverse steel reinforcements in the plastic hinge zone are considered as effective confinement for piers in the as-built condition. In actual construction practice, welded hoops or interlocking spirals are used for effective confinement of concrete. Otherwise, the ultimate pier curvature capacity only lead to an ultimate strain ε_{cu} = 0.005 for poorly confined columns. With CFRP jacketing, regardless of the confinement contribution of existing steel hoops, carbon fiber jackets can ensure a significant increase in the ultimate concrete strain and the expected ultimate curvature capacity. The histogram in Figs. 7-14 and Fig. 7-15 shows the ultimate compressive strains and ultimate curvature capacities of piers poorly confined by steel hoops, effectively confined by steel hoops, and confined by CFRP jacket cases. Although the ultimate flexural strength M_u of all the piers is not significantly affected by CFRP

jacketing, the flexural strength will not degrade in FRP-confined column until the rupture of CFRP. This is due to the fact that CFRP composites remain linear elastic and the lateral confining pressure they produce increases monotonically until rupture point. The chance of column strength degradation is insignificant for the columns wrapped by CFRP studied in this thesis.

Fig. 7-16 shows fragility curves for column strength degradation and ultimate condition damage states for the bridge in a as-built condition. Fragility curves for the ultimate condition damage states are presented for the cases of poorly confined and well confined concrete. Fig. 7-16 also shows the fragility curve for the column wrapped by CFRP for ultimate condition damage state. It is observed that fragility curves for the first two damage states, i.e., yielding in column longitudinal reinforcement and beginning of the column plastic hinge formation, will not be affected by FRP jacketing, and will be the same as those of the as-built bridge. The fragility curves corresponding to column strength degradation and column collapse damage states are replaced by tensile failure of jacket damage state (ultimate condition) in case of FRP wrapped columns. Because the chance of FRP rupture is small, this implies that the seismic risk of serious damage or collapse of bridge columns can be eliminated through CFRP wrapping of concrete columns for the MSC bridge in New York State.

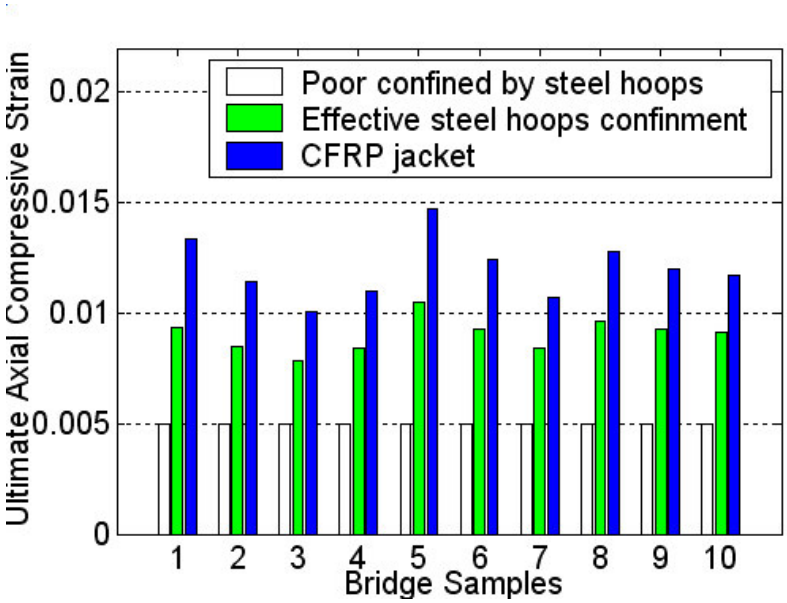

Figure 7-14. Ultimate Concrete Compressive Strain of Piers for as-Built and Retrofitted MSC Bridge Samples.

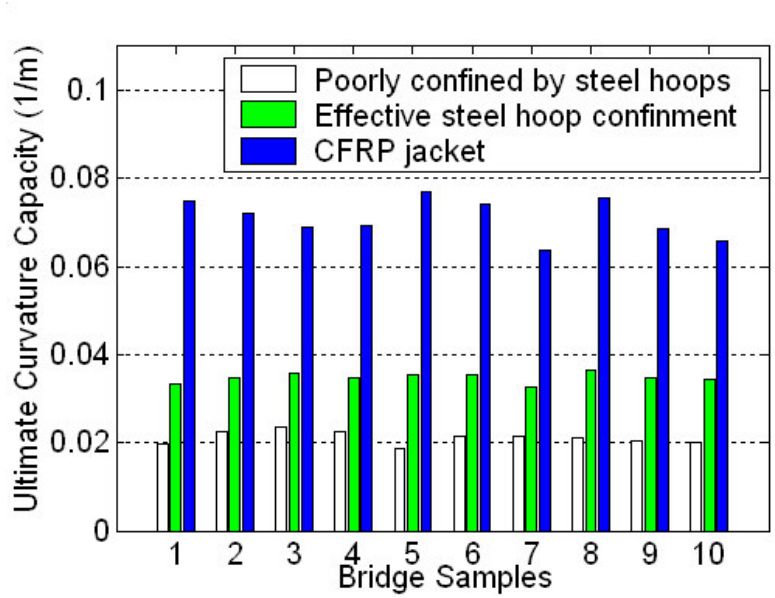

Figure 7-15. Ultimate Curvature Capacities of Piers for as-Built and Retrofitted MSC Bridge Samples.

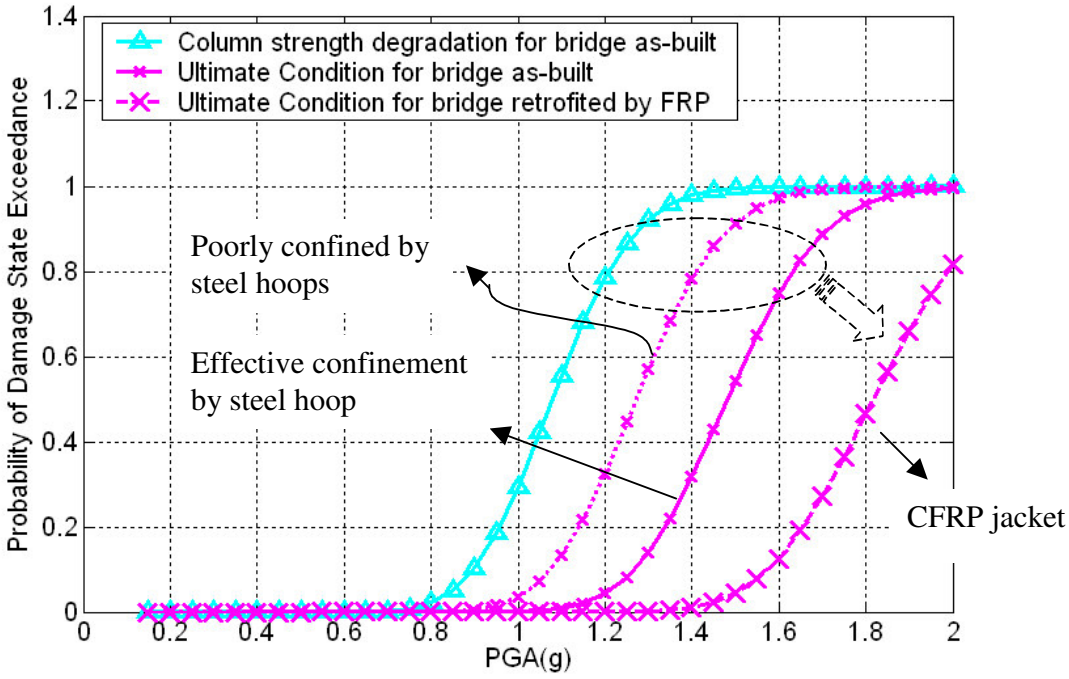

Figure 7-16. Fragility Curves of Piers versus PGA for MSC Bridges Retrofitted by CFRP Jackets.

This demonstrates that proper confinement of columns by CFRP can ensure a significant increase in pier curvature ductility capacity in the plastic hinge regions. Columns wrapped with CFRP require less maintenance and have a longer service life. Confinement by CFRP may be beneficial in non-seismic cases too, where, for instance, survivability during explosive attacks is required or axial load capacity of a column must be increased to accommodate increased traffic flow on a highway bridge [Bakis et al. (2002)].

7.1.5 Comparison of Retrofit Effects on MSC Steel Bridge

Figs. 7-17 and 7-18 shows comparisons between fragility curves using the four different retrofit strategies analyzed in this chapter. Elastomeric bearings effectively

reduce pier curvature fragility at the risk of increased fragility of bearing displacement. The increase in displacement demand is addressed through energy dissipation using viscous dampers or lead-cores in the elastomeric bearings. For moderate seismic regions, like North Eastern United States, viscous dampers generally show better performance than lead-rubber bearing since they can effectively reduce both displacement and pier curvature demands. An optimum seismic risk management strategy can be developed by choosing the damper coefficients appropriately to reduce overall seismic fragility of the bridge system below certain target levels. Lead rubber bearings limit bearing displacement by energy dissipation at the cost of a slight increase in pier curvature ductility. The effectiveness of LRB in reducing seismic fragility due to deck displacement is similar to that of elastomeric bearings in parallel with a viscous damper with damping coefficient c = 0.75 kip-in/sec. FRP jacketing effectively prevents column collapse by increasing the ultimate curvature capacity of the plastic hinge. For an earthquake with PGA=0.8g, the probability of forming a plastic hinge in a bridge pier reduces from 80 % for the as-built case to 44% after retrofit by lead-rubber bearings, 35% after retrofit by elastomeric bearings, and 7% after retrofit by combinations of elastomeric bearings with viscous dampers of coefficient c = 1.00 kip-in/sec. The probabilities of exceeding bearing displacement for these cases are 40%, 49%, 32% and 28% respectively. All four retrofit strategies can successfully eliminate potential problems with bridge column collapse during strong earthquakes. However, the retrofit strategy consisting of elastomeric bearings in parallel with a viscous damper with damping coefficient c = 1.00 kip-in/sec is the most effective approach in reducing the seismic fragility of both bridge pier curvature ductility and deck displacement.

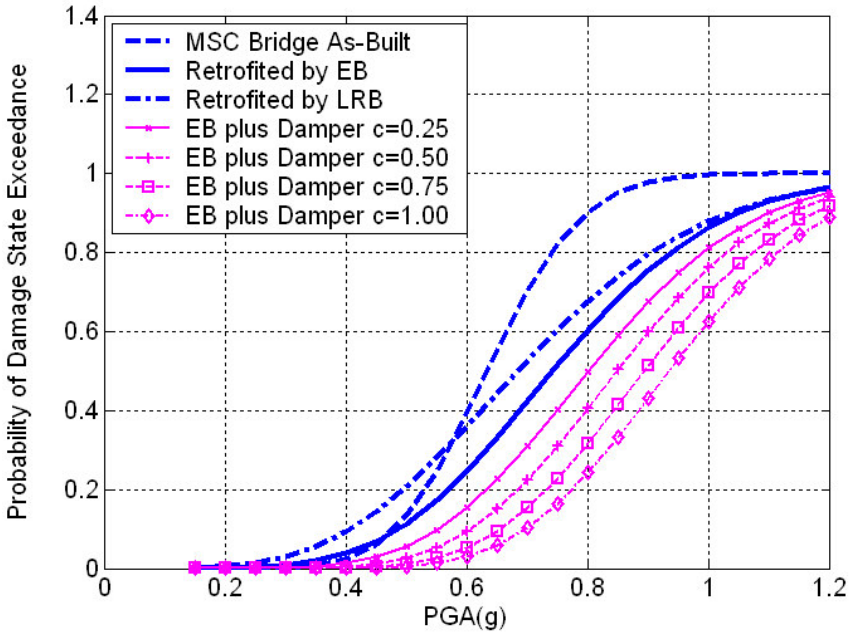

(a) Exceeding Pier Curvature $\phi_y^{'}$

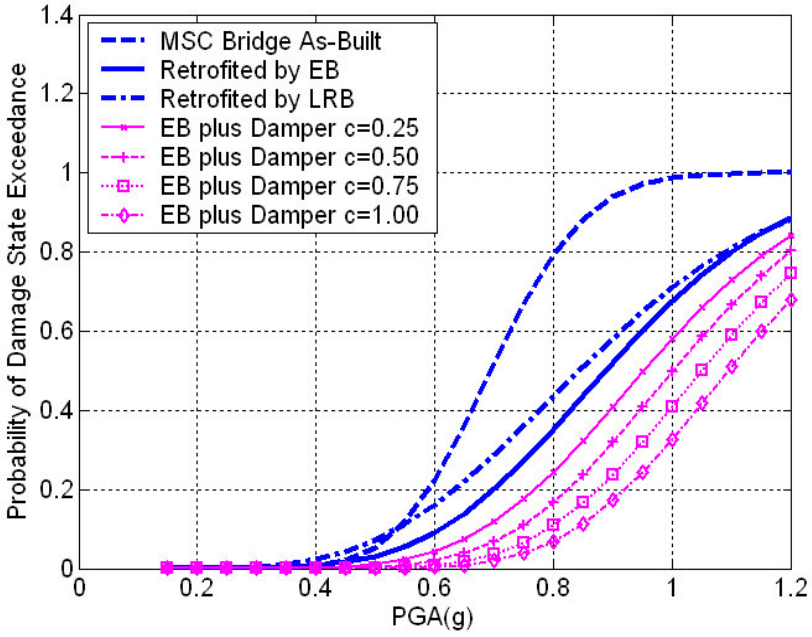

(b) Exceeding Pier Curvature ϕ_y

Figure 7-17. Fragility Curves of Piers versus PGA for MSC Bridges

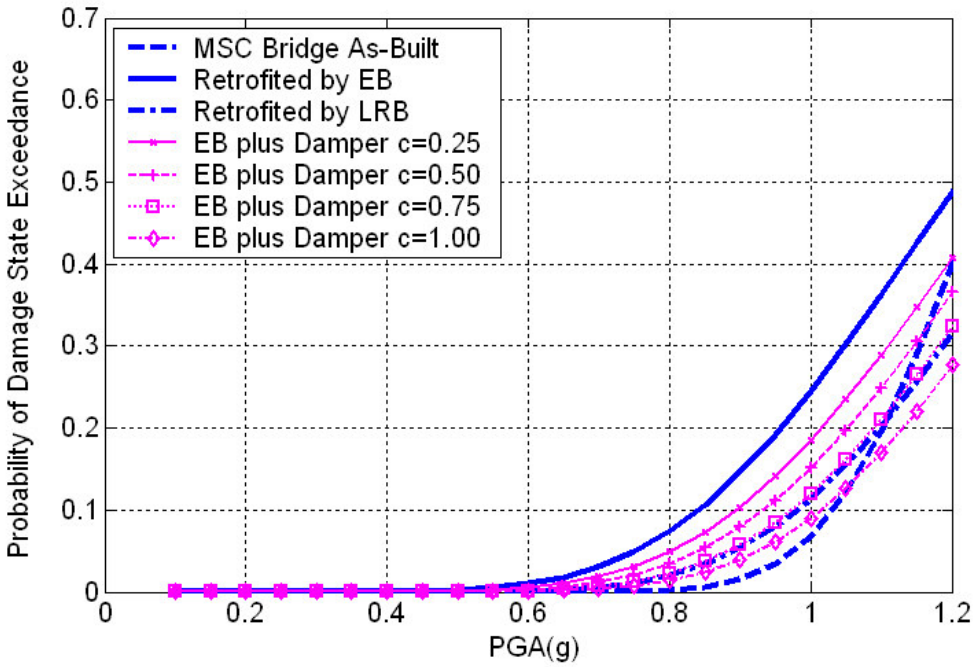

Figure 7-18. Fragility Curves of Bearings versus PGA for MSC Bridges.

7.2 Fragility Analysis of Retrofitted MSSS Steel Bridge

7.2.1 Replacement of Steel Bearings by Elastomeric Bearings

The natural periods of the multi-span simply supported bridge samples elongate from around 0.4 seconds for as-built case to around 1.1 seconds after the bridge was retrofitted by elastomeric bearings. Fig. 7-19 shows fragility curves for curvature ductility of piers of the retrofitted bridge. The median PGAs (with 50% probability of exceedance) are 0.78g and 1.06g for the first two column damage states, i.e. yielding in column longitudinal reinforcement and beginning of column plastic hinge formation. The other two more severe damage states, i.e. column strength degradation and concrete collapse,

have been eliminated because of retrofit by elastomeric bearings. These conclusions are verified through the fragility surfaces shown in Fig. 7-20 within the practical range of $M_w \le 7.5$ and $R \ge 10$.

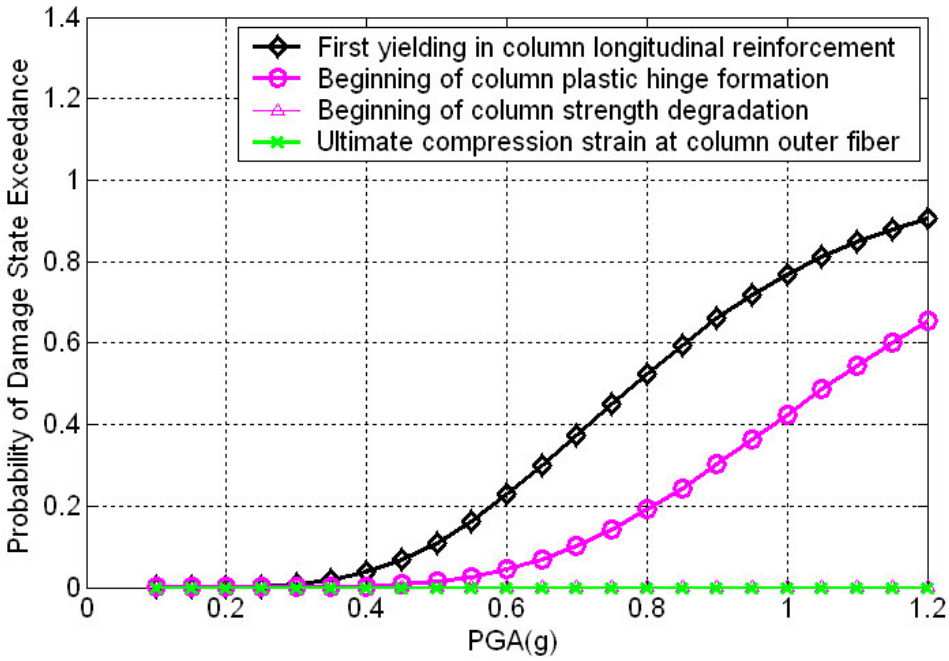

Figure 7-19. Fragility Curves of Piers versus PGA for MSSS Bridges Retrofitted by Elastomeric Bearings.

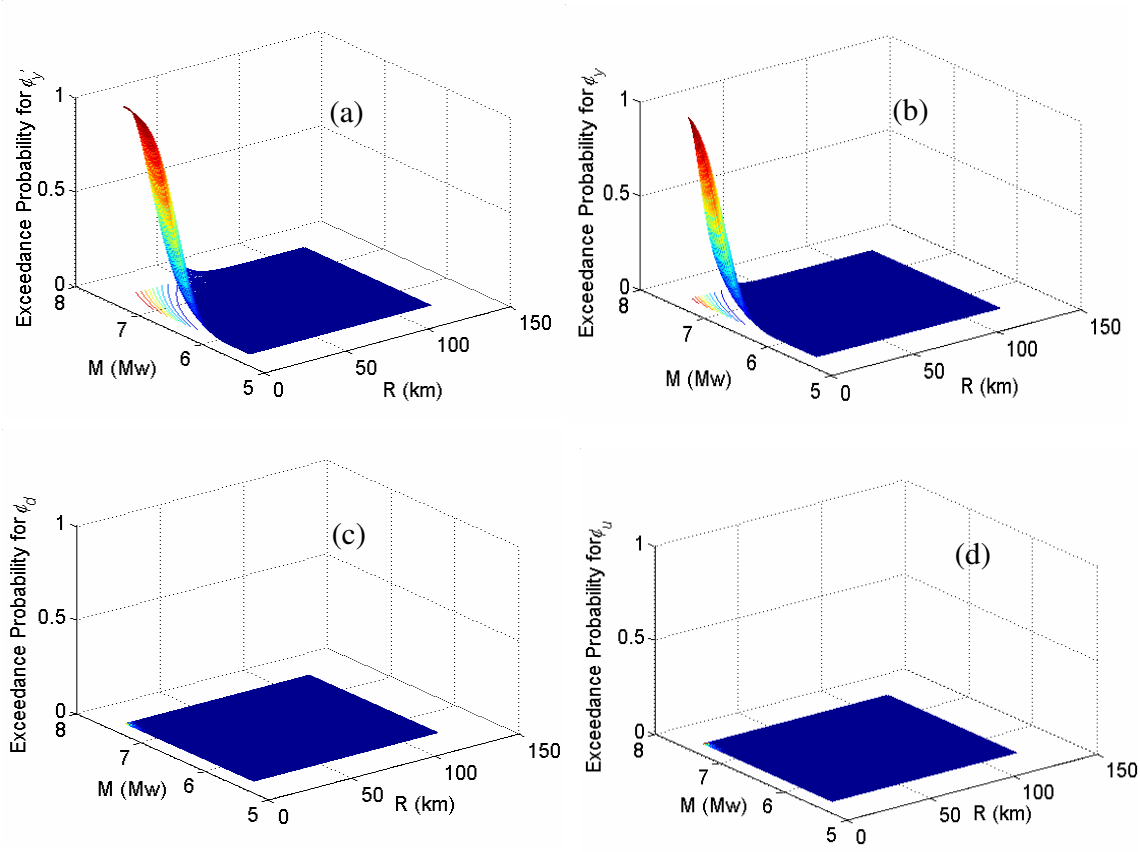

Figure 7-20. Fragility Surfaces for Different Damage States for Piers of MSSS Bridges Retrofitted by Elastomeric Bearings: (a) Pier Curvature $\phi_y^{'}$; (b) Pier Curvature ϕ_y; (c) Pier Curvature ϕ_d; (d) Pier Curvature ϕ_u.

Fixed steel bearings mounted on abutments in the as-built multi-span simply supported bridge have relatively larger probability of failing than steel expansion bearing and fixed steel bearings on pier bent. The failure of fixed steel bearings is because of bond fracture of anchor bolts and extensive spalling of concrete pedestals. After the replacement of fixed steel bearings and expansion bearings by elastomeric bearings, the load transfer mechanism of seismic forces in the bridge has been modified and the capacity of the bearings is effectively increased. Fig. 7-21 shows fragility curves for

bearing displacements after retrofit. It is observed that the fragility of the bearings is much lower after retrofit because of the reduced possibility of shear failure and toppling of the bearings. Other additional retrofit measures, such as viscous dampers or the use of lead-core in elastomeric bearings for energy dissipation, are not needed since the probability of failure is quite low in the practical range of PGAs.

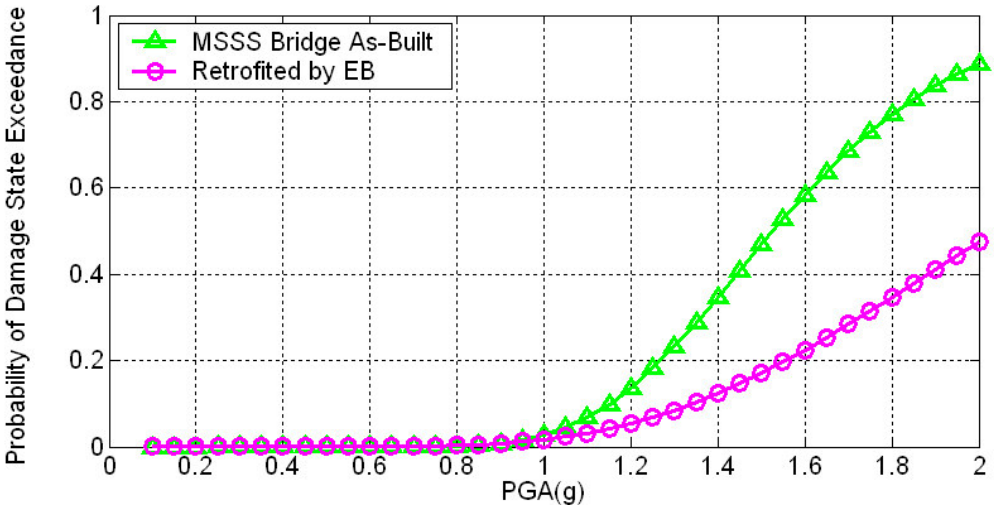

Figure 7-21. Fragility Curves versus PGA for Fixed Steel Bearings in as-Built and Elastomeric Bearings in Retrofitted MSSS Bridges

7.2.2 Retrofit by Combination of Span Continuity and Elastomeric Bearings

One option for retrofitting the multi-span simply supported bridge is to simultaneously make it continuous and install elastomeric bearings to enhance its structural integrity and solve leakage problems. The retrofit scheme has already been discussed in Chapter 6. The fragility curve for pier curvature ductility is shown in Fig. 7-22. Median PGAs (with 50% probability) for the first two damage states of yielding in

column longitudinal reinforcement and beginning of column plastic hinge formation are 0.74g and 1.02g. The fragility for the two other damage states, i.e. beginning of column strength degradation and column concrete collapse, is almost zero. Continuity also increases the resistance of the bridge to excessive superstructure displacements at the expansion joints by eliminating the possibility of having the displacements of the two adjacent spans out of phase. Fig. 7-23 (a) shows the fragility surface for the bearings in the bridge retrofitted by elastomeric bearings alone, and Fig. 7-23 (b) shows the fragility surface for the bridge retrofitted by continuity and bearing retrofits. It is observed that the probabilities of exceedance for bearing displacement are 34% and 5%, respectively, for the two retrofit cases.

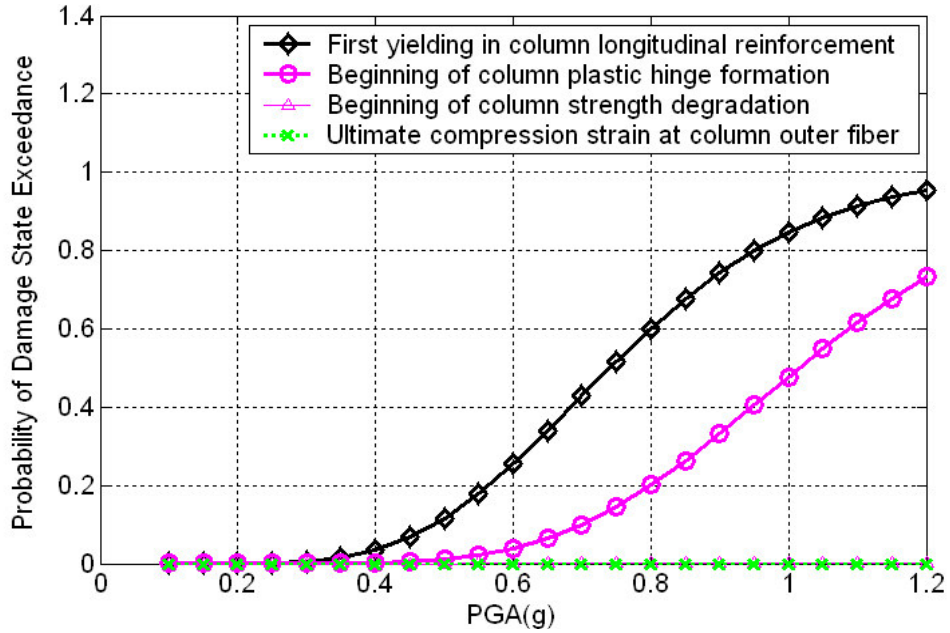

Figure 7-22. Fragility Curves of Piers versus PGA for MSSS Bridges with Continuity Retrofit and Elastomeric Bearings.

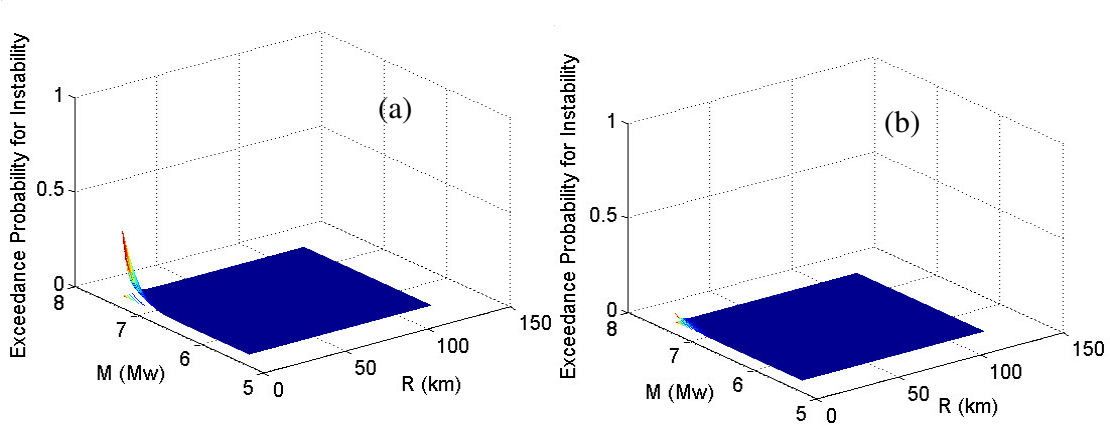

Figure 7-23. Fragility Surfaces of Elastomeric Bearings in Retrofitted MSSS Bridges.

7.2.3 Comparison of Retrofit Effects on MSSS Steel Bridge

Fig. 7-24 shows pier curvature fragility curves for the four damage states of the piers of the multi-span simply supported bridge. It is observed that the two retrofit strategies have almost the same seismic fragility for the first two damage states. This can also be verified from the fragility contour at 50% exceedance probability in Fig. 7-25 for the two retrofit cases. In fact, continuity plus elastomeric bearings increase the fragility slightly more than that of elastomeric bearings. The median PGA for plastic hinge formation damage state is increased by both these two retrofit strategies to 1.0g from 0.63g in as-built case. For an earthquake with PGA=0.8g, the probabilities of forming plastic hinges in bridge piers are 86 % for the as-built case, and only 20% for the two retrofit strategies.

It is observed from Fig. 7-25 that as-built bridges located at $R \le 31$ km from epicenter have 50% probability of forming plastic hinges at column bottoms during earthquakes of $M_w = 7.5$. For bridges retrofitted by either of the two strategies, only

bridges located with $R \leq 19$ km have this probability for such an earthquake magnitude. Bearings of bridges retrofitted both by continuity and elastomeric bearings have only 5% probability of instability. Hence, continuity combined with elastomeric bearings for multi-span simply supported bridges can effectively reduce seismic fragility for both pier curvature ductility and bearing displacement.

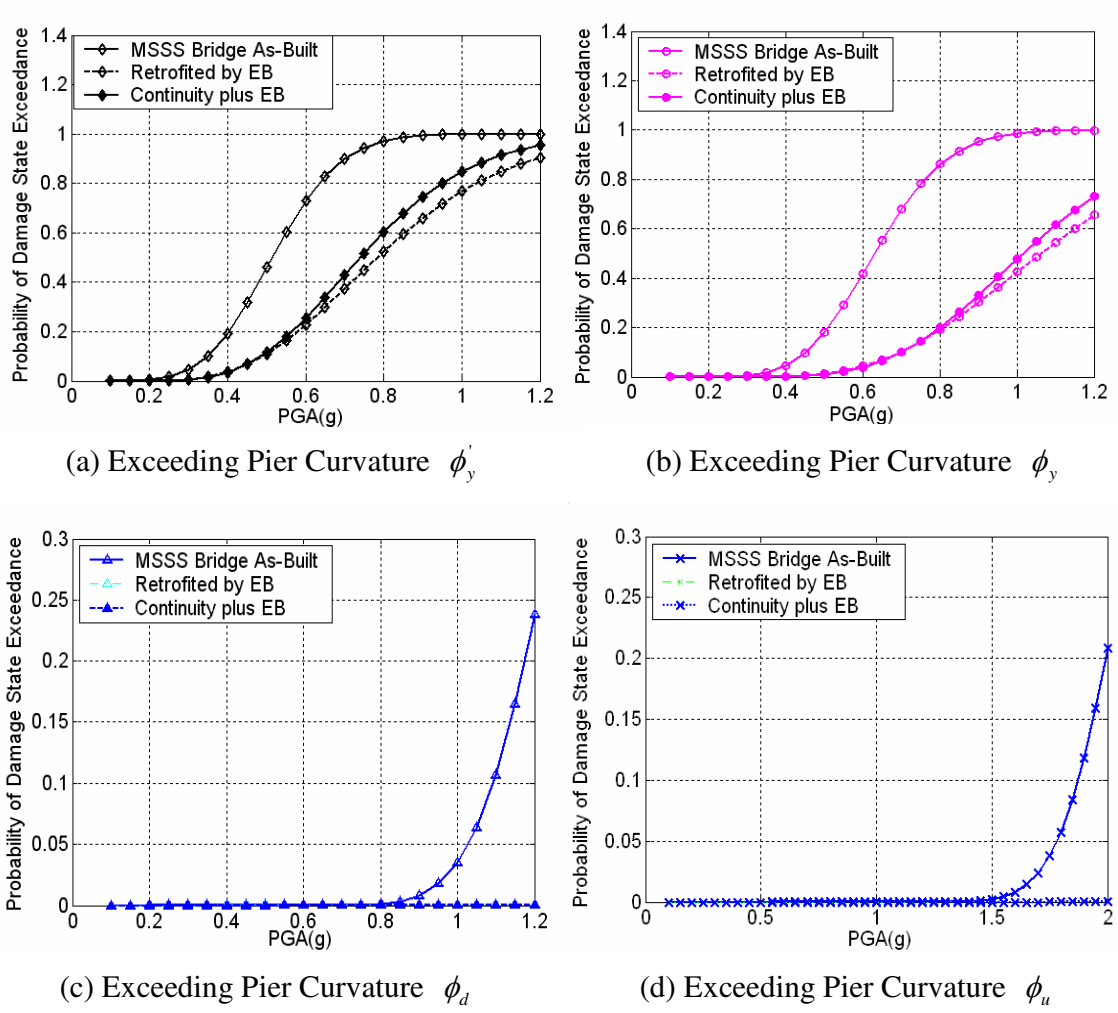

(a) Exceeding Pier Curvature $\phi_y^{'}$

(b) Exceeding Pier Curvature ϕ_y

(c) Exceeding Pier Curvature ϕ_d

(d) Exceeding Pier Curvature ϕ_u

Figure 7-24. Fragility Curves of Piers versus PGA for MSSS Bridges at the damage States: (a) First yielding in column longitudinal reinforcement; (b) Beginning of column plastic hinge formation; (c) Beginning of column strength degradation; (d) Ultimate compression strain at column outer fiber.

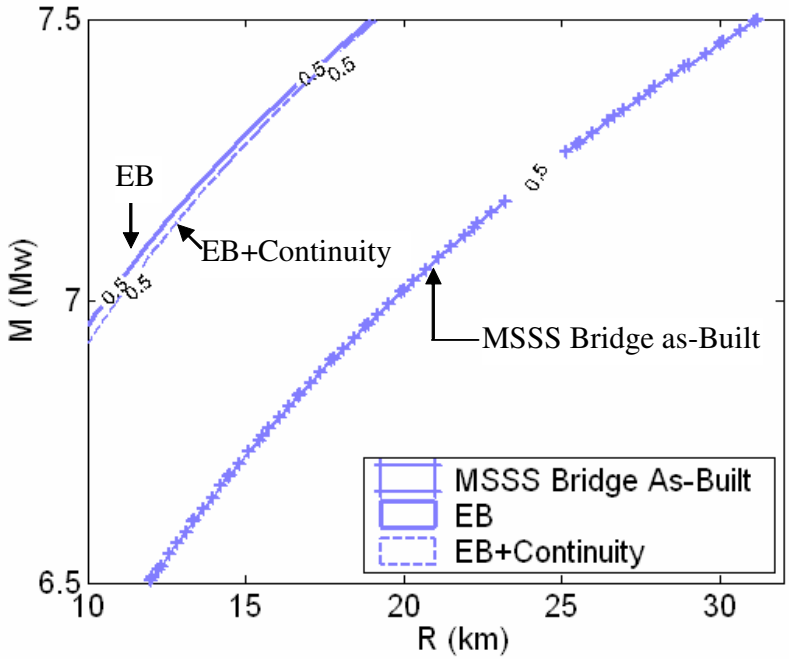

Figure 7-25. Contour Map of Bridge Piers in Retrofitted MSSS Bridges for Probability of Exceeding Pier Curvature ϕ_y.

7.3 Summary

The results of the fragility analyses for the original and retrofitted bridges are summarized in Table 7-2 through Table 7-4. Tables 7-2 and 7-3 show the changes in fragility of bridge piers at the limit state of plastic hinge formation. The analysis shows that isolators can significantly reduce pier fragility. This is due to the fact that the isolator help reduce the seismic demand on bridge columns. However, compared with elastomeric bearings (EB), lead rubber bearings (LRB) limit bearing displacements by energy dissipation at the cost of a slight increase in pier curvature ductility. This explains the higher reductions in fragility of bridges retrofitted by elastomeric bearings as compared to lead rubber bearings, observed when comparing column 3 and 4 to column 2 of Table 7-2. For continuous bridges, the combination of elastomeric bearings and viscous dampers could lead to an optimal retrofit effect with more effective reduction on fragility as shown in column 5 of Table 7-2.

As observed in Table 7-3, for simply supported bridges, the two retrofit strategies have similar effect on bridge piers. However, making the bridge continuous increases the resistance to seismic displacements and eliminates pounding between the decks. Therefore, the combination of elastomeric bearings and superstructure continuity could enhance both superstructure and substructure performance.

Table 7-4 displays the general retrofit effects as the median PGA is increased. This median PGA gives the values corresponding to 50% probability of exceeding slight, moderate, extensive, or ultimate damage. The table shows how retrofitted bridge can withstand higher PGA values at four different damage states. For example, slight damage will occur at 50% probability for original MSC bridge under earthquake PGA=0.6g. After

retrofit, MSC bridge may withstand slight damage under earthquakes with PGA up to 0.93g.

Table 7-2. MSC Bridge Pier Fragility at Damage State ϕ_y.

PGA	Original Bridge	Retrofitted Bridge		
		EB	LRB	EB+Damper
1.0g	100%	68%	71%	33% ~ 58%
0.7g	62%	20%	29%	2% ~ 12%
0.3g	0.2%	0%	0.2%	0%

Table 7-3. MSSS Bridge Pier Fragility at Damage State ϕ_y.

PGA	Original Bridge	Retrofitted Bridge	
		EB	Continuity +EB
1.0g	100%	43%	48%
0.7g	68%	10%	10%
0.3g	0.6%	0%	0%

Table 7-4. Median PGA for Bridges before and after Retrofitted at Four Damage States.

Damage States	Original MSC Bridge	Retrofitted MSC Bridge	Original MSSS Bridge	Retrofitted MSSS Bridge
Slight	0.60g	0.68g ~ 0.93g	0.51g	0.74g ~ 0.78g
Moderate	0.66g	0.84 g ~1.10g	0.63g	1.01g ~ 1.06g
Extensive	1.07g	> 1.2g	1.02g	> 1.2g
Ultimate	1.19g	> 1.2g	1.50g	> 1.2g

CHAPTER 8

CONCLUSIONS AND FUTURE RESEARCH

8.1 Conclusions

This thesis developed an improved methodology to perform the fragility analysis of typical steel bridges in New York State. The analysis leads to fragility curves and fragility surfaces, plotted as damage probability functions, which provide a means for predicting or estimating the extent of damage a bridge would experience for a given seismic event. The developed method integrates uncertainties in earthquake and structural characteristics into a reliability-based assessment of seismic performance. The vulnerable components were identified to propose seismic retrofit strategies. In the second part of this dissertation, various retrofit strategies used in New York State were elevated by studying the reduction in damage probability.

This dissertation first provided a review of the literature on traditional fragility analysis procedures and predominant retrofit technologies used in practice. To carry out the fragility analysis of typical bridges in Northeastern United States sites, two essential problems needed to be solved: (a) identification of representative earthquake accelerograms, and (b) determination of typical highway bridge configurations. Due to the insufficiency of actual earthquake records for this region, artificial ground motion accelerograms were simulated to represent different hazard levels. Potential seismic events defined in terms of magnitude-distance pairs are selected based on the USGS database using the method of Probabilistic Seismic Hazard Analysis (PSHA). These

earthquake data are input the SGMS code developed by Halldorsson and Papageorgiou (2004a, b) for the generation of one hundred acceleration time histories with PGA ranging from 0.1g to 1.2g. Typical highway bridges are identified by reviewing the files of the National Bridge Inventory database and New York State Bridge database. Multi-span simply supported (MSSS) steel bridges and multi-span continuous (MSC) steel bridges are found to be most typical in New York State. Two such bridges designed to have typical topological layout and structural details as per New York State bridge design guidelines are used to study the risk to these types of bridges. Three-dimensional finite element bridge models are established considering the nonlinear behavior of critical bridge components, such as columns, bearings and abutments for the earthquake input in the longitudinal direction.

Several significant new contributions are made to the analytical fragility procedure with the following advantages over existing approaches:

1. Parametric Analysis: Previous studies considered uncertainties only in material properties and gap sizes. In this research, a detailed parametric study was carried out to study the sensitivity of pier curvature ductility to superstructure weight, concrete compressive strength, reinforcement yield strength, abutment wall-soil stiffness, friction coefficient of expansion bearings and expansion-joint gap size. It was observed that uncertainties associated with estimating the friction coefficient of expansion bearings and superstructure weight have significant effects on bridge ductility in addition to material strength and expansion joint gap size. Hence, uncertainties associated with these five parameters must be considered in developing the fragility curves.

2. Bridge Sampling and Pairing: To consider uncertainties in the five parameters discussed above, the Latin Hypercube Sampling (LHS) approach is used to obtain samples based on the mean values and probability distributions of each parameter. The probability density function of each random variable is divided into a histogram with equal probability intervals so that the corresponding cumulative distributions are graded linearly from 5% to 95% corresponding to ten sample values. For the purpose of creating a set of nominally identical but statistically different bridge samples for fragility analysis, the Latin Hypercube Sampling (LHS) restricted pairing concept is used instead of pairing the variables randomly, so that the correlation matrix is as close as possible to the actual correlation matrix. This innovative application is used in this study to reduce the number of samples while increasing the accuracy of the probabilistic analysis.

3. Analysis of Uncertainties: Previous studies assumed a set of constant values as capacity criteria and adopted the empirical value suggested in HAZUS for the dispersion of seismic capacity and demand, which is based on engineering judgment. This HAZUS value is not tied to bridge type or damage state. Actually, the capacity varies with structural parameters, and the assumed dispersion values will largely influence the fragility results. To overcome this limitation, strength and deformation capacities are specifically evaluated for the components of each bridge sample. The nonlinear time history analyses of the 10 bridge samples are carried out respectively for the multi-span continuous bridge and the multi-span simply supported bridge by using 100 simulated earthquake accelerograms. Each bridge sample was analyzed for 10 different ground motions selected to cover a wide range of PGAs. Hence, a total of 100 analysis cases have been performed for the MSC bridge and the MSSS bridge. For each

of the 100 analysis cases, the maximum component responses and the estimated capacities at various damage states are collected. The dispersion of seismic capacity and demand are then estimated through a regression analysis of demand-capacity ratios.

4. Regression Analysis: Linear regression on bridge response quantities has been used in previous studies on fragility analysis. In this research, linear, quadratic and multivariate regressions are conducted on the ratio of seismic demand to capacity $\ln(S_d / S_c)$ to account for the uncertainties in demand and capacities simultaneously. It is observed that a quadratic regression provides a better fit as compared to the commonly used linear regression fit versus PGA. Using linear regression for strong earthquakes (>0.6g for New York State) is not reasonable because of the nonlinear trend in $\ln(S_d / S_c)$ for large PGAs. Multivariate regressions of the fragility show further improvement in the predictive model and establish relations among $\ln(S_d / S_c)$, earthquake moment magnitude, and epicentral distance.

5. Bridge Component Fragility: Fragility curves have been developed for individual bridge components at different damage states. Considering that earthquake moment magnitude and epicentral distance are more readily available than PGA, fragility surfaces as a function of earthquake magnitude and epicentral distance have been developed. Using contour maps or cut sections of a fragility surface, the range of earthquake magnitudes and epicentral distances that could cause seismic damage can be determined for different risk levels.

6. Bridge System Fragility: Fragilities of individual components are combined to develop fragility curves for the complete bridge system using multiple failure mode

theory. The second–order reliability bounds are shown to provide narrower bounds on fragility than the first-order reliability bounds used in previous studies.

The fragility analysis shows that multi-span continuous steel bridges in New York State have more than 50% probability of exhibiting slight damage, moderate damage, extensive damage, and collapse when subjected to earthquakes with PGAs equal to 0.60g, 0.66g, 1.07g and 1.19g respectively. On the other hand, the corresponding median PGAs for the multi-span simply supported bridge are 0.51g, 0.63g, 1.02g, and 1.50g for these four damage states. From the fragility surfaces, we can see that the maximum fragility of the multi-span continuous bridge for these four damage states could reach 100%, 100%, 88%, and 87% for the potentially most severe seismic event for this region within the practical range of $M_w \leq 7.5$ and $R \geq 10$. The corresponding maximum fragilities for the multi-span simply supported bridge shows that there is 100%, 100%, 98%, 72% probability to exceed these four damage states for the most severe earthquake event. This analysis shows that, among all the bridge components, piers and bearings (expansion bearings in MSC bridge, fixed bearings in MSSS bridge) are particularly vulnerable to damage during an earthquake. Their failure will result in collapse or loss of function of the superstructure. Hence, piers and bearings are prime candidates for retrofit.

In this study, various retrofit schemes are considered to reduce the specific structural vulnerabilities idealized by the fragility analysis of the as-built MSC and MSSS bridges. The retrofitted measures are meant either to reduce the seismic demand or to increase the seismic capacity of critical components. The retrofit measures include bearing replacement by elastomeric bearings, the use of energy dissipators such as lead

core or viscous dampers, and pier confinement by FRP jacketing. In addition, deck/girder-splicing is considered in order to provide continuity for the multi-span simply supported bridge. All necessary geometric, material and mechanical characteristic values are provided in this dissertation to model each retrofit scheme.

The retrofit measures are introduced into the bridges' finite element models for fragility analyses. The analyses quantified retrofit advantages through fragility curves and surfaces. It has been observed that isolators, i.e. elastomeric bearings and lead-rubber bearings, can help detune the bridge's fundamental period, and reduce the seismic demand of bridge columns. Also, energy dissipators, such as the use of lead cores and viscous dampers, can help reduce the seismic demand on bridge bearings. FRP jackets improve pier confinement and can enhance the ductility capacity of plastic hinges. The introduction of continuity in multi-span simply supported bridges can improve the structural integrity, reduce the pounding and increase the bridge's resistance to seismic displacements. For the MSC bridge in the study, the combination of elastomeric bearings and viscous dampers could lead to an optimal overall retrofit effect. For the MSSS bridge in this study, the combination of elastomeric bearings and superstructure continuity could enhance both superstructure and substructure performance. The lower seismic risks illustrated by fragility curves and surfaces can offer a clear measure of retrofit benefits.

8.2 Future Research

In this dissertation, fragility analyses have been carried out for typical bridge types in Northeastern United States. The developed fragility curves and surfaces give an estimation of the probability of seismic damage. More work could be performed in the future to extend the application of these research results, and to further improve the presented

methodology. Specifically, the following additional tasks could be considered for future work:

1. Loss and Cost Analysis: This dissertation has already quantified the seismic risk and retrofit effectiveness. Future investigations of the potential economic losses due to seismic bridge damage and the retrofit costs for bridges at different damage states can be helpful for developing optimization models for retrofit prioritization when a compromise between structural safety and economic costs is required. The loss estimation may include the cost for the repair of components, the economical impact due to disruption of traffic flow, and other user costs. The estimation of retrofit cost may consider the expense of material, installation and maintenance.

2. Refined Analysis of Parameter Uncertainty: In this study, the most critical parameters for the superstructure and substructure have been identified and considered in addition to the seismic characteristics of magnitude and epicentral distance. However, additional uncertainties in other site and structural parameters, such as focal depth, soil conditions, and bridge foundation, may also be important. Hence, statistical data should be assembled for these additional parameters. Furthermore, the parameters that have been considered as random variables in this study were mostly assumed to follow uniform, normal or lognormal distributions, and their statistical parameters were obtained from preliminary results published in the literature. For example, the ranges in the friction coefficient of steel bearings and the shear modulus of elastomers may be adequate for design but not necessarily sufficiently accurate for actual safety assessment, especially for bridges which may have been under-designed or that may have deteriorated over time. The collection of a large experimental database and site measurements may help improve the input data used during simulation.

3. Analysis of Modeling Uncertainty: As mentioned in section 5.8, another main

source of uncertainty is related to the models used for demand analysis and the models for capacity evaluation. It was found that the force-displacement models for component behavior generally have good agreement with experimental data. However, the analytical capacity estimation may exhibit more discrepancy from experimental results. For example, the comparison reported by Mander et al. (1988) shows that the ultimate strength capacity of confined concrete as calculated form the model varies from the experimentally observed values by as little as 1.7% on the average. However, the strain at steel hoop fracture as calculated varies from the experimental values by an average of 9.5% with a range of up to 33%. This confirms the importance of including modeling uncertainties in the capacity evaluation process as compared to its insignificant effect on the demand analysis. Hence, capacity modeling uncertainties should be the subject of additional research. For example, for bridge piers before and after FRP retrofit, the effectiveness of steel hoop and FRP confinement as well as the actual value of FRP hoop rupture strain may be some of the factors that need to be included in the analysis of capacity modeling uncertainties. Similarly, the uncertainties in modeling the bearing behavior should be considered in a systematic and consistent manner.

4. Bridge Fragility under Vertical Ground Motion: Most of the published research on fragility analysis did not explicitly address the response of bridges to vertical motions. In this study, the effects of axial forces in the columns on the shear and flexural capacities of bridge piers have been considered as explained in Chapter 5, assuming that the axial forces remain constant throughout the duration of the earthquakes. Similarly, the experimental hysteresis loops for the expansion bearings used in the models described in Chapter 4 are also functions of constant normal reaction forces on the bearings. Since vertical motions are known to cause fluctuations in axial forces, ignoring the vertical

earthquake component may lead to under-estimating the bridge fragility. Hence, future consideration of vertical component of seismic ground motions should lead to more refined fragility analysis. The modeling of horizontal-vertical hysteresis behaviors will need specific experimental data on key elements of typical bridge structures. The combined horizontal and vertical capacities of components under representative earthquake motions need to be identified based on experimental data. The damage states of bridge deck-girder shear failure and foundation uplift should also be considered. Subsequently, dynamic time history analyses, first excluding and then including the vertical component of earthquake ground motions can help assess the impact of vertical motion in determining the safety of critical elements.

The above issues require extensive sets of experimental data, which are not readily available at this stage. Further work should concentrate on collecting such data to carry forward this research.

Appendix I Regression Equations in Fragility Analysis for Retrofitted MSC Bridges

Regression Equations of ln (S_d / S_c) versus ln (PGA)					
Retrofit Strategy		**Bridge Component**	**Items**	**Regression Equations**	**Deviation**
Retrofitted by Elastomeric Bearing (EB)		Pier	$\ln(\phi/\phi_y^{'})$	$y = 0.2711x^2 + 1.240x + 0.3467$	0.3172
			$\ln(\phi/\phi_y)$	$y = 0.2733x^2 + 1.246x + 0.1445$	0.3159
			$\ln(\phi/\phi_d)$	$y = 0.2991x^2 + 1.304x - 1.0100$	0.3156
			$\ln(\phi/\phi_u)$	$y = 0.2627x^2 + 1.246x - 2.0080$	0.3010
		Bearing	$\ln(D_d/D_c)$	$y = 0.1827x^2 + 1.029x - 0.2023$	0.2928
Retrofitted by Lead-Rubber Bearing		Pier	$\ln(\phi/\phi_y^{'})$	$y = 0.2182x^2 + 1.086x + 0.3819$	0.3263
			$\ln(\phi/\phi_y)$	$y = 0.2204x^2 + 1.092x + 0.1797$	0.3237
			$\ln(\phi/\phi_d)$	$y = 0.2462x^2 + 1.150x - 0.9745$	0.3112
			$\ln(\phi/\phi_u)$	$y = 0.2098x^2 + 1.092x - 1.9730$	0.2959
		Bearing	$\ln(D_d/D_c)$	$y = 0.1903x^2 + 1.152x - 0.3596$	0.2979
Retrofitted by EB Plus Viscous Damper	C=0.25	Pier	$\ln(\phi/\phi_y^{'})$	$y = 0.2631x^2 + 1.240x + 0.2627$	0.2971
			$\ln(\phi/\phi_y)$	$y = 0.2653x^2 + 1.246x + 0.0605$	0.2958
		Bearing	$\ln(D_d/D_c)$	$y = 0.1807x^2 + 1.069x - 0.2722$	0.3036
	C=0.50	Pier	$\ln(\phi/\phi_y^{'})$	$y = 0.2610x^2 + 1.258x + 0.2010$	0.2818
			$\ln(\phi/\phi_y)$	$y = 0.2632x^2 + 1.264x - 0.0012$	0.2805
		Bearing	$\ln(D_d/D_c)$	$y = 0.1914x^2 + 1.137x - 0.3207$	0.3107
	C=0.75	Pier	$\ln(\phi/\phi_y^{'})$	$y = 0.2569x^2 + 1.262x + 0.1398$	0.2711
			$\ln(\phi/\phi_y)$	$y = 0.2591x^2 + 1.268x - 0.0624$	0.2697
		Bearing	$\ln(D_d/D_c)$	$y = 0.2088x^2 + 1.200x - 0.3685$	0.3130
	C=1.00	Pier	$\ln(\phi/\phi_y^{'})$	$y = 0.2542x^2 + 1.263x + 0.0852$	0.2636
			$\ln(\phi/\phi_y)$	$y = 0.2564x^2 + 1.270x - 0.1170$	0.2621
		Bearing	$\ln(D_d/D_c)$	$y = 0.2244x^2 + 1.248x - 0.4195$	0.3121
Retrofitted By CFRP		Pier	$\ln(\phi/\phi_u)$	$y = 0.7139x^2 + 2.804x - 1.930$	0.3968

Regression Equations of ln (S_d / S_c) versus ln (M_w) and ln (R)					
Retrofit Strategy		**Bridge Component**	**Items**	**Regression Equations**	**Deviation**
Retrofitted by Elastomeric Bearing (EB)		Pier	$\ln(\phi/\phi_y^{'})$	$y=-10.49+6.47\ln M_w-0.75\ln R$	0.2845
			$\ln(\phi/\phi_y)$	$y=-10.67+6.46\ln M_w-0.76\ln R$	0.2842
			$\ln(\phi/\phi_d)$	$y=-11.64+6.37\ln M_w-0.77\ln R$	0.2907
			$\ln(\phi/\phi_u)$	$y=-12.48+6.31\ln M_w-0.78\ln R$	0.2739
		Bearing	$\ln(D_d/D_c)$	$y=-10.13+5.95\ln M_w-0.70\ln R$	0.2651
Retrofitted by Lead-Rubber Bearing		Pier	$\ln(\phi/\phi_y^{'})$	$y=-10.51+6.44\ln M_w-0.69\ln R$	0.2834
			$\ln(\phi/\phi_y)$	$y=-10.69+6.43\ln M_w-0.70\ln R$	0.2816
			$\ln(\phi/\phi_d)$	$y=-11.66+6.34\ln M_w-0.71\ln R$	0.2741
			$\ln(\phi/\phi_u)$	$y=-12.50+6.28\ln M_w-0.72\ln R$	0.2570
		Bearing	$\ln(D_d/D_c)$	$y=-11.81+6.88\ln M_w-0.81\ln R$	0.2520
Retrofitted by EB Plus Viscous Damper	C= 0.25	Pier	$\ln(\phi/\phi_y^{'})$	$y=-10.62+6.51\ln M_w-0.77\ln R$	0.2617
			$\ln(\phi/\phi_y)$	$y=-10.79+6.50\ln M_w-0.77\ln R$	0.2613
		Bearing	$\ln(D_d/D_c)$	$y=-10.85+6.34\ln M_w-0.74\ln R$	0.2699
	C= 0.50	Pier	$\ln(\phi/\phi_y^{'})$	$y=-10.72+6.56\ln M_w-0.79\ln R$	0.2451
			$\ln(\phi/\phi_y)$	$y=-10.89+6.55\ln M_w-0.79\ln R$	0.2449
		Bearing	$\ln(D_d/D_c)$	$y=-11.55+6.74\ln M_w-0.79\ln R$	0.2711
	C= 0.75	Pier	$\ln(\phi/\phi_y^{'})$	$y=-10.72+6.55\ln M_w-0.80\ln R$	0.2348
			$\ln(\phi/\phi_y)$	$y=-10.90+6.54\ln M_w-0.81\ln R$	0.2345
		Bearing	$\ln(D_d/D_c)$	$y=-12.01+6.99\ln M_w-0.83\ln R$	0.2709
	C= 1.00	Pier	$\ln(\phi/\phi_y^{'})$	$y=-10.69+6.51\ln M_w-0.81\ln R$	0.2280
			$\ln(\phi/\phi_y)$	$y=-10.86+6.50\ln M_w-0.81\ln R$	0.2274
		Bearing	$\ln(D_d/D_c)$	$y=-12.36+7.17\ln M_w-0.85\ln R$	0.2677
Retrofitted By CFRP		Pier	$\ln(\phi/\phi_u)$	$y=-20.87+11.5\ln M_w-1.52\ln R$	0.3778

Appendix II Regression Equations in Fragility Analysis for Retrofitted MSSS Bridges

Regression Equations of ln (S_d / S_c) versus ln (PGA)				
Retrofit Strategy	**Bridge Component**	**Items**	**Regression Equations**	**Deviation**
Retrofitted by Elastomeric Bearing	Pier	$\ln(\phi/\phi_y^{'})$	$y = 0.1161x^2 + 0.9328x + 0.2214$	0.3014
		$\ln(\phi/\phi_y)$	$y = 0.1183x^2 + 0.9384x - 0.0567$	0.2977
		$\ln(\phi/\phi_d)$	$y = 0.08714x^2 + 0.9051x - 1.373$	0.2560
		$\ln(\phi/\phi_u)$	$y = 0.09277x^2 + 0.9117x - 2.486$	0.2639
	Bearing	$\ln(D_d / D_c)$	$y = 0.0711x^2 + 0.6612x - 0.5078$	0.2397
Retrofitted by Continuity and Elastomeric Bearings	Pier	$\ln(\phi/\phi_y^{'})$	$y = 0.1290x^2 + 0.9147x + 0.2636$	0.2571
		$\ln(\phi/\phi_y)$	$y = 0.1313x^2 + 0.9202x - 0.0145$	0.2540
		$\ln(\phi/\phi_d)$	$y = 0.1001x^2 + 0.8869x - 1.331$	0.2197
		$\ln(\phi/\phi_u)$	$y = 0.1057x^2 + 0.8936x - 2.443$	0.2216
	Bearing	$\ln(D_d / D_c)$	$y = -0.0607x^2 + 0.3699x - 0.7849$	0.2370
Regression Equations of ln (S_d / S_c) versus ln (M_w) and ln (R)				
Retrofit Strategy	**Bridge Component**	**Items**	**Regression Equations**	**Deviation**
Retrofitted by Elastomeric Bearing	Pier	$\ln(\phi/\phi_y^{'})$	$y = -10.22 + 6.28\ln M_w - 0.73\ln R$	0.2577
		$\ln(\phi/\phi_y)$	$y = -10.47 + 6.27\ln M_w - 0.74\ln R$	0.2542
		$\ln(\phi/\phi_d)$	$y = -11.14 + 5.97\ln M_w - 0.76\ln R$	0.2186
		$\ln(\phi/\phi_u)$	$y = -12.49 + 6.09\ln M_w - 0.76\ln R$	0.2229
	Bearing	$\ln(D_d / D_c)$	$y = -8.864 + 4.97\ln M_w - 0.54\ln R$	0.2007
Retrofitted by Continuity and Elastomeric Bearings	Pier	$\ln(\phi/\phi_y^{'})$	$y = -9.056 + 5.65\ln M_w - 0.69\ln R$	0.2216
		$\ln(\phi/\phi_y)$	$y = -9.310 + 5.63\ln M_w - 0.69\ln R$	0.2187
		$\ln(\phi/\phi_d)$	$y = -9.983 + 5.34\ln M_w - 0.72\ln R$	0.2186
		$\ln(\phi/\phi_u)$	$y = -11.33 + 5.46\ln M_w - 0.71\ln R$	0.1887
	Bearing	$\ln(D_d / D_c)$	$y = -7.542 + 4.11\ln M_w - 0.48\ln R$	0.2219

BIBLIOGRAPHY

AASHTO (1996). "Standard Specifications for Highway Bridges." 16th ed., Washington, D.C.

AASHTO (1998). "LRFD Bridge Design Specifications." 2nd ed., Washington, D.C.

Aiken, I. D., and Kelly, J. M. (1995). "Prequalification Testing of Viscous Dampers for the Golden Gate Bridge Seismic Rehabilitation Project." Report No. EERC-STI/95-02, Earthquake Engineering Research Center, University of California, Berkeley, Richmond, CA.

Alkhrdaji, T., and Nanni, A. (2000). "Flexural Strengthening of Bridge Piers Using FRP Composites." Section 46, Chapter 2, Structure Congress 2000-Advanced Technology in Structural Engineering.

Ang, A. H., and Tang, W. H. (1975). "Probability Concepts in Engineering Planning and Design." Vol. 1, Basic Principles, John Wiley & Sons, Inc.

ATC-13 (1985). "Earthquake Damage Evaluation Data for California." Applied Technology Council, Redwood City, CA.

ATC-32 (1996). "Improved Seismic Design Criteria for California Bridges: Provisional Recommendations." Applied Technology Council, Redwood City, CA.

ATC-40 (1996). "Seismic Evaluation and Retrofit of Concrete Buildings." Applied Technology Council, Redwood City, CA.

Ayyub, B. M., and Lai, K. (1989). "Structural Reliability Assessment Using Latin Hypercube Sampling." Proceedings of ICOSSAR'89, the 5th International Conference on Structural Safety and Reliability, Part II, ASCE, New York, NY, USA, 1177-1184.

Bakis, C. E., Bank, L. C., Brown, V. L., Cosenza, E., Davalos, J. F., Lesko, J. J., Machida, A., Rizkalla, S. H., and Triantafillou, T. C. (2002). "Fiber-Reinforced Polymer Composites for Construction: State-of-the-Art Review." Journal of Composites for Construction, Vol. 6, No. 2, 73-87.

Barker, R. M., and Puckett, J. A. (1997). "Design of Highway Bridges: Based on AASHTO LRFD Bridge Design Specifications." Wiley, New York, NY.

Barron-Corvera, R. (2000). "Spectral Evaluation of Seismic Fragility of Structures." Ph.D. Dissertation, Department of Civil, Structural & Environmental Engineering, State University of New York at Buffalo, N.Y.

Basoz, N., and Kiremidjian, A. (1998). "Evaluation of Bridge Damage Data from the Loma Prieta and Northridge, CA Earthquakes." Rep. No. MCEER-98-0004, Multidisciplinary Center for Earthquake Engineering Research, Buffalo, NY.

Bazzurro, P., and Cornell, C. A. (1999). "Disaggregation of Seismic Hazard." Bulletin of the Seismological Society of America, Vol. 89, 501-520

Beresnev, I. A., and Atkinson, G. M. (2002). "Source Parameters of Earthquakes in Eastern and Western North America based on Finite-Fault Modeling." Bull. Seism. Soc. Am. 92, 695-710.

Buckle, I. G., and Friedland, I. M. (1995). "Seismic Retrofitting Manual for Highway Bridges." FHWA Report FHWA-RD-94-052, Washington D.C.

California Department of Transportation (CALTRANS) (1989). "Bridge Design Specifications Manual."

California Department of Transportation (CALTRANS) (1999). "User's Manual for xSECTION, Cross section Analysis Programs."

Chai, Y. H., Priestley, M. J. N., and Seible, F. (1991). " Seismic Retrofit of Circular Bridge Columns for Enhanced Flexural Performance." ACI Structural Journal, Vol. 88, No. 5, 572-584.

Choi, E. (2002). "Seismic Analysis and Retrofit of Mid-America Bridges." Dissertation, Department of Civil and Environmental Engineering, Georgia Institute of Technology, Atlanta (GA).

Choi, E., DesRoches, R., and Nielson, B. (2004). "Seismic Fragility of Typical Bridges in Moderate Seismic Zones." Engineering Structures, 26, Issue 2, 187 – 199.

City of Los Angeles (COLA) (1995). "Earthquake hazard Reduction in Existing Reinforced Concrete Buildings and Concrete Frame Buildings with Masonry Infills." Los Angeles, CA.

Clark, P. W., Aiken, I. D., and Kelly, J. M. (1993). "Large-scale Earthquake Simulator Study of the Tohoku University Base-Isolated Building." Structural Engineering in Natural Hazards Mitigation, ASCE, New York, NY, 181-186.

Clough, C. W., and Duncan, J. M. (1991). "Foundation Engineering Handbook." 2nd ed., edited by H. Y. Fang, Chapman & Hall, New York, 223-235.

Constantinous, M. C., Symans, M. D., Tsopelas, P., and Taylor, D. P. (1993a). "Fluid Viscous Dampers in Applications of Seismic Energy Dissipation and Seismic Isolation." Proc. ATC 17-1 on Seismic Isolation, Energy Dissipation and Active Control, 2, 581-591.

Constantinous, M. C., and Symans, M. D. (1993b). "Experimental Study of Seismic Response of Buildings with Supplemental Fluid Dampers." Struct. Design Tall Bldgs., 2, 93-132.

Cornell, C. A. (1967). "Bounds on the Reliability of Structural System." J. Structural Div., ASCE, 93 (ST1)

Delis, E. A., Malla, R. B., Madani, M., and Thompson, K. J. (1996). "Energy Dissipation Devices in Bridges Using Hydraulic Dampers." Proc. Structures Congress XIV, Chicago, IL, Vol. 2, 188-1196.

Demers, M., and Neale, K. W. (1994). "Strengthening of Concrete Columns with Unidirectional Composite Sheets." Development in Short and Medium Span Bridge Engineering '94, Proc. of the 4th Int. Conf. on Short and Medium Span Bridges, Canadian Society for Civil Engineering, Montreal, 895–905.

Deodatis, G., Saxena, V., and Shinozuka, M. (2000). "Effect of Spatial Variability of Ground Motion on Bridge Fragility Curves." 8th ASCE Specialty Conference on Probabilistic Mechanics and Structural Reliability.

DesRoches, R., and Fenves, G. L. (2000). "Design of Seismic Cable Hinge Restrainers for Bridges." Journal of Structural Engineering, Vol. 126, No. 4, 500-509

DesRoches, R., Pfeifer, T., Leon, R. T., and Lam, T. (2003) "Full-Scale Tests of Seismic Cable Restrainer Retrofits for Simply Supported Bridges." Journal of Bridge Engineering, 8(4), 191-198.

DesRoches, R., Choi, E., Leon, R. T., Dyke, S. J., and Aschheim, M. (2004a). "Seismic Response of Multiple Span Steel Bridges in Central and Southeastern United States. I: As Built." Journal of Bridge Engineering, Vol. 9, No. 5, 464-472.

DesRoches, R., Choi, E., Leon, R. T., and Pfeifer, T. (2004b). "Seismic Response of Multiple Span Steel Bridges in Central and Southeastern United States. II: Retrofitted." Journal of Bridge Engineering, Vol. 9, No. 5, 473-479.

Dutta, A., and Mander, J. B. (1998). "Seismic Fragility Analysis of Highway Bridges." Center-to-Center Project Workshop on Earthquake Engineering Frontiers in Transportation Systems, International Center for Disaster-Mitigation Engineering (INCEDE), Tokyo, Japan.

Engineering Seismology Laboratory SUNY at Buffalo.
URL: http://civil.eng.buffalo.edu/ engseislab/disseishaz.htm

Federal Highways Administration (FHWA) (1987). "Seismic Design and Retrofit Manual for Highway Bridges." Rep. No. FHWA-IP-87-6, FHWA, Washington D.C.

Federal Highways Administration (FHWA) (1988). “Recording and Coding Guide for the Structure Inventory and Appraisal of the Nation's Bridges.” Rep. No. FHWA-ED-89-044, FHWA, Washington D.C.

Federal Emergency Management Agency (FEMA) (1997a). “NEHRP Guidelines for the Seismic Rehabilitation of Buildings.” FEMA-273, Washington, D.C.

Federal Emergency Management Agency (FEMA) (1997b). “NEHRP Commentary on the Guidelines for the Seismic Rehabilitation of Buildings.” FEMA-274, Washington, D.C.

Federal Highways Administration (FHWA) (2003). “National Bridges Inventory Data.” Office of Bridge Technology.

Feng, M. Q., and Bahng, E. Y. (1999). “Damage Assessment of Jacketed Columns.” Structural Engineering in the 21st Century, Proceedings of the 1999 Structures Congress, New Orleans, Louisiana, 357-360.

Feng, M. Q., Kim, J., Shinozuka, M., and Prasinghe, R. (2000). “Visco-Elastic Dampers at Expansion Joints for Seismic Protection of Bridges.” Journal of Bridge Engineering, No. 1, Vol. 5, 67-74.

Gergely, I., Pantelides, C. P., Nuismer, R. J., and Reaveley, L. D. (1998). “Bridge Pier Retrofit Using Fiber-Reinforced Plastic Composite.” Journal of Composites for Construction, Vol. 2, No. 4, 165-174.

Ghobarah, A., and Ali, H. M. (1988). “Seismic Performance of Highway Bridges.” Journal of Engineering Structures, 10(3), 157-166.

Graver, F., and Rubin, C. (1995). “New York Earthquake: The Quake Next Time—Waiting for the Big One.” Compuserve New York Magazine Online Cover, Vol. 20, No. 19.

Halldorsson, B., and Papageorgiou, A. S. (2004a). “Calibration of the Specific Barrier Model to Earthquakes of Different Tectonic Regions.” Manuscript Submitted to the Bull. Seism. Soc. Am.

Halldorsson, B., and Papageorgiou, A. S. (2004b). “Region Specific Ground Motion Simulations Using the Specific Barrier Model.” User’s Manual of SGMS.

Harmon, T. G., and Slattery, K. T. (1992). “Advanced Composite Confinement of Concrete.” Proceeding of International Conference on Advanced Composite Materials in Bridges and Structures, Canadian Society for Civil Engineering, 299-306.

Harmsen, S., Perkins, D., and Frankel, A. (1999). “Deaggregation of Probabilistic Ground Motions in the Central and Eastern United States.” Bulletin of the Seismological Society of America, Vol. 89, 1-13

Haroun, M., Feng, M., Bhatia, H., Baird, K., and Elsanadedy, H. (1999). "Structural Qualification Testing of Composite-Jacketed Circular and Rectangular Bridge Columns." Final report to the California Department of Transportation, RTA-59A0005.

HAZUS97 (1997/1999). "User's Manual." Federal Emergency Management Agency, Washington, D.C.

HAZUS99-SR2 (1999). "Technical Manual." National Institute of Building Sciences (NIBS) and Federal Emergency Management Agency, Washington D.C.

Howie, I., and Karbhari, V. M. (1994). "Effect of Materials Architecture on Strengthening Efficiency of Composite Wraps for Deteriorating Columns in the North-east." Infrastructure: New Materials and Methods of Repair, Proc. 3rd Materials Engineering Conf., K. D. Basham ed., Material Engineering Division, ASCE, N.Y., 199–206.

Hwang, H., and Huo, J. R. (1994). "Generation of Hazard-consistent Ground Motions." Soil Dynamics and Earthquake Engineering, 13(6), 377-386.

Hwang, H., and Huo, J. R. (1998). "Probabilistic Seismic Damage Assessment of Highway Bridges." the 6th U.S. National Conference on Earthquake Engineering, Seattle, Washington.

Hwang, H., Jernigan, J. B., and Lin, Y. (2000a). "Evaluation of Seismic Damage to Memphis Bridges and Highway Systems." Journal of Bridge Engineering, 5(4), 322-330.

Hwang, H., Jernigan, J. B., and Lin, Y. (2000b). "Seismic Fragility Analysis of Highway Bridges." Rep. No. MAEC RR-4, Center for Earthquake Research Information, Memphis, TN.

Hwang, H., Liu, J., and Chiu, Y. (2001). "Seismic Fragility Analysis of Highway Bridges." Center for Earthquake Research and Information, University of Memphis, Memphis, Technical Report.

Idriss, I. M., and Sun, J. I. (1992). SHAKE91, "A Computer Program for Conducting Equivalent Linear Seismic Response Analyses of Horizontally Layered Soil Deposits, User's Manual." Center for Geotechnical Modeling, Department of Civil and Environmental Engineering, University of California, Davis, CA.

Imbsen, R. A. (1981). "Improved Bearing Design Concepts for Increased Seismic Resistance of Highway Bridges." First World Congress on Joints and bearings (Niagara Falls, NY), Vol. I, American Concrete Institute, SP-70, Detroit, Michigan, 509-523.

Imbsen, R. A. (2001). "Use of Isolation for Seismic Retrofitting Bridges." Journal of Bridge Engineering, Vol. 6, No. 6, ASCE, 425-438.

Isachson, Y. W., Landing, E. and Lauber, J. M. (1991). "Do Earthquakes Occur in New York State?" Geology of New York: A simplified Account, Albany: New York State Museum/Geological Survey, 231-238.

Jacob, K. (1993). "Seismic Vulnerability of New York State: Code Implications for Buildings, Bridges, and Municipal Facilities." MCEER Bulletin, Vol. 7, No. 2.

Jacob, K. H., ed. (1987). "Proceedings from the Symposium on Seismic Hazards, Ground Motions, Soil-Liquefaction and Engineering Practice in Eastern North America." NCEER Symposium, Sterling Forest, NY, Report No. NCEER-87-0025.

Jacob, K. H., and Turkstra, C. J. (1987). "Earthquake Hazards and the Design of Constructed Facilities in the Eastern United States." Annals of the New York Academy of Science, Vol. 558, NY.

Jin, X. N., Pan J. L., Liu, G. Y., and Lai, W. H. (2003). "Research of Stress–Strain Curve of Concrete Confined by Fiber Reinforced Plastics under Axial Compression." J. Build. Struct., 24(4), 47–53 (in Chinese).

Karbhari, V. M., and Gao, Y. (1997). "Composite Jacketed Concrete under Uniaxial Compression—Verification of Simple Design Equations." Journal of Materials in Civil Engineering, 9(4), 185–193.

Karim, K. R., and Yamazaki, F. (2000). "Comparison of Empirical and Analytical Fragility Curves for RC Bridge Piers in Japan." 8th ASCE Specialty Conference on Probabilistic Mechanics and Structural Reliability, CD-ROM.

Kelly, J. M. (1997). "Earthquake–Resistant Design with Rubber." Springer, London.

Kent, D. C., and Park, R. (1971). "Flexural Members with Confined Concrete." Journal of the Structural Division, ASCE, 97(7), 1969-1990.

Kim, S., and Feng, M. Q. (2003). "Fragility Analysis of Bridges under Ground Motion with Spatial Variation." International Journal of Non-Linear Mechanics, Vol. 38, No. 5, 705-721.

Kottegoda, N. T., and Rosso, R. (1997). "Statistics, Probability, and Reliability for Civil and Environmental Engineers." The McGraw-Hill Companies, Inc.

Kramer, S. L. (1996). "Geotechnical Earthquake Engineering." Prentice Hall, Inc., Upper Saddle River, New Jersey.

Kunde, M. C., and Jangid, R. S. (2003). "Seismic Behavior of Isolated Bridges: A State-of-the-Art Review, Journal of Structural Engineering, Vol. 3, 140-170.

Lam, L., and Teng, J. G. (2003). "Design-Oriented Stress-Strain Model for FRP-Confined Concrete." Construction and Building Materials, 17 (6&7), 471-489.

Lam, L., and Teng, J. G. (2004). "Ultimate Condition of Fiber Reinforced Polymer-Confined Concrete." Journal of Composites for Construction, Vol. 8, No. 6, 539-548.

Lee, T. Y., and Kawashima, K. (2004). " Effectiveness of Supplementary Dampers for Isolated bridges under Strong Near-field Ground Motions." 13th World Conference on Earthquake Engineering, Vancouver, Canada.

MacGregor, J. G. (1992). "Reinforced Concrete Design." Prentice-Hall, Engle-wood Cliffs, New Jersey.

MacRae, G., Stanton, J., and Kim, J. (1999). " Design Issues for FRP Jacketed Concrete Columns." Materials and Construction: Exploring the Connection, Proceedings of the Fifth ASCE Materials Engineering Congress, Cincinnati, Ohio, 435-443.

Maine Department of Transportation (2003). "Bridge Design Guide."

Maleki, S. (2004). "Effect of Side Retainers on Seismic Response of Bridges with Elastomeric Bearings." Journal of Bridge Engineering, Vol. 9, No. 1, 95-100.

Mander, J. B., Priestley, M. J. N., and Park, R. (1984). "Seismic Design of Bridge Piers." Report 84-2, Department of Civil Engineering, University of Canterbury, Christchurch, New Zealand.

Mander, J. B., Priestley, M. J. N., and Park, R. (1988). "Observed Stress-Strain Behavior of Confined Concrete." Journal of Structural Engineering, Vol. 114, No. 8, 1827-1849.

Mander, J. B., Kim, D. K., Chen, S. S., and Premus, G. J. (1996). "Response of Steel Bridge Bearings to the Reversed Cyclic Loading." Technical Report NCEER 96-0014, NCEER, Buffalo, NY.

Mander, J. B., and Basoz, N. (1999). "Seismic Fragility Curve Theory for Highway Bridges." Proceeding of the 5th U.S. Conference on Lifeline Earthquake Engineering, Seattle, WA, 31-40.

Maroney, B., Kutter, B., Romstad, K., Chai, Y. H., and Vanderbilt, E. (1994). "Interpretation of Large Scale Bridge Abutment Test Results." Proceedings of 3rd Annual Seismic Research workshop, CALTRANS, CA.

Mayes, R. L., Buckle, I. G., Kelly, T. E., and Jones, L. R. (1992). "AASHTO Seismic Isolation Design Requirements for Highway Bridges." Journal of Structural Engineering, January, 284-304.

Melchers, R. E. (1999). "Structural Reliability Analysis and Prediction." John Wiley & Sons Ltd., West Sussex, England.

Mitronovas, W., and Nottis, G. N. (1993). "A Historical Look at Earthquakes in the Northeast." Proceedings from "Earthquakes in the Northeast-Are We ignoring the Hazard?" A workshop on Earthquake Science and Safety for Educators, Technical Report NCEER-93-0005.

Monti, G., Nistico, N., and Santini, S. (2001). "Design of FRP Jackets for Upgrade of Circular Bridge Piers." Journal of Composites for Construction, Vol. 5, No. 2, 94-101.

Moran, D. A., and Pantelides, C. P. (2002). "Stress-Strain Model for Fiber-Reinforced Polymer-Confined Concrete." Journal of Composites for Construction, 6(4), 233–240.

Mori, A., Moss, P. J., Cooke, N., and Carr, A. J. (1999). "The Behavior of Bearing Used for seismic Isolation Under Shear and Axial Load." Earthquake Spectra, 15(2).

Nanni, A., and Braford, N. M. (1995). "FRP Jacketed Concrete under Uniaxial Compression." Construction and Building Materials, 9(2), 115–124.

Nanni, A., and Norries, M. S. (1995). "FRP Jacketed Concrete under Flexure and Combined Flexure-Compression." Construction and Building Materials, 9(5), 273–281.

NEHRP (1997). "NEHRP Recommended Provisions for Seismic Regulations for New Buildings and Other Structures." Chapter4.

Neilson, B., and DesRoches, R. (2003). "Seismic Fragility Curves for Bridges: A Tool for Retrofit Prioritization." Proceedings of the Sixth U.S. Conference and Workshop on Lifeline Earthquake Engineering, 1060-1070.

Neilson, B. (2003). "Bridge Seismic Fragility-Functionality Relationships: A Requirement for Loss Estimation in Mid-America." Student Council Online Magazine, Vol. III, No. 2.

New York State Department of Transportation (1995). "Seismic Vulnerability Manual." Structures Design and Construction Division, Bridge Safety Assurance Unit, Albany, NY.

New York State Department of Transportation (1999). "New York State Standard Specifications for Highway Bridges." Albany, NY.

New York State Department of Transportation (2002). "Bridge Manual." Albany, NY.

New York State Department of Transportation (2004). "Bridge Inventory Manual." Bridge Data Management System, Albany, NY.

Nikolaou, S., Mylonakis, G., and Edinger, P. (2001). "Evaluation of Site Factors For Seismic Bridge Design in New York City Area." Journal of Bridge Engineering, Dec, 564-576.

Nordenson, G. J. P. (1987). "Seismic Hazard Evaluation for New York City." NYACE Ad-hoc Seismology Liaison Committee, Final Report, NY.

Nowak, A. S. (1993). "Calibration of LRFD Bridge Design Code." NCHRP Project 12-33, University of Michigan, ANN Arbor, MI.

Ocel, J. L., and DesRoches, R. (2002). "High Damping Steel Connections Using Shape Memory Alloys." Proceedings of the 12th European Conference on Earthquake Engineering, London, England.

Papageorgiou, A. S., and Aki, K. (1983a). "A Specific Barrier Model for the Quantitative Description of Inhomogeneous Faulting and the Prediction of Strong Ground Motion, I: Description of the Model." Bulletin of the Seismological Society of America, Vol. 73, No. 3, 693-722.

Papageorgiou, A. S., and Aki, K. (1983b). "A Specific Barrier Model for the Quantitative Description of Inhomogeneous Faulting and the Prediction of Strong Ground Motion. Part II, Applications of the Model." Bulletin of the Seismological Society of America, Vol. 73, No. 4, 953-978.

Park, R., Priestley, M. J. N., Gill, W. D. (1982). "Ductility of Square Confined Concrete Columns." Journal of the Structural Division, ASCE, Vol. 108, No. ST4, 929-950.

Parvin, A., and Wang, W. (2001). "Behavior of FRP Jacketed Concrete Columns under Eccentric Loading." Journal of Composites for Construction, Vol. 5, No. 3, 146-152.

Pessiki, S., Harries, K. A., Kestner, J. T., Sause, R., and Ricles, J. M. (2001). "Axial Behavior of Reinforced Concrete Columns Confined with FRP Jackets." Journal of Composites for Construction, Vol. 5, No. 4, 237-245.

Priestley, M. J. N., and Park, R. (1987). "Strength and Ductility of Concrete Bridge Columns under Seismic Loading." ACI Structural Journal, Vol. 84, No. 1, 61-76.

Priestley, M. J. N., Seible, F., and Chai, Y. H. (1992). "Design Guidelines For Assessment Retrofit and Repair of Bridges for Seismic Performance." San Diego.

Priestley, M. J. N., Seible, F., and Calvi, G. M. (1996). "Seismic design and retrofitting of bridges." Wiley, New York, NY.

Purba, B. K., and Mufti, A. A. (1999). "Investigation of the Behavior of Circular Concrete Columns Reinforced with Carbon Fiber Reinforced Polymer (CFRP) Jackets." Canadian Journal of Civil Engineering, Vol. 26, 590-596.

Randall, M. J., Saiidi, M. S., Maragakis, E. M., and Isakovic, T. (1999). “Restrainer Design Procedures for Multi-span Simply Supported Bridges.” Technical Report MCEER-99-0011.

Rejcha, C. (1964). “ Design of Elastomer Bearings.” PCI Journal, October, 62-78.

Risk Engineering, Inc. (1998). ‘‘Seismic Hazard for New York City.’’ Final Rep. for Weidlinger Associates, New York.

Robinson, W. H, (1982). “Lead-Rubber Hysteretic Bearing Suitable For Protecting Structures During Earthquakes.” Earthquake Engineering and Structural Dynamics, October, 593-604.

Roeder, C. W., and Stanton, J. F. (1983). “Elastomeric Bearings: State-of-the Art.” Journal of Structural Engineering, Vol. 109, No. 12, 2853-2871.

Roeder, C. W., Stanton, J. F., and Taylor, A. W. (1987). “Performance of Elastomeric Bearings.” National Cooperative Highway Research Program, Report 298, Transportation Research Board.

Roeder, C. W., Stanton, J. F., and Feller, T. (1989). “Low Temperature Behavior and Acceptance Criteria for Elastomeric Bridge Bearings.” National Cooperative Highway Research Program Report 325, Transportation Research Board.

Roeder, C. W., and Stanton, J. F. (1991). “State-of-the-Art Elastomeric Bridge Bearing Design.” ACI Structural Journal, Vol. 88, No. 1, 31-41.

Roeder, C. W., and Stanton, J. F. (1996). “Steel Bridge Bearing Selection and Design Guide”, Vol. II, Chap. 4, Highway structures Design Handbook, American Iron and Steel Institute, 1996.

Saadatmanesh, H., Ehsani, M. R., and Li, M. W. (1994). “Strength and Ductility of Concrete Columns Externally Reinforced with Fiber Composite Straps.” ACI Structural Journal, Vol. 91, No. 4, 434-447.

SAP2000, Integrated Software for Structural Analysis and Design: Analysis Reference Manual (2004). Version 9, Computers and Structures, Inc., Berkeley, CA.

Seible, F., Burgueno, R., Abdallah, M. G., and Nuismer, R. (1995). “Advanced Composite Carbon Shell Systems for Bridge Columns under Seismic loads.” Proceeding of National Seismic Conference on Bridges and Highways, San Diego, CA.

Seible, F., Priestley, M. J. N., Hegemier, G. A., and Innamorato, D. (1997). “Seismic Retrofit of RC Columns with Continuous Carbon Fiber Jackets.” Journal of Composites for Construction, Vol. 1, No. 2, 52-62.

Seible, F., and Priestley, M. J. N. (1999). "Lessons Learned from Bridge Performance During Northridge Earthquake." Seismic Response of Concrete Bridges, ACI, Farmington Hills, Michigan, 29-55.

Seible, F. (1999). "Design Considerations for bridge Column Retrofit with FRPs." Materials and Construction: Exploring the Connection, Proceedings of the Fifth ASCE Materials Engineering Congress, Cincinnati, Ohio, 427-434.

Shahawy, M., Mirmiran, A., and Beitelman, T. (2000). "Test and Modeling of Carbon-Wrapped Concrete Columns." Composites, Part B, 31, 471–480.

Sheikh, S, A., and Bayrak, O. (2001). "Seismic Behavior of FRP-Retrofitted Concrete Columns." Structures 2001-A Structural Engineering Odyssey, Proceedings of the 2001 Structural Congress and Exposition, Washington, D.C.

Shinozuka, M. (2000a). "Development of Bridge Fragility Curves Based on Damage Data." Earthquake Engineering and Engineer Seismology: An International Journal, Vol. 2, No. 2, 35-45.

Shinozuka, M., Feng, M. Q., Lee, J., and Naganuma, T. (2000b). "Statistical Analysis of Fragility Curves." Journal of Engineering Mechanics, ASCE, Vol. 126, No. 12, 1224-1231.

Shinozuka, M., Feng, M. Q., Kim, H., and Kim, S. (2000c). "Nonlinear Static Procedure for Fragility Curve Development." Journal of Engineering Mechanics, Vol. 126, No. 12, 1287-1295

Shinozuka, M., Feng, M. Q., Kim, H., Uzawa, T., and Ueda, T. (2001). "Statistical Analysis of Bridge Fragility Curves," unpublished MCEER Technical Report.

Shinozuka, M., Kim, S., Kushiyama, S., and Yi, J. H. (2002). "Fragility Curves of Concrete Bridges Retrofitted by Column Jacketing." Journal of Earthquake Engineering and Engineering Vibration, Vol. 1, No. 2.

Shome, N., Cornell, C. A., Bassurro, P., and Carballo, J. E. (1998). "Earthquakes, Records, and Nonlinear Responses." Earthquake Spectra, 14(3), 469-500.

Skinner, R. I., Robinson, W. H., and McVerry, G. H. (1993). "An Introduction to Seismic Isolation." John Wiley & Sons, New York, NY.

Soong, T. T., and Dargush, G. F. (1997). "Passive Energy Dissipation Systems in Structural Engineering." John Wiley & Sons, New York, NY.

Spoelstra, M. R., and Monti, G. (1999). "FRP-Confined Concrete Model." Journal of Composites for Construction, Vol. 3, No. 3, 143-150.

Stanton, J. F., and Roeder, C. W. (1982). "Elastomeric Bearings-Design, Construction, and Materials." National Cooperative Highway Research Program Report 248, Transportation Research Board.

Tantala, M. W., Nordenson, and Deodatis, G. (2000). "Earthquake Loss Estimation Study for the New York City Area." NYCEM, Year Two Technical Report.

Teng, J. G., and Lam, L. (2004). "Behavior and Modeling of Fiber Reinforced Polymer-Confined Concrete." Journal of Structural Engineering, Vol. 130, No. 11, 1713-1723.

Theriault, M., Neale, K. W., and Claude, S. (2004). "Fiber-Reinforced Polymer-Confined Circular Concrete Columns: Investigation of Size and Slenderness Effects." Journal of Composites for Construction, Vol. 8, No. 4, 323-331.

Tonen Corporation (1995). "Forca Tow Sheet Technical Notes." Tokyo, Japan.

Tonias, D. E. (1994). "Bridge Engineering: Design, Rehabilitation and Maintenance of Modern Highway Bridges." New York: McGraw-Hill.

Tsopelas, P. (1994). "Testing and Modeling of a Class of Bridge Seismic Isolation Systems." Ph.D. Dissertation, State University of New York at Buffalo, NY.

USGS a. URL: http://neic.usgs.gov/neis/general/seismicity/us_east.html

USGS b. URL: http://neic.usgs.gov/neis/states/new_york/new_york_history.html

Wallace, J. W. (1992). "BIAX, A Computer Program for the Analysis of Reinforced Concrete and Reinforced Masonry Sections." Report No. CU/CEE-92/4, Department of Civil Engineering, Clarkson University, Potsdam, New York.

Wallace, J. W., and Ibrahim, Y. A. (1996). User's manual for BIAX, "Strength analysis of reinforced concrete sections program."

Watson, S., and park, R. (1994). "Simulated Seismic Load Tests on Reinforced Concrete Columns." Journal of Structural Engineering, Vol. 120, No. 6, 1825-1849.

Weidlinger Associates (1998). "New York City Seismic Hazard Study and Its Engineering Applications." New York, NY.

Wen, Y. K., Ellingwood, B. R., Veneziano, D., and Bracci, J. (2003). Rep. No. MAE-FD-2, Mid-America Earthquake Center, Urbana, IL.

Wyss, G. D., and Jorgensen, K. H. (1998). "A User's Guide to LHS: Sandia's Latin Hypercube Sampling Software." Risk Assessment and Systems Modeling Department, Sandia National Laboratories, Albuquerque, NM.

Xiao, Y., Tomii, M., and Sakino, K. (1991). “Triaxial Compressive Behavior of Confined Concrete.” Concrete Res. Technol., Japan, Vol. 2, No. 1, 1-14.

Xiao, Y., and Wu, H. (2000).” Compressive Behavior of Concrete Confined by Carbon Fiber Composite Jackets.” Journal of Materials in Civil Engineering, Vol. 12, No. 2, 139-146.

Yamazaki, F., Hamada, T., Motoyama, H., and Yamauchi, H. (1999). “Earthquake Damage Assessment of Expressway Bridges in Japan.” Technical Council on Lifeline Earthquake Engineering Monograph, (16), 361-370.

Yeh, Y.-K., and Mo, Y. L. (2005). “Shear Retrofit of Hollow Bridge Piers with Carbon Fiber-Reinforced Polymer Sheets.” Journal of Composites for Construction, Vol. 9, No. 4, 327-336.

Yura, M. J., Kumar, A., Yakut, A., Topkaya, C, Becker, E., and Collingwood, J. (2001) “Elastomeric Bridge Bearings: Recommended Test Methods.” National Cooperative Highway Research Program Report 449, Transportation Research Board.